AD_____

Award Number: W81XWH-10-1-0562

TITLE: Improved Image-Guided Laparoscopic Prostatectomy

PRINCIPAL INVESTIGATOR: Ioana Fleming

CONTRACTING ORGANIZATION: Johns Hopkins University
Baltimore, MD 21218

REPORT DATE: July 2013

TYPE OF REPORT: Annual Summary

PREPARED FOR: U.S. Army Medical Research and Materiel Command
Fort Detrick, Maryland 21702-5012

REPORT DOCUMENTATION PAGE

Form Approved
OMB No. 0704-0188

1. REPORT DATE	2. REPORT TYPE	3. DATES COVERED
July 2013	Annual Summary	15 July 2010 – 14 April 2013

4. TITLE AND SUBTITLE

Improved Image-Guided Laparoscopic Prostatectomy

5a. CONTRACT NUMBER

5b. GRANT NUMBER
W81XWH-10-1-0562

5c. PROGRAM ELEMENT NUMBER

6. AUTHOR(S)

Ioana Fleming

E-Mail: inicola1@jhu.edu

5d. PROJECT NUMBER

5e. TASK NUMBER

5f. WORK UNIT NUMBER

7. PERFORMING ORGANIZATION NAME(S) AND ADDRESS(ES)

Johns Hopkins University
Baltimore, MD 21218

8. PERFORMING ORGANIZATION REPORT NUMBER

9. SPONSORING / MONITORING AGENCY NAME(S) AND ADDRESS(ES)
U.S. Army Medical Research and Materiel Command
Fort Detrick, Maryland 21702-5012

10. SPONSOR/MONITOR'S ACRONYM(S)

11. SPONSOR/MONITOR'S REPORT NUMBER(S)

12. DISTRIBUTION / AVAILABILITY STATEMENT
Approved for Public Release; Distribution Unlimited

13. SUPPLEMENTARY NOTES

14. ABSTRACT

Laparoscopic ultrasound probe has been integrated with the daVinci robotical surgical system. The new integrated system has been tested on tissue mimicking phantoms. Automatic robotic-assisted palpation has been designed, implemented and tested. Two studies have been completed: 1) ex-vivo prostate specimens using standard ultrasound probe as surrogate LAPUS probe and 2) comparative elastography study of LAPUS and TRUS probes on modified prostate elastography phantoms. Results show elastography with LAPUS has the potential to detect prostate cancer through direct interrogation techniques, but there are concerns about probe manipulation due to its size. Advanced 2D and 3D elastography algorithms improve robustness, ability to overcome decorrelated areas. They have been tested and validated on tissue mimicking phantoms, prostate ex-vivo specimens and in-vivo porcine ablated tissue. A robust iterative motion compensation algorithm for strain induced thermal imaging has been developed and it is described. The algorithm was validated on ex-vivo ablated tissue phantoms.

15. SUBJECT TERMS
Prostate Cancer, Ultrasound Elastography

16. SECURITY CLASSIFICATION OF:			17. LIMITATION OF ABSTRACT	18. NUMBER OF PAGES	19a. NAME OF RESPONSIBLE PERSON
a. REPORT	b. ABSTRACT	c. THIS PAGE			USAMRMC
U	U	U	UU	177	19b. TELEPHONE NUMBER *(include area code)*

Table of Contents

Page

1. INTRODUCTION

Prostate cancer is the second leading cause of cancer death and the most common cancer detected in men in the United States. An estimated 238,590 new cases of prostate cancer will be diagnosed in the United States, and approximately 29,720 men will die of prostate cancer during 2013. Radical Prostatectomy (RP) aims for complete cancer resection and has been shown to improve cancer survival. Robotic-assisted laparoscopic prostatectomy (RALP) has recently emerged as an alternative to open and laparoscopic procedures. The daVinci Surgical System (Intuitive Surgical, Sunnyvale, CA) provides 3-D visualization, higher magnification, hand tremor elimination and refined dexterity by incorporating wristed instrumentation. From 250 robotic cases in the beginning (2001), the number has reached 73,000 in 2009 (86 % of the 85,000 American men who had prostate cancer surgery). Alternative surgical systems are in the work and are awaiting FDA approval.

Initial experiences with the daVinci surgical system have been positive: short learning curve, limited blood loss, less post-operative pain, favorable complication rates, and short hospital stay. Despite fewer perioperative complications and shorter hospital stay, a recent paper found patients were three times more likely to require salvage therapy. One theoretical disadvantage with regards to robotic surgery is the lack of tactile feedback. In open RPs, the surgeon uses his fingers to feel the periphery of the prostate gland. Without tactile feedback, a robotic surgeon is unable to appreciate differences in tissue texture or firmness and therefore may not be able to tailor precisely the extent of tissue excision around the prostate gland in efforts to eradicate all cancerous tissue. Inadvertently leaving residual cancer cells behind, called a positive surgical margin (PSM), is highly associated with cancer recurrence. PSM rates were initially higher in RALP than in the open procedure, but they have been shown to decrease with surgeon's experience and improved technique.

As manual palpation helps guide the surgeon in the open procedure, an equivalent real-time guiding tool is needed for robotic prostatectomy. Imaging modalities like MRI or CT are not feasible intra-operatively, nor do they possess the sensitivity or specificity for accurate detection and localization of prostate cancer. Trans-rectal ultrasound (TRUS) is routinely used in diagnosis, in conjunction with digital rectal examination (DRE) and biopsies. One center used TRUS for real-time monitoring and guidance during Laparoscopic RP and reported technical feasibility and enhanced precision by decreased PSM rates. TRUS was capable of imaging a substantial percent of non-palpable prostate cancers. The authors recognized however, the limitations of TRUS guidance; it requires considerable prior expertise and tends to identify primarily hypoechoic lesions, which were just 47\% of the cancer nodules studied. Today's prostate cancer patients are more likely to present with echogenic or isoechoic lesions because aggressive screening techniques lead to a shift toward smaller, early-stage cancers ; classic B-mode gray-scale ultrasound alone cannot identify these lesions.

Ultrasound (US) Elastography (USE) is emerging as a valuable tool in the field of imaging. Elastography is a qualitative technique based on the principle that tissue compression produces strain (displacement) within that tissue; strain is smaller in harder, stiffer tissue than in softer, more compliant tissue. Analyzing the ultrasound raw radio frequency signal results in a strain map, commonly called *elastogram*, where harder tissue is darker than surrounding soft tissue. Cancers tend to present as hard lesions due to increased cellularity. Echogenicity and stiffness of tissue are generally uncorrelated; USE can identify hypoechoic lesions, but also echogenic or isoechoic cancers that classic gray-scale ultrasonography cannot. Elastography through the trans-rectal approach has already been proven feasible in guiding biopsies of the prostate. Integrating USE technology with a laparoscopic ultrasound probe will give robotic and laparoscopic surgeons an important image-guidance tool, which until this point does not exist.

There is a need for real-time intraoperative guidance in laparoscopic prostatectomies. Hence the objective of this proposal was to develop such a capability. USE technology can be integrated with the robotic probe. Elastography is ideal as a technology as it allows for real-time acquisition of images of the prostate gland and, similar to human palpation, allows for contact based interrogation of the prostate’s surface. USE is affordable and minimally invasive and can also be miniaturized and incorporated into robotically assisted prostatectomy. USE using a laparoscopic ultrasound probe (LAPUS) can help the surgeon visualize the anatomy of the prostate gland, identify the contours of the cancerous tumors as well as any extra capsular extension. The contribution of

the proposed research project is in allowing for real-time intraoperative acquisition of images of the prostate gland and the surrounding tissues. We are proposing a safe, simple and robust technique for direct interrogation of the prostate surface aided by a laparoscopic US probe. USE can be a valuable tool in the identification of cancerous lesions and the trajectory of cavernous nerves and thus improve the chances for a cancer-free, nerve-sparing outcome.

2. BODY

This final report will address each of the tasks we proposed to accomplish in the Statement of Work as outlined in Table 1. Additional research accomplishments will also be reported.

	Year 1	Year 2	Year 3 (9 months)
Task 2. System Integration and Clinical Evaluation			
2a. Integration, testing, pre-operative plan			
2b. IRB approval			
2c. Clinical study (N= 5-10)			
Task 3. Design and build new LAPUS probe			
3a. Evaluate data from clinical study			
3b. Design and build New LAPUS probe			
3c. Automatic robotic-assisted palpation			
Task 4. Laparoscopic Prostatectomy with Advanced US Imaging Methods			
4a. Probe evaluation - phantoms			
4b. Probe evaluation – animal models			
4c. Cavernous nerves imaging			

Table 1: Statement of Work for Engineering Tasks 2,3,4

Task 1. Education and Training (Year 1-3)

Throughout the two years and nine months of the award, I have been constantly learning and improving as a prostate cancer scientist. I had regular meetings with my mentors, Dr. Allaf, Dr. Macura and Dr. Boctor which provided me with urology and radiology insights. I completed relevant coursework (*Surgical* Robotics, *Computer Integrated Surgery* Seminar) and also the education needed to prepare and propose to the IRB for human and animal studies (Human subject research, Animal safety, Radiation safety, Animal care and use, Research ethics, Privacy issues, Blood borne pathogens). The biggest gains were made however discussing the direction and means of accomplishing our study's goals. I spent valuable time with the Johns Hopkins Hospital Pathology department, where I have witnessed firsthand both the macro pathology and the micro pathology processing of prostate specimens. The pathology staff and doctors provided me with step by step directions through the process which was very helpful for developing a study in which ultrasound imaging would not hinder subsequent pathological processing. In preparing for the animal study I also interacted with surgeons skilled in radical prostatectomy. These discussions, coupled with operating room observations with Dr. Allaf and Dr. Su are the foundation of my prostate cancer education and training. With respect to my engineering education and training, I have completed all the courses recommended by my mentors but I continue to learn by participating in departmental and surgical robotics specific seminars, in which I am enrolled every semester.

In the last three years I have attended the following conferences:

1. PCRP Innovative Minds in Prostate Cancer (IMPaCT) conference Orlando, FL in 2011. I presented (oral presentation and poster) the proposal for this award. Attached in the appendix is the poster presentation.
2. In 2012, I attended the SPIE Medical Imaging Conference which provided me with insight into the frequent collaborations between engineers and physicians.

Task 2. System Integration and Clinical Evaluation (months 1-12)

We proposed an integration of an existing laparoscopic ultrasound probe (Intuitive Surgical, Sunnyvale, CA) of 7.5 MHz frequency with the daVinci surgical system. **Task 2a: Integration, testing (months 1-6)** has been done successfully in our lab in 2011, as shown in the publication submission in Appendices.

Billings, S., Nishikant, D., Kang, H. J., Taylor, R., Boctor, E., "*System for robot-assisted real-time laparoscopic ultrasound elastography*," presented and published at SPIE Medical Imaging Conference, 2012.

Figure 1 shows a block diagram of our complete system for robot-assisted ultrasound elastography. The daVinci S surgical robot is the primary component of our system. The experimental "Read/Write" Research Application Programming Interface (API) provided by Intuitive Surgical Inc. was used to enable robot motion to be controlled from computer in addition to control inputs from the master console. The daVinci robot manipulates a prototype version of a robotically articulated laparoscopic ultrasound probe, also developed by Intuitive Surgical Inc., which was built into the form factor of a standard daVinci tool. The ultrasound probe is driven by a Sonix RP ultrasound system (Ultrasonix Medical Corp., Richmond BC Canada), which provides an Ultrasound Research Interface granting access to pre-beam formed RF data from the ultrasound probe. The RF is read and processed in real time using elastography algorithms developed in our lab. A high-performance external NVIDIA Tesla series GPU, which connects locally to the Sonix RP system, provides sufficient parallel computing power to generate strain images from RF data in real. The elastography images from the GPU are streamed from the Sonix RP system to a network port on the system's central workstation. The workstation also receives a parallel stream of conventional B-mode ultrasound images from the Sonix RP machine directly. The workstation sends both image streams to picture-in-picture overlays shown in the stereo display of the daVinci console (Figure 2). The picture overlays enable the surgeon to observe the ultrasound and elastography image feeds in real-time without releasing control of the robot arms or diverting attention away from the task at hand.

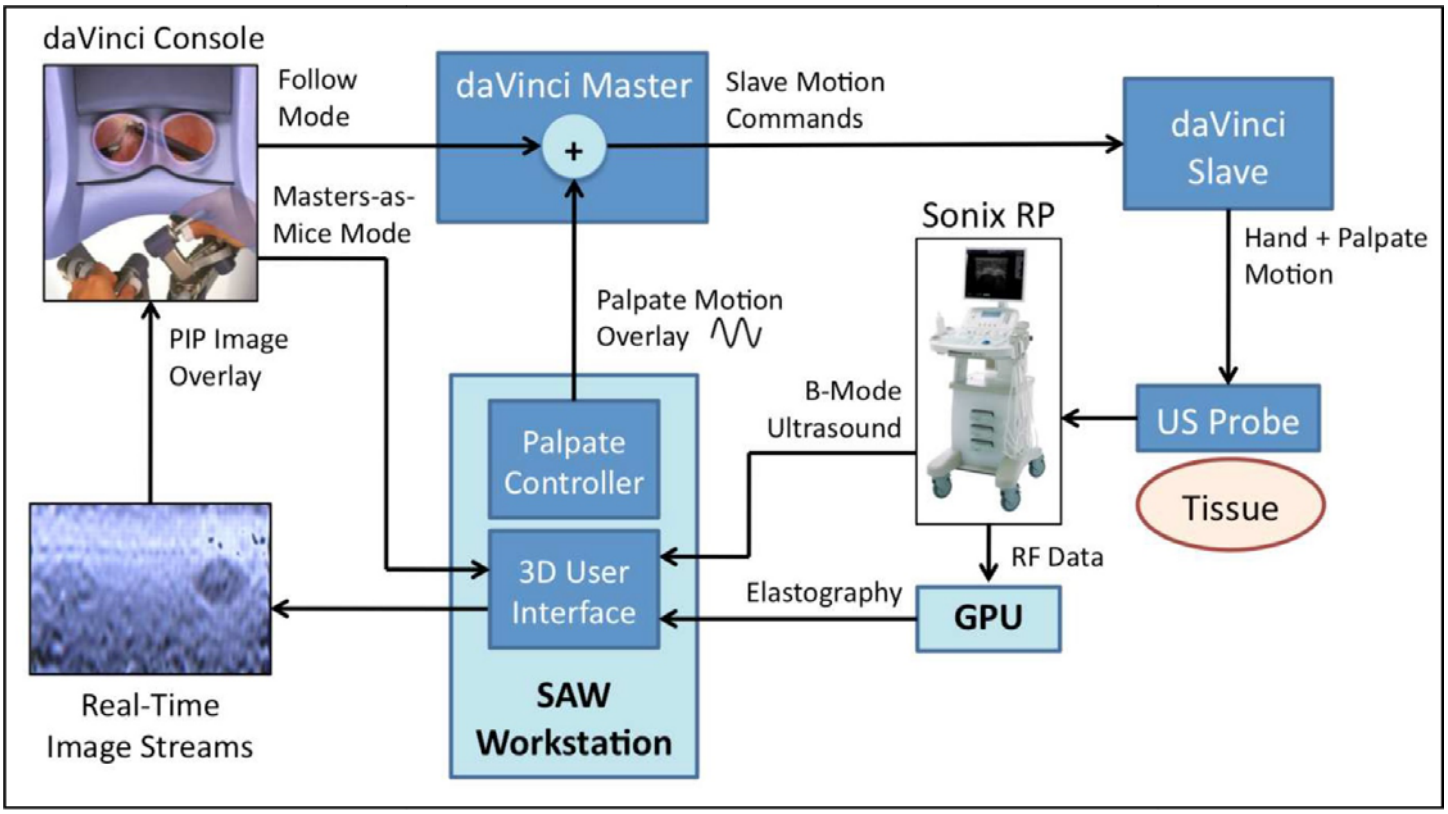

Figure 1. Block diagram of the robot-assisted system for real-time ultrasound elastography

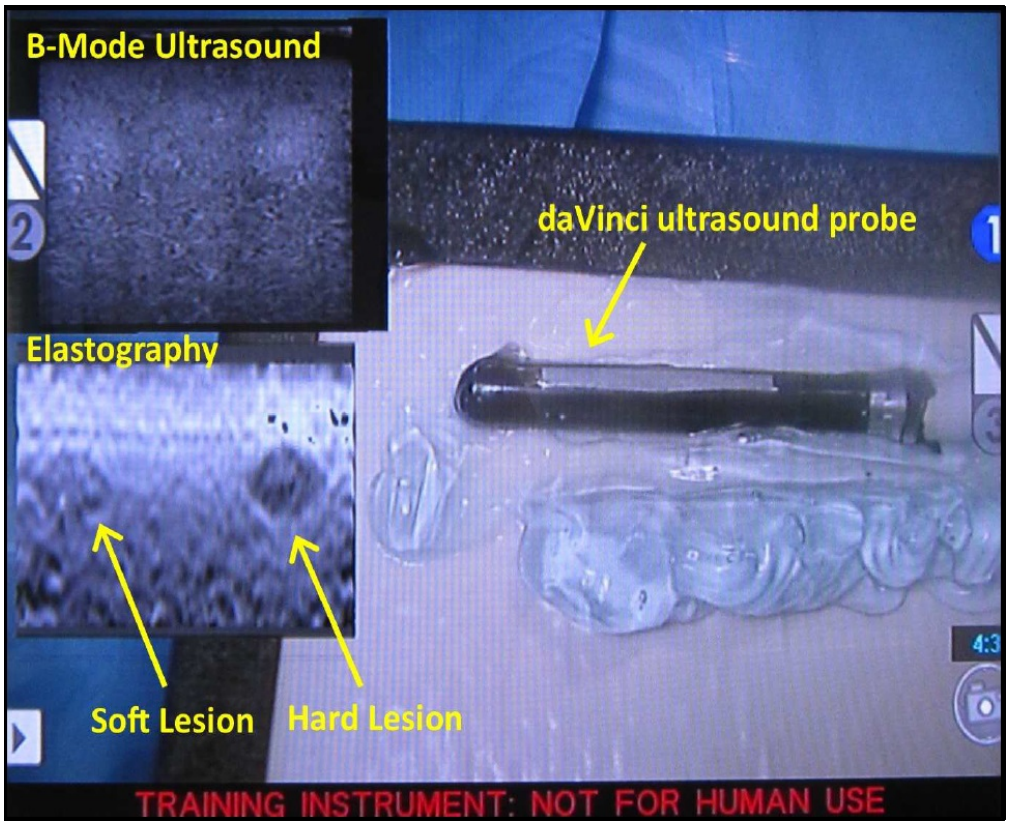

Figure 2. View of the daVinci console display during a test with an elasticity phantom; the elastography image overlay differentiates lesions of different stiffness.

Part of task 2a was to work with Dr. Allaf and our clinical team to put together a plan to be carried into the operating room for testing of the laparoscopic ultrasound probe in a clinical setting. This plan would have been done in conjunction with **task 2b: IRB approval (months 1-6)** in which Institutional Review Board approval for a small (N=5-10) clinical study using the LAPUS probe was going to be sought and the subsequent **2c: Clinical evaluation (months 6-12).** Given the successful system integration, the implementation of automatic palpation and the successful testing on tissue mimicking phantoms, our team felt the next step would be to test the system on *ex-vivo* prostate specimens. This comes as an intermediary step and a natural bridge to clinical testing. At the end of the first year of the award, we had not yet achieved tasks **2b and c.** We experienced delays in the submission of the IRB due to institutional issues. As the Johns Hopkins Hospital (JHH) performs hundreds of prostatectomies every year, we were pressed to come up with a process which would not disrupt the workflow of the Pathology department and would not extend the surgical procedures more than 10-15 minutes. Our urology team lead by Dr Allaf was confident they could perform the prostate gland interrogation with minimum impact in the duration of the surgery. The Pathology department was concerned with the additional processing of the specimens. We responded by designing a phantom box to improve the process so that pathologists could process the specimens faster and with higher accuracy. For our study only, a trained resident pathologist would have had to create a 3D map of the pathological findings, which was needed in order to align and compare the Elastography findings with the current gold standard represented by the pathology report. This is not currently the standard procedure at JHH so this was viewed as a hurdle for approval of the study by the JHH Review Board.

Having been experiencing delays in the submission of the IRB proposal, out team debated in year two of the award how to best accomplish the proposed project goals in the time left available. Our goals were to evaluate the capabilities of the Laparoscopic Ultrasound (LAPUS) probe (Figure 3) in imaging prostate cancerous tissue and also to prepare for clinical testing of LAPUS as an imaging tool during robotic-assisted laparoscopic prostatectomy.

Figure 3: LAPUS Probe

In our clinical study, the standard ultrasound probe Siemens VF10-5 linear array was used as a surrogate transducer, with similar capabilities with the LAPUS probe. Existing ultrasound data from *ex-vivo* prostate specimens (collected recently by our team as part of an ongoing study) were used to assess the capability of the standard VF10-5 probe. **N = 6** prostate specimens from patients enrolled in our study, provided **N = 10** target areas, **8** hard nodules in the peripheral zone, **1** hard and **1** soft nodule in the central part of the gland. The results of the study will be presented below, at task 3a.

Task 3. Design and build new LAPUS probe (months 13-24)

Data from the *ex-vivo* prostate specimens study was evaluated (**Task 3a**) and the elastography findings compared favorably with pathology reports and MRI findings - Figure 8 and Table 2. Our analysis proved that an ultrasound probe fitted with a transducer similar with our LAPUS probe can produce elastograms which can help the surgeon identify hard and soft lesions in the prostate tissue. We submitted our findings and our paper has been accepted for publication in the Medical Science Monitor Journal in 2012 (attached in Appendices):

Ioana Nicolaescu Fleming, Carmen Kut, Katarzina Macura, Li-Ming Su, Hassan Rivaz, Caitlin Schneider, Ulrike Hamper, Tamara Lotan, Russ Taylor, Gregory Hager, Emad Boctor, *" Ultrasound elastography as a tool for imaging guidance during prostatectomy: Initial experience*", Med Sci Monit, 2012; 18(9)

Table 2. Prostate specimen data: A total of 10 (ten) elastography lesions were identified in 6 (six) patients' specimens (8 malignant and 2 benign).

#	Location	Gleason score	Size (cm)		
			Elastography	Pathology	MRI
1.1	PZ base	3+5	1.4×0.8	1.3×0.8	1.3×1.1
1.2	CG base	N/A-Solid	0.7×1.1	1.0×1.0	1.0×1.1
1.3	CG base	N/A-Soft	1.1×0.8	1.0×1.0	1.0×0.9
2.1	PZ base	5+3	3.0×1.3	2.4×1.0	2.0×1.5
3.1	PZ mid	4+5	2.4×0.8	1.9×1.0	1.5×1.2
4.1	PZ mid	3+3	1.0×0.5	0.5×0.4	0.6×0.7
4.2	PZ mid	3+4	1.5×0.9	1.1×0.5	1.1×0.8
5.1	PZ apex	3+3	0.5×0.6	0.5×0.5	0.6×0.6
5.2	PZ apex	4+3	0.6×1.0	0.8×0.9	0.9×0.9
6.1	PZ base	3+3	0.7×1.2	0.7×1.8	0.7×0.7

PZ – peripheral zone; CG – central gland.

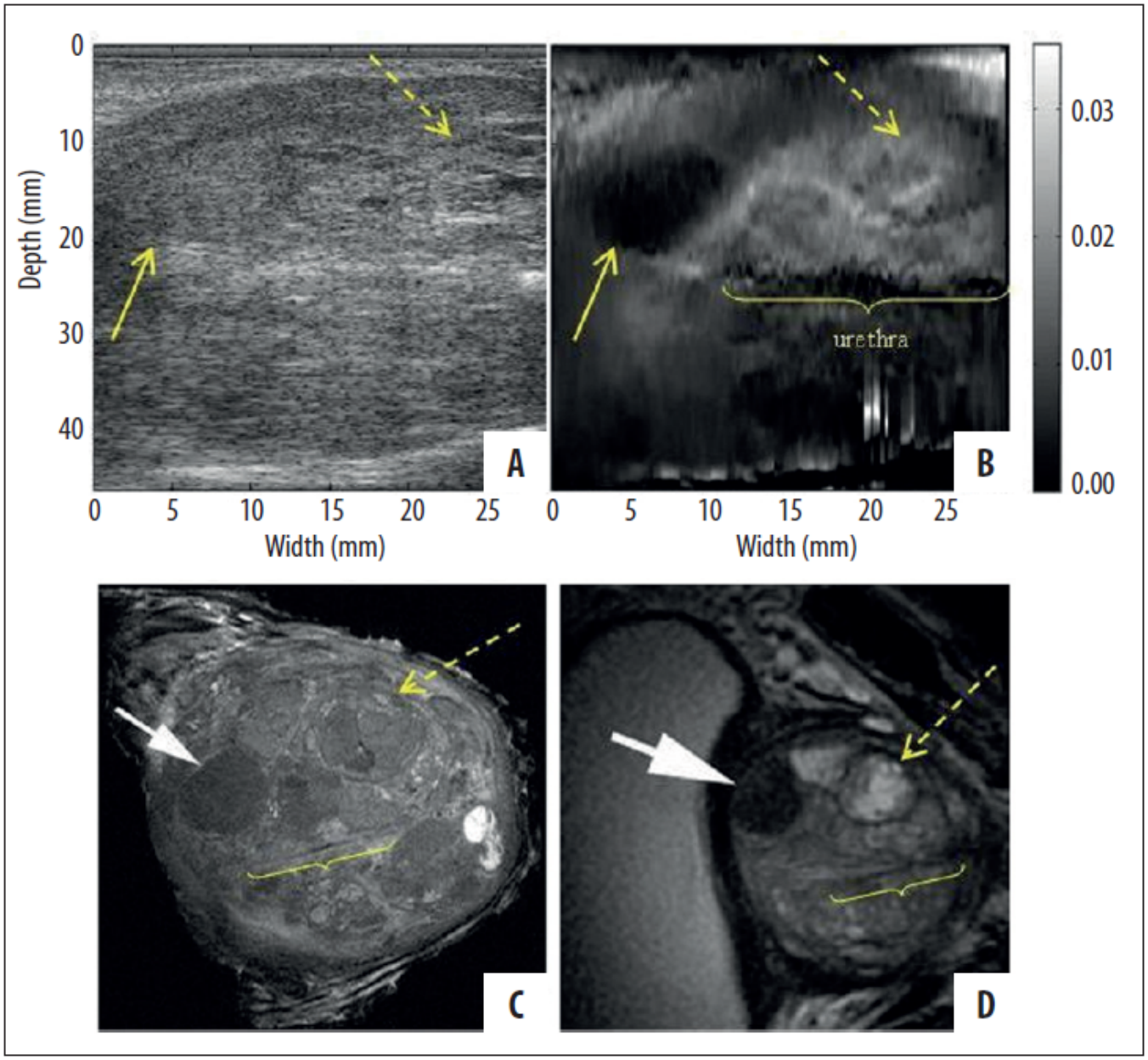

Figure 8: Coronal section of prostate specimen #1 at the level of the central gland: Classic ultrasound B-mode (A) and elastogram (B). 9.4 Tesla *ex-vivo* (C) and 3 Tesla *in-vivo* (D) MRI images are presented in coronal planes, in CCW (counter clock wise) orientation for better visualization of the correlation between USE and MRI of the specimen. Benign solid (arrow) and soft (dashed arrow) nodules and urethra are visible.

For **task 3c. Automatic robotic-assisted palpation (months 18-24)**, we used our integrated Sonix RP + daVinci system (task 2a, Figure 1). The assumption was that automatic pressure application will produce more stable and repeatable images and thus eliminate inter-observer variability in interpretation. In this implementation the tissue is autonomously compressed along the axial direction of the ultrasound probe. The system computer generates a sinusoidal palpation motion that is overlaid onto motion commands from the master manipulators. The surgeon retains control over the position and orientation of the ultrasound probe but the computer provides the tremor-free, precise compression motion necessary for achieving a high quality strain image. Continual palpation of tissue under manual control is a tedious task imposing a large cognitive burden and demand of focus. By relieving this burden through computer assistance, the user is able to focus on more important tasks such interpreting real-time imaging information and conducting surgery.

After the automatic palpation motion sequence was implemented, the system was tested on tissue mimicking phantoms. Figure 2 shows a view of the daVinci console display. The overlay of the elastogram shows a clear differentiation of harder and softer lesions. The conclusion of the study was that the new system provides an

improvement over manual elastography techniques by unifying motion commands from a user with the precision and accuracy of computer-assisted motion control to ensure consistent and precise tissue strain. This approach effectively reduces the cognitive load of the human operator while maintaining a user's control of the procedure. Preliminary tests using an elasticity phantom demonstrate the system's capability to generate strain images in real-time that can be used to delineate simulated lesion boundaries and differentiate lesions of varying stiffness.

The results are reported in the same publication attached in Appendices:

Billings, S., Nishikant, D., Kang, H. J., Taylor, R., Boctor, E., "*System for robot-assisted real-time laparoscopic ultrasound elastography*," Presented and published at SPIE Medical Imaging 2012.

Task 3b: Design and build new LAPUS probe has proved unnecessary as our award progressed. Other research teams at Johns Hopkins were also tasked with evaluating the same LAPUS probe for other surgical procedures. The manufacturer, Intuitive Surgical, felt the initial LAPUS probe met the conditions for successful deployment in the clinical setting and is seeking FDA approval without further modifications.

Task 4. Laparoscopic Prostatectomy with Advanced Elastography Imaging Methods (months 25-33)

For **task 4a: probe evaluation on phantoms, o**ur study focused on evaluating the LAPUS probe in its ability to access and interrogate the surface of the prostate in a robotic-assisted approach. For our goal we employed a custom made prostate elastography phantom (CIRS, Inc. - Model 066, Figure 4). The phantom was modified and its top was removed to allow for LAPUS probe access and imaging through direct contact - Figure 5.

Phantom Model 066 contains 3 isoechoic lesions that are at least two times stiffer than the simulated prostate tissue. Under standard B-mode ultrasound they cannot be detected but they should be readily visible on elastograms - Figure 5.

We attempted to image the lesions inside the phantom using the LAPUS probe in comparison with a trans-rectal ultrasound (TRUS) probe - Figure 6. The phantom allows for rectal-like examination and the TRUS probe is routinely used in practice for imaging the prostate tissue during biopsies and sometimes during prostatectomies.

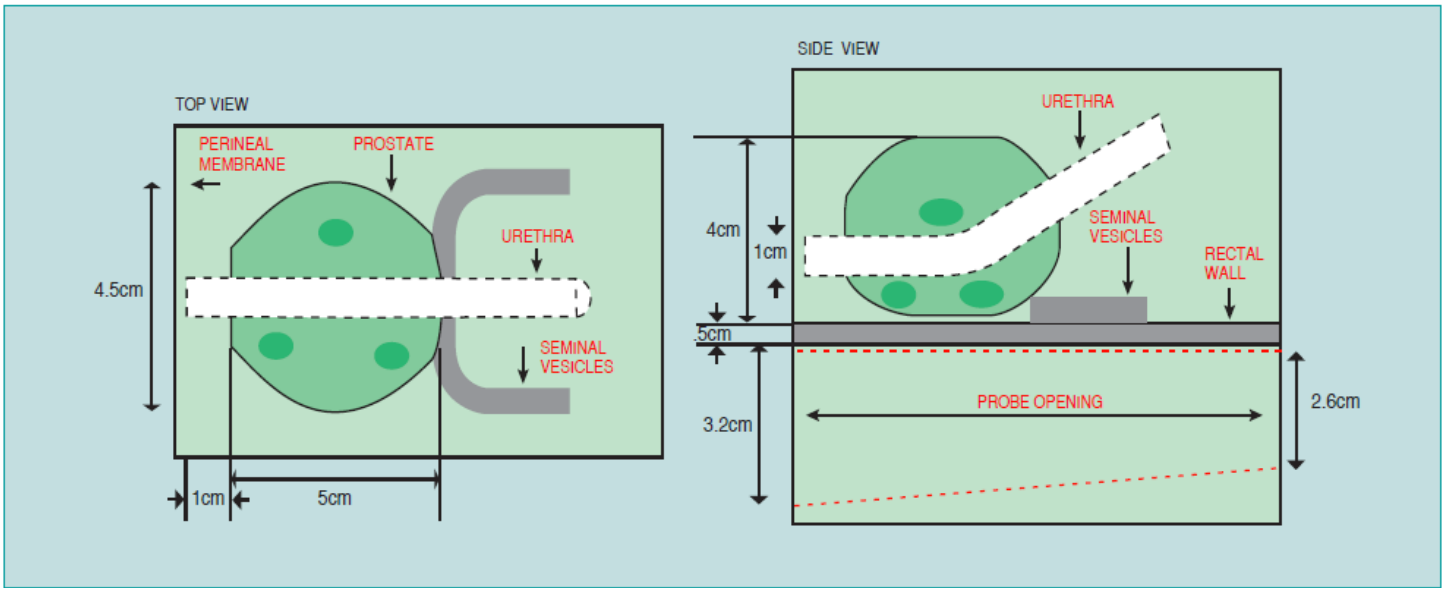

Figure 4: Position of stiffer lesions inside the Model 066 phantom.

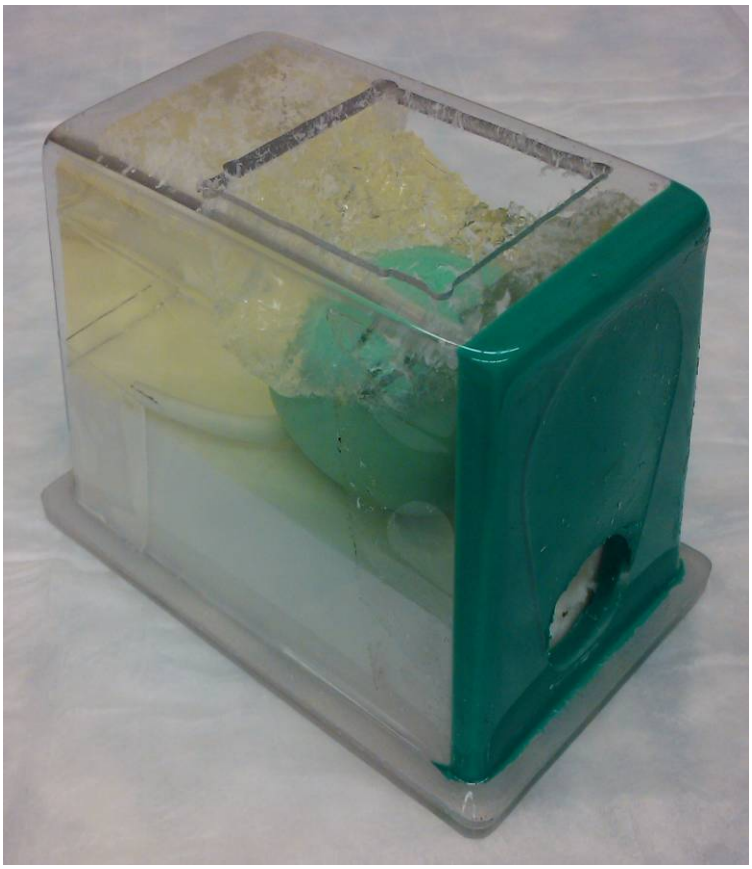

Figure 5: Modified CIRS 066 Prostate Elastography phantom. The top has been removed and direct access to the prostate-mimicking tissue was made available.

The LAPUS probe presented some challenges we took note of, particularly its length appeared big with respect to the size of the prostate. If a custom probe is to be built in the future just for prostatectomy, it is our conclusion that is should be shorter than the current size of our LAPUS probe. Even though the size presented a challenge, we were able to image a majority of the prostate mimicking tissue. Palpation with the probe was needed in order to identify the stiffer lesions using our elastography algorithm - Figure 7.

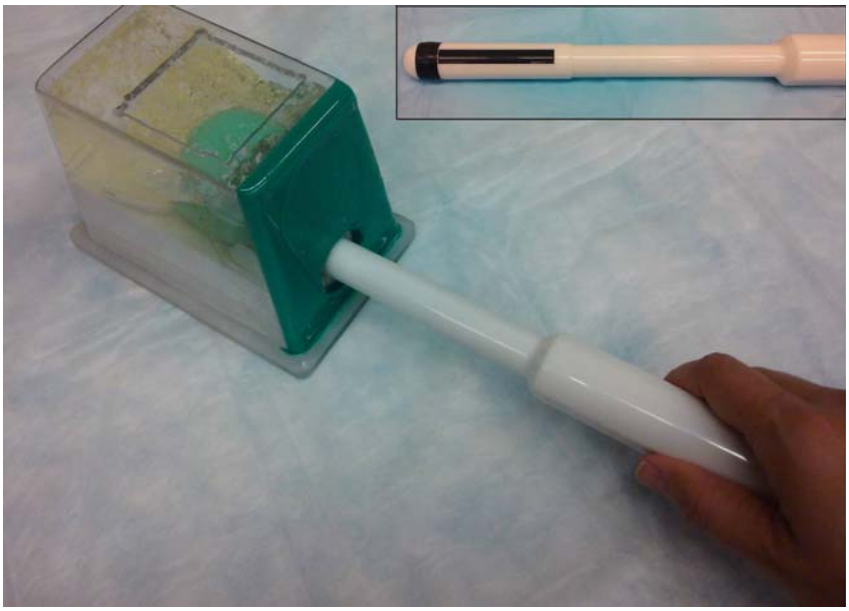

Figure 6: TRUS probe in use with the prostate elastography phantom.

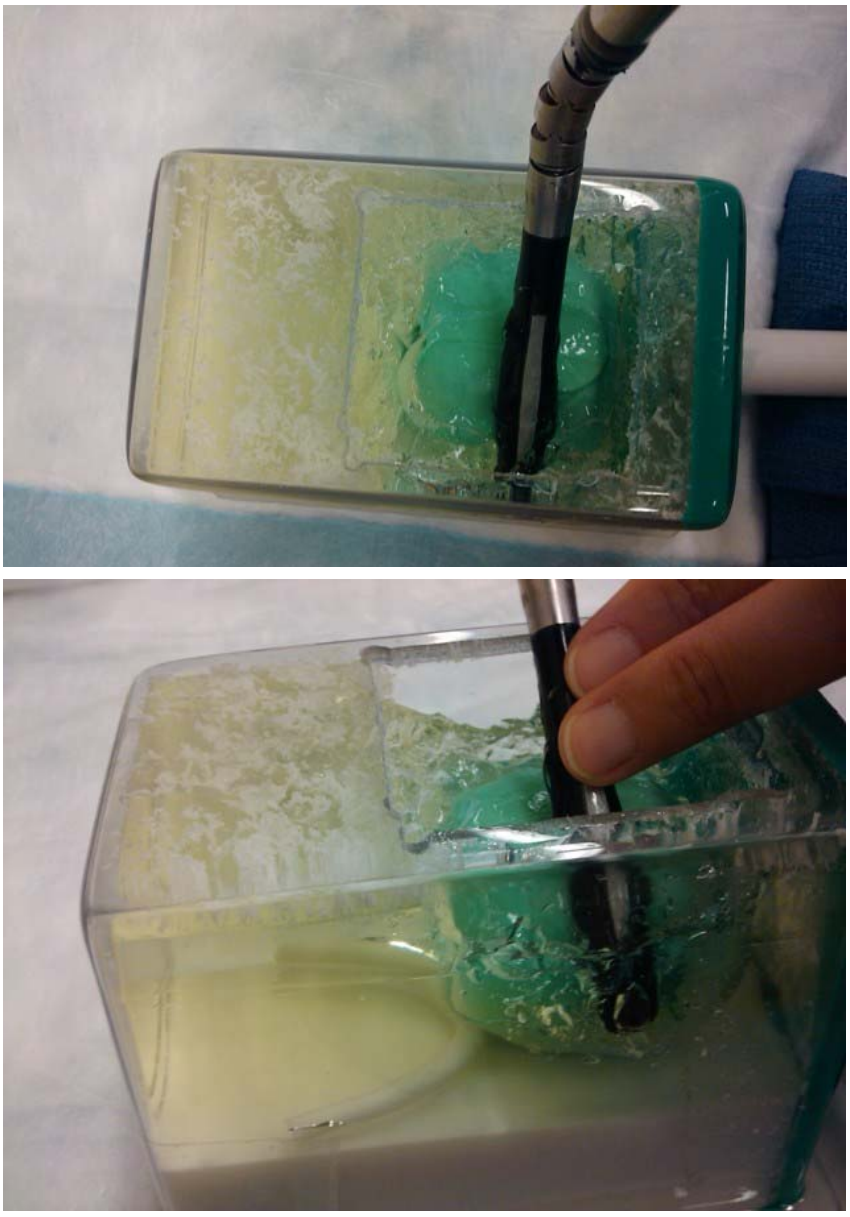

Figure 7: Imaging the prostate phantom with the LAPUS probe.

The analysis of our comparative elastography study between the LAPUS and the TRUS ultrasound showed that LAPUS was just as capable as TRUS probe in identifying the stiffer lesions. One important thing to mention is that in order to obtain elastograms with TRUS, we applied compression on the tissue from the top, which is equivalent to palpating the prostate during prostatectomy. Classic B-mode ultrasound and elastograms obtained using TRUS are presented in Figure 9 and the corresponding findings using LAPUS are shown in Figure 10.

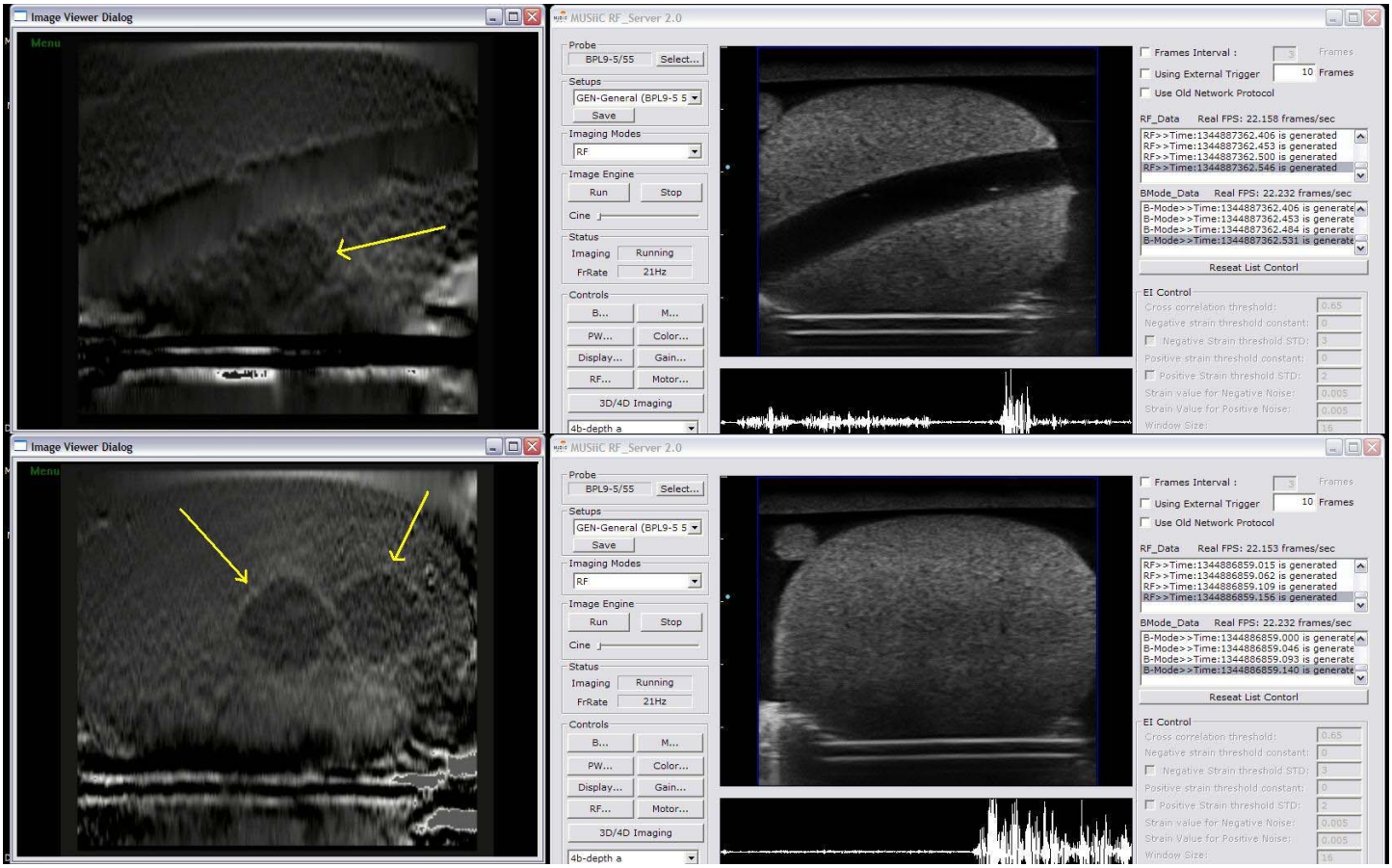

Figure 9: Elastogram and classic B-mode ultrasound for 3 stiff lesions (phantom Model 066) - TRUS imaging

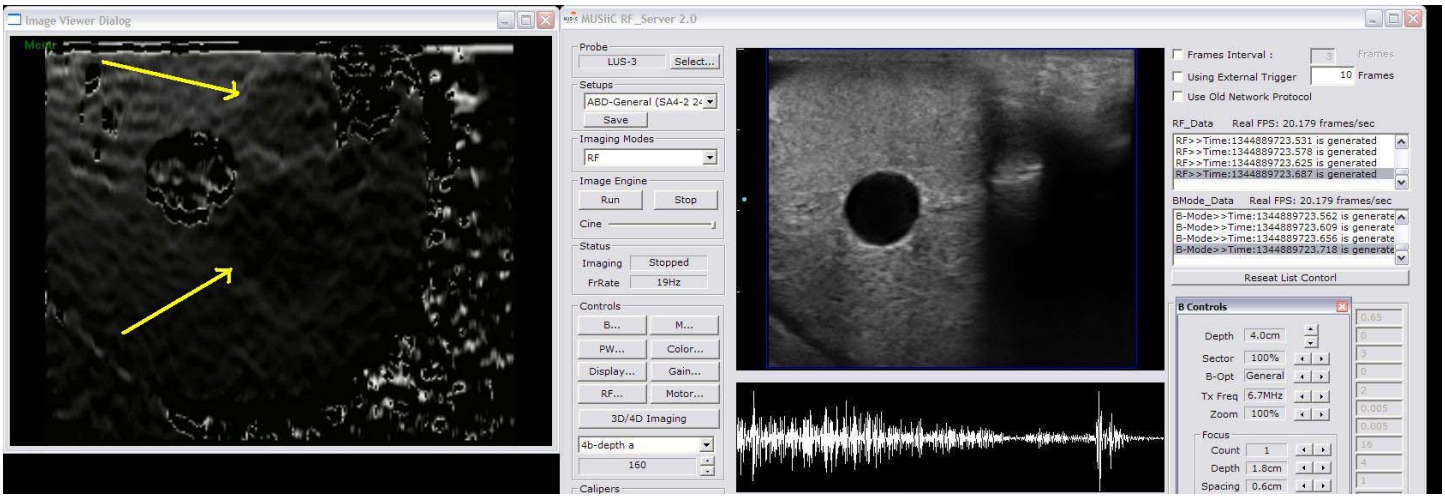

Figure 10: Elastogram and classic B-mode ultrasound for 3 stiff lesions (phantom Model066) - LAPUS imaging

For **task 4b: probe evaluation on animal models**, we intended to submit for IRB approval a study evaluating the LAPUS probe on the porcine model. During the last nine month of the award our team debated the merit of such a study in the context of the research findings of 2012.

A recent study at our institutions was just publishing their findings on the evaluation of the same LAPUS probe in an animal model for hepatic surgery. This study evaluated a new integrated ultrasonography (US) device with the da Vinci Surgical System for laparoscopic visualization (same LAPUS probe as in Figure 3), comparing it with conventional handheld laparoscopic ultrasound probe for performing key tasks in hepatic surgery: (1) In vivo porcine hepatic visualization and probe manipulation, (2) lesion detection accuracy, and (3) biopsy precision. Their results looked favorable for the robotic probe: the robotic ultrasound probe proved better than conventional laparoscopic ultrasound in liver surface exploration (85% success vs 73%; P = .030) and tool manipulation (79% vs 57%; P = .028), whereas no difference was detected in lesion identification (63 vs 58; P = .41) and needle biopsy tasks (57 vs 48; P = .11). Subjects found the robotic ultrasound probe to facilitate better probe positioning (80%), decrease fatigue (90%), and be more useful overall (90%) on the post-task questionnaire". The study concluded the robot-assisted intra-operative ultrasound system to be practical and useful in the performance of important tasks required for hepatic surgery, outperforming free-hand laparoscopic ultrasound probes for certain tasks, and was more subjectively usable to the surgeon. Two journal papers resulted from this study and they are attached as Appendices.

The study we intended to submit for IRB approval intended to explore similar hypotheses in prostate surgery. Our team felt the questions posed by the hepatic surgery study were just as valid in other abdominal surgeries. We concluded our study would prove repetitive and we could direct our effort in other research areas.

Task 4c proposed the development of Advanced Ultrasound Imaging methods aimed at improving the surgeons experience with ultrasound imaging technology. Throughout the two years and nine months of the award, we have made important contributions to the ultrasound imaging field. We summarize below our most important research outcomes, as outlined in the doctoral dissertation of PI Ioana Fleming. The first four chapters are included in the Appendices (The Thermal Imaging chapters are still a work in progress).

Despite ongoing progress, current strain imaging systems still need improvements for a successful adoption into clinical use. The medical community needs a reliable technique which can achieve repeatable, user independent, high strain signal-to-noise-ratio (SNR) images/volumes in real-time. The displacement estimation step has the biggest impact on the speed and accuracy of elasticity algorithms. One concern is applying careful, optimal compression in order to minimize the potential for global and local decorrelation between pre- and post-compression ultrasound signals which usually affects the signal-to-noise-ratio (SNR). In *in-vivo* data, other sources of decorrelation could also affect the computation of strain images, such as incoherent fluid (blood) motion, out-of-plane motion of structures within one image due to transducer or respiratory motion, subsample speckle motion, or a high degree of compression.

Thesis Statement:
Robust methods for displacement estimation in ultrasonic strain imaging help overcome displacement discontinuities and regions of poorly correlated RF data. In thermal imaging, estimation of heat-induced echo strain can be improved by detecting and removing unwanted motion from the environment which would otherwise mask the very small tissue displacements due to heating.

Contributions:
This thesis addresses limitations of current displacement estimation techniques in ultrasound imaging. We briefly summarize the major contributions of this dissertation as follows:

A. Robust Motion Estimation Methods for Ultrasound Elastography.

We present a robust algorithm which improves on the dynamic programming 2D AM displacement estimation method (Rivaz et al 2007) in its ability to overcome displacement discontinuities and decorrelated regions. Signal decorrelation is widely viewed as the major limiting factor for adoption of ultrasound elastography into clinical practice. Our contribution is important as it increases the chances of obtaining real-time, repeatable, user independent elastograms. The robust implementation addresses multiple weak points in the Rivaz method:

- By addressing the selection of the seed RF line, our method insures a robust, stable starting point for the algorithm (Figure 11).
- By controlling the displacement propagation step, we provide true displacement in regions which otherwise would present just decorrelation artifacts.

We evaluated the method on tissue mimicking phantoms and we explore applications to detection of cancerous nodules in the prostate gland during open or robotic-assisted prostatectomy (Figure 12).

We extended the robust displacement estimation method to three dimensions by pairing it with the frame selection algorithm of Foroughi et al (Pre-doctoral DOD training award recipient for breast cancer research). Combining the strengths of both techniques improves the robustness to signal decorrelation. Every step of the method is highly parallelizable. With the use of GPU technology, the method in its current form could be suitable for real-time 3D elastography. We validated the 3D method on human *in-vivo* data from a hepato-carcinoma ablation.

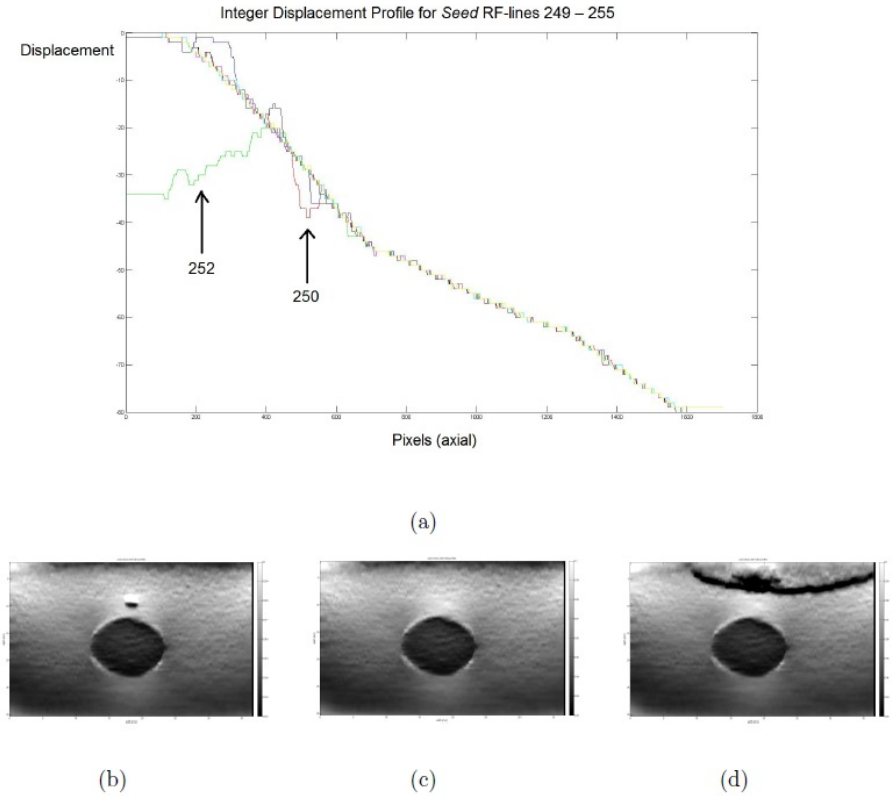

Figure 11. Integer DP displacement estimation for seed RF lines 249 - 255 (a). Note the areas (for lines 250 and 252 respectively) which exhibit a change in displacement slope. Strain images with corresponding artifacts for seed lines 250 (b), 251 (c), 252 (d)

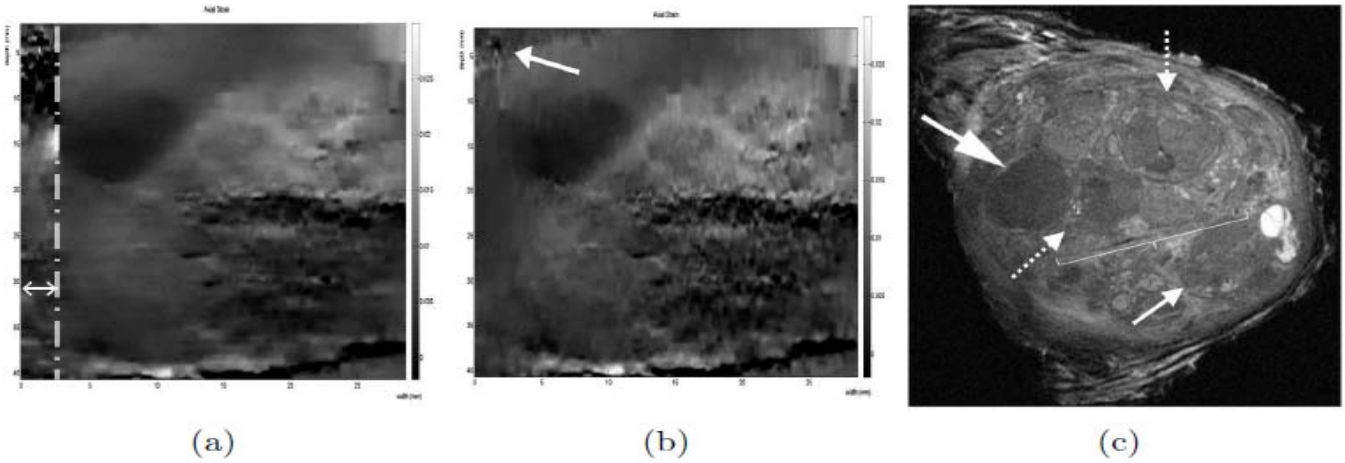

Figure 12. Prostate data set example: (a) an unsuitable seed line is selected for subimage I1, (b) no suitable seed line is found in sub-image I1, which forces the algorithm to propagate displacement from line #35, and (c) 9.4 Tesla MRI coronal scan of the prostate specimen showing hard lesions (arrows), soft lesions (dashed arrows) and urethra (bracket).

B. Robust Motion Estimation Methods for Thermal Imaging

Thermal ablation therapies, using energy sources like RF, laser, microwave, or focused ultrasound, aim to destroy malignant tumors without damaging the surrounding tissue. But despite promising results, current systems remain highly dependent on operator skill, and there is little control of the size and shape of the ablated area. Monitoring the spatial distribution of heating is necessary to control the degree of tissue damage produced. Conventional B-mode ultrasound has been used historically for guiding the ablative tools. The ablation lesion and surrounding tissue have similar backscatter characteristics, making conventional B-mode ultrasound images alone unable to visualize the response to heating. Many have observed an increased echogenicity at the site of the ablation and shadowing below the thermal lesion (cavitation effects). It has been concluded that it is difficult to accurately ascertain the size and position of the thermal lesion on B-mode images alone and, furthermore, it is nearly impossible to delineate the treated tissue margins with conventional ultrasound.

Although conventional B-mode ultrasound does not provide a clear delineation of the ablated region, algorithms have been proposed which use the raw RF signals and are very similar to strain estimation. Heat-induced echo strain is a time-delay estimation problem where the shifts in the RF echo signals are caused primarily by variations in the speed of sound in tissue with temperature. A secondary cause for changes in the echo signals is the thermal expansion of tissue with heating. The motion produced by the changes in the speed of sound is apparent or virtual, while thermal expansion of the tissue introduces an actual physical shift in the scatterer positions. The variations in the echo arrival times due to changes in the speed of sound with temperature are larger than the changes due to thermal expansion of tissue. As tissue reaches temperatures higher than 50 degrees Celsius and the speed of sound in tissue plateaus, thermal expansion effects become more visible.

The main challenge in thermal imaging is measuring very small, apparent tissue motion (on the order of 10’s of microns). Native tissue deformations due to breathing and cardiac cycle generate echo and spectral shifts. Other sources of movement could be found outside the patient’s body, as even small vibrations due to the equipment in the surgical suite can easily mask the very small temperature-induced shifts. In this thesis we develop a robust method for heat-induced echo strain estimation in thermal imaging. An iterative motion compensation algorithm is developed which can detect and alter displacement of tissue due to other sources of deformation/movement. Estimating temperature-induced echo shifts is a very difficult problem because the apparent movement can be very small, on the order of tens of microns. We show that removing extraneous motion helps unmask the effects of heating (Figure 13). The method is evaluated on ablated lesions in *ex-vivo* tissue.

The Iterative Compensation algorithm is summarized below:

1. One RF frame is selected from the 1st data point and one RF frame from the last data point. Estimate displacement between the two RF frames using the robust algorithm (**A**). Compute strain data.
2. Create mask for the region least affected by the heating. The masks use a) 5%, b) 10% or c) 15% lowest axial and lateral strain areas. The resulting masks for two data sets are presented in Figure 13.

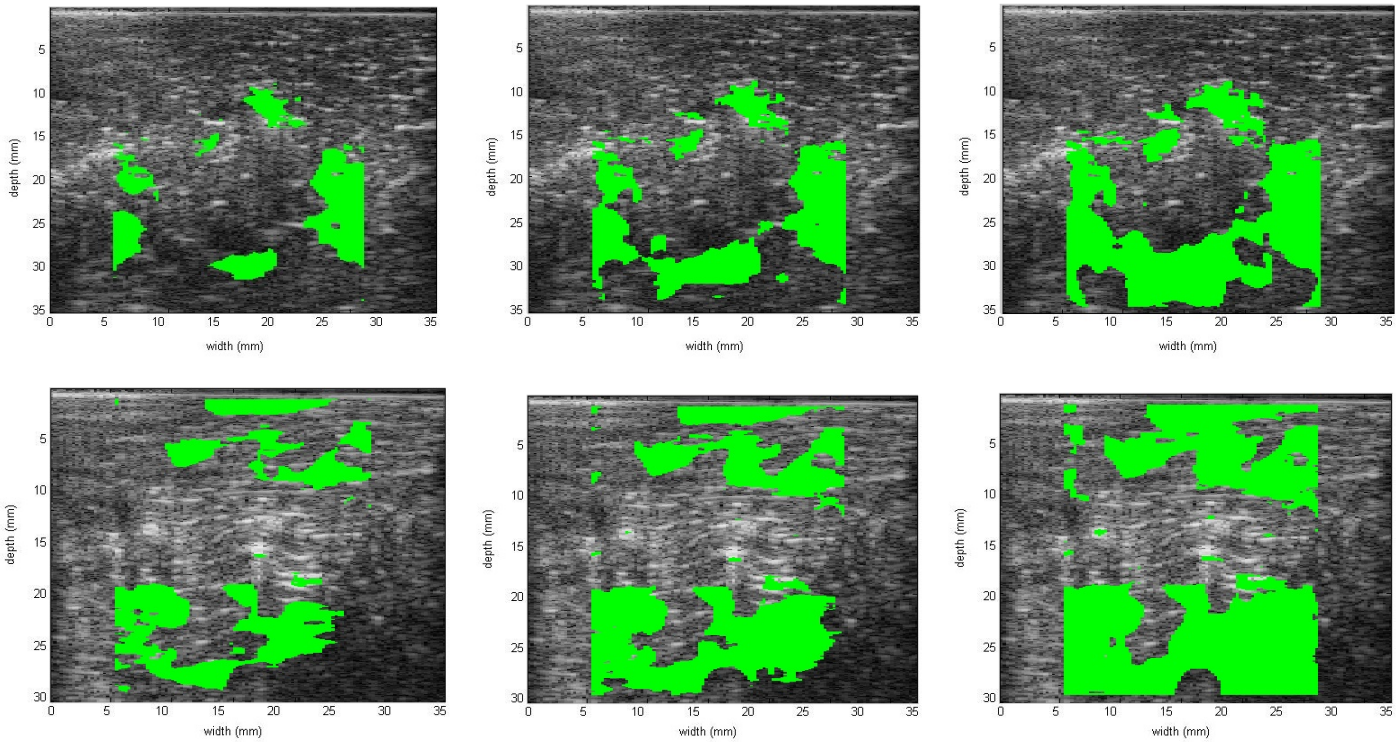

Figure 13: Masks for the regions least affected by the heating. The masks use a) 5%, b) 10% or c) 15% lowest axial and lateral strain areas. First row corresponds to the handheld data set, second row to the fixed, robot held data set.

3. Iterate back to intermediate data points. Compute motion (axial and lateral displacement) in the areas masked. Subtract motion (median value) to achieve compensated motion field (Figure 14).
4. Compare new strain images with old ones (Figure 15).
5. Select ROIs (Figure 19)
6. Compute min, max, mean lateral strain for each ROI. Compare the original values with the new values after IMC (iterative motion compensation) algorithm (Figure 20 – Fig. 7, 8, 9 selected from poster presentation).

We validated our algorithm on two data sets acquired on ablated *ex-vivo* tissue. In the first data set the ultrasound probe was hand held, while in the second data set the transducer was fixed, supported by a robotic arm. Figure 14 shows the uncovered additional motion during the heating process. The hand held data is obviously corrupted by the motion of the operator's hand (physiological tremor). In contrast, the motion uncovered in the data set with the fixed robot-supported probe, in three orders of magnitude smaller and the three masks employed uncovered very similar results (Figure 14, a versus b).

Our results show the IMC approach improves the heat induced echo-strain images. The ablated region is represented more clearly in the strain images after the IMC algorithm was applied (Figure 15). The size and shape of the ablated region is in alignment with the gross pathology findings (Figure 16). Elastographic signal to noise ratio (SNR) remains approximately constant after the IMC approach (figure 17), while the contrast to noise ratio (CNR) is shown to greatly improve, regardless of the mask used in IMC (figure 18)

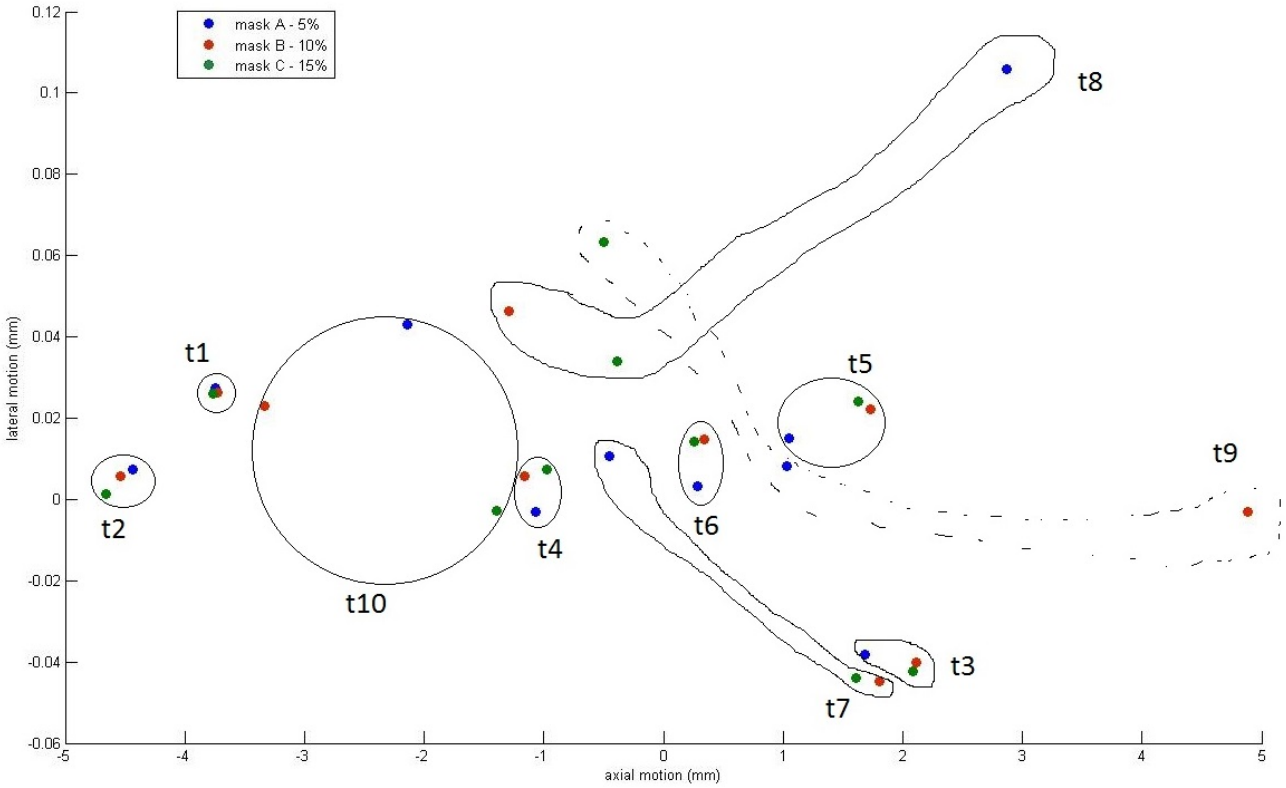

a)

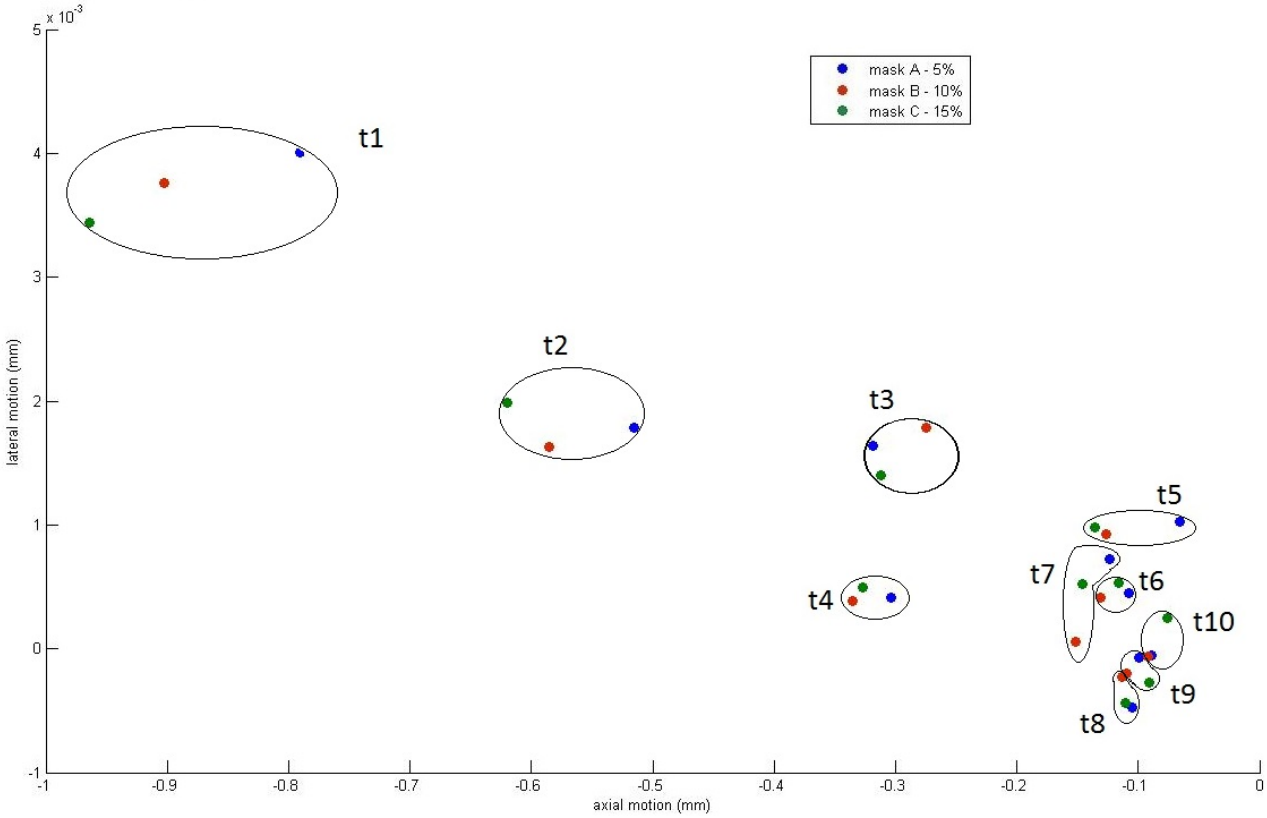

b)

Figure 14: Motion vectors uncovered by the IMC algorithm. a) hand-held probe, b) robot supported, fixed probe

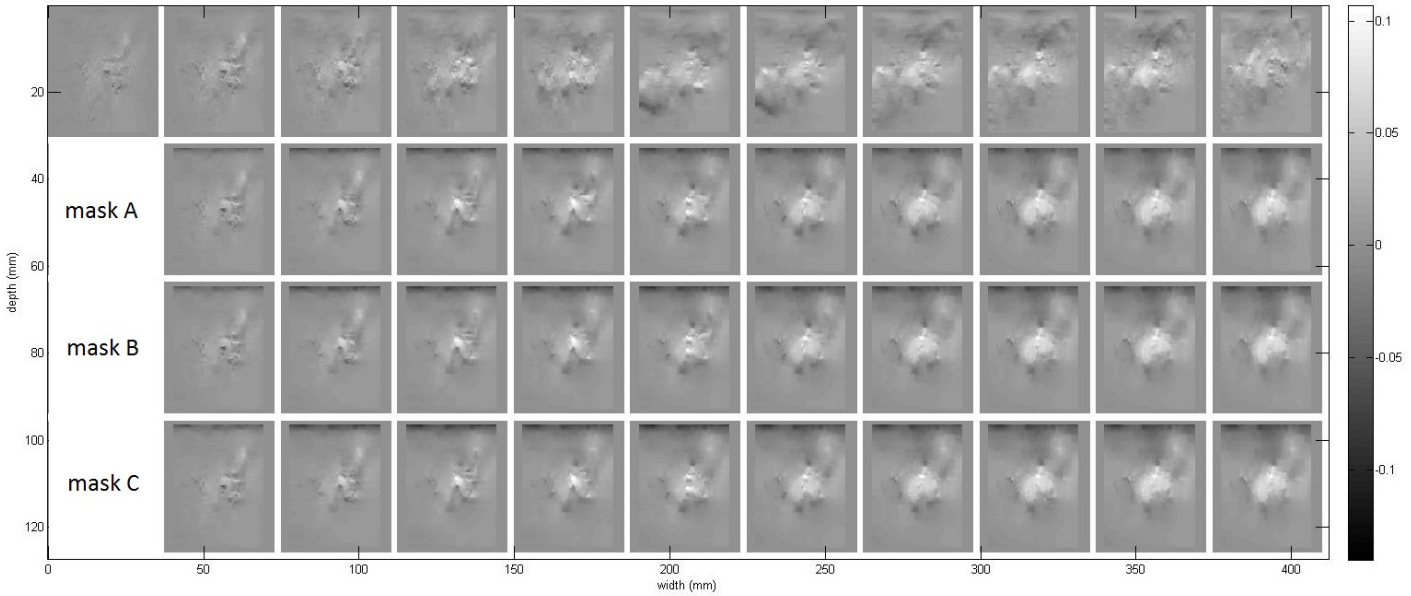

Figure 15: Axial echo strain induced by tissue heating. First row shows the original computed axial strain at each step of the heating process. The last three rows show the axial strain obtained with the Iterative Motion Compensation algorithm, using respectively a 5% mask (A), 10% (B), and 15% (C).

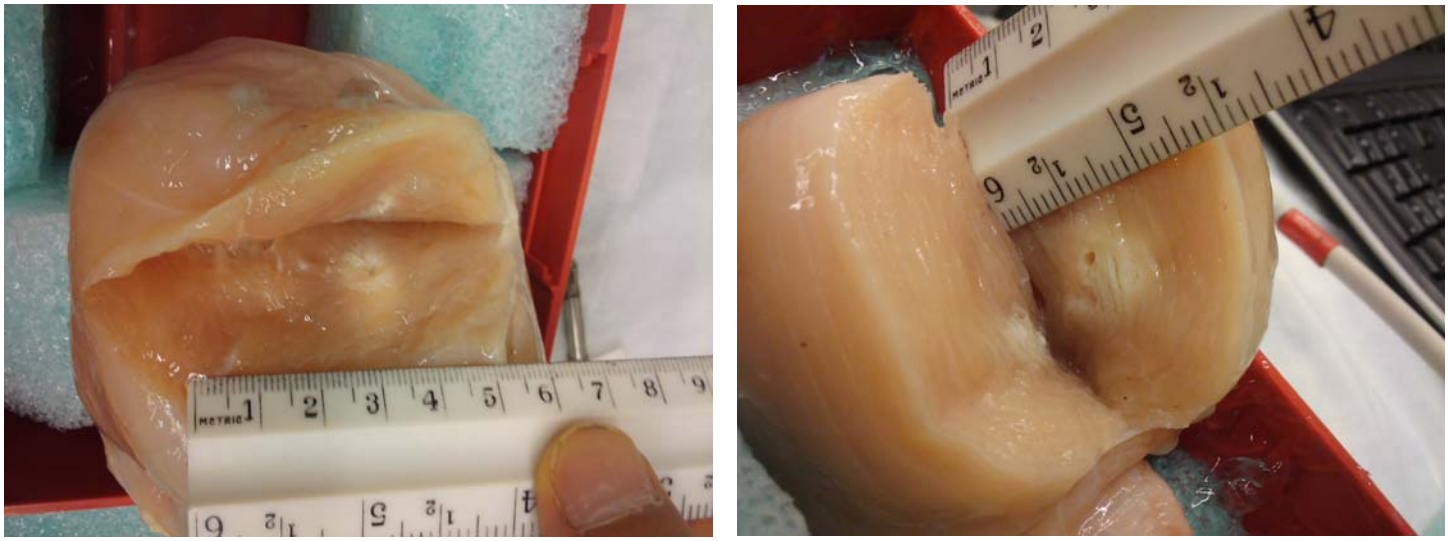

Figure 16: Gross pathology images of ablated lesion in hand-held probe experiment (left) and robot-supported probe experiment (right).

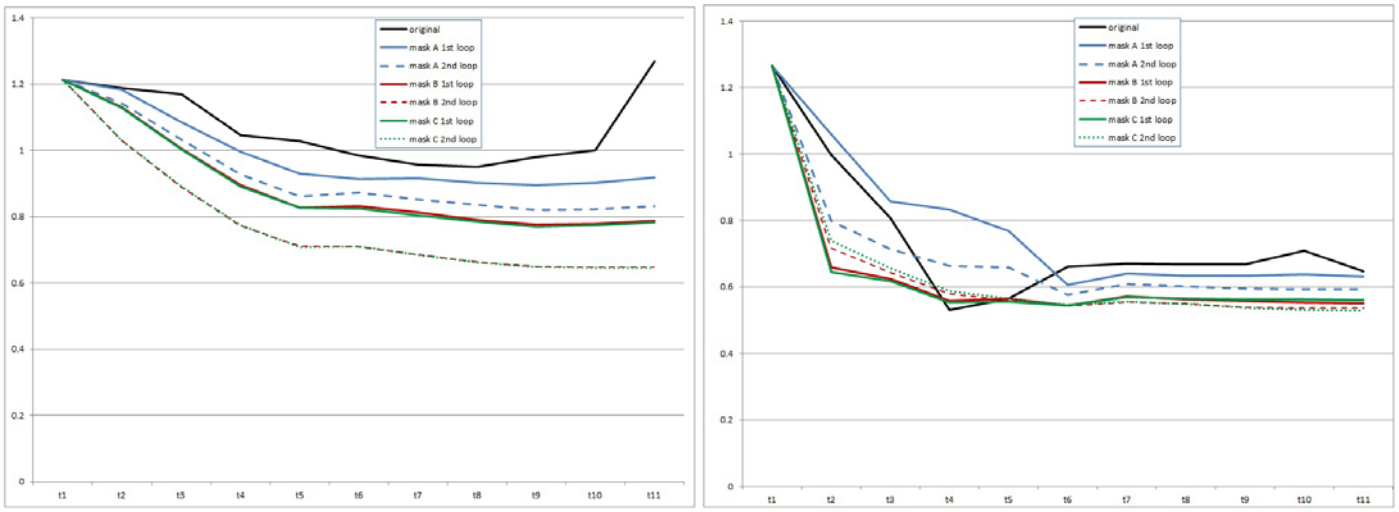

Figure 17: Elastographic SNR of resulting axial (left) and lateral (right) strain: Original computation versus after IMC algorithm.

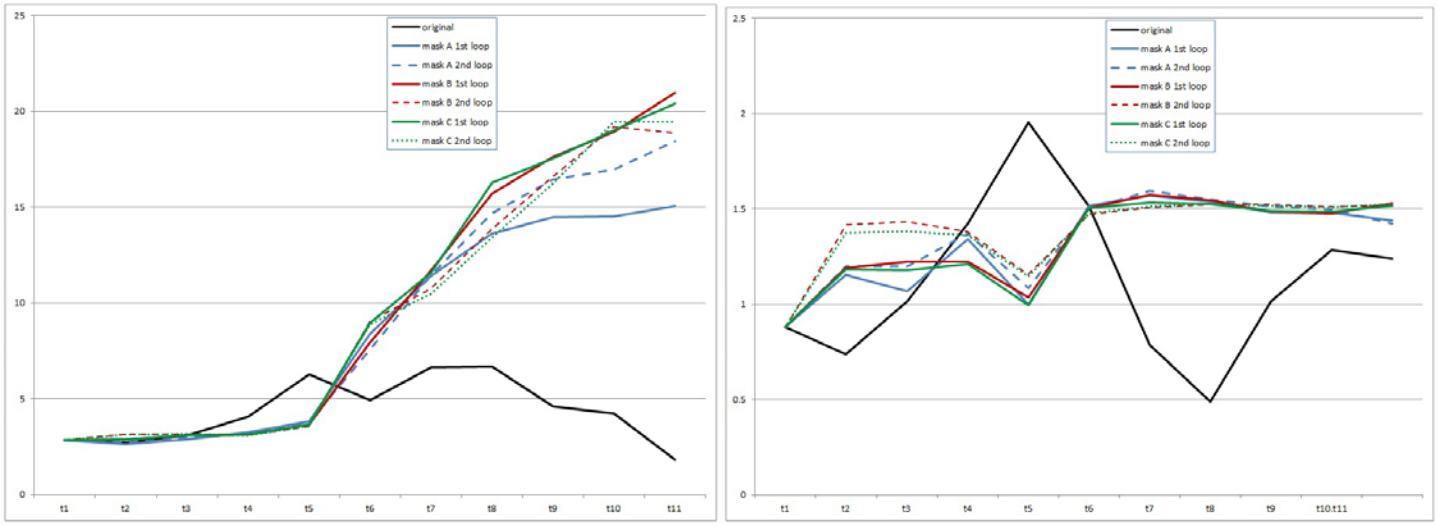

Figure 18: Elastographic CNR of resulting axial (left) and lateral (right) strain: Original computation versus after IMC algorithm.

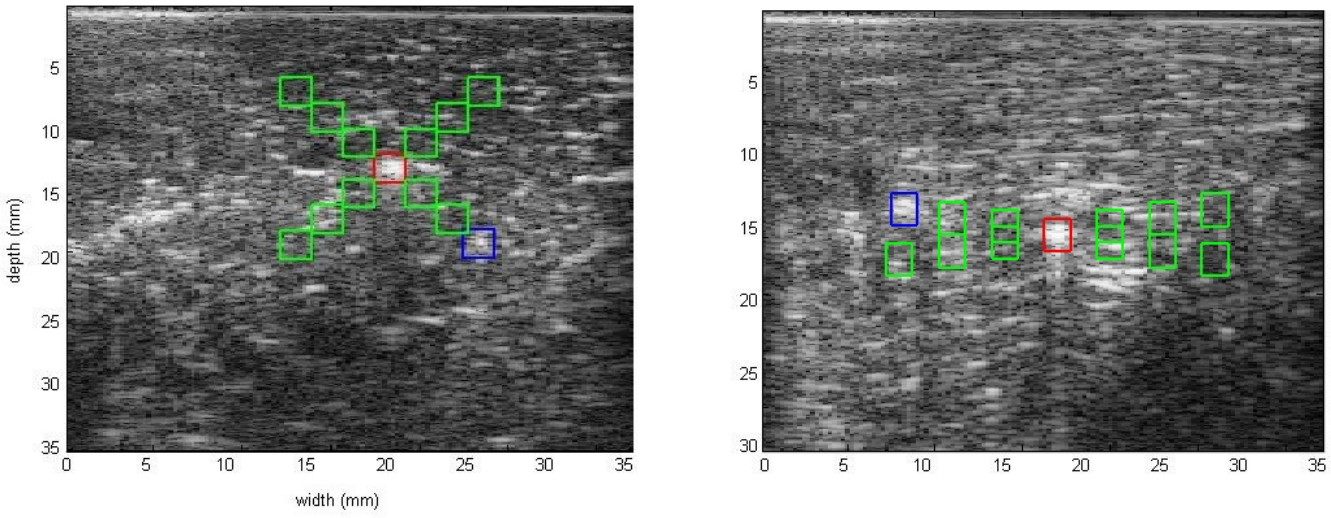

Figure 19: Regions of interest selected for comparison of strain values before and after IMC algorithm (green). Red ROI represents the location of the heating element. Blue ROI represents the location of the temperature reading probe. Hand-held probe experiment (left) and robot-supported probe experiment (right).

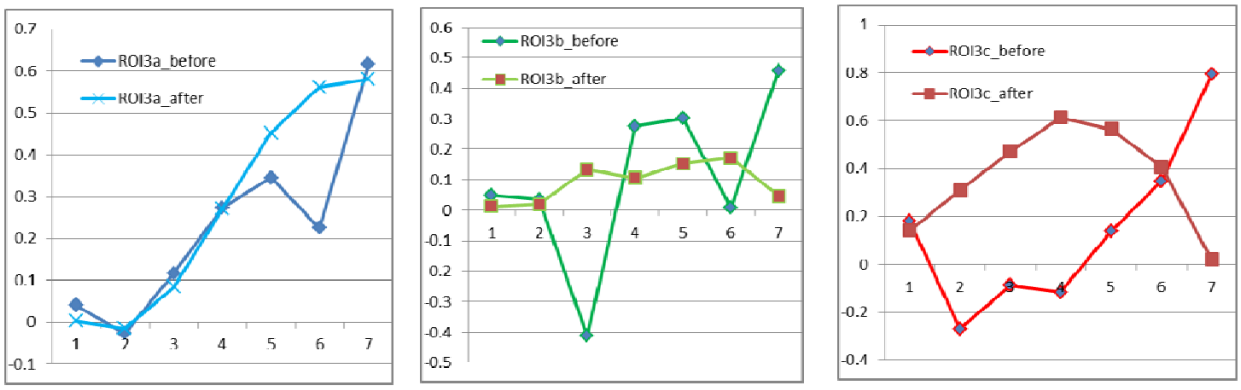

Fig. 7: Mean lateral displacement in outer regions of interest (blue), before and after IMC

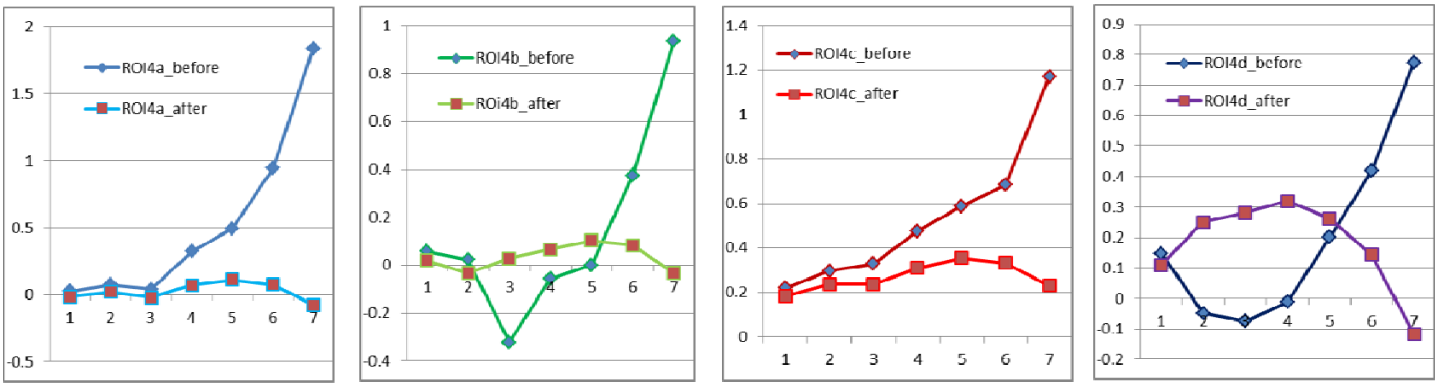

Fig. 8: Mean lateral displacement in inner regions of interest (green), before and after IMC

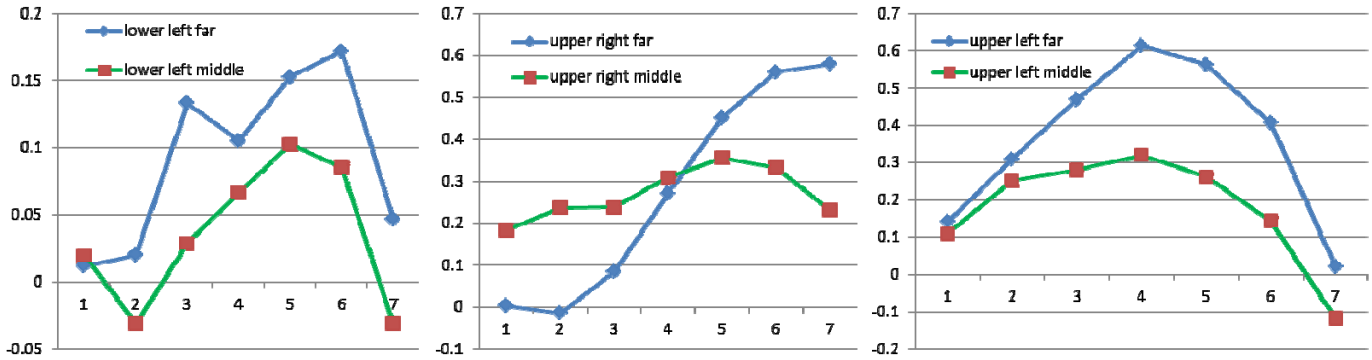

Fig. 9: Mean lateral displacement in outer vs. inner regions of interest (blue vs. green), before and after IMC

Figure 20: Examples of lateral displacement values in the selected ROIs for robot-supported, fixed probe experiment.

C. Ultrasound Elastography Mosaicking

Compared to other imaging modalities like CT and MR, ultrasound suffers from a limited field of view (FOV). Monitoring a structure can be particularly challenging when it is too large to be visualized in a single image or 3D sweep. Size and distance measurements are unreliable in large organs. With the ability to obtain a 3D ultrasound volume, the next evolutionary step in 3D ultrasound is to create an extended field of view by stitching several volumes together. Panoramic ultrasound imaging is emerging as a prevalent technique in clinical practice with a high clinical value. Also referred to as stitching or panorama, ultrasound mosaics aim to achieve several clinical advantages which come along with extended FOV: 1) improving the understanding of spatial relationships among structures when the size of a single image/volume is not large enough to cover the entire region of interest, 2) visualizing structures that are too large for a single volume and 3) allowing for measurements of size and distance in large organs and lesions, and 4) compounded volumes of higher quality will offer the ability to visualize the anatomical structures from a variety of angles.

In the literature of ultrasound mosaicking, registering the underlying displacement field for elastography has not yet been addressed. The clinical advantages of ultrasound mosaics can be improved with the additional corresponding strain information. In particular, strain information can help in multi-modal registration and fusion with pre-operative data for guidance in minimally-invasive interventions. In this thesis, we propose a technique for generating a reliable, wide field-of-view displacement field, robust to sources of decorrelation. Elastography mosaics are generated from two pairs of ultrasound images, and then from multiple image pairs. The method is extended to 3D ultrasound elastography mosaicking using multiple 3D volume pairs.

We develop, to the best of our knowledge, the first algorithm for generating reliable multi-image ultrasound elastography mosaics, robust to regions of decorrelation. For proof-of-concept, the method is evaluated on 2D and 3D data from tissue-mimicking phantoms (Figure 21).

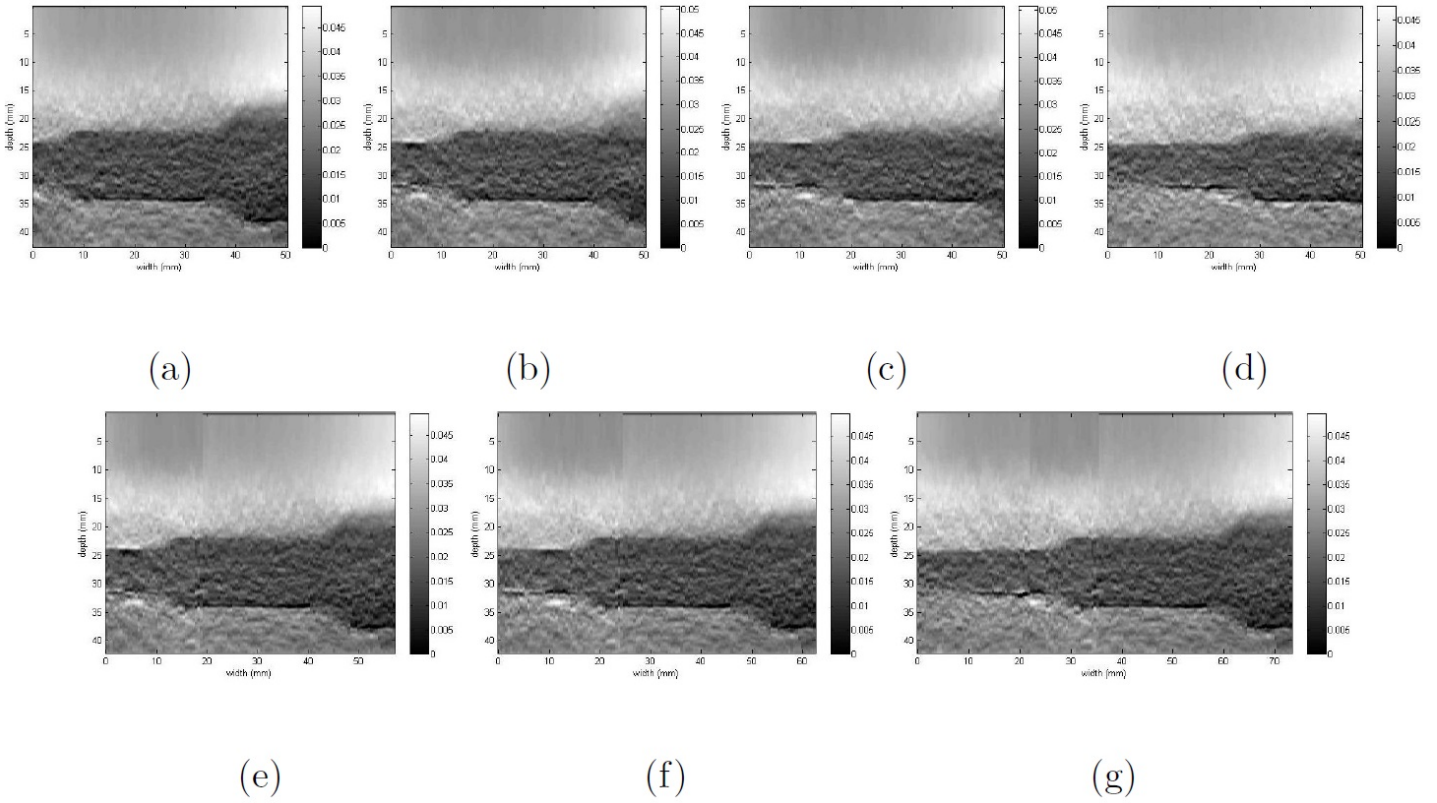

Figure 21: Tissue mimicking phantom: ultrasound elastography at position t0 (a), t1 (b), t2 (c), t3 (d) and elastography mosaic of positions t0 and t1 (e), t0, t1 and t2 (f), and t0, t1, t2 and t3 (g).

3. KEY RESEARCH ACCOMPLISHMENTS

- Integration of an existing laparoscopic ultrasound probe with the daVinci robotical surgical system.
- Testing of the new integrated system on tissue mimicking phantoms.
- Automatic robotic-assisted palpation: design, implementation and testing.
- Completion of study on *ex-vivo* prostate specimens using standard ultrasound probe as an equivalent to the LAPUS probe.
- Analysis of study data; results show elastography has the potential to detect prostate cancer through direct interrogation techniques.
- Phantom study using a modified prostate elastography phantom; comparison of LAPUS and TRUS; results show feasibility in lesion detection with elastography but there are concerns about probe manipulation due to its size.
- Development of a robust displacement estimation method (2D and 3D) which improved the ability to overcome areas of signal decorrelation. The method was validated on tissue mimicking phantoms, prostate *ex-vivo* specimens and *in-vivo* porcine ablated tissue.
- Development of a robust iterative motion compensation algorithm for strain induced thermal imaging. The algorithm was validated on *ex-vivo* ablated tissue.

4. REPORTABLE OUTCOMES

Journal Articles:

1. **Fleming IN**, Kut C, Macura KJ, Su LM, Rivaz H, Schneider CM, Hamper U, Lotan T, Taylor R, Hager, G, Boctor E "*Ultrasound elastography as a tool for imaging guidance during prostatectomy: Initial experience*", Medical Science Monitor 2012; 18(11): CR 635 - 642
2. Schneider CM, Peng PD, Taylor RH, Dachs GW 2nd, Hasser CJ, DiMaio SP, Choti MA, *"Robot-assisted laparoscopic ultrasonography for hepatic surgery"*. Surgery. 2012 May;151(5):756-62
3. **Fleming IN**, Foroughi P, Boctor E, Hager G "*Robust Displacement Estimation Method for 3D Ultrasound Elastography "* Ultrasonic Imaging (in preparation)
4. **Fleming, IN**, Foroughi P, Hager G, Boctor E, " *Temperature Estimation in Tissue Ablation Using an Iterative Motion Compensation Approach*" (in preparation)

Peer-Reviewed Conference Papers:

1. **Fleming**, **I. N.,** Rivaz, H., Boctor, E. M., Hager, G. D. "*Robust dynamic programming method for ultrasound elastography*", in Medical Imaging 2012: Ultrasonic Imaging, Tomography, and Therapy, Proceedings of SPIE Vol. 8320, 83201K.
2. Billings, S., Nishikant, D., Kang, H. J., Taylor, R., Boctor, E., "*System for robot-assisted real-time laparoscopic ultrasound elastography*," in Medical Imaging 2012: Ultrasonic Imaging, Tomography, and Therapy, Proceedings of SPIE
3. **Fleming**, **IN,** Foroughi, P., Boctor, E. M., Hager, G. D. "*Ultrasound Elastography Mosaicking*", CARS 2013.

Other achievements:

The PI has developed and served as the main instructor in a Johns Hopkins Intersession course entitled "Introduction to Medical Imaging". For four years, approximately 25 Hopkins undergraduate enrolled every Winter Intersession in Ioana Fleming's course. The course became very popular and seats were frequently completely occupied the day enrollment opened for the session. Feedback from students as expressed in written evaluations has been overwhelmingly positive. In addition to teaching about the physics and applications of various medical imaging technologies, the PI has used the course to raise awareness for Prostate Cancer and its treatments, from minimally invasive surgery to ultrasound elastography.

5. CONCLUSION

The work completed under the sponsorship of the DOD award has advanced research in prostate cancer therapies. PI will defend PhD dissertation in the Fall of 2013.

6. APPENDICES

1. Fleming IN "*Robust Displacement Estimation Methods for Ultrasound Elastography and Thermal Imaging*" – PhD dissertation (chapters 1-4)
2. Fleming, I., Kut, C., Macura, K., Su, L.-M., Rivaz, H., Schneider, C., Hamper, U., Lotan, T., Taylor, R., Hager, G., Boctor, E., " *Ultrasound elastography as a tool for imaging guidance during prostatectomy: Initial experience*", Med Sci Monit, 2012; 18(9)
3. Schneider CM, Peng PD, Taylor RH, Dachs GW 2nd, Hasser CJ, DiMaio SP, Choti MA, *"Robot-assisted laparoscopic ultrasonography for hepatic surgery"*. Surgery. 2012 May;151(5):756-62
4. Fleming, I., Fouroughi, P., Boctor, E., Hager, G., " *Ultrasound Elastography Mosaicing*", CARS 2013
5. Fleming, I., Rivaz, H., Boctor, E., Hager, G. "*Robust Dynamic Programming Method for Ultrasound Elastography*", Proceedings of SPIE Medical Imaging, San Diego, CA, February 2012 - published paper
6. Fleming, I., Rivaz, H., Boctor, E., Hager, G. "*Robust Dynamic Programming Method for Ultrasound Elastography*", Proceedings of SPIE Medical Imaging, San Diego, CA, February 2012 - presented poster.
7. Billings, S., Nishikant, D., Kang, H. J., Taylor, R., Boctor, E., "*System for robot-assisted real-time laparoscopic ultrasound elastography*," Proceedings of SPIE Medical Imaging, San Diego, CA, February 2012 - published paper.

Chapter 1

Introduction

1.1 Ultrasound Imaging

The field of medical imaging is advancing at a rapid pace. Medical imaging modalities like x-ray radiography, computed tomography (CT), nuclear imaging and magnetic resonance imaging (MRI), are being used in laboratories and hospitals today not only to visualize anatomical structures, but also to detect diseases and plan out surgical interventions. Ultrasound imaging stands alone as the cheapest and safest imaging modality. It is also the world's most frequently used imaging modality, with the largest number of images created annualy [1].

Sound waves are the organized vibrations of atoms or molecules in tissue. The audible range of human ear is from 20 Hz to 20 kHz. Ultrasound represents sound waves generally above 20 kHz, with medical ultrasound usually in the 1 to 10 MHz range. The basic principle of ultrasound imaging can be described as follows [1]:

An ultrasound pulse is transmitted into tissue where it encounters interfaces and scatters that produce echoes (reflections) as the pulse penetrates tissue. The echoes are recorded and their magnitude and timing are used to form an image.

The component that generates the pulses and measures the echoes is a piezoelectric crystal. Piezoelectric crystals, often refered to as transducers, can be used for ultrasound transmission and reception. They are the interface between the electronic circuits of an ultrasound machine and the physical world.

In ultrasound **A-mode** imaging, a transducer with a single piezoelectric element is excited with a voltage spike to transmit a pulse into tissue. As the pulse travels into the tissue, it generates echos from the reflections at tissue boundaries. The returning echos generate voltage spikes which are recorded and digitized. We refer to the raw unprocessed array of electric signals as the radio-frequency (RF) signal. The total time between the initial pulse and the echo is proportional to the depth of the boundary, while the amplitude of the echo is proportional to the difference in acoustic impedances at the tissue boundaries. These two pieces of information, coupled with

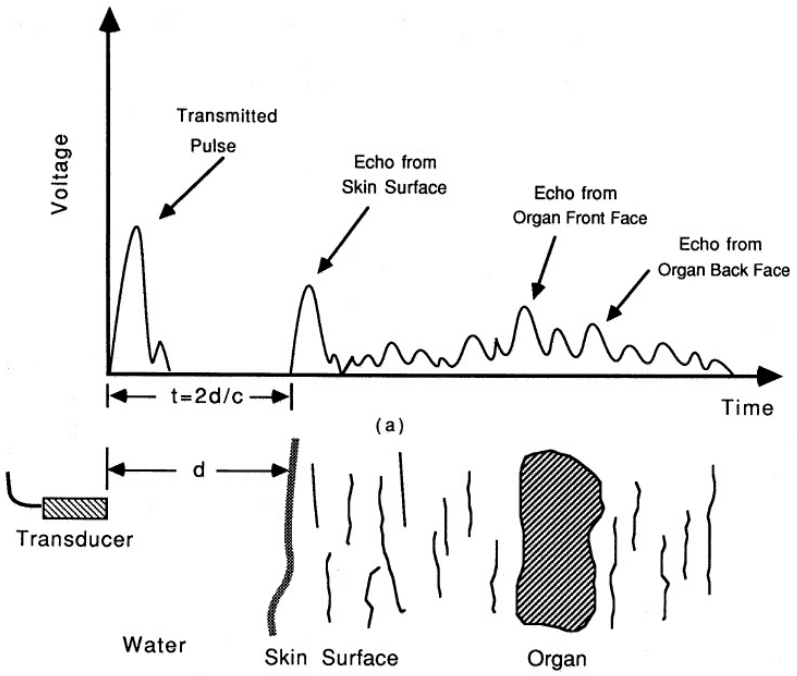

Figure 1.1: Illustration of A-mode ultrasound imaging and the pulse-echo technique (J. L. Prince and J. Links, *Medical Imaging Signals and Systems*. Prentice Hall, 2005)

a known or approximate value for the speed of sound in the imaged tissue, allow a one-dimensional mapping of the tissue boundaries along the line of propagation of the pulse. The pulse-echo technique of A-mode imaging produces 1D signals (Fig. 1.1), where the amplitude of the echoes are displayed to the user as a function of depth.

B-mode imaging is the natural extension of A-mode imaging into 2D. A modern ultrasound hand-held probe contains a line of piezoelectric elements. Instead of displaying the amplitude versus distance, here brightness is used, hence the B in B-mode. The RF signals are combined in columns and the resulting 2D image contains pixels of brightness, calculated as the logarithmically scaled envelope of the RF signal at

each depth/location.

1.2 Motion Estimation in Ultrasound Images

Research developments have transformed ultrasonography from a qualitative tool for imaging soft tissue to a quantitative tool for measuring tissue properties. In particular, two cases have seen increased interest in recent years: 1) measurement of tissue stiffness (known as strain imaging or elasticity imaging), and 2) measurement of change in tissue temperature (known as thermal imaging). Both elastography and thermal imaging rely fundamentally on the measurement of real or apparent motion in ultrasound image sequences.

1.2.1 Ultrasound Elastography

Physicians have used palpation for thousands of years and for some diseases it is still the primary diagnostic tool. Examples include breast self-examination for early detection of breast lumps and digital rectal examination for prostate cancer nodules. The reason palpation is so effective as a medical tool is based on the fact that many

diseases cause changes in tissue mechanical properties. Various inflamatory and neoplastic processes result is an increase in stiffness or elastic modulus of the tissue. It is also worth noting that surgeons routinely use manual palpation intra-operatively to asses the degree of stiffness in tissues undetected preoperatively by CT, MRI, or conventional B-mode ultrasound.

Several years ago Ophir et al [2] introduced a new method termed *elastography* for direct ultrasound imaging of the stiffness of tissues. Emulating manual palpation, the tissue was compressed and apparent motion of regions of the image were compared. From this information, measurements related to tissue stiffness were computed.

The main components of elasticity imaging are:

1. Data capturing during externally or internally applied tissue motion or deformation,
2. Evaluation of tissue response, and,
3. Reconstruction of the elastic modulus or other physical properties based on the theory of elasticity.

Static elasticity methods involve applying compression directly to the tissue [2, 3, 4], while dynamic ones induce motion by applying a low-frequency vibration to the tissue

[5, 6, 7, 8, 9]. Many literature reviews describe various dynamic and static elasticity imaging techniques [10,11,12,13,14]. In both methods, RF signals are acquired before and after tissue excitation and are then used to estimate tissue motion. For some elasticity methods the final resulting image maps physical parameters, like Youngs modulus and Poissons ratio, while others provide a more qualitative image of stiffness distribution in tissue. The literature refers to measurements acquired under static and dynamic excitation collectively as *elasticity imaging*. Medical applications range from tumor detection [15], to characterization of vascular plaques [16] and assessment of vascular health [17] to the study of skeletal muscle contraction [18], assessment of fetal lung maturity [19], and renal transplant rejection [20].

Among the techniques used for tissue displacement estimation in quasi-static elastography, two have been studied in depth: correlation based approaches and phase-based methods. The method as first proposed by Ophir et al [2] used correlation maximization between windows of RF signal from the pre and post-deformation images. It still remains the most widely used method today. Local axial strain is estimated from the A-line motion as [21]:

$$e_{11,local} = \frac{(t_{1b} - t_{1a}) - (t_{2b} - t_{2a})}{t_{1b} - t_{1a}} \tag{1.1}$$

where t_{1a} and t_{1b} represent the arrival times of the pre-compression echo from the

distal and proximal windows, and t_{2a} and t_{2b} the corresponding arrival times of the post-compression echo. The reference region is translated in small overlapping steps along the RF echo signal and one measure of tissue motion is calculated for each depth. The strain image produced by displaying spatial derivatives from the estimated displacement field was called an *elastogram*.

The second dominant approach for tissue displacement estimation was pioneered by ODonnell et. al. [3, 4], who showed that there is a direct relationship between the relative displacement between two windows and the phase of the complex correlation between baseband signal windows. At time t, the baseband representation of two signals $x_1(t)$ and $x_2(t)$ are [3, 4]:

$$\tilde{x}_1(t) = A(t - \tau_1)e^{-i\omega_0\tau_1}, \tag{1.2}$$

$$\tilde{x}_2(t) = A(t - \tau_2)e^{-i\omega_0\tau_2}, \tag{1.3}$$

where A is the real envelope of the transceived pulse, ω_0 is the angular frequency of the ultrasound carrier, and τ_1 is the round-trip propagation time from the transducer to the point scatterer. The complex correlation function between the two signals can be evaluated as:

$$\tilde{C}(t) = \frac{1}{T}\int_0^T \tilde{x}_1\tilde{x}_2^*(t + \tau)d\tau = A(t - \tau_1)A(t - \tau_2)e^{-i\omega_0(\tau_2 - \tau_1)}, \tag{1.4}$$

The time delay between $x_1(t)$ and $x_2(t)$ can be estimated from the zero phase of $\tilde{C}$, while a non-zero phase can be used to estimate the location of the peak without further search [4]:

$$\Delta\phi(0) = tan^{-1}\left[\frac{Im(\tilde{x}(0))}{Re(\tilde{x}(0))}\right] \tag{1.5}$$

$$\Delta x = \frac{c * \Delta\phi}{2\omega_0}, \tag{1.6}$$

where c is the speed of sound.

Despite ongoing progress, current strain imaging systems still need improvements for a successful adoption into clinical use. The medical community needs a reliable technique which can achieve repeatable, user independent, high strain signal-to-noise-ratio (SNR) images/volumes in real-time. The displacement estimation step has the biggest impact on the speed and accuracy of elasticity algorithms. One concern is applying careful, optimal compression in order to minimize the potential for global and local decorrelation between pre- and post-compression ultrasound signals which usually affects the signal-to-noise-ratio (SNR). In *in-vivo* data, other sources of decorrelation could also affect the computation of strain images, such as incoherent fluid (blood) motion, out-of-plane motion of structures within one image due to transducer or respiratory motion, subsample speckle motion, or a high degree of compression. In window/block matching methods, decorrelation introduces significant noise into the displacement map. Correlation-based methods cannot tollerate large tissue deformations which would be desirable for high SNR [21, 22, 12]. Phase zero estimation

methods also require an estimate of the center frequency of the ultrasound RF signal, which varies with depth due to frequency-dependent attenuation in tissue [23].

Many enhancements to the displacement estimation step have been proposed to reduce signal decorrelation effects, most notably signal companding (compression and expanding) [24, 22, 25]. Axial stretching can only compensate for decorrelation due to scatterer motion in the axial direction; decorrelation due to lateral and elevational motion or other sources do not benefit from these methods. In addition, there has been active research in improving the quality of strain estimation. Tracking approaches have focused on the way the displacement map is accumulated. Assuming displacement continuity, Pesavento et al.[26] and Zhu et al. [27] were the first to propose elastography algorithms where each point's displacement is initialized to the previously calculated displacement value of it's neighbor. Other row-to-row tracking algorithms have been proposed [28] and similar techniques have been developed for column [29, 30], diagonal [31] or other [28, 32] directions of propagation. Chen et al. [33] rejected the displacement continuity assumption and implemented an algorithm governed by the presence of high-quality data areas, where displacement is propagated around these regions first and poorly correlated data segments are estimated last to limit their overall influence.

In general, these post-processing steps improve signal quality, but they also introduce significant computation demands, making it challenging to display elastograms in

real-time. The ability to display the strain map in real-time to the user is very valuable in the medical community, where such capability greatly increases the potential elastography might become the tool of choice for image guided surgical interventions. The speed of the displacement estimation becomes even more important in three-dimensional elasticity imaging, where the volume of the data increases computational demands. Jiang el al [30] and Rivaz et al. [34] were the first to frame the displacement estimation as an optimization problem solved by dynamic programming. Rivaz et al [35] greatly improved the speed of the displacement estimation without sacrificing accuracy. The 2D Analytic Minimization (AM) method uses dynamic programming to estimate 2D sub-pixel displacement values on one *seed* axial RF line, which are later propagated laterally throughout the entire image.

First 3D ultrasound imaging systems used 1D arrays being mechanically translated in the elevational direction [36]. A similar technique was adopted in 3D strain imaging, with additional small variations in the applied compression between adjacent frame pairs [37,38]. Another technique for 3D strain imaging is to acquire the pre- and post-compression volumes sequentially. A small pressure is applied to the tissue between volume acquisitions using a mechanical or simulated fixture [39, 40, 41, 42, 43, 44], or by freehand compression between volume acquisitions [32]. These methods are slow and cumbersome in the data acquisition phase, requiring great care to avoid signal decorrelation between the pre- and post-compression frames.

Two hybrid approaches stand out recently. Houdsen et al. [45] applied freehand compression at each step of the sweep and selected several frames, then the stepper motor advanced to the next location in the elevational direction. This method has ease of acquisition as it bypasses the practical difficulty of performing careful and optimal compression between pre- and post-compression frames. It still suffers however from the point of view of data acquisition, which can be quite slow for large volumes. Tracking the 2D wobbler transducer using a position sensor, allows Foroughi et al. to select aligned pairs of RF frames with minimal out-of-plane motion, ensuring high quality strain [46, **?**]. The acquisition is fast as RF data is continuously collected while the operator performs freehand compression and relies on the tracking algorithm to select suitable pairs.

In this thesis we develop an algorithm which improves on the robustness and accuracy of the 2D AM displacement estimation method [35] and extends it to three dimensions. This method enhances the dynamic programming approach to displacement estimation, improving its ability to overcome displacement discontinuities and regions of poorly correlated RF data. Pairing the robust methods with the frame selection algorithm [**?**] combines the strenghts of both techniques and allows for fast displacement estimation for 3D data. Every step of the algorithm is highly paralallelizable, thus greatly decreasing the computational time.

1.2.2 Thermal Imaging

Thermal ablation therapies, using energy sources like RF, laser, microwave, or focused ultrasound, aim to destroy malignant tumors without damaging the surrounding tissue. But despite promising results, current systems remain highly dependent on operator skill, and there is little control of the size and shape of the ablated area. Monitoring the spatial distribution of heating is necessary to control the degree of tissue damage produced. Conventional B-mode ultrasound has been used historically for guiding the ablative tools. The ablation lesion and surrounding tissue have similar backscatter characteristics, making conventional B-mode ultrasound images alone unable to visualize the response to heating. Many have observed an increased echogenity at the site of the ablation and shadowing below the thermal lesion (cavitation effects) [47, 48]. It has been concluded that it is difficult to accurately ascertain the size and position of the thermal lesion on B-mode images alone and, furthermore, it is nearly impossible to delineate the treated tissue margins with conventional ultrasound.

Although conventional B-mode ultrasound does not provide a clear delineation of the ablated reagion, algorithms have been proposed which use the raw RF signals and are very similar to strain estimation. Heat-induced echo strain is a time-delay estimation problem where the shifts in the RF echo signals are caused primarily by variations in the speed of sound in tissue with temperature. A secondary cause for changes in

the echo signals is the thermal expansion of tissue with heating [49]. The motion produced by the changes in the speed of sound is apparent or virtual, while thermal expansion of the tissue introduces an actual physical shift in the scatterer positions. The variations in the echo arrival times due to changes in the speed of sound with temperature are larger than the changes due to thermal expansion of tissue [49, 50]. As tissue reaches temperatures higher than 50^oC and the speed of sound in tissue plateaus, thermal expansion effects become more visible .

Several techniques are based on estimating the echo-shift using speckle tracking [49, 50, 51, 52, 53], and differentiating the time-shift estimates along the axial direction to obtain a temperature map. Temperature estimates are obtained using a cross-correlation algorithm applied to raw ultrasound RF data acquired at discrete intervals during heating [47]. Measurements were validated experimentally in tissue and tissue-mimicking samples [48, 54, 55, 56].

The main challenge in thermal imaging is measuring very small, apparent tissue motion (on the order of 10s of microns). Native tissue deformations due to breathing and cardiac cycle generate echo and spectral shifts. Other sources of movement could be found outside the patients body, as even small vibrations due to the equipment in the surgical suite can easily mask the very small temperature-induced shifts. In this thesis we develop a robost method for thermal strain estimation based on the dynamic programming 2D AM technique by Rivaz et al [35]. The robustness is obtained by

developing an iterative motion compensation algorithm which can detect and remove displacement of tissue due to changes in the environment.

1.2.3 Ultrasound Elastography Mosaicking

Compared to other imaging modalities like CT and MR, ultrasound suffers from a limited field of view (FOV). Monitoring a structure can be particularly challenging when it is too large to be visualized in a single image or 3D sweep. Size and distance measurements are unreliable in large organs. With the ability to obtain a 3D ultrasound volume, the next evolutionary step in 3D ultrasound is to create an extended field of view by stitching several volumes together. Panoramic ultrasound imaging is emerging as a prevalent technique in clinical practice with a high clinical value. Also referred to as stitching or panorama, ultrasound mosaicks aim to achieve several clinical advantages which come along with extended FOV: 1) improving the understanding of spatial relationships among structures when the size of a single image/volume is not large enough to cover the entire region of interest, 2) visualising structures that are too large for a single volume and 3) allowing for measurements of size and distance in large organs and lesions, and 4) compounded volumes of higher quality will offer the ability to visualise the anatomical structures from a variety of angles.

In the literature of ultrasound mosaicing, registering the underlying displacement field for elastography has not yet been addressed. The clinical advantages of ultrasound mosaics can be improved with the additional corresponding strain information. In particular, strain information can help in multi-modal registration and fusion with pre-operative data for guidance in minimally-invasive interventions. In this thesis, we propose a technique for generating a reliable, wide field-of-view displacement field, robust to sources of decorrelation. Elastography mosaics are generated from two pairs of ultrasound images, and then from multiple image pairs. The method is extended to 3D ultrasound elastography mosaicing using multiple 3D volume pairs.

1.3 Thesis Statement

Robust methods for displacement estimation in ultrasonic strain imaging help overcome displacement discontinuities and regions of poorly correlated RF data. In thermal imaging, estimation of heat-induced echo strain can be improved by detecting and removing unwanted motion from the environment which would otherwise mask the very small tissue displacements due to heating.

1.4 Contributions

This thesis addresses limitations of current displacement estimation techniques in ultrasound imaging. We briefly summarize the major contributions of this dissertation as follows:

- We present a robust algorithm which improves on the dynamic programming 2D AM displacement estimation method [35], in its ability to overcome displacement discontinuities and decorrelated regions. Signal decorrelation is widely viewed as the major limiting factor for adoption of ultrasound elastography into clinical practice. Our contribution is important as it increases the chances of obtaining real-time, repeatable, user independent elastograms. The robust implementation addresses multiple weak points in the Rivaz method [35]:
  - By addressing the selection of the *seed* RF line, our method insures a robust, stable starting point for the algorithm.
  - By controlling the displacement propagation step, we provide true displacement in regions which otherwise would present just decorrelation artefacts.

  We evaluate the method on tissue mimicking phantoms and we explore applications to detection of cancerous nodules in the prostate gland during open or robotic-assisted prostatectomy.

- We extend the robust displacement estimation method to three dimensions by pairing it with the frame selection algorithm of Foroughi et al [57]. Combining the strenghts of both techniques improves the robustness to signal decorrelation. Every step of the method is highly parallelizable. With the use of GPU technology, the method in its current form could be suitable for real-time 3D elastograpy. We validated the 3D method on human *in-vivo* data from a hepatocarcinoma ablation.

- We develop a robust method for heat-induced echo strain estimation in thermal imaging. An iterative motion compensation algorithm is developed which can detect and filter displacement of tissue due to other sources of deformation/movement. Estimating temperature-induced echo shifts is a very difficult problem because the apparent movement can be very small, on the order of tens of microns. We show that removing extraneous motion helps unmask the effects of heating. The method is evaluated on ablated lesions in *ex-vivo* tissue.

- We develop, to the best of our knowledge, the first algorithm for generating reliable multi-image ultrasound elastography mosaics, robust to regions of decorrelation. For proof-of-concept, the method is evaluated on 2D and 3D data from tissue-mimicking phantoms.

1.5 Outline

In **Chapter 2** we focus on the robust displacement estimation method for ultrasound elastography. We first introduce the reader to the regularized dynamic programming displacement estimation technique by [35]. Methods are presented for robust *seed* RF line selction and for correlation-guided displacement propagation. The effects of signal decorrelation are then presented in a tissue mimicking phantom data set. The chapter ends with experimental results from 2D phantom and 2D *ex-vivo* prostate data.

Chapter 3 elaborates on the 3D extension of the robust method for displacement estimation. The methods section contains a discussion about the benfits of using random *seed* RF posts throughout the 3D volume versus estimating displacement frame-by-frame. Experimental results are presented from tissue mimicking phantom and from *in-vivo* porcine hepatic tissue following thermal ablation.

In **Chapter 4** we present a robust algorithm for ultrasound elastography mosaicking. Methods and experimental results are presented for 2D pair-wise, 2D multi-image and 3D multi-volume mosaicking. Tissue mimicking phantoms are used in the experimental evaluation.

Displacement estimation methods for thermal imaging are presented in **Chapter**

5. Using an iterative motion compensation approach, we detect and subtract the extraneous, non heat-induced, tissue motion. The efficacy of the method is evaluated on ablated lesions using *ex-vivo* chicken breast tissue. We also present a statistical analysis on the ability of the method to predict *cooler* versus *warmer* regions of the tissue.

Finally, in **Chapter 6**, we summarize the conclusions of our research work and future directions.

Chapter 2

Robust Displacement Estimation for Ultrasound Elastography

2.1 Introduction

Ultrasound elasticity imaging is easy to use, cheap and portable, as it requires no extra hardware. This makes it particularly appealing for medical applications; diagnosis or monitoring could be done at the patient bed side. Despite much research effort and some reported success [11,15,16,58], elastography is still not routinely used in clinical practice. The main reason is the difficulty in elastogram interpretation, as images

can be highly qualitative and hard to reproduce reliably by different operators. In quasistatic elasticity imaging the tissue is compressed and data is aquired before and after the deformation. Elasticity algorithms usually involve two steps: 1) the pre- and post-compression ultrasound raw frequency (RF) data is compared to estimate a displacement map, and then 2) a strain image is obtained by axial differentiation of the displacement data. The speed and accuracy of elasticity algorithms are influenced most by the displacement estimation step. The user is required to apply very careful tissue compression in the axial direction in order to avoid signal decorrelation due to probe slippage and out-of-plain motion between the pre- and post-compression RF frames. Even with a skilled operator, other sources of decorrelation can also affect the estimation of tissue displacement, such as movement of structures as the patient breathes or incoherent fluid motion inside blood vessels. The resulting strain images present with motion artifacts, which could be easily misinterpreted as lesions (Figure 2.1 b,d). The goal of achieving reliable, repeatable, user independent elastograms depends heavily on solving the decorrelation problem.

Among the approaches to reduce signal decorrelation effects, Pesavento et al.[26] and Zhu et al. [27] were the first to propose taking advantage of displacement continuity within the tissue. In their block matching algorithms, each point's displacement is initialized to the previously calculated displacement value of it's neighbor. Other similar methods tracked displacement form row to adjacent row [28], column-to-column [29],

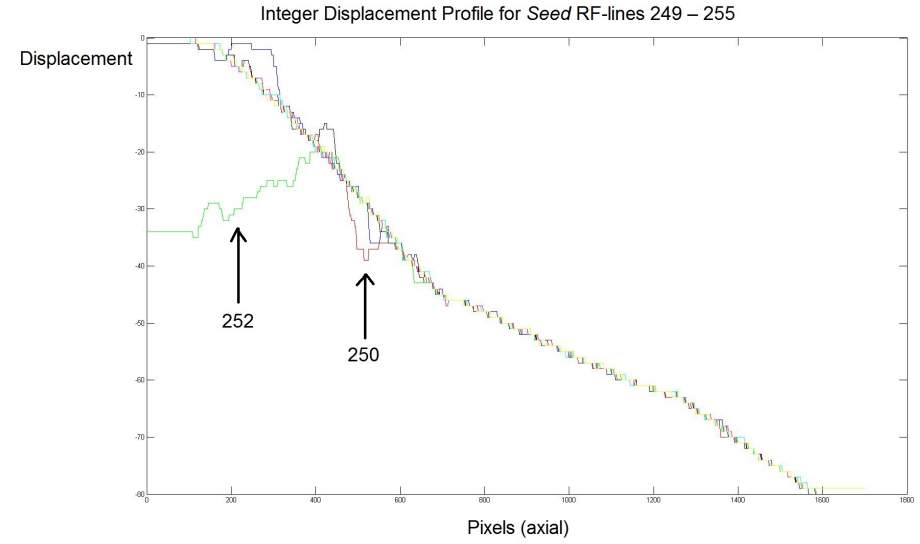

(a)

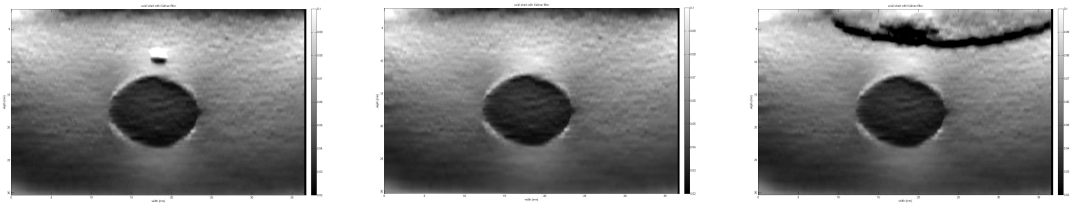

(b) (c) (d)

Figure 2.1: Integer DP displacement estimation for *seed* RF lines 249 - 255 (a). Note the areas (for lines 250 and 252 respectively) which exhibit a change in displacement slope. Strain images with corresponding artifacts for *seed* lines 250 (b), 251 (c), 252 (d)

and diagonally [31]. Jiang el al [30] and Rivaz et al. [34] posed the displacement estimation as an optimization problem solved by dynamic programming (DP). Rivaz et al [35] further regularized the displacement estimation by introducing a 2D analitic minimization (AM) technique, which greatly improved the speed of the displacement estimation without sacrificing accuracy. The speed-up comes from reducing the costly DP computation to only one RF line pair, known as the *seed* line. For the rest of the RF line pairs, the displacement is estimated by propagating the *seed* values laterally throughout the entire image.

The contribution of this chapter is the development of robust methods and quality metrics which improve on the 2D AM technique [35]. The algorithm addresses the choice of one or more robust starting *seed* RF lines, as well as the propagation of displacement values from column to column. Compared to the original algorithm, the current implementation is more robust to signal decorrelation and it can estimate tissue motion even in poorly correlated regions of the ultrasound images.

Chen et al. [33] implemented an algorithm governed by the presence of high-quality data areas, where displacement is propagated around these regions first and poorly correlated data zones are estimated last to limit their overall influence. They did not consider a preferential displacement propagation direction and they also rejected the displacement continuity assumption. This resulted in some areas not being displayed to the user, as the display of strain was suppressed in low quality regions. Our work's

additional contribution is that it addresses the continuity problem by using data quality metrics which can detect changes in the degree of correlation, allowing for reliable estimation of displacement even in poorly correlated regions.

The remainder of this chapter is organized as follows. Section 2 summarizes the DP technique for tissue displacement estimation and the 2D AM regularization. The robust methods for *seed* RF line selection and for correlation-guided displacement propagation are discussed in Section 3, followed by validation experiments using tissue mimicking phantoms and *ex-vivo* human prostate data in Section 4. Section 5 concludes the chapter and future research directions are discussed.

2.2 Prior Work

2.2.1 2D Dynamic Programming Displacement Estimation

We first summarize the DP technique for 2D displacement estimation [34]. Consider two ultrasound RF frames $I_1(i)$ and $I_2(i)$ acquired before and after tissue compression. Let n be the number of RF lines, with each signal sampled at $i = 1,\ 2 \cdots m$. Rivaz estimates the integer axial a_i and lateral l_i displacements of each RF line pair using

DP [**?**]. The cost function is generated combining the prior of displacement continuity (smoothness term) and an amplitude similarity term. The smoothness term takes into account displacement continuity in both axial and lateral direction:

$$R_j(a_i, l_i, a_{i-1}, l_{i-1}) = \alpha_a(a_i - a_{i-1})^2 + \alpha_l(l_i - l_{i-1})^2 \tag{2.1}$$

where α_a and α_l are axial and lateral regularization weights respectively.

The distance between pre- and post-compression signals for line pair j can be written as:

$$\Delta(i, j, a_i, l_i) = [I_1(i, j) - I_2(i + a_i, j + l_i)]^2 \tag{2.2}$$

The cost function at the ith sample of the jth A-line becomes:

$$C_j(a_i, l_i, i) = \min_{d_a, d_l} \left\{ \frac{C_j(d_a, d_l, i-1) + C_{j-1}(d_a, d_l, i)}{2} + w\Delta(i, j, a_i, l_i) \right\} \tag{2.3}$$

where w is a regularization weight for smoothness; d_a and d_l are temporary axial and lateral displacements which are varied in order to minimize eqn.(2.3). The integer displacement estimates are then refined to subpixel displacement estimation, by comparing the original pre-compression signal I_1 (not downsampled) with the post-compression signal I_2 upsampled by a factor of γ using parabolic interpolation [34]. Repeating the refinement procedure n times results in a refinement factor of $(\frac{1}{\gamma})^n$ [34]. The process is repeated for all n RF line pairs, which makes the entire displacement estimation algorithm very computationally expensive.

2.2.2 2D Analitic Minimization Displacement Estimation

In the Analitic Minimization (AM) method, the speed of the algorithm is improved without sacrificing accuracy. Axial a_i and lateral l_i integer displacements are first obtained using DP on only one RF line pair, called the *seed* line. The subsample displacement estimation algorithm continues as follows:

1. a_i and l_i are first subsampled using linear interpolation. Then they become initial guesses for the 2D AM subsample displacement estimation for the *seed* line [35].

   Let s be the *seed* RF line. The aim is to calculate Δa_i and Δl_i such that the duple $(a_i + \Delta a_i, l_i + \Delta l_i)$ gives the axial and lateral displacements at the sample i. The regularized cost function becomes [35]:

$$\begin{aligned} &C_s(\Delta a_1, ..., \Delta a_m, \Delta l_1, ..., \Delta l_m) = \\ &= \textstyle\sum_m^{i=1}\{[I_1(i,s) - I_2(i + a_i + \Delta a_i, s + l_i + \Delta l_i)]^2 + \\ &+\alpha\left(a_i + \Delta a_i - a_{i-1} - \Delta a_{i-1}\right)^2 + \beta_a\left(l_i + \Delta l_i - l_{i-1} - \Delta l_{i-1}\right)^2\} \end{aligned} \tag{2.4}$$

   ,where α and β_a are regularization terms which ensure continuity in displacements with respect to the top: α for axial and β_a for lateral.

2. Propagate the solution of the *seed* RF line from column to column to the left

and right of the frame, using the displacement of the previous RF line as an initial estimate. The regularized cost function for the j^{th} RF line becomes [35]:

$$\begin{aligned} &C_j(\Delta a_1, ..., \Delta a_m, \Delta l_1, ..., \Delta l_m) = \\ &= \textstyle\sum_m^{i=1} \{[I_1(i,j) - I_2(i + a_i + \Delta a_i, j + l_i + \Delta l_i)]^2 + \\ &+\alpha \left(a_i + \Delta a_i - a_{i-1} - \Delta a_{i-1}\right)^2 + \beta_a \left(l_i + \Delta l_i - l_{i-1} - \Delta l_{i-1}\right)^2 + \\ &+\beta_l^{'} \left(l_i + \Delta l_i - l_{i,j-1}\right)^2\} \end{aligned} \tag{2.5}$$

,where $l_{i,j-1}$ is the lateral displacement of the previous RF line. α, β_a and $\beta_l^{'}$ are regularization terms which ensure continuity in displacements with respect to the top (axial α), and the top and left/right (lateral β_a and $\beta_l^{'}$).

The presence of decorrelation affects the displacement estimation algorithm in two ways. Choosing the *seed* RF line in a decorrelated region will result in a poor displacement estimate for that line, as well as allow incorrect estimates to propagate laterally though the AM part of the method. The choice of a robust *seed* RF line does not guarantee proper estimates for the entire frame. If the AM displacement propagation encounters a wide region of poorly correlated RF data, it is unlikey the estimates will mentain correct values as the region is traversed, potentially corrupting even the estimates in the highly correlated region beyond. Methods are needed both for robust *seed* line selection and also for displacement propagation.

2.3 Methods

We are porposing a set of methods to address the presence of signal decorrelation. The first subsection 2.3.1 presents two tools which will constrict the choice of *seed* line in an area unaffected by decorrelation to insure a robust starting point for the displacement estimation algortihm. The next subsection 2.3.2 introduces quality metrics to be used in displacement propagation, while subsection 2.3.3 makes the case for dividing the image frames in multiple sub-images, each with their own *seed* line, to allow parallelization and speed up of the overall run time without sacrificing accuracy.

2.3.1 Seed RF-line selection

The following methods address the selection of a robust *seed* RF line, unaffected by signal decorrelation.

- *Displacement Slope*

  In a continuous piece of tissue, the axial displacement profile resulting from a stress field induced by applied compression has a monotonous ramp [59]. A pair of decorrelated RF signals could affect the DP displacement estimation algorithm. Instead of a globally optimal solution, the estimate could exhibit

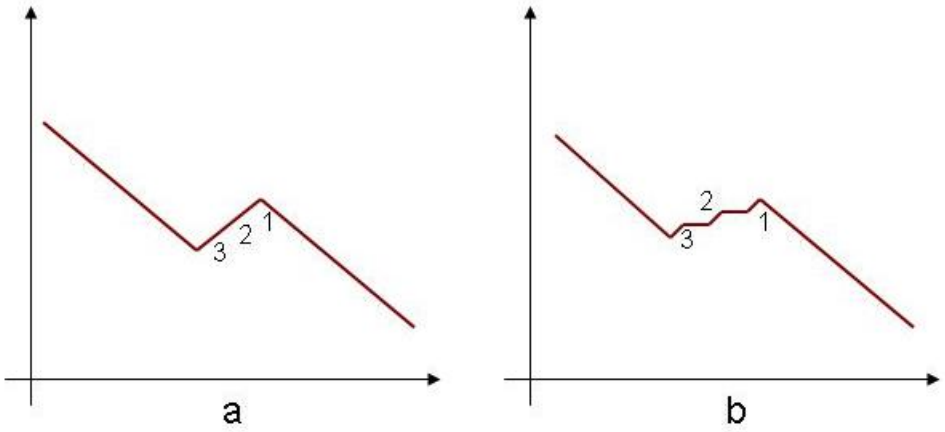

Figure 2.2: *Displacement slope*. The 3 (three) positions where the change in slope is exhibited could be consecutive (a) or not (b)

regions of locally optimal solutions. We hypothesized that for small deformations, these locally optimal solutions would correspond to perturbations in the monotonously decreasing slope of their displacement profile, which in turn would result in *artifacts* in the final strain image (Fig. 2.1). A change in the slope along the displacement profile for at least ϵ consecutive data points indicates a region of poorly correlated data. In our phantom study, we found that a value of $\epsilon = 3$ was sufficient to detect artifact-inducing regions of signal decorrelation, as explained in 2.4. Note that the three data points don't need to be consecutive, as long as the ramp stays flat or continues to change direction (Figure 2.2 a, b).

- *Displacement Stability*

  In the DP algorithm [34], w is a smoothness regularization parameter (2.3); it

prevents regions with high local decorrelation from introducing errors in displacement estimation, but if chosen too large would result in oversmoothing. We hypothesized highly correlated pairs of RF lines would give consistent displacement estimation results regardless of the chosen value for w. Regions of poorly correlated RF data would give different displacement estimation results, given different values of w (in a chosen range). We thus compute the metric I for *instability* as:

I = the percentage of data points along an RF line, which exhibit a discrepancy in the displacement estimate of at least δ units (pixels).

A high value of I suggests a poorly correlated RF signal pair. In our phantom study, we found that a value of $\delta = 3$ was sufficient for the detection of signal decorrelation, as explained in 2.4.

2.3.2 Robust, High-Quality Displacement Propagation

At the end of the displacement estimation process on the j^{th} pair of RF lines, $A_i = a_i + \Delta a_i, L_i = l_i + \Delta l_i$ are the axial and lateral displacements at each sample i (eq.

2.5). Using the estimated displacement values, and the raw RF signals pre- and post-compression, we can calculate how well the estimates fit the data. A high-quality estimate would exhibit a high degree of correlation between the RF signals. We chose the magnitude of the normalized cross-correlation as an indicator for the degree of matching between the pre- and post-compression data. For the j^{th} pair of RF lines, we computed:

$$C(I_1(j), I_2(j)) = \left| \frac{\sum_m^{i=1}(I_1(i,j)-\bar{I_1})(I_2(i+A_i,j+L_i)-\bar{I_2})}{\sqrt{\sum_m^{i=1}(I_1(i,j)-\bar{I_1})^2 \sum_m^{i=1}(I_2(i+A_i,j+L_i)-\bar{I_2})^2}} \right| \tag{2.6}$$

where $\bar{I_1}$ and $\bar{I_2}$ are the means of RF values along the j^{th} line.

$C(I_1(j), I_2(j))$ is a good indicator of the quality of the DP + AM displacement estimate for line j. As the array of A_is and L_is become the initial guesses for propagating forward to line $(j+1)^{th}$ (eq. 2.5), we can assess if the displacement propagation should continue or not. A poor initial guess would result in a potentially corrupted forward estimation. Even starting with a high-quality estimate could result in a corrupt forward estimation if the adjacent RF line pair $((j+1))$ exhibits a region of poorly correlated data. We can compute the same correlation metric (eq. 2.6) using the estimated displacements for line j with the raw RF data for line $j+1$:

$$C_{fwd}(I_1(j+1), I_2(j+1)) = \left| \frac{\sum_m^{i=1}(I_1(i,j+1)-\bar{I_1})(I_2(i+A_i,(j+1)+L_i)-\bar{I_2})}{\sqrt{\sum_m^{i=1}(I_1(i,j+1)-\bar{I_1})^2 \sum_m^{i=1}(I_2(i+A_i,(j+1)+L_i)-\bar{I_2})^2}} \right| \tag{2.7}$$

where A_i and L_i are the displacements for RF line j, and $\bar{I}_1$ and $\bar{I}_2$ are the means of RF values along the $(j+1)^{th}$ line.

As discussed in section 2.1, tracking algorithms which use the quality of data as an indicator of signal decorrelation, fail to produce displacements estimates in the presence of high noise or signal decorrelation [33]. As suggested by [33], a quality metric enforcing continuity of displacement estimates would be desirable, to avoid differentiation across displacement discontinuities which can generate artifacts. To ensure a continuity of high quality, highly correlated data, we compute the ratio ρ as follows:

$$\rho = \left| \frac{C_{fwd} - C}{C} \right| \tag{2.8}$$

2.3.3 Robust 2D Elastography Method with Multiple *Seed* Lines

Given two ultrasound RF frames I_1 and I_2 which exhibit areas of poor correlation, we are proposing a displacement estimation method which relies on the selection of a robust starting *seed* RF line, followed by displacement propagation guided by each adjacent line's underlying degree of similarity.

We consider the question of selecting a **single** starting location, or **multiple** *seed* lines. As displacement is tracked from column-to-column, the presence of a poorly correlated signal pair would stop the propagation, practically requiring the selection of a new *seed* RF line, on the other side of the troublesome area. To reduce the time of the displacement estimation over the entire image, one could divide the image into K sub-regions from the start, each requiring a robust *seed* RF line. The selection of multiple robust *seed* RF lines presents the advantage of initializing in multiple high correlation regions, incresing the chances for a more robust, artifact-free elastogram.

Let each sub-image I_k $(k = 1..K)$ contain m_k RF lines. We first select a *seed* line as follows (Figure 2.3):

1. Select $p = 5$ random potential candidates for the *seed* RF line pair.
2. Compute integer displacement estimation $p = 5$ times for each pair, using p random w values in a chosen range (see section 2.4.1).
3. Keep only the pairs which satisfy the monotonous displacement slope criteria for ALL values of w (2.3.1).
4. From the remaining pairs, the one with the lowest *instability* value I becomes the *seed* RF line (2.3.1).

After the selection of a robust *seed* RF line j, the estimated displacement values are

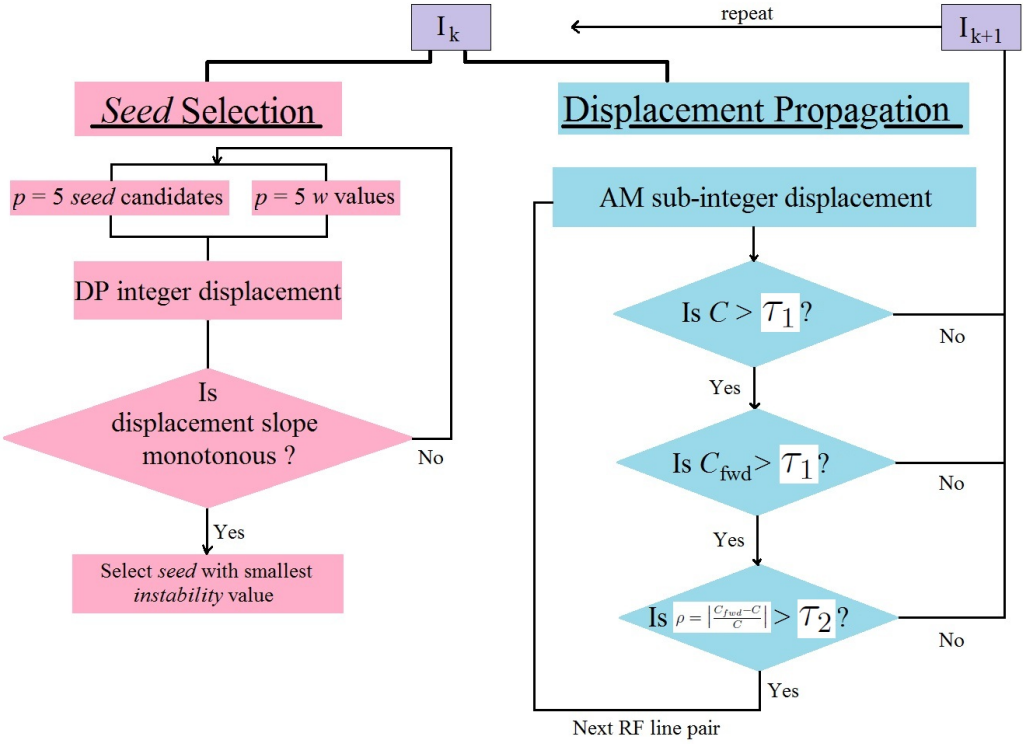

Figure 2.3: Algorithm flowchart. Left side represents the *seed* selection step, while right side presents the displacement propagation decisions. If the thresholds are not met, propagation stops and the remaining portion of the RF frame will be treated as a new sub-image I_{k+1}, where a new *seed* RF line will need to be selected.

propagated lateraly to the adjacent lines until all m_k lines are processed. For each adjacent line pair $j+1$, using as initial displacement estimate the values calculated for pair j, we calculate C, C_{fwd}, and $\rho = \left|\frac{C_{fwd}-C}{C}\right|$ as indicators of data quality (2.3.2). Two thresholds govern the following set of conditions which will guide the displacement propagation:

1. If the j^{th}'s displacement estimate is a good fit for line pair j, C should be bigger than τ_1.

2. If the j^{th}'s displacement estimate is a good initial guess for line pair $j+1$, C_{fwd} should be bigger than τ_1.

3. To ensure a continuity of high quality, highly correlated data, ρ should be smaller than τ_2.

We study the impact of w on the *instability* value I, as well as the choice of thresholds τ_1 and τ_2 in section 2.4.1. If all the conditions are met, the displacement for line $j+1$ will be estimated according to equation 2.5, and then the same set of conditions will be used to asses the quality of the next RF line pair $j+2$. If the thresholds are not met, propagation stops and the remaining portion of the RF frame will be treated as a new sub-image I_{k+1}, where a new *seed* RF line will need to be selected (Figure 2.3).

2.4 Results and Discussion

2.4.1 Displacement estimation in 2D phantom data

To study the choice of algorithm parameters and their impact, we palpated and scanned a CIRS (CIRS Inc. Norfolk, Virginia) breast elastography phantom model 059 (Figure 2.4). According to the manufacturer specifications, the phantom presented with a 10 mm diameter dense mass at least two times stiffer than the background, which had an elastic modulus of $20kPa \pm 5kPa$. The raw ultrasound data were obtained from ACUSON Antares (Siemens Medical Solutions USA, Malvern, PA, USA), while the tissue was palpated freehand using an ultrasound transducer (VF13-5SP) at a center frequency of 7.27 MHz. The Axius Direct Ultrasound Research Interface was used to enable RF acquisition at a sampling rate of 40MHz, with each frame comprising 508 lines of 1700 samples.

Two RF frames were selected which exhibited some unknown regions of poorly correlated RF data. In order to evaluate the magnitude of the problem, we first set out to evaluate the percentage of decorrelated RF line pairs. Integer displacements were estimated for each RF line pair using DP (equation 2.3). Every line pair was treated as a *seed* and thus processed individually, using no prior information for an initial guess. Visualizing the individual axial displacements as a unified map makes it easy

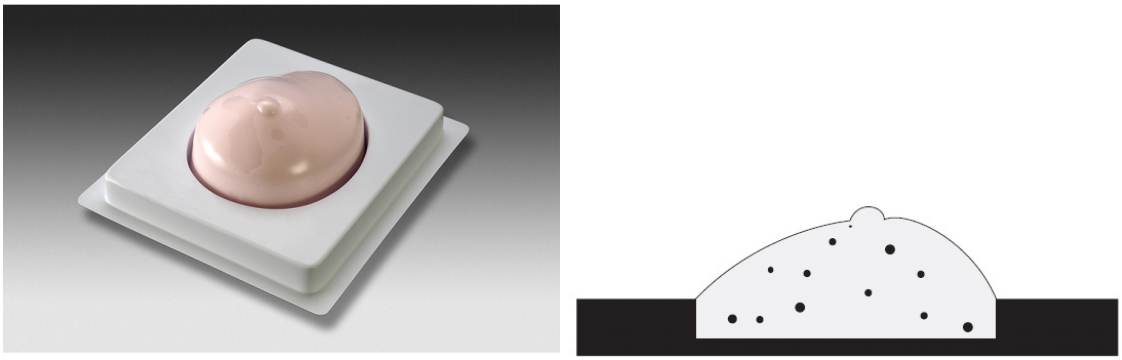

(a) (b)

Figure 2.4: CIRS breast phantom 059. The elasticity of each dense mass is at least two times greater than the elasticity of the background, which has an elastic modulus of 20kPa ± 5 kPa. They range in size between 3 and 10 mm (b)

to observe potential discontinuities and poorly correlated areas (Figure 2.5).

Further more, the choice of w value affects the final strain image (Figure 2.6). In the DP displacement computation, w is a smoothness regularization parameter (equation 2.3) intended to prevent poorly correlated regions from introducing errors in displacement estimation. 5346 strain images were obtained with the 2D AM method using each RF line as a *seed*, each for eleven values for w between 0.10 and 0.60 (Table 2.1). Knowing the shape and size of the expected lesion, we visually inspected each resulting elastogram for the presence of artifacts. Some lines produced very faint, very small artifacts on the order of a couple of pixels which were not propagated to the adjacent lines; if these artifacts were not easily identifiable at first inspection, the corresponding line was categorized as *indeterminate* (Table 2.1).

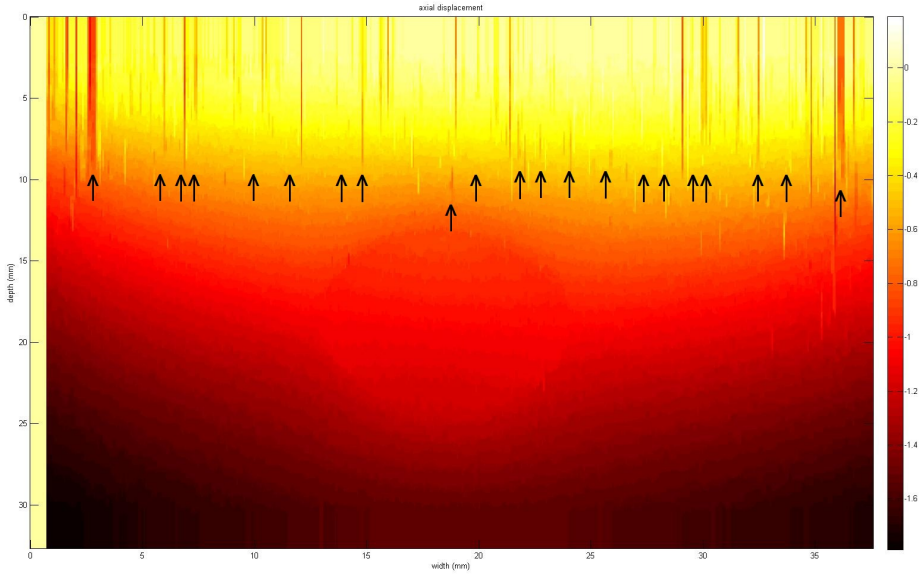

Figure 2.5: Breast phantom data. Integer displacement estimation using dynamic programming method. Note: RF lines pairs #13 - 498 are each used as *seed*. Many areas prone to produce artifacts are relatively easy to identify (arrows).

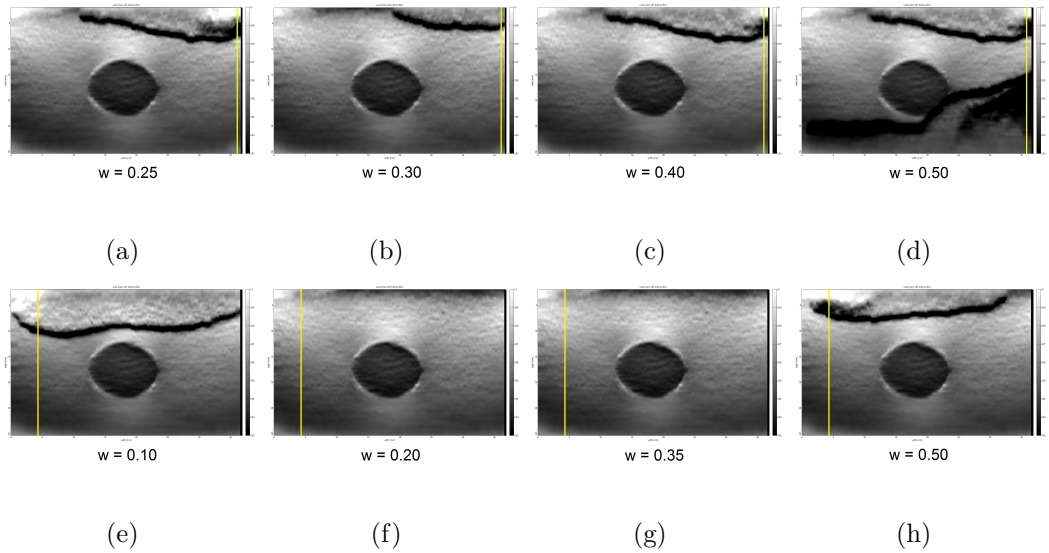

Figure 2.6: Examples of artifacts in strain images for various values of w. First row represents strain images originating from *seed* RF line #487, second row from *seed* RF line #55. *Seed* line is emphasized in color yellow.

Table 2.1: Percentage distribution for *seed* RF lines, given multiple values for w (smoothness regularization parameter)

	w										
Lines (%)	0.10	0.15	0.20	0.25	0.30	0.35	0.40	0.45	0.50	0.55	0.60
W/o artifacts	44.2	57.8	61.3	68.1	65.0	61.7	53.3	53.1	43.4	32.1	24.3
W/ artifacts	55.8	42.2	33.6	30.0	30.5	32.0	41.8	46.9	56.6	67.9	75.8
Indeterminate	-	-	5.1	1.9	4.5	5.3	4.9	-	-	-	-

For the breast phantom data, we focused our remaining analysis on values of w in the 0.20 - 0.35 range, where over 60% of lines produced no strain artifacts (Table 2.1). For this w range, **113 (23.25 %)** lines produced artifacts for all four values of w (0.2, 0.25, 0.3, 0.35), **263 (54.12%)** lines never produced artifacts and **110 (22.63%)** lines oscillated in their behavoir.

The monotonous displacement slope criterium (2.3.1) was very effective as an initial test for filtering out most of the poorly correlated line pairs. As a filter by itself, it had a **74.18%** sensivity and **77.78%** specificity.

The *instablity* metric I (2.3.1) clearly differentiated between high quality data and regions of signal decorrelation (Figure 2.7). Our algorithm uses this metric to select from the *seed* candidates the line pair with the lowest I value. Our study indicates one could also constrain I to be within a user-selected threshold of high instability; boxplot in figure 2.7 suggests a possible value could be chosen in the 3-5% range.

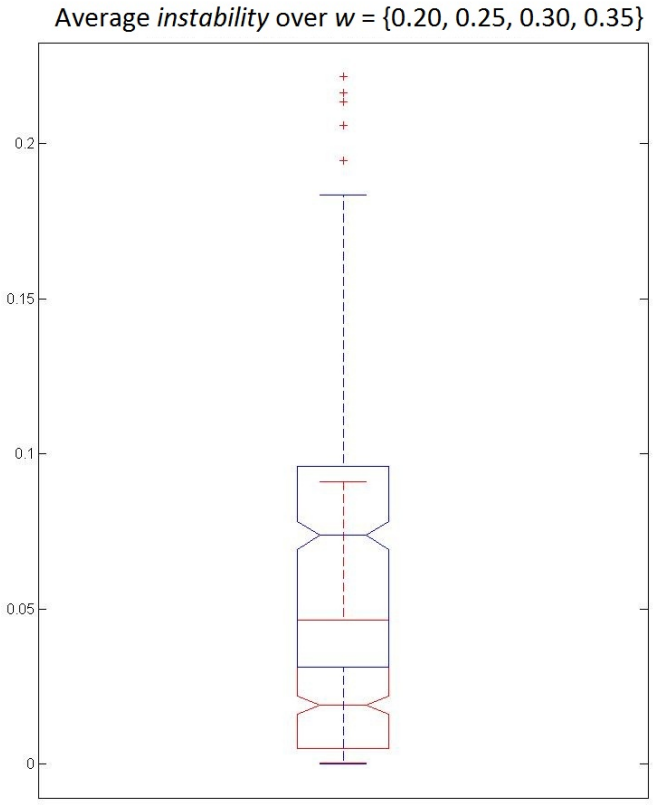

Figure 2.7: Box and wiskers plot: *Instability* metric I (averaged over w = 0.2, 0.25, 0.3, 0.35). Values corresponding to the artifact producing lines are shown in blue while the robust lines are shown in red.

Using the phantom data, we evaluated the magnitude of the normalized cross-correlation $C(I_1(j), I_2(j))$ (equation 2.6) as an indicator of the degree of matching between the pre- and post-compression data. The spread and distribution of $C(I_1(j), I_2(j))$ with respect to w is presented in Figure 2.8. Once again, w values in the 0.20 - 0.35 range resulted in a clear differentiation of robust vs. artifact producing lines. The results in Figure 2.8 determined our choice of values for the two thresholds used in the correlation-guided displacement propagation: we reject all lines with C or C_{fwd}

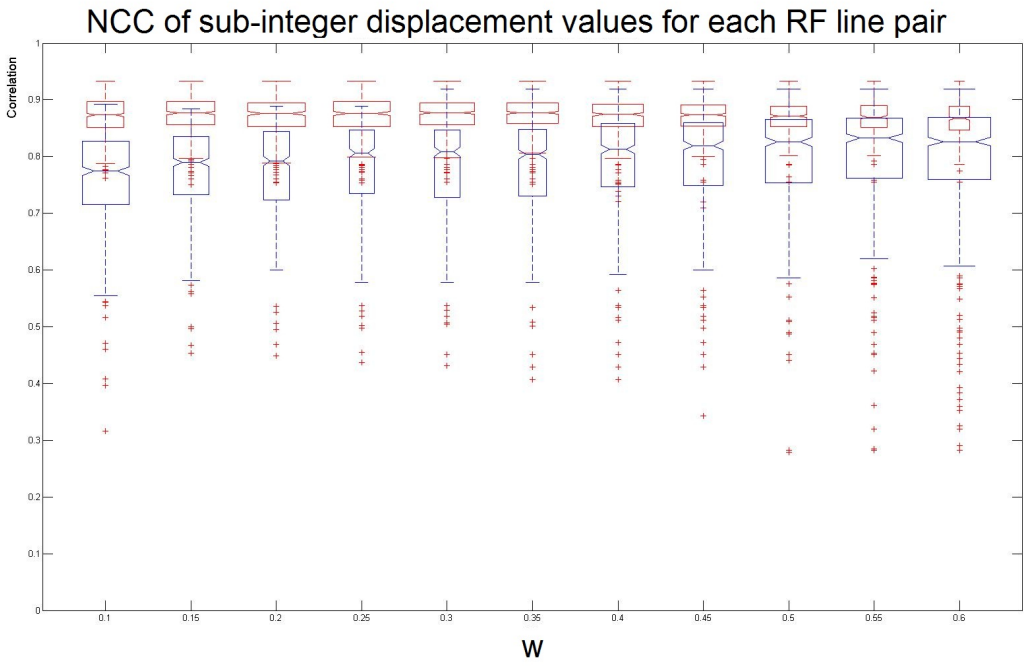

less than $\tau_1 = 75\%$ or lines for which the ratio $\rho = \left|\frac{C_{fwd}-C}{C}\right|$ is higher than $\tau_2 = 10\%$.

Figure 2.8: Box and wiskers plot: magnitude of normalized cross-correlation C. Values corresponding to the artifact producing lines are shown in blue while the robust lines are shown in red.

2.4.2 Displacement Estimation in 2D human prostate *ex vivo* data

Ex vivo ultrasound data was collected from resected human prostates, following prostatectomy. In accordance with the Institutional Review Board approval, each prostate specimen also underwent a post-operative ultra high-resolution MRI at 9.4

Tesla. The RF ultrasound data were obtained from ACUSON Antares (Siemens Medical Solutions USA, Malvern, PA, USA), while the specimen was palpated free-hand using an ultrasound transducer (VF10-5) at a center frequency of 6.67 MHz. The Axius Direct Ultrasound Research Interface was used to enable RF acquisition at a sampling rate of 30MHz, with each frame comprising 350 lines of 2236 samples. Post-operative MR scans were used for anatomical correlation with the strain images.

The full results of the study are presented in Appendix A. Here we will present data from one specimen, for experimental validation of our algorithm on *ex vivo* data.

The robust multi-*seed* algorithm was used for displacement estimation. w ranged from 0.20 to 0.35 for the *seed* selection step, and $\tau_1 = 75\%$ and $\tau_2 = 10\%$ for the displacement propagation step. We discuss in details below how we dealt with two challenging situations.

Given sub-image I_k, one or more RF line pairs could be highly decorrelated, preventing displacement propagation and effectively stopping the progression of the algorithm. In this prostate data example, we considered the initial sub-image as the entire frame. RF line pair #146 was selected as *seed* (Figure 2.9 a, dotted line). During displacement propagation, the algorithm encountered two decorrelated regions indicated by values for C under the threshold τ_1 (see circled areas in Figure 2.9 a). The values for C_{fwd} closely follwed C and also fell under the threshold (Figure 2.9 b,

c). Two new sub-images were defined (I_1 to the left and I_2 to the right) for which the algorithm started anew with the selection of a robust *seed* line.

The second situation arises when in a remaining (small) sub-image, the RF data could exhibit such poor correlation that no line would fit the criteria for a robust *seed* selection. In our implementation, we maintain an array of size n containing the values of C for each RF line pair. They are initialized to 0 (zero) and, as each sub-image I_k is being processed, we update the values of C for each RF line pair. When a *seed* selection is not possible, some lines remain unprocessed. After all sub-images finish propagation, a linear search is used for the detection of unprocessed lines. For each such line, C_{fwd} and $\rho = \left|\frac{C_{fwd}-C}{C}\right|$ are calculated for both possible directions of propagation (from the adjacent left line or right line). The highest quality boundary determines which displacement values will be used as an initial guess. This insures possible small artifacts will be confined to small regions and will not impact the displacement estimate of other lines.

In our prostate data example, we needed to select a *seed* line in sub-image I_1 defined to the left of the frame, consisting of thirty-four RF line pairs. Only one line pair passed the displacement slope criterium. Continuing on, our threshold τ_1 of 75% was not met, so we were left with a sub-image with no suitable *seed* line. The lines in I_1 were processed at the end, using displacement values propagated from line #35 towards line #1, and the final strain image (incorporating the displacement values

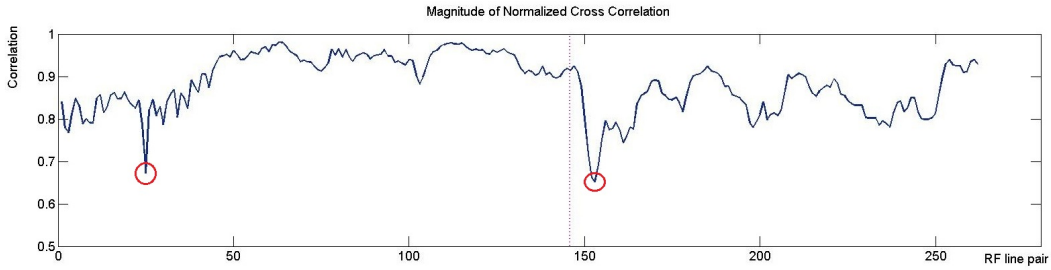

(a)

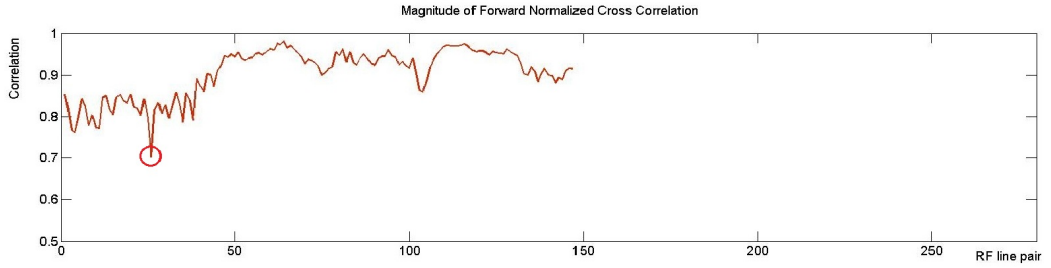

(b)

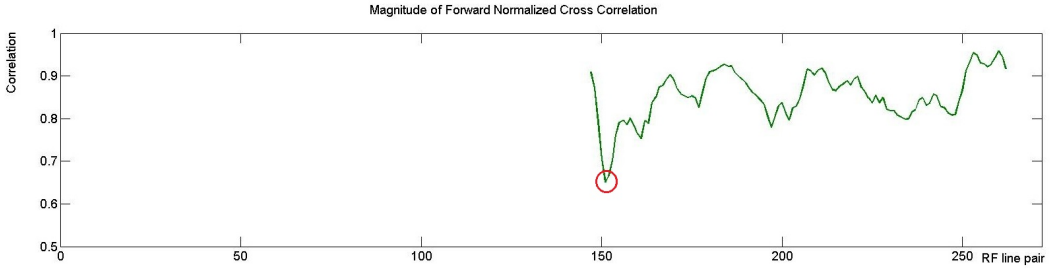

(c)

Figure 2.9: Prostate data set example: correlation values for each line pair (a), forward correlation for displacement propagation in I_1 (b), and I_2 (c). *Seed* line is shown by dotted line in (a). Also shown are breaking points due to low correlation values (circles)

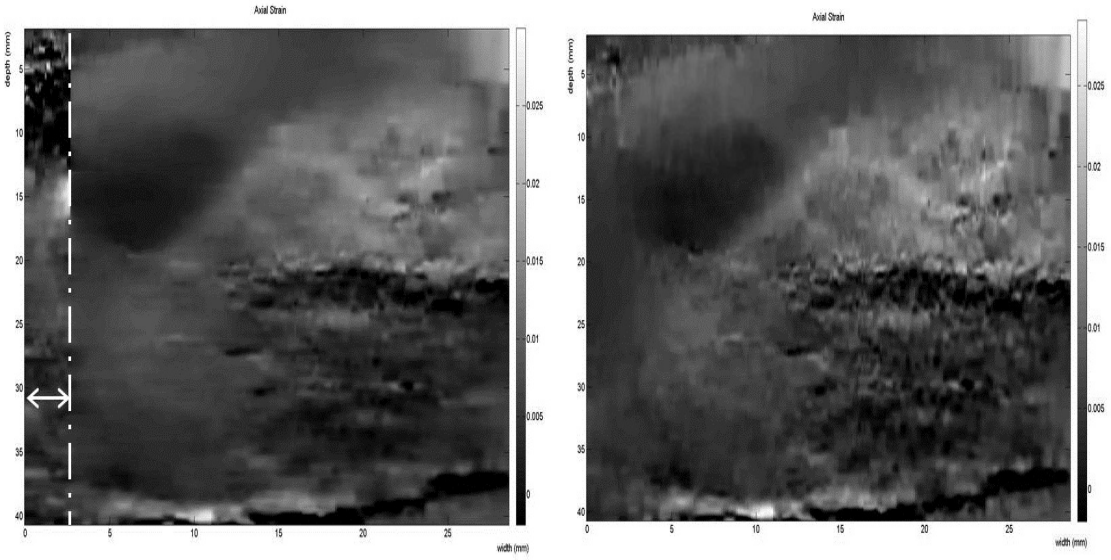

(a) (b)

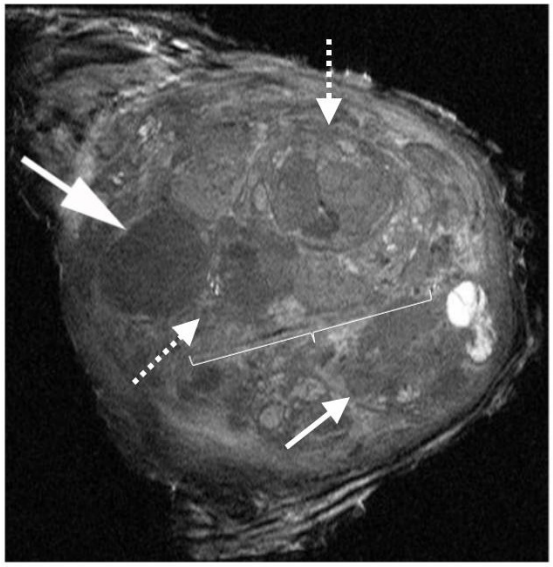

(c)

Figure 2.10: Prostate data set example: (a) an unsuitable *seed* line is selected for sub-image I_1, (b) no suitable *seed* line is found in sub-image I_1, which forces the algorithm to propagate displacement from line #35, and (c) 9.4 Tesla MRI corronal scan of the prostate specimen showing hard lesions (arrows), soft lesions (dashed arrows) and urethra (bracket).

from sub-image I_2) is presented in Figure 2.10 b).

If τ_1 is set at a lower value (for example 70% instead of 75%), one *seed* line will be accepted and displacement estimates will be propagated throughout sub-image I_1. The resulting elastogram in Figure 2.10 a) looks very different from the one in b), clearly illustrating the importance of sellecting a high value for threshold τ_1. Figure 2.10 c) shows a 9.4 Tesla MRI corronal scan. The pathological examination showed the lesions pointed by full arrows to be hard, while the ones pointed by dashed arrows were soft. All the lesions were uncovered in a very convincing manner by the elastography algorithm. Also visible in the MRI scan is the urethra, whose rigid walls make it appear hard in the strain image.

2.4.3 Algorithmic Complexity

Making use of multi-threaded parallel processing greatly reduces the computational time for the entire displacement estimation. The number of sub-images K dictates, in part, the total time. For each sub-image $k = 1..K$, the computational time is divided between the DP displacement estimation for the *seed* line selection and the subsequent propagation to the remaining $m_k - 1$ lines in the region. Choosing a large K divides the image in many small strips, reducing the value of m_k. From a run-time point of view, this does not have a great reducing effect, as the AM part of the algorithm

which is used for displacement propagation is an order of magnitude faster than the intial DP estimation for the *seed* line. A value of K too large increases the chance of encountering a sub-image where no suitable *seed* line, thus extending the overall run-time. Choosing a small K would increase the chances of encountering a poor quality data region, thus forcing a new DP estimation for *seed* selection and affecting again the total run-time. In our experience, initial sub-images of approximately 10% of the total number of lines produced the best results.

2.5 Conclusion and future work

We have proposed a robust method for displacement estimation in ultrasonic strain imaging. This method enhances the dynamic programming approach to displacement estimation, improving its ability to overcome displacement discontinuities and regions of poorly correlated RF data. The innovative methods proposed for *seed* line selection focus on robustness as well as stability over varying algorithm parameters. The method also addresses the robustness of displacementt propagation using analytic minimization. Enforcing robustness and stability does not add a significant overhead to the total run-time of the displacement algorithm. The method is highly parallelizable at every step, from the *seed* selection tools to the displacement propagation. The new algorithm is one step closer towards achieving repeatable, user-independent

elastograms.

Chapter 3

3D Displacement Estimation for Ultrasound Elastography

3.1 Introduction

The introduction of ultrasound elasticity by Ophir in 1991 was soon followed by three dimensional attempts. Early work relied on multiple frames being acquired using a conventional 2D ultrasound transducer [60, 39], while more recently 3D ultrasound transducers were employed [43, 32]. Similar to 2D elastography, signal decorrelation is the main factor affecting the quality of 3D strain images. Additionally, the speed

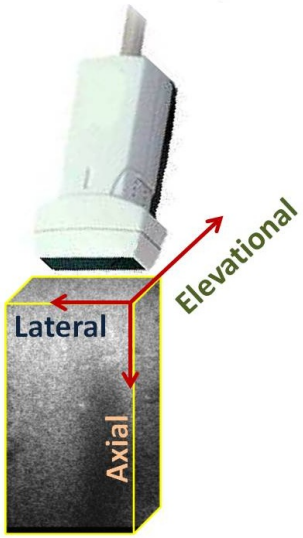

Figure 3.1: Conventional perpendicular motion directions in ultrasound data

of displacement estimation becomes even more important for clinically significant, *in vivo* applications of three-dimensional elasticity imaging .

Two techniques have emerged for acquiring the raw signals used for 3D displacement estimation. In the first case, a 2D transducer is slowly moved deliberatly in the elevational direction (Figure 3.1), while continuously acquiring data [37, 38]. This acquisition mode results in small variations in the applied compression between adjacent probe locations. This approach requires a slow enough transducer movement to keep consecutive scans not too far apart in the elevational direction, making the method prone to decorrelation due to out-of-plane motion. Lindop et al [28] later improved the quality of strain volumes by applying a 3D filter to deal with this issue, but the data acquisition step remained slow.

In the second technique two volumes, pre- and post-compression, are acquired sequentially, and a small pressure is applied to the tissue between volume acquisitions using a mechanical or simulated fixture [39,40,41,42,43,44], or freehand [32]. This approach requires great care in applying even axial compression over the entire tissue imaged to avoid signal decorrelation. Further more, the operator has to hold the probe very still during the lenghty acquisition of the pre- and post-compression volumes, which is very difficult in practice without the use of steady mechanical/robotic arms or stages.

Two hybrid acquisition techniques stand out recently. Houdsen et al. [45] used a mechanically-swept (wobbler) 3D probe (Figure 3.2) to control the elevational motion. While the probe gradually sweeps out a volume, it pauses at each motor step and collects several RF frames, as the operator performs the tissue deformation continuously, by up and down hand movement in the axial direction. This method has ease of acquisition as it bypasses the practical difficulty of performing careful and optimal compression between pre- and post-compression frames. It still suffers however from the speed of acquisition, which can take an extended time for large volumes.

Foroughi et al. used a tracked 3D wobbler transducer with an attached position sensor [57]. RF data is continuously collected as the transducer sweeps the volume, while the operator performs continuous freehand compression. Data is acquired without pause and the tracking information is exploited to select suitable RF frame pairs with minimal out-of-plane motion. The acquisition of several volumes is fast and

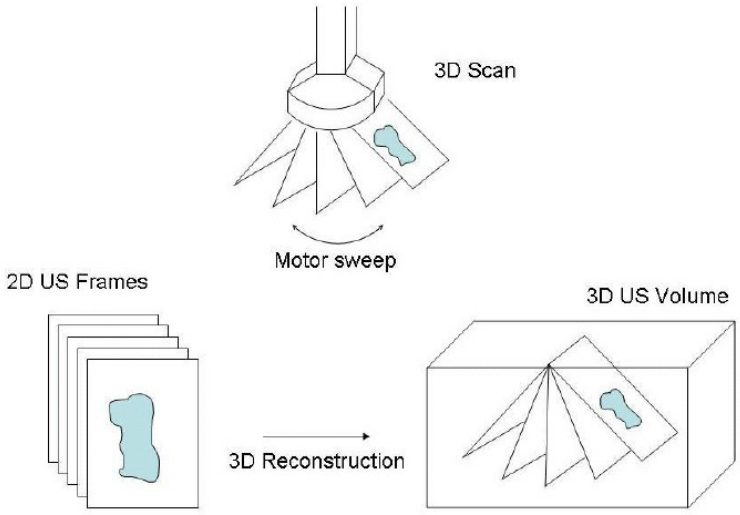

Figure 3.2: 3D wobbler transducer principles: data acquisition and 3D volume reconstruction.

no operator training is required as the frame selection technique minimizes signal decorrelation due to hand motion.

In this chapter we extend the robust displacement estimation to three dimenssions. The 3D data sets were collected using the Foroughi system [57]. Next we summarize the Foroughi tracked ultrasound elastography (TrUE) techinque [57], followed by a description of the three dimensional robust estimation methodology. The chapter continues with a section on 3D validation experiments using tissue mimicking phantoms and *in vivo* intra-operative porcine liver data and concludes with a discussion on future research directions.

3.2 Tracked Ultrasound Elastography (TrUE)

For freehand 3D data collection, the quality of strain images becomes extremely sensitive to the user's level of expertise. Precise axial deformation is needed to avoid out-of-plane motion which results in signal decorrelation. Here we give an overview of the Foroughi system which makes use of position information to select pairs of RF frames which have a higher probability of generating high quality strain [57]. A few recent ultrasond systems have already incorporated tracking devices to exploit position information (The LOGIQ E9 (GE, Schenectady, New York) and the SonixGPS (Ultrasonix Medical Corp., Richmond, BC, Canada) are two examples of such systems).

As data is acquired while the 2D element array sweeps the volume, synchronized position information is recorded simultaneously. A transformation matrix is computed which determines the position and orientation of every slice. The geometry of the probe and the acquisition angle of the slice determine each transformation matrix. In the case of our transducer, a volume is constructed by sliding a linear array over the sector of a circle with radius r as shown in Figure 5.1. θ is the angle of the slice at each step of the wobbler motor. r and θ are known from the probe manufacturer specifications.

The position information helps select pairs of RF frames which have a high probability

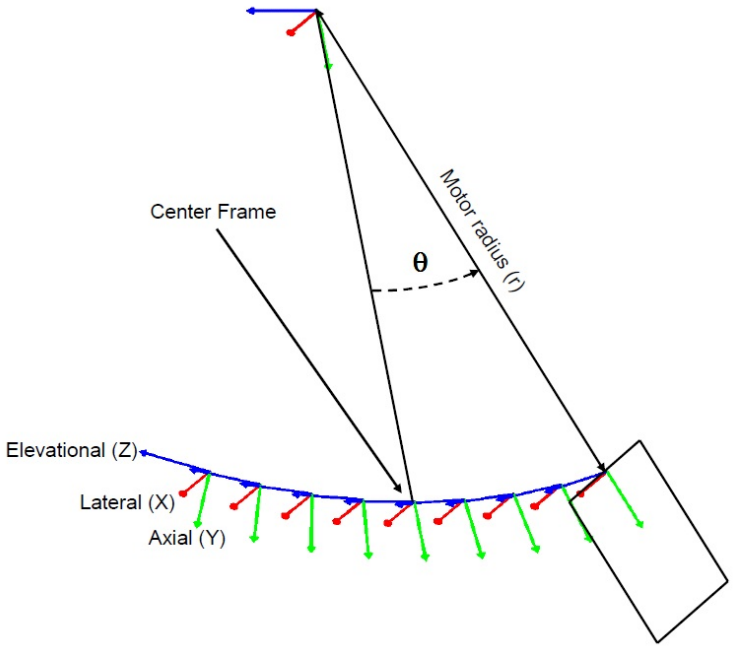

Figure 3.3: Overview of the TrUE approach. Given r and θ, each RF slice within a volume is localized. Courtesy of Foroughi et al [57].

of producing good-quality strain images. The goal is to find frame pairs for which the motion is mainly in axial direction, with minimal lateral and elevational motion (Figure 3.1). Foroughi's solution is found by maximizing the following cost function [57]:

$$Crr(D) = exp(-K_x D_x^2 - K_y \frac{|D_y - topt|^3}{D_y + c} - K_z D_z^2) \tag{3.1}$$

where K_x, K_y, and K_z determine the sensitivity to motion in lateral, axial, and elevational directions respectively, and $D = [D_x D_y D_z]$ is the sample-wise root mean square of the displacement. t_{opt} represents the desired compression, and c is a small

number that limits the cost of zero compression.

Due to the continuous freehand deformation, the axial direction for each acquired frame varies depending on the acquisition angle θ (Figure 5.1). Imperfect hand motion is generally an obstacle for elasticity algorithms. Foroughi et al [57] consider it however beneficial for their algorithm. As they attempt to maximize the cost function for optimal compression in a given axial direction, they evaluate every frame at the respective motor step location, but also the ones at one preceding and one succeeding location. The result is an improved strain quality at the center slice, and also at the adjacent slices [57].

3.3 Methods

3.3.1 Robust 3D Elastography with Multiple *Seed* Lines

For 3D displacement estimation we combine the frame selection algorithm of Foroughi et al [57] with the robust methods presented in Chapter (2). During freehand palpation using a tracked ultrasound transducer, the Foroughi method automatically selects pairs of RF frames with minimal lateral and out-of-plane motions, and also

has the possibility to select frames with a predefined compression range with respect to one another [57]. While the frame selection technique resolves signal decorrelation due to out-of-plane motion, the robust 2D displacement estimation addresses small local decorrelations, which can be present only in a small number of frames in a swept volume. One example is the presence of fluid (blood or lymphmatic vessels, billiary ducts) which can affect the entire 3D displacement estimation.

The robust 2D displacement estimation is performed after the frame pair selection. The position of each frame is available to us from the tracking information, so we can use it to automatically adjust the search range for the DP part of the algorithm (chapter 2.2.2). This results in a faster integer displacement estimation for the selection of *seed* lines. A strain image is computed for each frame pair, then all frames are combined in one 3D strain volume by applying a scaling factor represented by a 3D smoothing kernel, weighted by the mean strain of each pair. To display the results, strain images are stacked and scan-conversion is applied to the resulting volume.

3.4 Experimental Results

3.4.1 3D Ex-vivo Displacement Estimation

For 3D evaluation we palpated and scanned a CIRS (CIRS Inc. Norfolk, Virginia) phantom, model 049A (Figure 3.4). The ultrasound data were obtained from Sonix-CEP ultrasound system (Ultrasonix Medical Corp., Richmond, BC, Canada). The phantom was palpated freehand using the $4DL14-5/38$ transducer at a center frequency of 6.7 MHz. A passive marker was attached to the transducer and was tracked using the Polaris optical tracker (Northern Digital Inc., Waterloo, Ontario, Canada). Customized in-house software was used to enable continous acquisition of RF data and synchronized tracker readings through the Ultrasonix Research Interface. The volumes consisted of 120 slices. About 15 forward sweep scans were collected for each series of volumes.

Phantom model 49a includes four types of cylinders with varying diameters, from 1.58 to 6.49 mm (Figure 3.4). Our scan captured three of these cylinders with elasticities of 80 kPa, 45 kPa and 14 kPa, vs. 25 kPa for the background. The elastograms obtained using our algorithm captured both the harder and the softer cylinders (Figure 3.5). The harder cylinders apear darker and the softer one apears brighter than the background. One of the hard cylinders is almost two times harder than the other;

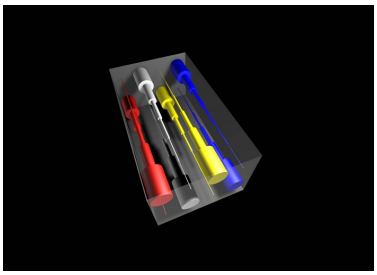

(a)

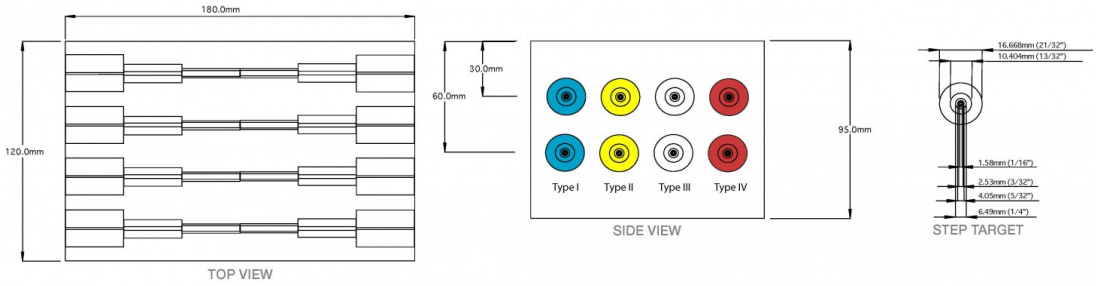

(b)

Figure 3.4: CIRS phantom model 49a. The elasticity of the cylinders is 80 kPa, 45 kPa, 14 kPa and 8kPa, vs. 25 kPa for the background. The cylinders range in diameter from 1.58 to 6.49 mm (b).

on the elastogram the left cylinder appears darker than the middle one (Figure 3.5 a, e). This is important as it underscores the algorithm's ability to differentiate among lesions with different elasticity values within one large volume, using the maximum range of the wobbler probe. In the area scanned, the diameters of the cylinders were 2.53, 4.05 and 6.49 mm, which agrees with the dimensions on the elastograms.

3.4.2 3D *In vivo* Displacement Estimation

In the *in vivo* experiment, a pig was prepared to undergo liver ablation surgery. After gaining access to the liver, an ablation needle was placed in a thick portion of the liver under ultrasound guidance. The hepatic tissue was ablated using the RITA ablation device (RITA Medical Systems Inc, Mountain View, California). The resulting thermal lesions were 1 to 2 cm in diameter. The ablated zone was then scanned following the approved protocol during a breath-hold period which lasted less than 20 seconds (Figure 3.6(a)). The strain scans of the two thermal lesions apear in Figure 3.6 d-i, where the ablated regions are clearly visible. The first ablation appears to be smaller than the second one which was confirmed by the gross-pathology (Figure 3.6(b), 3.6(c)). The diameter of the first lesion is about 1.5 cm whereas the second lesion is closer to 2 cm. The surgical gauze placed underneath the liver has created some distortion in the deeper parts of the scans.

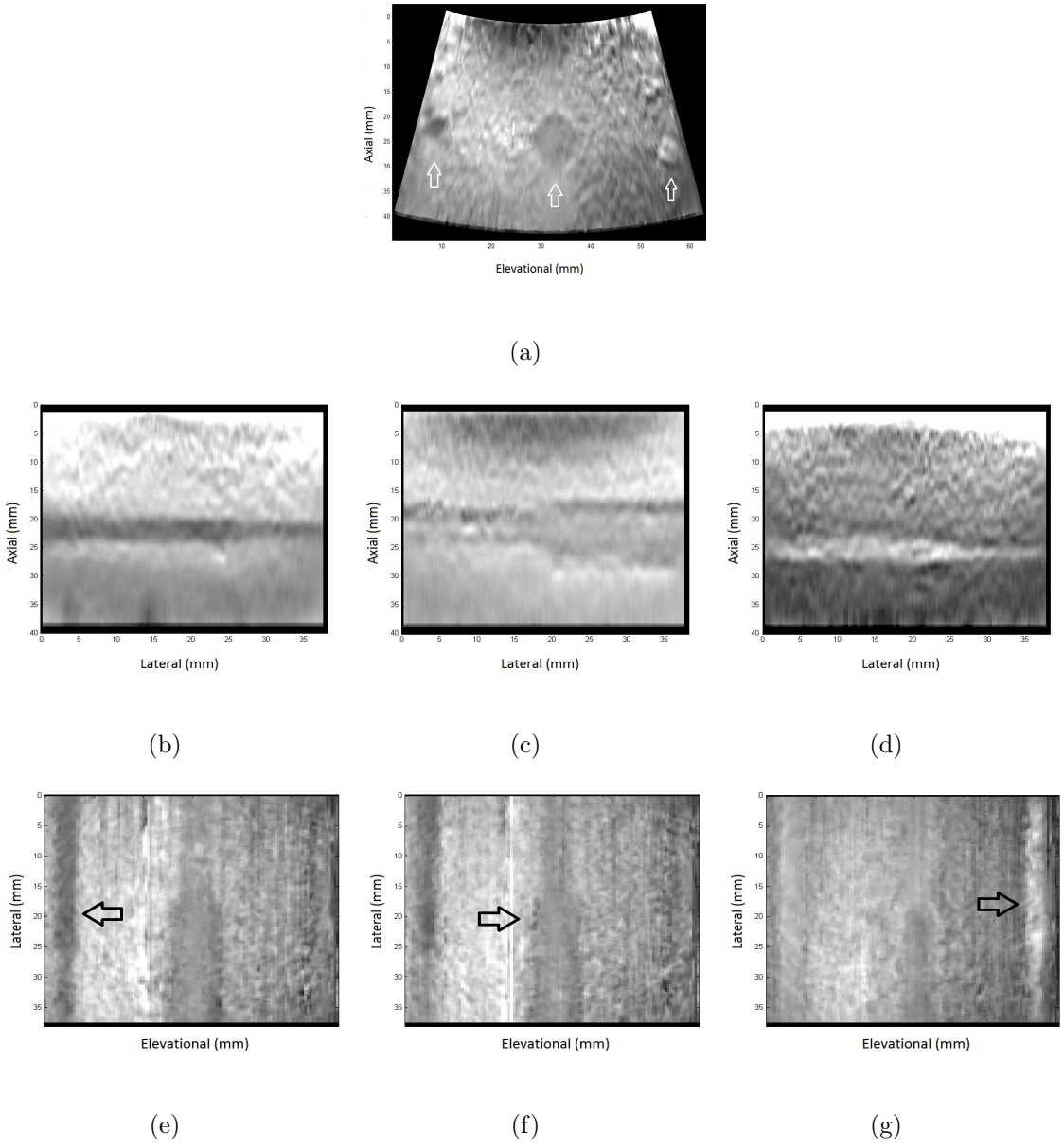

Figure 3.5: Elastograms of phantom model 49a: (a) cross-section of three cylinders with different elasticity values; (b-d) The axial-lateral elastograms of the three cylinders. (e-g) Lateral-elevational elastograms of the three cylinders. From left to right, the elasticity of the cylinders is 80 kPa, 45 kPa and 14 kPa, vs. 25 kPa for the background. The harder cylinders apear darker and the softer one apears brighter than the background.

3.5 Conclusion and future work

As we extended this method to 3D volumes of data, we considered a *multi-seed* approach where robust *seed* axial posts would be selected at random locations throughout the volume. In this case, displacement would propagate in a radial fashion, with the eight RF line pairs adjacent to the *seed* being evaluated first. We concluded that such an approach did not reduce the total run-time, nor did it appear to improve the overall displacement estimate. One of the constraints of this approach was the aspect of propagating the displacement in the elevational direction. As the estimation gets deeper, the distance between samples increases and continuity constraints can lead to the wrong local solution. As capabilities of the 3D wobbler transducers improve, we consider this area a worthy future direction.

Pairing the robust methods with the frame selection algorithm combines the strenghts of both techniques. Frame pairs with large out-of-plane motion are avoided, while small intra-frame decorrelations are addressed in a frame-by-frame fashion. In the future, we consider incorporating a full 3D displacement estimation technique to enforce smoothness constraints among the frame pairs. Another future direction is the addition of a real-time feedback during palpation and data collection, which would signal when enough suitable frame pairs have been collected.

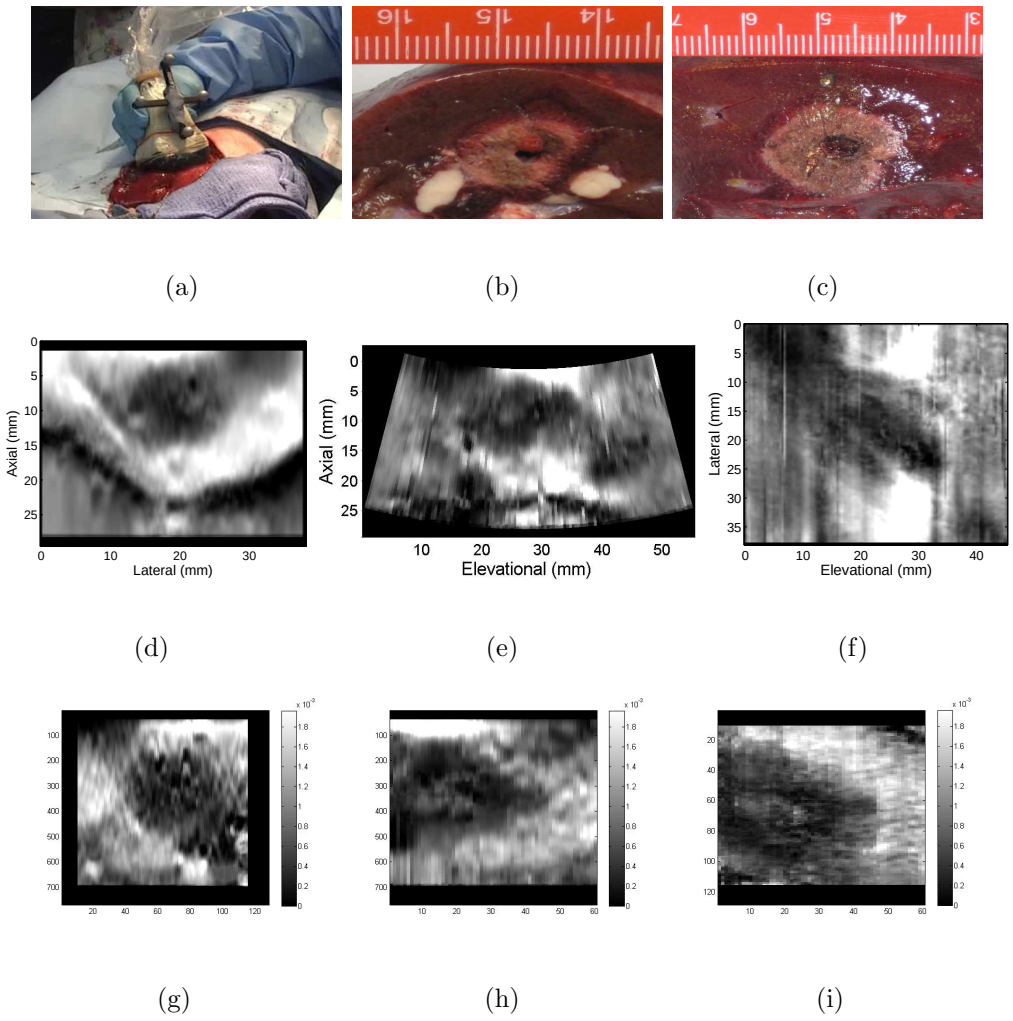

Figure 3.6: *Ex-vivo* hepatic ablation. (a) 3D transducer positioned on top of liver during elastography scan; (b) and (c) Cross-sections of the ablated regions with ruler visible; (d-f) Middle cross-sections of strain volume for ablated lesion #1 and (g-i) lesion #2.

Chapter 4

Ultrasound Elastography Mosaicing

4.1 Background

Compared to other imaging modalities like CT and MR, ultrasound suffers from a limited field of view. Monitoring a structure can be particularly challenging when it is too large to be visualized in a single image or 3D sweep. Size and distance measurements are unreliable in large organs. Panoramic imaging is emerging as a prevalent technique used in widening the field of view (FOV) of medical ultrasound

images. Also referred to as stitching or panorama, the ultrasound mosaic aims to achieve several clinical advantages which come along with extended FOV: 1) improving the understanding of spatial relationships among structures when the size of a single image/volume is not large enough to cover the entire area, 2) allowing for measurements of size and distance in large organs and lesions, 3) allowing multi-modal registration and fusion with pre-operative data for guidance in minimally-invasive interventions. Since ultrasound elastography was first proposed two decades ago for the clinical imaging of tissue stiffness, numerous clinical applications have been investigated, among them imaging cancerous tissue [11], ablation monitoring [58], and the detection and grading of deep vein thrombosis [61]. In this work we focus on extended FOV displacement estimation for quasi-static ultrasound elastography. The tissue is imaged while it is slowly deformed using an external mechanical force and the images are used for the estimation of tissue motion or displacement [11].

Elastography maps the mechanical properties of tissue which can add valuable features to the B-mode panorama. Many clinical applications deal with large cancerous lesions which expand beyond the span of one ultrasound image [15]. An ultrasound elastography mosaic can improve the understanding of the size of the lesion and its layout among surrounding structures. In the ablation of hepatic cancerous tissue, the size of the HIFU-induced ablative lesions often exceeds 4 cm in

diameter, which is the width of a typical ultrasound transducer. Thermal lesions are not visible in conventional B-mode ultrasound but a panoramic ultrasound elastogram can help visualize the entire extent of the ablation [58], monitoring and insuring all cancerous tissue is ablated. In the assessment of venous thrombi, a combination of ultrasound B-mode and Doppler imaging help detect the presence of the blood clot, but it is elastography which can provide its age and clinical grading [61]. An in-plane ultrasound elastography mosaic can provide mapping of the thrombi all along the femoral vein. It could take up to eight mosaiced volumes to depict an entire organ like the liver or kidney [62], but having the corresponding elastography mosaic would allow for registration with pre-operative imaging data (CT or MRI) which would help with intra-operative navigation. Although the basics of medical elastography have long been defined, new clinical applications are constantly emerging are we are seeing an increasing commercial and clinical interest.

Multiple approaches have been published in the literature on 2D and 3D wide FOV ultrasound mosaics [63, 62, 64, 65], but very little of it concerns registering the underlying strain field. As various sources of decorrelation are usually affecting the computation of strain images, this problem becomes even more important when attempting to generate a unified, wide displacement field. Further more, most elastography algorithms result in qualitative strain; 2 image pairs with even very slightly different degrees of compression will produce 2 strain images in which

different structures could be visible. Another problem rises in the ambiguity of the interpretation of strain images: low strain can be indicative of high stiffness but this interpretation may not be the right one if the stress field is not uniform throughout the tissue [11, 38]. To address these issues and to improve the quality of strain images, several metrics of stability, consistency/persistency and reliability have been developed [30, 28, 66]. In this paper we propose using similar techniques to select a stable pair of RF lines which will become the *seed* for generating a reliable, wide FOV displacement field. Displacement on the *seed* line is calculated using dynamic programming and later propagated in both lateral directions of the mosaic using an analytic minimization approach [35]. Each new image pair adds to the unified displacement field. Here we present tissue mimicking phantom data for 2D validation. Finally, the method is extended to 3D ultrasound elastography mosaicing using multiple 3D volume pairs.

4.2 Methods

Consider a sequence of radio frequency (RF) data (Im_{11}, Im_{12}) collected at position t_0, before and after the compression of tissue using a 2D ultrasound transducer (Fig. 4.2a). Each sequence is contains n RF-lines of length m. A second sequence (Im_{21}, Im_{22}) is collected (Fig. 4.2b) after the transducer has been moved in the lateral

direction of the probe to position t_1, with the help of a moving stage (Fig. 4.1). A vertical stage was used to achieve an almost identical compression rate between the two sequences. The translation between the 2 image sequences is:

$$T_{lines} = T_{mm} * n/w \tag{4.1}$$

where w is the width of the ultrasound transducer in millimeters (mm), n is the number of RF-lines, T_{mm} is the ground truth translation in mm as read on the stage and T_{lines} is the corresponding translation as number of RF-lines. The overlap area consists of (n - T_{lines}) RF-lines (Fig. 4.3).

4.2.1 2D Pair-wise Mosaicing

In Analytic Minimization (AM) elastography [35], 2D integer displacements are first obtained using dynamic programming (DP) on a single pair of RF-lines and are later propagated to produce 2D subsample displacements for the entire image. We aim to find a robust and stable *seed* RF-line in the overlap area, which also gives consistent DP integer displacement results in the two sequences. The displacement estimate on the *seed* line will serve as initial guess in the AM propagation.

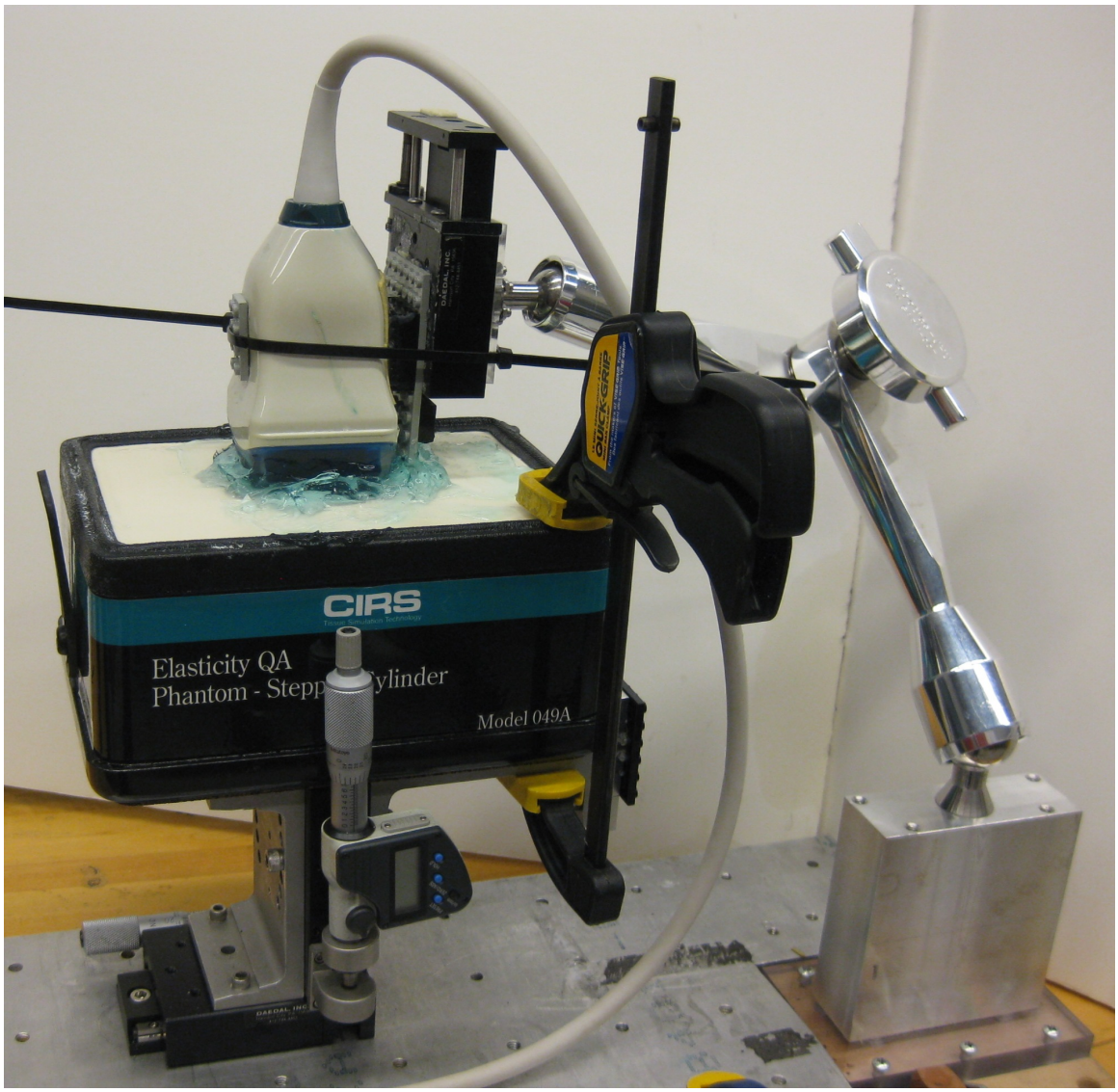

Figure 4.1: Experimental setup.

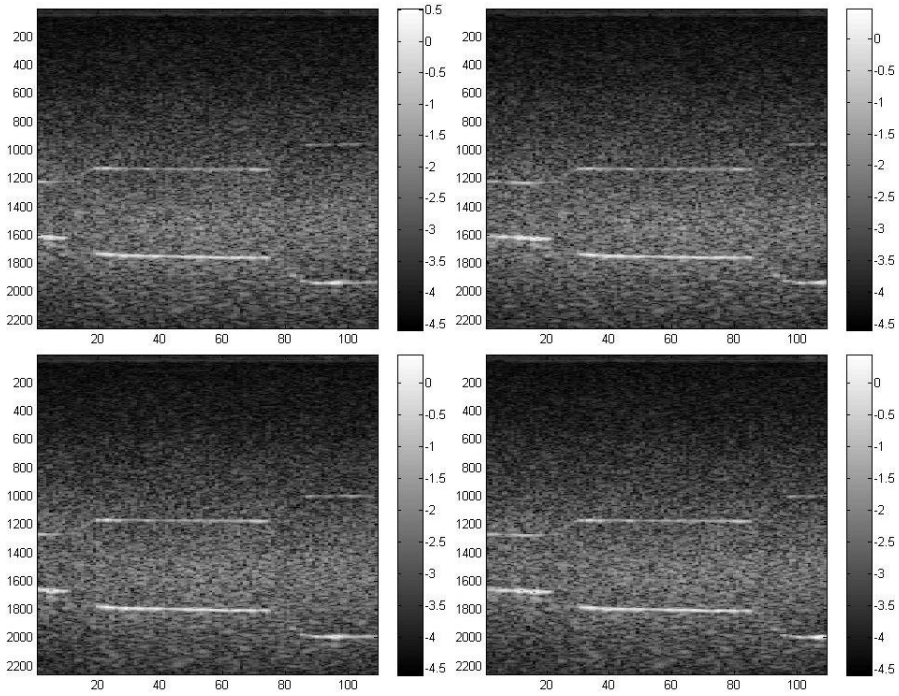

(a) (b)

Figure 4.2: Bmode ultrasound data before and after compression for (a) position t_0, and (b) position t_1.

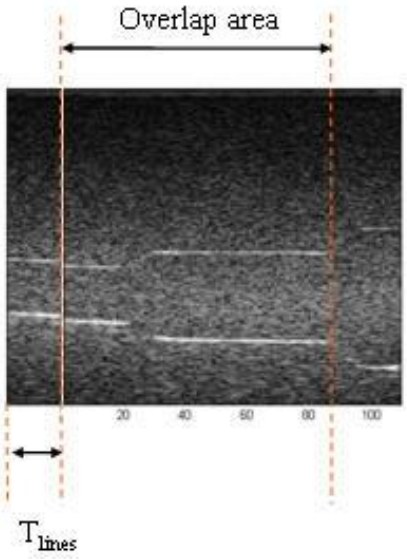

Figure 4.3: Bmode ultrasound data: translation T_{lines} and the length of the overlap area.

4.2.1.1 Algorithm Overview

The pairwise strain mosaicing is implemented as follows:

1. Robustness and stability measures are used to identify in the overlap area a suitable *seed* RF line for the mosaicing algorithm, similarly to [12]. The process filters those candidates which exhibit a high degree of decorrelation (Figure 4.4):

   - $k = 5$ $(i_1, i_2, ..., i_5)$ random corresponding positions (RF line pairs) are selected from the overlap area (Fig. 4.5-1).
   - Integer axial displacement is computed for each RF line pair using the dynamic programming approach [35]: $(a_1^1, a_2^1, ..., a_5^1)$ and $(a_1^2, a_2^2, ..., a_5^2)$ (Fig. 4.5-2). Note: in this step, both axial and later integer displacements are computed, but from here on only axial displacement values will be used.
   - In a continuous piece of tissue, the axial displacement profile resulting from a stress field induced by applied compression has a monotonous ramp [59]. A pair of decorrelated RF lines would affect the DP displacement estimation algorithm. Instead of a globally optimal solution, the estimate could exhibit regions of locally optimal solutions. For small deformations, these locally optimal solutions would correspond

to perturbations in the monotonously decreasing slope of their displacement profile, which in turn could result in *artifacts* in the final strain image. If three or more positions along the displacement profile would exhibit a continuous change in the slope of displacement, this could point to a region of poorly correlated data.

- For the remaining positions which satisfy the monotonous slope criterion,

$$d_k = abs(a_k^1 - a_k^2); avg_k = mean(d_k); std_k = stdev(d_k) \tag{4.2}$$

We select the *seed* RF line s as the position with the minimum std_k and $avg_k < 1$.

- At the end of the subinteger displacement estimation process on the a pair of RF lines, $(A_i = a_i + \Delta a_i)$, $(L_i = l_i + \Delta l_i)$ are the axial and lateral displacements at each sample i. The magnitude of the normalized cross-correlation could be used to assess the degree of matching between the pre- and post-compression data.

$$C(I_1(s), I_2(s)) = \left| \frac{\sum_m^{i=1}(I_1(i,s) - I_1)(I_2(i + A_i, s + L_i) - I_2)}{\sqrt{\sum_m^{i=1}(I_1(i,s) - I_1)^2 \sum_m^{i=1}(I_2(i + A_i, s + L_i) - I_2)^2}} \right| \tag{4.3}$$

where $\bar{I_1}$ and $\bar{I_2}$ are the means of RF values along the *seed* line s. The value of C could be used as an additional check to verify if the displacement estimate for the selected *seed* line is a good fit. If C value would fall below a certain threshold (to be established by the user), the

seed line would be deemed not suitable and the next stable *seed* line would be selected (Fig. 4.5-3).

2. Subinteger displacements values are calculated for *seed* line s (Fig. 4.5-4).

3. The subinteger displacement values are propagated using AM:

   - in one sequence towards the first RF line, and]
   - in the second sequence towards the last RF line.]

   The unified displacement field will have $n + T_{lines}$ RF lines and the stitch will be around RF line number $s + T_{lines}$ (Fig. 4.5-5).

4. Generate the ultrasound elastography mosaic from the unified displacement field (Fig. 4.5-6).

4.2.2 2D Multi-image Mosaicing

Given an existing n_t wide displacement map, computed for image pairs 1 through t, we expand our displacement map to include information from image pair $t + 1$ as follows:

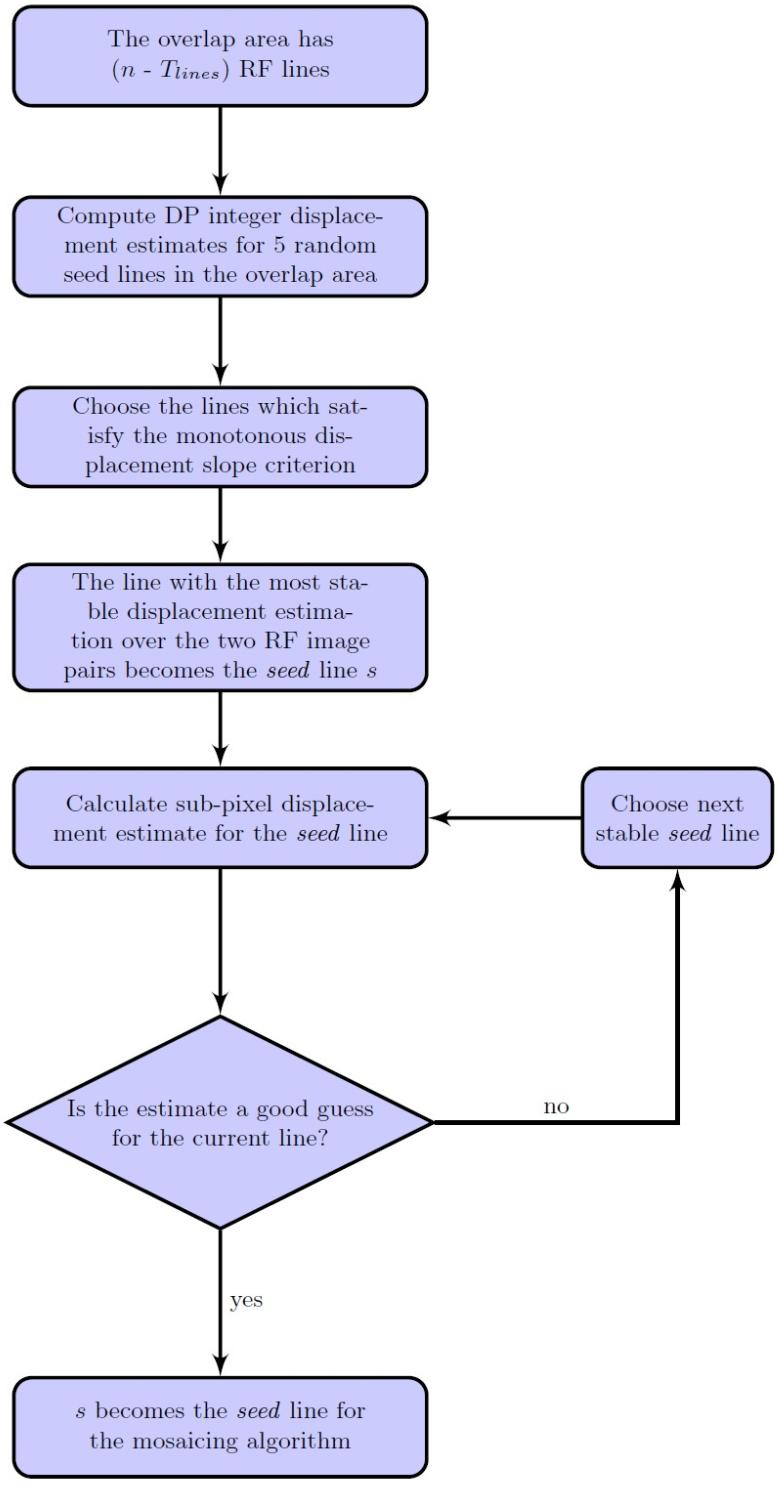

Figure 4.4: Robust *seed* selection method.

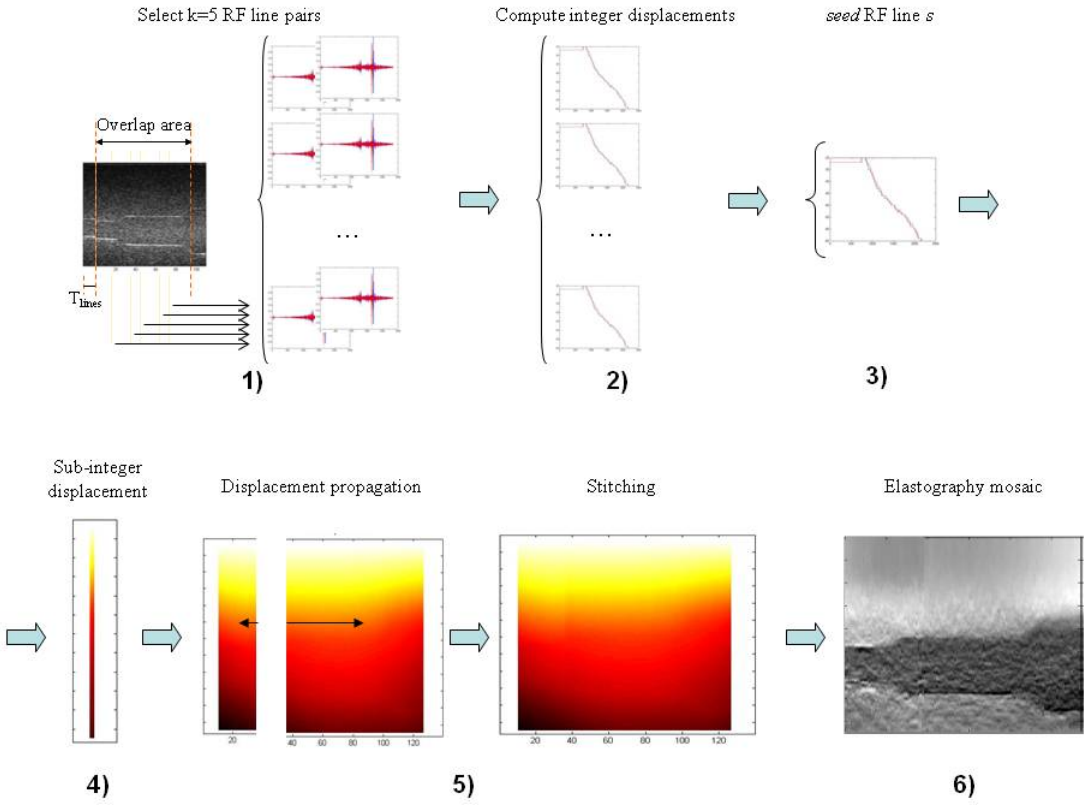

Figure 4.5: Pairwise Mosaicing workflow: $k = 5$ random RF positions are selected (1), integer displacement is calculated for each position (2), the *seed* RF line s is selected (3), subinteger displacement values are calculated for s (4), propagated in the 2 sequences and stitched (5). The ultrasound elastography mosaic is generated from the unified displacement field (6).

4.2.2.1 Algorithm Overview

1. Compute the translation T_{lines}^{t+1} between position t and position $t+1$ and the overlap area.

2. Select the *seed* RF-line s_{t+1} in the new overlap area.

3. Use the subinteger values form the wide FOV displacement map at RF-line number $s_{t+1} + T_{lines}$ as *seed* values to propagate using AM:

   - in the new sequence towards the first RF-line.

   Stitch the newly computed $(s_{t+1} + T_{lines})$ lines at the beginning of the previous displacement map. The new mosaiced displacement field will have $n_t + T_{lines}^{t+1}$ RF lines.

4. Generate the new ultrasound elastography mosaic from the updated displacement field.

4.2.3 3D Elastography Mosaicing

In the three-dimenssional case, consider a pair of RF volumes (V_{11}, V_12) collected at position t_0, before and after the compression of tissue using a 3D ultrasound wobbler transducer (NEED FIGURE OF WOBBLER HERE). Each volume

contains k frames and each frame has n RF lines of length m. One or more subsequent pairs of volumes are collected after the wobbler transducer is moved in the lateral direction of the probe with the help of a moving stage. Once again, a vertical stage was used to achieve an almost identical compression rate between the two sequences (Figure 4.1). Using the lateral and axial stages ensures the first frame of the first volume pair is alligned with the first frame of each subsequent pair volume, and all the other frames are simillarly aligned, with no out-of-plane motion between each position. The same steps of multi-image mosaicing can be applied on a frame by frame basis, resulting in an unified displacement field for each elevational position of the wobbler motor.

Note: here we employed a fixed rigid setup to controll the acquizition of 3D ultrasound data for the purpose of building 3D strain mosaics. In a routine 3D ultrasound exam, using stages to control the imaging of a certain human tissue is absolutely not feasibile. This does not, however invalidate our framework. As electromagnetic trackers become integrated into ultrasound transducers, it is feasibile to select ultrasound volumes consisting only of aligned frames with no out-of-plane rotation. The work presented here makes a case for in-plane mosaicing where translation is the only component of the transformation. One can easily envision an ultrasound system equipped with a tracked transducer like in the Foroughi set-up [**?**].

4.2.3.1 Algorithm Overview

Here we used a controlled setup for proof of concept, but using the Foroughi method [**?**] one could achieve a 3D elastography mosaic as follows:

1. Perform freehand palpation with tracked 3D transducer,
2. Use the tracking information [**?**] to select suitable aligned frames separated only by in-plane translation,
3. Apply 2D multi-image mosaicing method on a frame-by-frame basis to estimate an unified displacement field, and
4. Generate the 3D elastography mosaic from the resulting displacement field.

4.3 2D Mosaicing Experimental Setup

For experimental validation we palpated a CIRS (Norfolk, VA) elastography phantom *049a* (Figure 4.1) using a high-frequency ultrasound transducer (L14-5W/60) at center frequency of 10 MHz. Ultrasound RF data was acquired from an Ultrasonix system (Vancouver, BC) at 40MHz sampling rate. The *049a* CIRS phantom consists of a series of stepped cylinders of varying diameters (NEED

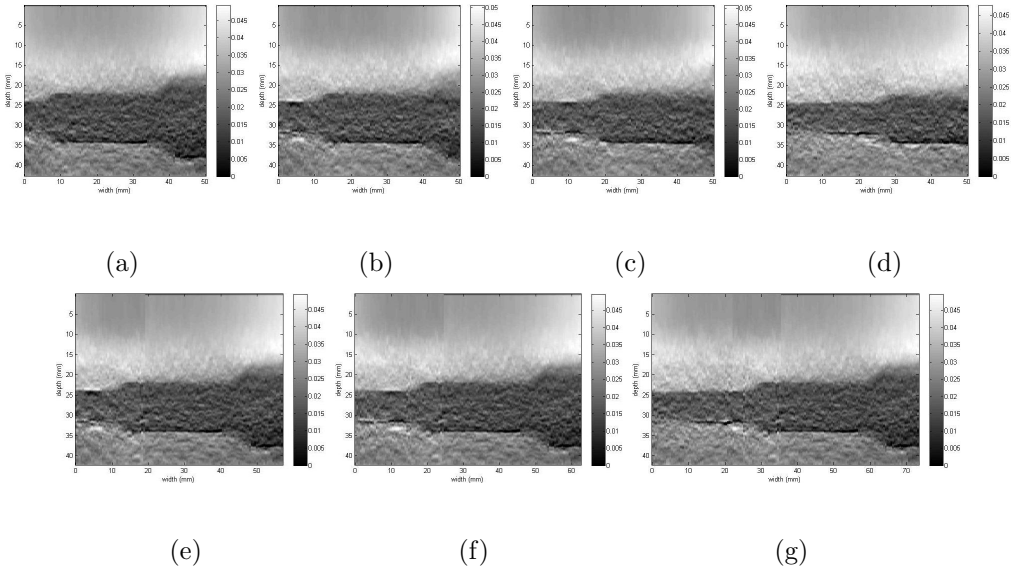

Figure 4.6: Ultrasound elastography at position t_0 (a), t_1 (b), t_2 (c), t_3 (d) and elastography mosaic of positions t_0 and t_1 (e), t_0, t_1 and t_2 (f), and t_0, t_1, t_2 and t_3 (g).

PICTURES FROM THE CIRS BROCHURE). The transducer was placed on top of one of the cylinders, parallel with its direction. The phantom was placed on a stage which controlled the compression in the axial direction and the translation in the lateral direction (Figure 4.1). RF data sequences were acquired from four axial compression levels ($c_0 = 0$, $c_1 = 2.54$mm, $c_2 = 5.08$mm, $c_3 =$ back to 0), for each of four lateral translation positions of the transducer ($t_0 = 0$, $t_1 = 5.08$mm, $t_2 = 10.16$mm, $t_3 = 20.32$mm), for a total of sixteen data sets. The width of the ultrasound transducer L14-5W is 59mm, and as a consequence any 2 sets separated by a lateral translation had some amount of overlap.

Ultrasound elastography images were obtained for each translation position t_0 - t_3

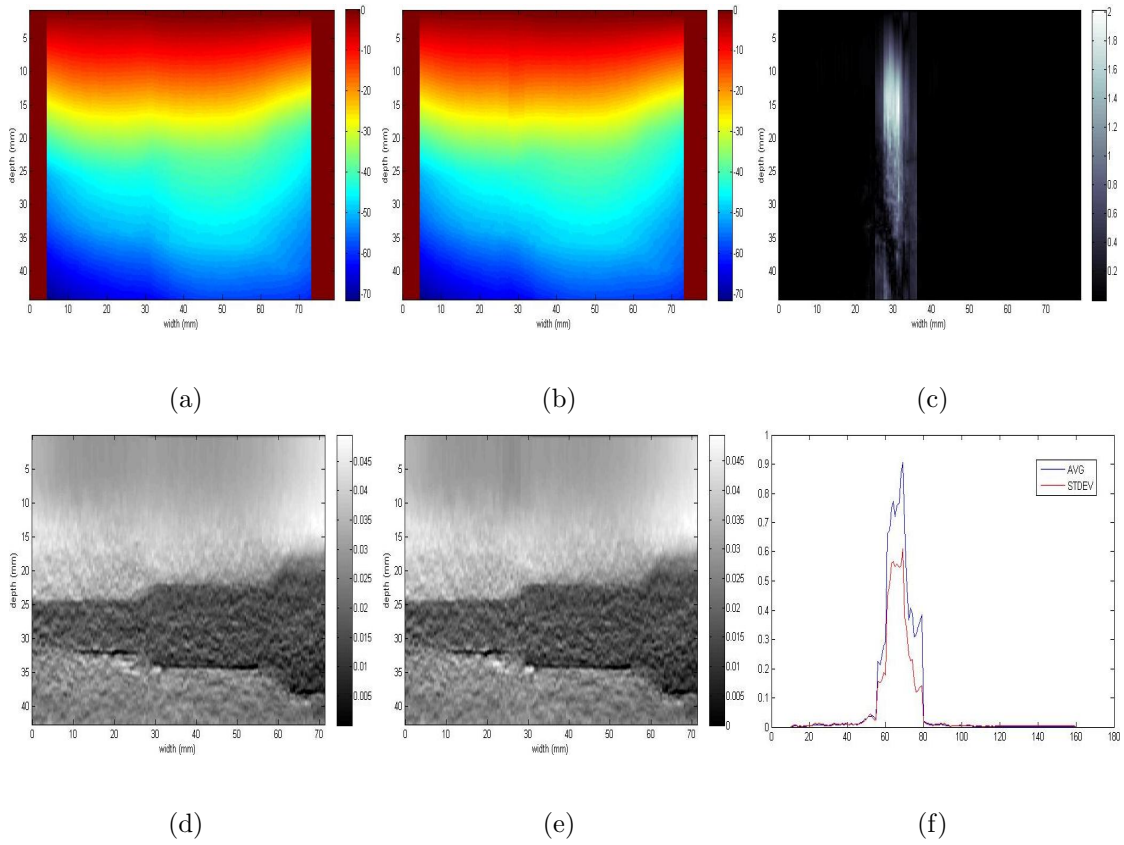

(a) (b) (c)

(d) (e) (f)

Figure 4.7: Panoramic displacement map of positions t_0 and t_3 (a), and of positions t_0, t_1, t_2 and t_3 (b), the absolute difference between them (c), and the mean and standard deviation of this difference, per line (f). The unit of displacement is pixels. Corresponding ultrasound elastography mosaics of positions t_0 and t_3 (d), and t_0, t_1, t_2 and t_3 (e).

((Fig. 4.6a-d). A pairwise elastography mosaic was produced from positions t_0 and t_1 (Fig. 4.6e), and then multi-image elastography mosaics from positions t_0, t_1 and t_2 (Fig. 4.6f), and t_0, t_1, t_2 and t_3 (Fig. 4.6g).

4.3.1 Phantom Results

Figure 4.7 shows the results of the validation experiment. The two panoramic displacement maps agree almost exactly; the absolute difference for the entire image had a mean of 0.0755 and a standard deviation of 0.2386 pixels. The maximum difference was 2.0168 pixels and it did not exceed 1 pixel on a mean, per-line basis. For a metric correspondent, 2.0168 pixels, is the equivalent of 0.0406 mm in the axial direction. Once the displacement maps are converted in elastogram mosaics (Fig. 4.7 e,f), the difference becomes indistinguishable even on close inspection. With the clinical application in mind, we conclude that these small differences are acceptable.

4.4 3D Mosaicing Experimental Setup

For 3D validation, RF data was acquired using an Ultrasonix system (Vancouver, BC) at 20MHz sampling rate. The same CIRS (Norfolk, VA) phantom was palpated with a 38mm width linear 4D volumetric transducer (4DL14-5/38) (Figure FIG OF WOBBLER). As with the 2D experiment, the phantom was placed on a stage to controll the compression in the axial direction and the translation in the lateral direction (Fig. 4.1). RF data sequences were acquired from four axial compression levels ($c_0 = 0$, $c_1 = 2.54$mm, $c_2 = 5.08$mm, $c_3 =$ back to 0), for each of five lateral

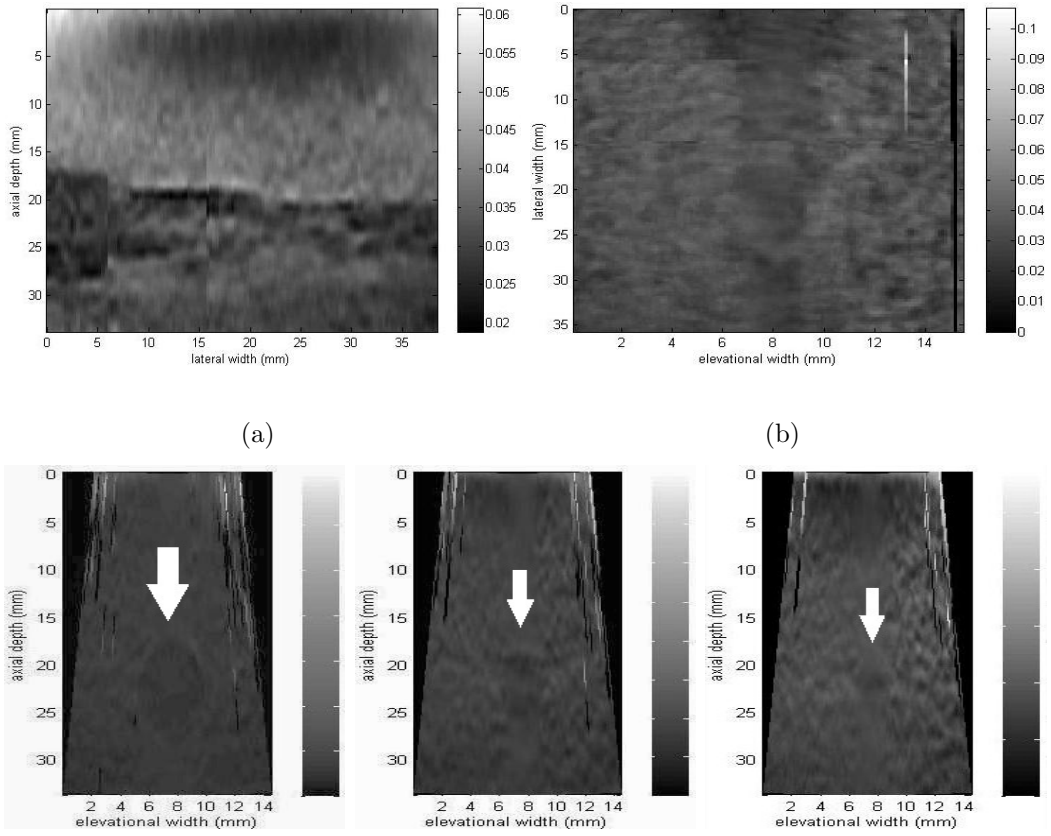

(a) (b)

(c) (d) (e)

Figure 4.8: 3D ultrasound elastography mosaic: axial-lateral plane (a), lateral-elevational plane (b), and 3 axial-elevational planes through 3 different diameters of the stepped cylinder (c, d, e)

translation positions of the transducer ($t_0 = 0$, $t_1 = 5.08$mm, $t_2 = 10.16$mm, $t_3 =$

20.32mm, $t_4 = 22.86$mm), for a total of twenty data sets.

4.4.1 Phantom Results

Figure 4.8 shows the results of the 3D ultrasound elastography mosaic. Strain in the middle frames of the axial-lateral plane (Figure 4.8a), lateral-elevational plane (Figure 4.8b), and 3 axial-elevational planes (Figure 4.8c-e) is shown. The diameters of the stiff cyclinder along the mosaicing direction were: 4:05 mm (Figure 4.8c), 2:53 mm (Figure 4.8d) and 1:58 mm (Figure 4.8e).

4.5 Conclusion and Future Work

We have presented an algorithm for generating reliable multi-image ultrasound elastography mosaics, robust to regions of decorrelation. Panoramic B-mode ultrasound has been reported with success in the literature and, with the addition of corresponding elastograms, an ultrasound system with these capabilities has great potential in clinical diagnostic and monitoring. Elastography has the advantage that it requires no additional hardware to be implemented, and a majority of commercial ultrasound systems now present an elastography interface. Furthermore, the challenge of mosaicing while freehand scanning can be met as efforts are under way to incorporate electromagnetical (EM) tracking in ultrasound transducers.

Appendix A

Ultrasound Elastography as a Tool for Imaging Guidance During Prostatectomy: Initial Experience

A.1 Clinical Significance

Prostate cancer is the second leading cause of cancer death and the most common cancer detected in men in the United States. An estimated 217,730 new cases of prostate cancer were diagnosed in the United States, and approximately 32,050 men died of

prostate cancer during 2010 [67]. Radical Prostatectomy (RP) aims for complete cancer resection and has been shown to improve cancer survival [68]. Robotic-assisted laparoscopic prostatectomy (RALP) has recently emerged as an alternative to open and laparoscopic procedures. The daVinci Surgical System (Intuitive Surgical, Sunnyvale, CA) provides 3-D visualization, higher magnification, hand tremor elimination and refined dexterity by incorporating wristed instrumentation. From 250 robotic cases in the beginning (2001), the number has reached 73,000 in 2009 (86 % of the 85,000 American men who had prostate cancer surgery) [69, 70].

Initial experiences with the daVinci surgical system have been positive: short learning curve, limited blood loss, less post-operative pain, favorable complication rates, and short hospital stay [69, 70, 71, 72, 73, 74, 75, 76]. Despite fewer perioperative complications and shorter hospital stay, a recent paper found patients were three times more likely to require salvage therapy [77]. One theoretical disadvantage with regards to robotic surgery is the lack of tactile feedback. In open RPs, the surgeon uses his fingers to feel the periphery of the prostate gland [78]. Without tactile feedback, a robotic surgeon is unable to appreciate differences in tissue texture or firmness and therefore may not be able to tailor precisely the extent of tissue excision around the prostate gland in efforts to eradicate all cancerous tissue. Inadvertently leaving residual cancer cells behind, called a positive surgical margin (PSM), is highly associated with cancer recurrence. PSM rates were initially higher in RALP than in the

open procedure, but they have been shown to decrease with surgeon's experience and improved technique [75, 77].

As manual palpation helps guide the surgeon in the open procedure, an equivalent real-time guiding tool is needed for robotic prostatectomy. Imaging modalities like MRI or CT are not feasible intraoperatively, nor do they possess the sensitivity or specificity for accurate detection and localization of prostate cancer. Transrectal ultrasound (TRUS) is routinely used in diagnosis, in conjunction with digital rectal examination (DRE) and biopsies [79]. One center used TRUS for real-time monitoring and guidance during Laparoscopic RP and reported technical feasibility and enhanced precision by decreased PSM rates [80, 81]. TRUS was capable of imaging a substantial percent of nonpalpable prostate cancers. The authors recognized however, the limitations of TRUS guidance; it requires considerable prior expertise and tends to identify primarily hypoechoic lesions, which were just 47% of the cancer nodules studied [80]. Today's prostate cancer patients are more likely to present with echogenic or isoechoic lesions because aggressive screening techniques lead to a shift toward smaller, early-stage cancers [82, 83] ; classic B-mode gray-scale ultrasound alone cannot identify these lesions.

Ultrasound (US) Elastography (USE) is emerging as a valuable tool in the field of imaging. Elastography is a qualitative technique based on the principle that tissue compression produces strain (displacement) within that tissue; strain is smaller in

harder, stiffer tissue than in softer, more compliant tissue 11. Analyzing the ultrasound raw radio frequency signal results in a strain map, commonly called *elastogram*, where harder tissue is darker than surrounding soft tissue. Cancers tend to present as hard lesions due to increased cellularity [11]. Echogenicity and stiffness of tissue are generally uncorrelated; USE can identify hypoechoic lesions, but also echogenic or isoechoic cancers that classic gray-scale ultrasonography cannot. Elastography through the transrectal approach has already been proven feasible in guiding biopsies of the prostate [84, 85, 86, 87]. Integrating USE technology with a laparoscopic ultrasound probe will give robotic and laparoscopic surgeons an important image-guidance tool, which until this point does not exist [88, 89, 90].

Here we describe the methodology and results of a pilot study evaluating the diagnostic accuracy and efficacy of using USE to identify the cancerous nodules in the prostate gland. In the study, human *ex-vivo* prostatectomy specimens where used to assess the accuracy of USE in the identification and characterization of hard cancerous nodules. We compared the elastogram results with histopathology maps (the gold standard) and also to pre- and post-operative MR scans of the prostate gland in order to assess and co-localize anatomically USE with the reference histopathology and MR scans.

A.2 Materials and Methods

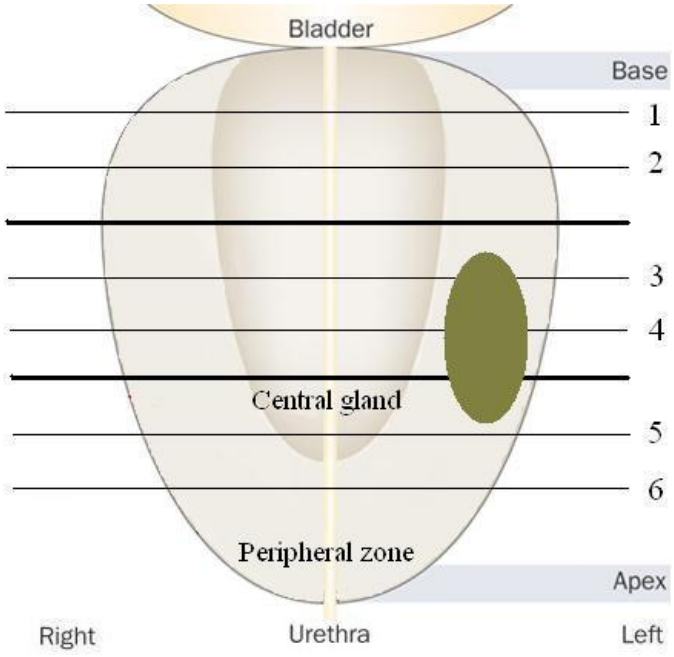

Figure A.1: Ultrasound elastography data collection process using the sextant approach; RF data was acquired in axial planes (1 - 6) from the gland's base towards the apex. For illustration purposes, a lesion is outlined in the left mid section, peripheral zone of the specimen, similar with the case of specimen #3

Prostate cancer patients, candidates for prostatectomy, were prospectively enrolled in the study, following an informed consent approved by the Institutional Review Board. The objective of the study was to evaluate the efficacy of using elastography to identify and precisely localize hard nodules such as seen with prostate cancer just beneath the surface of the prostate gland in the peripheral zone. In this area, cancerous lesions are at most risk of invasion beyond the confines of the prostate gland and also more likely to be cut across by a well meaning surgeon. We recruited patients who underwent

both open and assisted prostatectomies given that the process of removing the gland was not a focus of our study. Patients underwent multiple radiological procedures. 1) Pre-operative 3 Tesla MRI of the pelvis was performed right before the surgery procedure. 2) Post-operative ultra high-resolution MRI at 9.4 Tesla was performed on the excised prostate specimen to correlate the results to *in-vivo* pre-operative imaging. 3) USE was then performed on the prostate specimen by an experienced radiologist blinded to the surgeon's findings and to the pre-operative pathology report. The collected radio-frequency (RF) data was used offline to recreate classic B-mode grey-scale images, and also to compute elastograms showing the stiffness of the tissue scanned [34, 35].

Pre-operative and post-operative MR scans were used for anatomical correlation with the computed elastograms. For USE, the prostate specimens were placed in prone position on a surgical table. USE scans were performed in a systematic sextant approach, similar to that used for image guided biopsies. RF data was acquired in axial planes (from gland's base, through mid gland, to apex) on the left and right side of the gland (Figure A.1). The sextant approach was necessary to ensure that the scans were in the same plane with the histopathology diagrams (axial) which constituted the gold standard for comparison. USE coronal scans from the left to the right of the gland were also performed; these scans were in alignment with the MR coronal scans.

APPENDIX A. APPENDIX A

Hardware and Software Specification

USE acquisition was conducted using a Siemens Antares US scanner (Siemens Medical Solutions USA, Inc. Ultrasound Division, Issaquah, WA) with an ultrasound research interface to access raw RF data. Data was acquired by manual handling using a Siemens VF 10-5 linear array for prostate specimens. After RF data collection, elastograms were obtained using the dynamic programming (DP) elastography algorithm developed by Rivaz et al [34, 35].

Each prostate specimen underwent routine pathologic processing and analysis. Due to the high volume of prostatectomies performed at our institution, the routine pathological process does not result in a whole mount mapping. Instead, for histopathological evaluation the prostatectomy specimens were initially sliced at every 3-4 mm from apex to base, according to the Stanford protocol. Each slice (6 to 10 master slices) were then incorporated in a paraffin block and sliced at 5 μ meter thickness. The slices were stained with hematoxylin-eosin and were then analyzed under a microscope by a pathologist blinded to the surgeon's findings and also to the elastography results. The localization and size of each tumor focus were documented for all step master slices on axial diagrams, with Gleason score. Large macro photographs were reconstructed in several specimens (Figure 4.6(c)). All data collected were stored in the database.

N = 10 target areas were analyzed from N = 6 patients enrolled so far into the elas-

tography analysis. Histological findings served as the *gold standard* in determining the presence, location and size of any prostatic nodules, malignant and benign. The objective of our study was then to compare axial elastograms findings with the histological findings recorded by the pathologist (mapping diagrams, measurements and nodule characteristics such as malignant vs. benign). Since histopathology diagrams often specified just the maximum diameter of a lesion, coronal elastograms were used to better establish the location and extent of the identified lesions. MRI images (both axial and coronal planes) were aligned to the elastograms and provided help with their anatomical co-registration using anatomical details such as urethra or boundaries of peripheral zone vs. central gland.

A.3 Results

Elastography identified N=10 lesions, 8 hard nodules in the peripheral zone, 1 hard and 1 soft nodule in the central gland (Table 1). Pathology reports showed 8 of these lesions as malignant and 2 as benign. Diameter measurements correlation proved difficult because of the inability to perfectly register the three investigative modalities. USE and MRI measurements were within on average 2.05 mm vs. 2.25 mm of the diameters measured by pathology (standard deviation of 1.9 mm for USE and 2.9 mm for MRI). Size measurements and Gleason score are reported in Table 1.

Table A.1: Prostate specimen data: A total of 10 (ten) elastography lesions were identified in 6 (six) patients specimens (8 malignant and 2 benign). PZ = peripheral zone, CG = central gland

#	Location	Gleason	Size (cm)		
		Score	Elastography	Pathology	MRI
1.1	PZ base	3+5	1.4 x 0.8	1.3 x 0.8	1.3 x 1.1
1.2	CG base	N/A-Solid	0.7 x 1.1	1.0 x 1.0	1.0 x 1.1
1.3	CG base	N/A-Soft	1.1 x 0.8	1.0 x 1.0	1.0 x 0.9
2.1	PZ base	5+3	3.0 x 1.3	2.4 x 1.0	2.0 x 1.5
3.1	PZ mid	4+5	2.4 x 0.8	1.9 x 1.0	1.5 x 1.2
4.1	PZ mid	3+3	1.0 x 0.5	0.5 x 0.4	0.6 x 0.7
4.2	PZ mid	3+4	1.5 x 0.9	1.1 x 0.5	1.1 x 0.8
5.1	PZ apex	3+3	0.5 x 0.6	0.5 x 0.5	0.6 x 0.6
5.2	PZ apex	4+3	0.6 x 1.0	0.8 x 0.9	0.9 x 0.9
6.1	PZ base	3+3	0.7 x 1.2	0.7 x 1.8	0.7 x 0.7

APPENDIX A. APPENDIX A

Specimen #1 presented multiple hard and soft lesions, located in the central gland of the prostate (Figure A.2). The *ex-vivo* T2-weighted coronal image from specimen MRI obtained at 9.4 Tesla (Figure A.2 (C) - here in counter clock wise orientation for better visualization of the correlation between USE and MRI of the specimen) shows detailed anatomy of the heterogeneous central gland with a solid benign prostatic hypertrophy nodule (BPH) confirmed by pathology. Elastography was able to detect this solid nodule despite the heterogeneity of the prostate (Figure A.2 (B)) - solid arrow, whereas the lesion was not clearly identified by gray scale ultrasound. *Ex-vivo* T2-weighted 9.4 Tesla coronal image from specimen MRI also shows an additional soft cystic BPH nodule (dashed arrow). Urethra is also visible on the elastogram , as well as MRI exam (labeled *urethra*).

Axial scans of the same specimens were compared with histopathology axial cross-sections. The prostate, submitted for histological processing in four quadrant sections per slice, was digitally realigned to reconstruct a full histological cross-section (Figure A.3(c)). Specimen #1 was found with a tumor with Gleason score of 8 at the prostate base, left side (outlined). Figure A.3(a) shows an ultrasound B-mode image and an elastogram obtained through an axial plane at the prostate's base on the left side. The same tumor was identified by elastography (Figure A.3(b)- dashed contour) but is not visible on grey-scale ultrasound. For an anatomical correlation, a soft - cystic nodule anterior to cancer can be seen on B-mode image and USE (Figure A.3(a), (b)

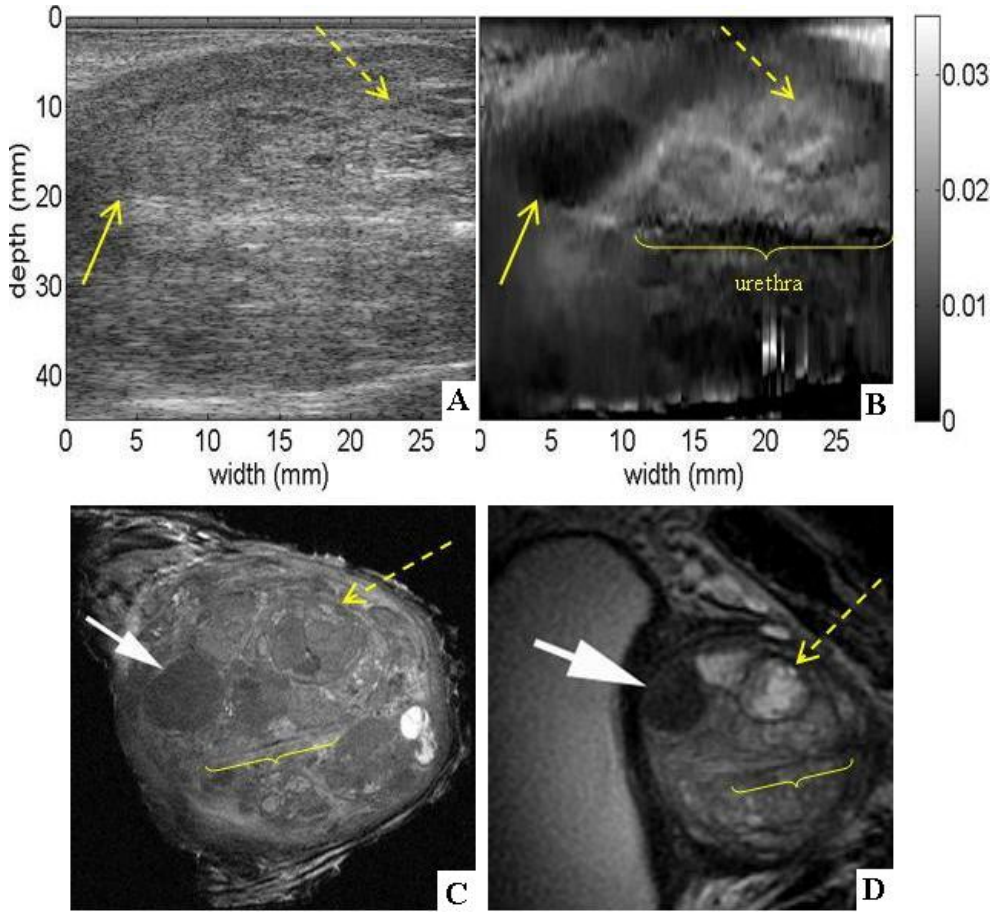

Figure A.2: Coronal section of prostate specimen #1 at the level of the central gland. Classic ultrasound B-mode (A) and elastogram (B). 9.4 Tesla *ex-vivo* (C) and 3 Tesla *in-vivo* (D) MRI images are presented in coronal planes, in CCW (counter clock wise) orientation for better visualization of the correlation between USE and MRI of the specimen. Benign solid (arrow) and soft (dashed arrow) nodules and urethra are visible.

- arrows) and on histopathology (Figure A.3(c) - arrows).

The remaining 5 (five) prostate specimens presented with superficial lesions in the peripheral zone of the gland. USE identified multiple hard malignant lesions in various locations, from the base to the apex of the prostate gland. One can notice the clear delimitations of these lesions on USE (Figure A.4) as well as the close estimations of size versus pathology and MRI.

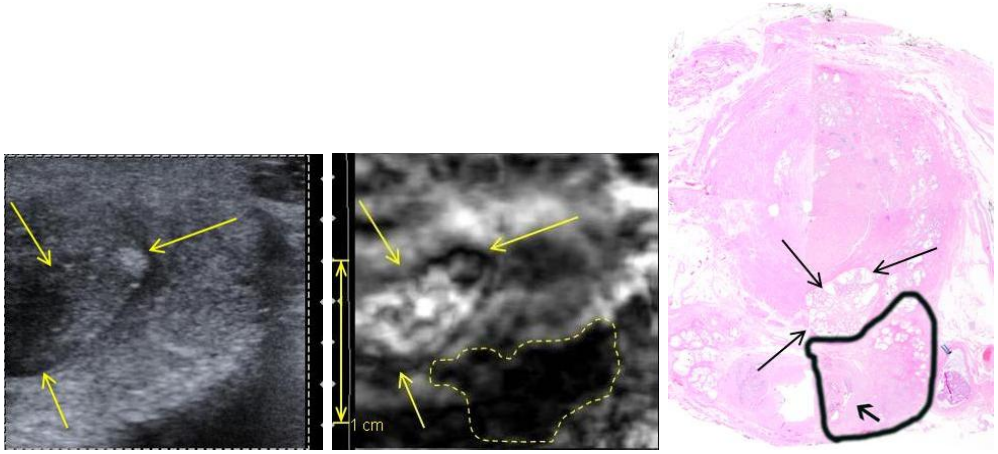

(a) (b) (c)

Figure A.3: Axial section of prostate specimen #1 peripheral zone. Left lateral section of the prostate's base; classic ultrasound B-mode (a) and elastogram (b). Hard lesion is outlined, arrows point to adjacent nodule. (c) Hematoxylin & eosin stained histological section of prostate base. The tumor (Gleason score 3+5 = 8, outlined in black) extended beyond the prostatic capsule in this section and invaded the left seminal vesicle (arrow).

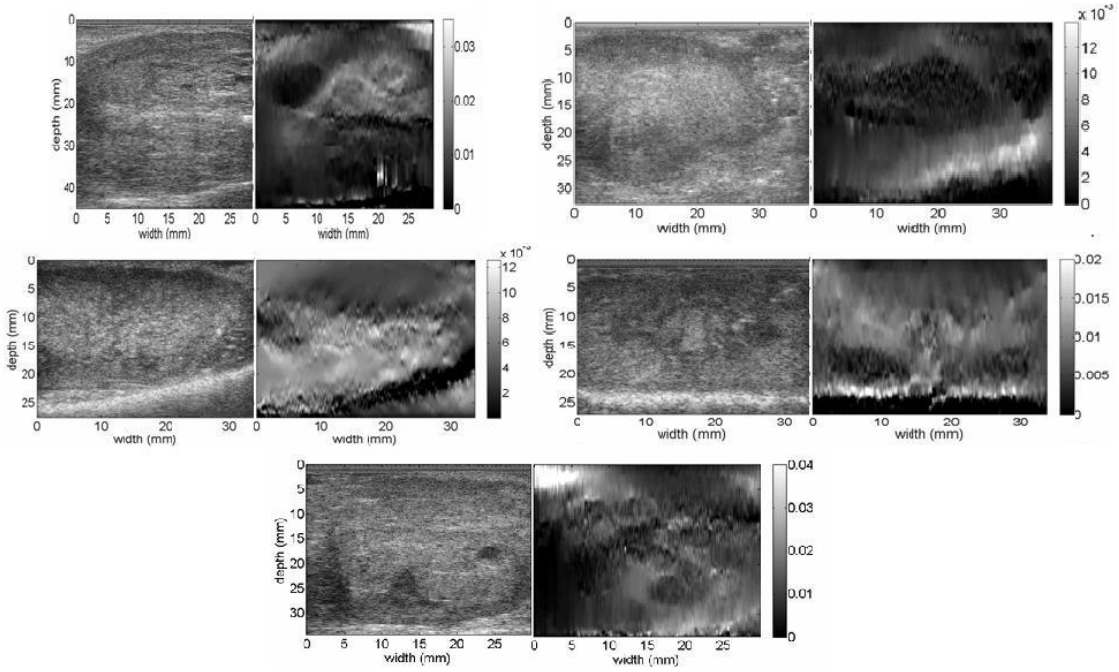

Figure A.4: B-mode image (left) and elastogram (right) from specimens # 2-6. Dark regions at the very bottom of elastograms represent structures outside the prostate tissue (e.g. operating table). The border of the prostatic tissue can be easily noticed as a highly reflective band at the bottom of B-mode images.

A.4 Discussion

In surgical procedures where manual palpation would be helpful but not possible to perform, e. g. laparoscopic robotic surgery, USE can offer added value if proven to be accurate in detecting pathologic lesions. Our feasibility study showed that USE was able to identify both hard and soft lesions in the *ex-vivo* prostate specimens, located in the deep prostatic central gland and in the peripheral zone. Histopathologic findings validated USE, and results compared favorably with the *in-vivo* pre-surgical and *ex-vivo* post-surgical MRI scans. In the central gland of the prostate, elastography showed excellent detection of hard and soft areas, despite the complexity of the central gland. Elastography was able to identify both hard and soft BPH nodules and anatomical landmarks like the urethra (note excellent anatomical correlation to MR scan findings). In the peripheral zone USE identified multiple hard malignant lesions, from the base to the apex of the prostate gland. These preliminary results demonstrate the ability of USE to detect hard nodules in the prostate and are encouraging in the pursuit of this technology as a palpation equivalent imaging tool for prostatectomy.

USE maps tissue elasticity which makes it an ideal imaging modality to serve as a surrogate and possible equivalence to manual palpation in identifying hard cancerous tissue in the prostate gland, especially in the peripheral zone but also in the

central gland. Real-time intra-operative imaging guidance is needed for identifying the presence of cancer within the prostate, especially near the capsule where tumor can invade and spread outside of the gland, and also for studying surrounding structures. If diseased hard lymph nodes could be detected, then lymphadenectomy may provide a more accurate cancer staging, help tailor future therapy, and potentially prevent recurrence. A better delineation of the bladder neck and apex during dissection, especially when prostate cancer is located at the apex could perhaps improve patients' outcome. If deemed possible, imaging cavernous nerves (CNs) located along the immediate surface of the prostate gland may lead to their preservation, and thus improved preservation of potency and urinary continence [91]. Further more, the development of the elastography technology as an imaging guiding tool during prostatectomy could potentially be useful in the open procedures as well, where the manual palpation would not be enough to identify deeper lesions. It has been documented in the literature that prostate carcinoma originates in the central gland and transitional zone in up to 30% of cases [92, 93].

A.5 Conclusions

Our initial experience showed USE was able to reliably identify hard nodules in the peripheral zone of the prostate that were prostate cancers. Additionally, USE showed

its ability to define tissue hardness of BPH nodules despite the underlying tissue complexity in the central gland. Our initial experience with USE encourages us to pursue further the evaluation of this technique. Further testing of a laparoscopic ulrasound probe is needed in a real laparoscopic environment. We can conclude that there is promise is integrating laparoscopic ultrasound elastography as a real-time, *in-vivo* imaging tool to guide surgeons during robotic-assisted prostatectomies.

Bibliography

[1] D. Christensen, *Ultrasonic Bioinstrumentation*, ser. Third Edition. Press, 2004.

[2] J. Ophir, I. Céspedes, H. Ponnekanti, Y. Yazdi, and X. Li, "Elastography: a quantitative method for imaging the elasticity of biological tissues," *Ultrasonic Imaging*, vol. 13, pp. 111–134, 1991.

[3] M. O'Donnell, A. R. Skovoroda, and B. M. Shapo, "Measurement of arterial wall motion using fourier based speckle tracking algorithms," in *Proceedings of IEEE Ultrasound Symposium*, 1991, pp. 1101–1104.

[4] M. O'Donnell, A. R. Skovoroda, B. M. Shapo, and S. Y. Emelianov, "Internal displacement and strain imaging using ultrasonic speckle tracking," *IEEE Transactions on Ultrasonics, Ferroelectrics, and Frequency Control*, vol. 41, no. 3, pp. 314–325, 1994.

[5] T. A. Krouskop, D. R. Dougherty, and S. F. Levinson, "A pulsed doppler ultra-

sonic system for making noninvasive measurements of the mechanical properties of soft tissues," *Journal Rehabil Res Dev*, vol. 24, pp. 1–8, 1987.

[6] R. M. Lerner and K. J. Parker, "Sono-elasticity in ultrasonic tissue characterization and echographic imaging," in *Proceedings of 7th European Community Workshop (Ed. J. M. Thijssen), Nijmegen, The Netherlands*, 1987.

[7] R. M. Lerner, S. R. Huang, and K. J. Parker, "Sonoelasticity images derived from ultrasound signals in mechanically vibrated tissues," *Ultrasound in medicine & Biology*, vol. 16, pp. 231–239, 1990.

[8] Y. Yamakoshi, J. Sato, and T. Sato, "Ultrasonic imaging of internal vibration of soft tissue under forced vibration," *IEEE Transactions on Ultrasonics, Ferroelectrics, and Frequency Control*, vol. 37, pp. 45–53, 1983.

[9] S. K. Alam, D. W. Richards, and K. J. Parker, "Detection of intraocular pressure change in the eye using sonoelastic doppler ultrasound," *Ultrasound Medicine & Biology*, vol. 20, pp. 751–758, 1994.

[10] L. Gao, K. J. Parker, R. M. Lerner, and S. F. Levinson, "Imaging of the elastic properties of tissue – a review," *Ultrasound in Medicine & Biology*, vol. 22, no. 8, pp. 959–977, 1996.

[11] J. Ophir, S. K. Alam, B. Garra, F. Kallel, E. Konofagou, T. Krouskop, and T. Varghese, "Elastography: ultrasonic estimation and imaging of the elastic

properties of tissues," *Proceedings of the Institution of Mechanical Engineers. Part H, Journal of Engineering in Medicine*, vol. 213, no. 3, pp. 203–233, 1999.

[12] J. Greenleaf, M. Fatemi, and M. Insana, "Selected methods for imaging elastic properties of biological tissues," *Annu. Rev. Biomed. Eng.*, vol. 5, pp. 57–78, April 2003.

[13] T. J. Hall, "AAPM/RSNA Physics Tutorial for Residents: Topics in US Beyond the Basics: Elasticity Imaging with US," *Radiographics*, vol. 23, pp. 1657–1671, 2003.

[14] K. J. Parker, L. Gao, R. M. Lerner, and S. F. Levinson, "Techniques for elastic imaging: A review," *IEEE Engineering in Medicine and Biology*, vol. 15, no. 6, pp. 52–59, 1996.

[15] B. Garra, E. Céspedes, J. Ophir, S. Spratt, R. Zuurbier, C. Magnant, and M. Pennanen, "Elastography of breast lesions: initial clinical results." *Radiology*, vol. 202, no. 1, pp. 79–86, 1997.

[16] C. L. DeKorte, E. I. Cespedes, A. F. W. van der Steen, and C. T. Lancee, "Intravascular elasticity imaging using ultrasound: feasibility studies in phantoms," *Ultrasound in Medicine & Biology*, vol. 23, pp. 735–746, 1997.

[17] A. P. G. Hoeks, P. J. Brands, J. M. Willigers, and R. S. Reneman, "Non-invasive

measurement of mechanical properties of arteries in health and disease," *Proc. Inst. Mech. Eng.*, vol. 213, pp. 195–202, 1999.

[18] S. F. Levinson, M. Shinagawa, and T. Sato, "Sonoelastic determination of human skeletal muscle elasticity," *Journal Biomechanics*, vol. 28, pp. 1145–1154, 1995.

[19] R. S. Adler, J. M. Rubin, P. H. Bland, and P. L. Carson, "Quantitative tissue motion analysis of digitized m-mode images: gestational differences of fetal lung," *Ultrasound Medicine & Biology*, vol. 16, pp. 561–569, 1990.

[20] S. Y. Emelianov, M. A. Lubinski, A. R. Skovoroda, R. Q. Erkamp, and S. F. Leavey, "Reconstructive ultrasound elasticity imaging for renal transplant diagnosis: kidney ex-vivo results," *Ultrason Imaging*, vol. 22, pp. 178–194, 2000.

[21] R. Righetti, F. Kallel, R. J. Stafford, R. E. Price, T. A. Krouskop, J. D. Hazle, and J. Ophir, "Elastographic characterization of hifu-induced lesions in canine livers," *Ultrasound in Medicine & Biology*, vol. 25, no. 7, pp. 1099–1113, 1999.

[22] T. Varghese and J. Ophir, "Enhancement of echo-signal correlation in elastography using temporal stretching," *IEEE Transactions on Ultrasonics, Ferroelectrics, and Frequency Control*, vol. 44, no. 1, pp. 173–180, 1997.

[23] H. Xie, T. Gauthier, and A. Fernandez, "The role of local center frequency estimation in doppler-based strain imaging," in *Proceedings of IEEE Ultrasonics Symposium*, October 2007, pp. 1965–1968.

[24] I. Céspedes, J. Ophir, H. Ponnekanti, and N. Maklad, "Elastography: elasticity imaging using ultrasound with application to muscle and breast in vivo," *Ultrasonic Imaging*, vol. 15, pp. 73–88, 1993.

[25] P. Chaturvedi, M. Insana, and T. Hall, "2D companding for noise reduction in strain imaging," *IEEE Transactions on Ultrasonics, Ferroelectrics, and Frequency Control*, vol. 45, no. 1, pp. 179–191, January 1998.

[26] A. Pesavento, C. Perrey, M. Krueger, and H. Ermert, "A time-efficient and accurate strain estimation concept for ultrasonic elastography using iterative phase zero estimation," *Ultrasonics, Ferroelectrics and Frequency Control, IEEE Transactions on*, vol. 46, no. 5, pp. 1057–1067, September 1999.

[27] Y. Zhu and T. J. Hall, "A modified block matching method for real-time freehand strain imaging," *Ultrasonic Imaging*, vol. 24, no. 3, pp. 161–176, 2002.

[28] J. Lindop, G. Treece, A. Gee, and R. Prager, "An intelligent interface for freehand strain imaging," *Ultrasound in Medicine & Biology*, vol. 34, no. 7, pp. 1117–1128, 2008.

[29] J. Jiang and T. Hall, "A regularized real-time motion tracking algorithm using dynamic programming for ultrasonic strain imaging," in *IEEE Ultrasonics Symp.*, Vancouver, Canada, October 2006, pp. 606–609.

[30] J. Jiang, T. J. Hall, and A. M. Sommer, "A novel image formation method for

ultrasonic strain imaging," *Ultrasound in Medicine & Biology*, vol. 33, no. 4, pp. 643–652, 2007.

[31] R. Zahiri-Azar and S. Salcudean, "Motion estimation in ultrasound images using time domain cross correlation with prior estimates," *Biomedical Engineering, IEEE Transactions on*, vol. 53, no. 10, pp. 1990 –2000, oct. 2006.

[32] G. M. Treece, J. E. Lindop, A. H. Gee, and R. W. Prager, "Freehand ultrasound elastography with a 3-d probe," *Ultrasound in Medicine and Biology*, vol. 34, no. 3, pp. 463 – 474, 2008.

[33] L. Chen, G. M. Treece, J. E. Lindop, A. H. Gee, and R. W. Prager, "A quality-guided displacement tracking algorithm for ultrasonic elasticity imaging," *Medical Image Analysis*, vol. 13, no. 2, pp. 286 – 296, 2009.

[34] H. Rivaz, E. Boctor, P. Foroughi, R. Zellars, G. Fichtinger, and G. Hager, "Ultrasound elastography: a dynamic programming approach," *IEEE Transactions on Medical Imaging*, vol. 27, no. 10, pp. 1373–1377, 2008.

[35] H. Rivaz, E. Boctor, M. Choti, and G. Hager, "Real-time regularized ultrasound elastography," *IEEE Transactions on Medical Imaging*, vol. 30, no. 4, pp. 928–945, 2011.

[36] A. Fenster and D. Downey, "3-D ultrasound imaging: a review," *Engineering in Medicine and Biology Magazine, IEEE*, vol. 15, no. 6, pp. 41 –51, nov/dec 1996.

[37] J. Schaar, C. De Korte, F. Mastik, L. Van Damme, R. Krams, P. Serruys, and A. Van Der Steen, "Three-dimensional palpography of human coronary arteries: Ex vivo validation and in-patient evaluation," *Herz*, vol. 30, no. 2, pp. 125–133, 2005.

[38] J. Lindop, G. Treece, A. Gee, and R. Prager, "3D elastography using freehand ultrasound," *Ultrasound in Medicine & Biology*, vol. 32, no. 4, pp. 529–545, 2006.

[39] M. Krueger, A. Pesavento, H. Ermert, K. Hiltawsky, L. Heuser, H. Rosenthal, and A. Jensen, "Ultrasonic strain imaging of the female breast using phase root seeking and three-dimensional optical flow," in *Ultrasonics Symposium (IUS), 1998 IEEE*, vol. 2, 1998, pp. 1757 –1760.

[40] A. Lorenz, A. Pesavento, M. Pesavento, and H. Ermert, "Three-dimensional strain imaging and related strain artifacts using an ultrasonic 3D abdominal probe," in *Ultrasonics Symposium (IUS), 1999 IEEE*, vol. 2, 1999, pp. 1657 –1660.

[41] S. I. Awad and J. T. Yen, "3D Strain Imaging Using a Rectilinear 2D Array," *Ultrasonic Imaging*, vol. 29, no. 4, pp. 220–230, 2007.

[42] J.-F. Deprez, E. Brusseau, C. Schmitt, G. Cloutier, and O. Basset, "3D estimation of soft biological tissue deformation from radio-frequency ultrasound volume acquisitions," *Medical Image Analysis*, vol. 13, no. 1, pp. 116 – 127, 2009.

[43] T. Fisher, J. Jiang, and T. Hall, "Volumetric strain imaging," in *Ultrasonics Symposium (IUS), 2007 IEEE*, oct. 2007, pp. 355–358.

[44] T. G. Fisher, T. J. Hall, S. Panda, M. S. Richards, P. E. Barbone, J. Jiang, J. Resnick, and S. Barnes, "Volumetric Elasticity Imaging with a 2-D CMUT Array," *Ultrasound in Medicine and Biology*, vol. 36, no. 6, pp. 978–990, 2010.

[45] R. J. Housden, L. Chen, A. H. Gee, G. M. Treece, C. Uff, J. Fromageau, L. Garcia, R. W. Prager, N. L. Dorward, and J. C. Bamber, "A new method for the acquisition of ultrasonic strain image volumes," *Ultrasound in Medicine & Biology*, vol. 37, no. 3, pp. 434–441, 2011.

[46] P. Foroughi, H. Rivaz, I. N. Fleming, G. D. Hager, and E. M. Boctor, "Tracked ultrasound elastography (TrUE)," in *Proceedings of the International Conference on Medical Image Computing and Computer-Assisted Intervention*, ser. MICCAI'10, 2010, pp. 9–16.

[47] T. Varghese, J. A. Zagzebski, Q. Chen, U. Techavipoo, G. Frank, C. Johnson, A. Wright, and F. T. Lee Jr., "Ultrasound monitoring of temperature change during radiofrequency ablation: Preliminary in-vivo results," *Ultrasound in Medicine & Biology*, vol. 28, no. 3, pp. 321–329, 2002.

[48] N. R. Miller, J. C. Bamber, and P. M. Meany, "Fundamental limitations of noninvasive temperature imaging by means of ultrasound echo strain estimation," *Ultrasound in Medicine & Biology*, vol. 28, pp. 1319–1333, 2002.

[49] R. Maass-Moreno and C. A. Damianou, "Noninvasive temperature estimation in tissue via ultrasound echo-shifts. Part I, Analytical Model," *J Acoust Soc Am*, vol. 100, no. 4, pp. 2514–2521, 1996.

[50] R. Maass-Moreno, C. A. Damianou, and N. T. Sanghvi, "Noninvasive temperature estimation in tissue via ultrasound echo-shifts. Part II. In Vitro study," *J Acoust Soc Am*, vol. 100, no. 4, pp. 2522–2530, 1996.

[51] R. Seip, P. VanBaren, C. Cain, and E. S. Ebbini, "Noninvasive spatio-temporal temperature change estimation using diagnostic ultrasound," *IEEE Transactions on Ultrasonics, Ferroelectrics, and Frequency Control*, vol. 43, pp. 1068–1078, 1996.

[52] C. Simon, P. VanBaren, and E. S. Ebbini, "Two-dimensional temperature estimation using diagnostic ultrasound," *IEEE Transactions on Ultrasonics, Ferroelectrics, and Frequency Control*, vol. 45, no. 4, pp. 1088–1099, 1998.

[53] Z. Sun and H. Ying, "A multi-gate time-of-flight technique for estimation of temperature distribution in heated tissue: Theory and computer simulation," *Ultrasonics*, vol. 37, pp. 107–122, 1999.

[54] M. Pernot, M. Tanter, J. Bercoff, K. Waters, and M. Fink, "Temperature estimation using ultrasonic spatial compounding," *Ultrasonics, Ferroelectrics and Frequency Control, IEEE Transactions on*, vol. 51, no. 5, pp. 606–615, May 2004.

[55] R. Souchon, O. Rouviere, A. Gelet, V. Detti, S. Srinivasan, J. Ophir, and J. Y. Chapelon, "Visualization of hifu lesions using elastography of the human prostate in vivo: Preliminary results," *Ultrasound in Medicine & Biology*, vol. 29, no. 7, pp. 1007–1015, 2003.

[56] A. N. Amini, E. S. Ebbini, and T. Georgiou, "Noninvasive estimation of tissue temperature via high-resolution spectral analysis techniques," *IEEE Trans. Biomed. Eng.*, vol. 52, no. 2, pp. 221–228, 2005.

[57] P. Foroughi, H.-J. Kang, D. A. Carnegie, M. G. van Vledder, M. A. Choti, G. D. Hager, and E. M. Boctor, "A Freehand Ultrasound Elastography System With Tracking for *In Vivo* Applications," *Ultrasound in Medicine & Biology*, vol. 39, no. 2, pp. 211–225, 2013.

[58] T. Varghese, J. A. Zagzebski, and F. T. Lee Jr., "Elastographic imaging of thermal lesions in the liver in vivo following radiofrequency ablation: preliminary results," *Ultrasound in Medicine & Biology*, vol. 28, no. 11-12, pp. 1467–1473, 2002.

[59] G. Mase, R. Smelser, and G. Mase, *Continuum Mechanics for Engineers, Third Edition*, ser. Computational Mechanics and Applied Analysis Series. CRC Press, 2009.

[60] M. Insana, P. Chaturvedi, T. Hall, and M. Bilgen, "3-D companding using linear

arrays for improved strain imaging," in *Ultrasonics Symposium, 1997. Proceedings., 1997 IEEE*, vol. 2, 1997, pp. 1435–1438.

[61] S. Y. Emelianov, X. Chen, M. O'Donnell, B. Knipp, D. Myers, T. W. Wakefield, and J. M. Rubin, "Triplex ultrasound: elasticity imaging to age deep venous thrombosis," *Ultrasound in Medicine & Biology*, vol. 28, no. 6, pp. 757–767, 2002.

[62] T. C. Poon and R. N. Rohling, "Three-dimensional extended field-of-view ultrasound," *Ultrasound in Medicine & Biology*, vol. 32, no. 3, pp. 357–369, 2006.

[63] A. H. Gee, G. M. Treece, R. W. Prager, C. J. Cash, and L. Berman, "Rapid registration for wide field of view freehand three-dimensional ultrasound," *IEEE Transactions on Medical Imaging*, vol. 22, no. 11, pp. 1344–1357, 2003.

[64] C. Wachinger, W. Wein, and N. Navab, "Registration strategies and similarity measures for three-dimensional ultrasound mosaicing," *Academic Radiology*, vol. 15, no. 11, pp. 1404–1415, 2008.

[65] K. Rajpoot, J. A. Noble, V. Grau, C. Szmigielski, and H. Becher, "Multiview RT3D echocardiography image fusion," in *Functional Imaging and Modeling of the Heart*, N. Ayache, H. Delingette, and M. Sermesant, Eds. Berlin, Heidelberg: Springer Berlin Heidelberg, 2009, vol. 5528, pp. 134–143.

[66] I. Fleming, H. Rivaz, E. Boctor, and G. Hager, "Robust dynamic programming

method for ultrasound elastography," *Proceedings of the SPIE Medical Imaging*, vol. 8320, no. 1, pp. 83 201–83 206, 2012.

[67] A. Jemal, R. Siegel, J. Xu, and E. Ward, "Cancer statistics, 2010," *CA: A Cancer Journal for Clinicians*, vol. 60, no. 5, pp. 277–300, 2010.

[68] A. Bill-Axelson, L. Holmberg, M. Ruutu, H. Garmo, J. R. Stark, C. Busch, S. Nordling, M. Hggman, S. Andersson, S. Bratell, A. Spngberg, J. Palmgren, G. Steineck, H. Adami, and J. Johansson, "Radical prostatectomy versus watchful waiting in early prostate cancer," *The New England Journal of Medicine*, vol. 364, no. 18, pp. 1708–1717, 2011.

[69] G. N. Box and T. E. Ahlering, "Robotic radical prostatectomy: long-term outcomes," *Current Opinion in Urology*, vol. 18, no. 2, pp. 173–179, 2008.

[70] R. S. Pruthi and E. M. Wallen, "Current status of robotic prostatectomy: promises fulfilled," *The Journal of Urology*, vol. 181, no. 6, pp. 2420–2421, 2009.

[71] B. Nelson, M. Kaufman, G. Broughton, M. S. Cookson, S. S. Chang, S. D. Herrell, R. G. Baumgartner, and J. Smith, Joseph A, "Comparison of length of hospital stay between radical retropubic prostatectomy and robotic assisted laparoscopic prostatectomy," *The Journal of Urology*, vol. 177, no. 3, pp. 929–931, 2007.

[72] W. Artibani, S. Fracalanza, S. Cavalleri, M. Iafrate, M. Aragona, G. Novara, M. Gardiman, and V. Ficarra, "Learning curve and preliminary experience with

da vinci-assisted laparoscopic radical prostatectomy," *Urologia Internationalis*, vol. 80, no. 3, pp. 237–244, 2008.

[73] J. Colombo, Jose R, B. Santos, J. Hafron, T. Gianduzzo, G. Haber, and J. H. Kaouk, "Robotic assisted radical prostatectomy: surgical techniques and outcomes," *International Braz J Urol: Official Journal of the Brazilian Society of Urology*, vol. 33, no. 6, pp. 803–809, 2007.

[74] K. K. Badani, S. Kaul, and M. Menon, "Evolution of robotic radical prostatectomy: assessment after 2766 procedures," *Cancer*, vol. 110, no. 9, pp. 1951–1958, 2007.

[75] V. Ficarra, S. Cavalleri, G. Novara, M. Aragona, and W. Artibani, "Evidence from robot-assisted laparoscopic radical prostatectomy: a systematic review," *European Urology*, vol. 51, no. 1, pp. 45–55; discussion 56, 2007.

[76] J. Berryhill, Roy, J. Jhaveri, R. Yadav, R. Leung, S. Rao, A. El-Hakim, and A. Tewari, "Robotic prostatectomy: a review of outcomes compared with laparoscopic and open approaches," *Urology*, vol. 72, no. 1, pp. 15–23, 2008.

[77] J. C. Hu, Q. Wang, C. L. Pashos, S. R. Lipsitz, and N. L. Keating, "Utilization and outcomes of minimally invasive radical prostatectomy," *Journal of Clinical Oncology: Official Journal of the American Society of Clinical Oncology*, vol. 26, no. 14, pp. 2278–2284, 2008.

[78] P. C. Walsh, H. Lepor, and J. C. Eggleston, "Radical prostatectomy with preservation of sexual function: anatomical and pathological considerations," *The Prostate*, vol. 4, no. 5, pp. 473–485, 1983.

[79] G. Salomon, J. Kllerman, I. Thederan, F. K. H. Chun, L. Budus, T. Schlomm, H. Isbarn, H. Heinzer, H. Huland, and M. Graefen, "Evaluation of prostate cancer detection with ultrasound real-time elastography: a comparison with step section pathological analysis after radical prostatectomy," *European Urology*, vol. 54, no. 6, pp. 1354–1362, 2008.

[80] O. Ukimura, I. S. Gill, M. M. Desai, A. P. Steinberg, M. Kilciler, C. S. Ng, S. C. Abreu, M. Spaliviero, A. P. Ramani, J. H. Kaouk, A. Kawauchi, and T. Miki, "Real-time transrectal ultrasonography during laparoscopic radical prostatectomy," *The Journal of Urology*, vol. 172, no. 1, pp. 112–118, 2004.

[81] O. Ukimura, C. Magi-Galluzzi, and I. S. Gill, "Real-time transrectal ultrasound guidance during laparoscopic radical prostatectomy: impact on surgical margins," *The Journal of Urology*, vol. 175, no. 4, pp. 1304–1310, 2006.

[82] C. M. Coley, M. J. Barry, C. Fleming, and A. G. Mulley, "Early detection of prostate cancer. part i: Prior probability and effectiveness of tests. the american college of physicians," *Annals of Internal Medicine*, vol. 126, no. 5, pp. 394–406, 1997.

[83] W. F. Daehnert, U. M. Hamper, J. C. Eggleston, P. C. Walsh, and R. C. Sanders,

"Prostatic evaluation by transrectal sonography with histopathologic correlation: the echopenic appearance of early carcinoma," *Radiology*, vol. 158, no. 1, pp. 97–102, 1986.

[84] D. L. Cochlin, R. H. Ganatra, and D. F. R. Griffiths, "Elastography in the detection of prostatic cancer," *Clinical Radiology*, vol. 57, no. 11, pp. 1014–1020, 2002.

[85] K. Koenig, U. Scheipers, A. Pesavento, A. Lorenz, H. Ermert, and T. Senge, "Initial experiences with real-time elastography guided biopsies of the prostate," *The Journal of Urology*, vol. 174, no. 1, pp. 115–117, 2005.

[86] M. Sumura, K. Shigeno, T. Hyuga, T. Yoneda, H. Shiina, and M. Igawa, "Initial evaluation of prostate cancer with real-time elastography based on step-section pathologic analysis after radical prostatectomy: a preliminary study," *International Journal of Urology: Official Journal of the Japanese Urological Association*, vol. 14, no. 9, pp. 811–816, 2007.

[87] J. Leven, D. Burschka, R. Kumar, G. Zhang, S. Blumenkranz, X. D. Dai, M. Awad, G. D. Hager, M. Marohn, M. Choti, C. Hasser, and R. H. Taylor, "DaVinci canvas: a telerobotic surgical system with integrated, robot-assisted, laparoscopic ultrasound capability," *Medical Image Computing and Computer-Assisted Intervention: MICCAI ... International Conference on Medical Image*

Computing and Computer-Assisted Intervention, vol. 8, no. Pt 1, pp. 811–818, 2005.

[88] C. M. Schneider, G. W. Dachs, II, C. J. Hasser, M. A. Choti, S. P. DiMaio, and R. H. Taylor, "Robot-assisted laparoscopic ultrasound," in *Proceedings of the First international conference on Information processing in computer-assisted interventions*, ser. IPCAI'10. Berlin, Heidelberg: Springer-Verlag, 2010, pp. 67–80.

[89] C. M. Schneider, P. D. Peng, R. H. Taylor, G. W. D. II, C. J. Hasser, S. P. DiMaio, and M. A. Choti, "Robot-assisted laparoscopic ultrasonography for hepatic surgery," *Surgery*, vol. 0, no. 0, pp. –, 2011.

[90] S. Billings, N. Deshmukh, H. J. Kang, R. H. Taylor, and E. Boctor, "System for robot-assisted real-time laparoscopic ultrasound elastography," in *Proceedings of the SPIE Medical Imaging*, vol. 67, February 2012, pp. 8316–8316.

[91] L. Su, R. E. Link, S. B. Bhayani, W. Sullivan, and C. P. Pavlovich, "Nerve-sparing laparoscopic radical prostatectomy: replicating the open surgical technique," *Urology*, vol. 64, no. 1, pp. 123–127, 2004.

[92] J. E. McNeal, E. A. Redwine, F. S. Freiha, and T. A. Stamey, "Zonal distribution of prostatic adenocarcinoma. correlation with histologic pattern and direction of spread," *The American Journal of Surgical Pathology*, vol. 12, no. 12, pp. 897–906, 1988.

[93] R. J. Cohen, B. A. Shannon, M. Phillips, R. E. Moorin, T. M. Wheeler, and K. L. Garrett, "Central zone carcinoma of the prostate gland: a distinct tumor type with poor prognostic features," *The Journal of Urology*, vol. 179, no. 5, pp. 1762–1767; discussion 1767, 2008.

© Med Sci Monit, 2012; 18(11): CR635-642
PMID: 23111738

Received: 2012.03.21
Accepted: 2012.04.16
Published: 2012.11.01

Ultrasound elastography as a tool for imaging guidance during prostatectomy: Initial experience

Authors' Contribution:
A Study Design
B Data Collection
C Statistical Analysis
D Data Interpretation
E Manuscript Preparation
F Literature Search
G Funds Collection

Ioana Nicolaescu Fleming[1ABCDEF], Carmen Kut[1,2ABCDF], Katarzyna J. Macura[2ABDEG], Li-Ming Su[3ABD], Hassan Rivaz[1ABC], Caitlin Schneider[1ABC], Ulrike Hamper[2D], Tamara Lotan[2C], Russ Taylor[1ADG], Gregory Hager[1ADG], Emad Boctor[1,2ABDEG]

[1] Johns Hopkins University, Baltimore, MD, U.S.A.
[2] Johns Hopkins University School of Medicine, Baltimore, MD, U.S.A.
[3] Department of Urology, University of Florida College of Medicine, Gainesville, FL, U.S.A.

Source of support: This work was supported by: NSF ERC grant EEC9731748, NIH grant 2R42RR019159, and NIH/NCI grant P50CA103175

Summary

Background: During laparoscopic or robotic assisted laparoscopic prostatectomy, the surgeon lacks tactile feedback which can help him tailor the size of the excision. Ultrasound elastography (USE) is an emerging imaging technology which maps the stiffness of tissue. In the paper we are evaluating USE as a palpation equivalent tool for intraoperative image guided robotic assisted laparoscopic prostatectomy.

Material/Methods: Two studies were performed: 1) A laparoscopic ultrasound probe was used in a comparative study of manual palpation versus USE in detecting tumor surrogates in synthetic and *ex-vivo* tissue phantoms; N=25 participants (students) were asked to provide the presence, size and depth of these simulated lesions, and 2) A standard ultrasound probe was used for the evaluation of USE on *ex-vivo* human prostate specimens (N=10 lesions in N=6 specimens) to differentiate hard versus soft lesions with pathology correlation. Results were validated by pathology findings, and also by *in-vivo* and *ex-vivo* MR imaging correlation.

Results: In the comparative study, USE displayed higher accuracy and specificity in tumor detection (sensitivity=84%, specificity=74%). Tumor diameters and depths were better estimated using USE versus with manual palpation. USE also proved consistent in identification of lesions in *ex-vivo* prostate specimens; hard and soft, malignant and benign, central and peripheral.

Conclusions: USE is a strong candidate for assisting surgeons by providing palpation equivalent evaluation of the tumor location, boundaries and extra-capsular extension. The results encourage us to pursue further testing in the robotic laparoscopic environment.

key words: **prostatectomy • laparoscopy • robotics • ultrasonography • elastography**

Full-text PDF: http://www.medscimonit.com/fulltxt.php?ICID=883540

Word count: 3631
Tables: 2
Figures: 7
References: 31

Author's address: Ioana Fleming, 112 Hackerman Hall, 3400 N. Charles Street, Baltimore, MD 21218, U.S.A., e-mail: inicola1@jhu.edu

Background

Prostate cancer is the second leading cause of cancer death and the most common cancer detected in men in the United States. An estimated 217,730 new cases of prostate cancer were diagnosed in the United States, and approximately 32,050 men died of prostate cancer during 2010 [1]. Radical Prostatectomy (RP) aims for complete cancer resection and has been shown to improve cancer survival [2]. Robotic-assisted laparoscopic prostatectomy (RALP) has recently emerged as an alternative to open and laparoscopic procedures. The daVinci Surgical System (Intuitive Surgical, Sunnyvale, CA) provides 3-D visualization, higher magnification, hand tremor elimination and refined dexterity by incorporating wristed instrumentation. From 250 robotic cases in the beginning (2001), the number has reached 73,000 in 2009 (86% of the 85,000 American men who had prostate cancer surgery) [3,4].

Initial experiences with the daVinci surgical system have been positive: short learning curve, limited blood loss, less post-operative pain, favorable complication rates, and short hospital stay [3–10]. Despite fewer perioperative complications and shorter hospital stay, a recent paper found patients were three times more likely to require salvage therapy [11]. One theoretical disadvantage with regards to robotic surgery is the lack of tactile feedback. In open RPs, the surgeon uses his fingers to feel the periphery of the prostate gland [12]. Without tactile feedback, a robotic surgeon is unable to appreciate differences in tissue texture or firmness and therefore may not be able to tailor precisely the extent of tissue excision around the prostate gland in efforts to eradicate all cancerous tissue. Inadvertently leaving residual cancer cells behind, called a positive surgical margin (PSM), is highly associated with cancer recurrence. PSM rates were initially higher in RALP than in the open procedure, but they have been shown to decrease with surgeon's experience and improved technique [9,11].

As manual palpation helps guide the surgeon in the open procedure, an equivalent real-time guiding tool is needed for robotic prostatectomy. Imaging modalities like MRI or CT are not feasible intraoperatively, nor do they possess the sensitivity or specificity for accurate detection and localization of prostate cancer. Transrectal ultrasound (TRUS) is routinely used in diagnosis, in conjunction with digital rectal examination (DRE) and biopsies [13]. One center used TRUS for real-time monitoring and guidance during Laparoscopic RP and reported technical feasibility and enhanced precision by decreased PSM rates [14,15]. TRUS was capable of imaging a substantial percent of nonpalpable prostate cancers. The authors recognized however, the limitations of TRUS guidance; it requires considerable prior expertise and tends to identify primarily hypoechoic lesions, which were just 47% of the cancer nodules studied [15]. Today's prostate cancer patients are more likely to present with echogenic or isoechoic lesions because aggressive screening techniques lead to a shift toward smaller, early-stage cancers [16,17]; classic B-mode gray-scale ultrasound alone cannot identify these lesions.

Ultrasound (US) Elastography (USE) is emerging as a valuable tool in the field of imaging. Elastography is a qualitative technique based on the principle that tissue compression produces strain (displacement) within that tissue; strain is smaller in harder, stiffer tissue than in softer, more compliant tissue [18]. Analyzing the ultrasound raw radio frequency signal results in a strain map, commonly called *elastogram*, where harder tissue is darker than surrounding soft tissue. Cancers tend to present as hard lesions due to increased cellularity [18]. Echogenicity and stiffness of tissue are generally uncorrelated; USE can identify hypoechoic lesions, but also echogenic or isoechoic cancers that classic gray-scale ultrasonography cannot. Elastography through the transrectal approach has already been proven feasible in guiding biopsies of the prostate [19–22]. Integrating USE technology with a laparoscopic ultrasound probe will give robotic and laparoscopic surgeons an important image-guidance tool, which until this point does not exist [23–25].

This paper describes two experiments and results of an ongoing study evaluating the diagnostic accuracy and efficacy of using USE to identify the cancerous nodules in the prostate gland. The aim of the first study was to compare the ability of subjects to detect hard tissue (tumor surrogates) in synthetic and *ex-vivo* phantoms. We attempted to mimic an OR setting of open *vs.* robotic procedures, by asking the subjects to identify properties of the tissue using manual palpation in one arm, versus using ultrasound elastograms in the other arm. The elastograms were obtained with a laparoscopic ultrasound probe. In the second study, human *ex-vivo* prostatectomy specimens where used to assess the accuracy of USE in the identification and characterization of hard cancerous nodules. We compared the elastogram results with histopathology maps (the gold standard) and also to pre- and post-operative MR scans of the prostate gland in order to assess and co-localize anatomically USE with the reference histopathology and MR scans.

Material and Methods

Comparative study for USE *vs.* manual palpation in tumor detection

Institutional Review Board approval was obtained for the comparative study. We recruited N=25 local students to asses human ability to feel hard lesions through palpation, versus elastography's ability to distinguish the same lesions. Our decision to use local students instead of seasoned surgeons stemmed from the rationale that all humans are born with the sense of touch and thus have the innate sensory ability to palpate; we were also able to recruit more subjects in order to assess inter-observer variability. Participants were asked to identify lesions present in both synthetic and *ex-vivo* phantoms. The subjects evaluated the phantoms using manual palpation and ultrasound based elastograms. The hypothesis of the study was that subjects could identify lesions easier on the elastograms versus using manual palpation. Seven synthetic and four *ex-vivo* tissue phantoms were created. The phantoms mimicked the mechanical properties of prostate tissue and the acoustic scattering properties of human tissue. *Synthetic phantoms* exhibited deeper spherical hard lesions, consistent with deeper prostatic cancerous nodules, while *Ex-vivo phantoms* had superficial, free-form ablated lesions, more consistent with extra-capsular cancer extension.

Synthetic phantoms (3×2×2 inches) were made from Liquid Plastic (M-F Manufacturing Co., Inc., Haltom City, TX) and

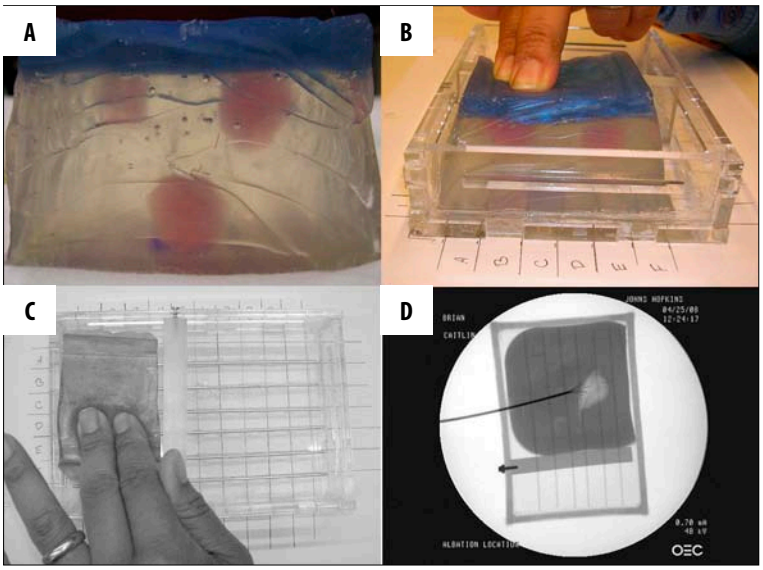

Figure 1. Synthetic phantoms: (**A**) lesions are visible from the side (pink) and the top is opaque (dark blue); (**B,C**) inside the grid calibration container; (**D**) X-ray of *ex-vivo* chicken phantom. Ablation probe, tines and the grid calibration container are visible.

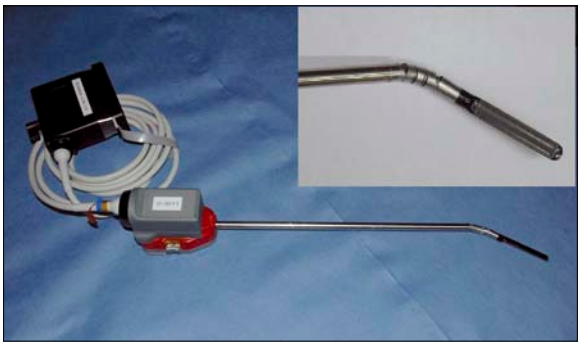

Figure 2. Laparoscopic ultrasound probe; close-up view of the probe's head (insert). Prototype courtesy of Intuitive Surgical.

glass micro-beads. The micro-beads were used as a scattering material. They were added to the plastic mix in an 1% concentration to mimic the acoustic scattering properties of human tissue; both the lesions and the rest of the phantom appeared isoechoic under B-mode ultrasound. Lesions were created by varying the mixing ratios of liquid plastic types; the ratio between 4116S Plastic Softener or 7116 Plastic Hardener and 8116 Super-Soft Plastic determined the final density and the elastic modulus of the lesions and the background [26]. Each phantom contained 0-3 harder spherical lesions (1-2 cm diameter) colored pink for ground truth identification (Figure 1A). The exposed top surface was colored opaque blue, to prevent the subjects from visually identifying the lesions (Figure 1A). The *synthetic phantoms* were sliced and sectioned at study end, following axial planes parallel with the ultrasound scanning plane. The depth of each lesion was measured as the distance between the surface of the phantom and the top of the lesion itself. The final depth of lesions for these 7 (seven) phantoms was measured to be between 7 and 25 mm.

Ex-vivo phantoms were constructed from raw chicken breast tissue. Hard lesions of various diameters were created using radio frequency (RF) ablation, at an average temperature of 95 degrees Fahrenheit for 20 minutes. This formed a hard spherical lesion at a depth of 1–6 mm below the surface, which allowed for possible palpation but not the visual localization of lesions. Before ablation, each tissue was placed in a small plastic container and surrounded by 150 Bloom porcine gelatin (Bloom represents an unit of measure for rigidity of gelatin). X-ray axial scans (projection plane parallel with the ultrasound scanning plane) were used to localize and measure the lesions (Figure 1D). The tissue phantoms were sliced on the same axial plane at study end to determine the depth and extent of the ablated areas. The depth of each lesion was measured as the distance between the surface of the phantom and the top of the lesion itself. For *ex-vivo* lesions, the final depth of lesions was measured to be less than 7 mm.

Hardware and software specification

For the comparative study, a laparoscopic ultrasound probe was used, fitted with a transducer (Gore Tetrad, Englewood, CO) with a center frequency of 7.5 MHz, and 128 elements (Figure 2) [23–25]. Ultrasound raw radio-frequency data was acquired using an Ultrasonix US scanner (Ultrasonix Medical Corporation, Richmond, BC, Canada). Due to the relative inexperience of our subjects, it was not possible to have the subjects perform real-time elastography. Thus, to maintain consistent image quality and to minimize user dependence, elastography images were obtained in a standardized manner by one of our researchers, prior to the evaluation. Elastograms were generated using the corresponding radio frequency data and our dynamic programming (DP) elastography algorithm [27,28].

During the study, each subject reviewed 3–4 phantoms, each placed in a self-designed calibration container, which consisted of a 5-by-5 grid, 0.5 inches apart, labeled with numbers and letters along the two axis (Figure 1B, C). Subjects were asked to identify by manual palpation the location based on the provided grid (i.e. B4 or A3), and also the diameter and depth of each lesion using 0.5 inches as the unit of reference. For the USE arm of the study, the subjects first underwent an USE training session, where they were explained the concept and shown sample elastograms. They were then presented with 3–4 elastograms of the phantoms and they were asked to provide the presence, size and

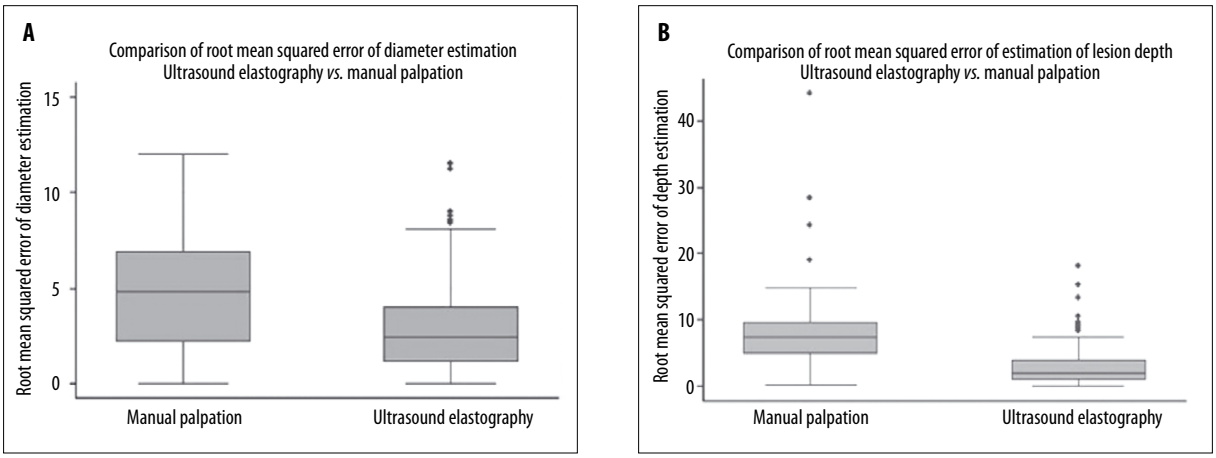

Figure 3. Synthetic phantom study results: Box-and-whisker plots for lesion diameter (**A**) and depth from surface (**B**).

depth of lesions given the scale of the images. The order in which the subjects completed the USE and manual palpation tasks was randomized.

Accuracy was determined descriptively using box and whiskers plots (Figure 3A,B), sensitivity and specificity calculations, and root mean squared error of estimation (RMSE) obtained from subtracting the estimated value of the measured parameter (diameter, depth) from the ground truth value determined from direct measurement. STATA 9 (StataCorp LP, College Station, TX) was used to perform the statistical analysis, which consisted of Student's t-test for comparison between the means of the RMSE of both diameter and depth as estimated via manual palpation versus USE. The p-values reported were generated by t-test calculations assuming unequal variances for a two-tailed test where p=0.05.

Ex-vivo human prostate study for tumor detection

Prostate cancer patients, candidates for prostatectomy, were prospectively enrolled in our study, following an informed consent approved by the Institutional Review Board. The objective of the study was to evaluate the efficacy of using elastography to identify and precisely localize hard nodules such as seen with prostate cancer just beneath the surface of the prostate gland in the peripheral zone. In this area, cancerous lesions are at most risk of invasion beyond the confines of the prostate gland and also more likely to be cut across by a well meaning surgeon. We recruited patients who underwent both open and assisted prostatectomies given that the process of removing the gland was not a focus of our study. Patients underwent multiple radiological procedures. 1) Pre-operative 3 Tesla MRI of the pelvis was performed right before the surgery procedure. 2) Post-operative ultra high-resolution MRI at 9.4 Tesla was performed on the excised prostate specimen to correlate the results to *in-vivo* pre-operative imaging. 3) USE was then performed on the prostate specimen by an experienced radiologist blinded to the surgeon's findings and to the pre-operative pathology report. The collected radio-frequency (RF) data was used offline to recreate classic B-mode grey-scale images, and also to compute elastograms showing the stiffness of the tissue scanned [27,28].

Pre-operative and post-operative MR scans were used for anatomical correlation with the computed elastograms. For

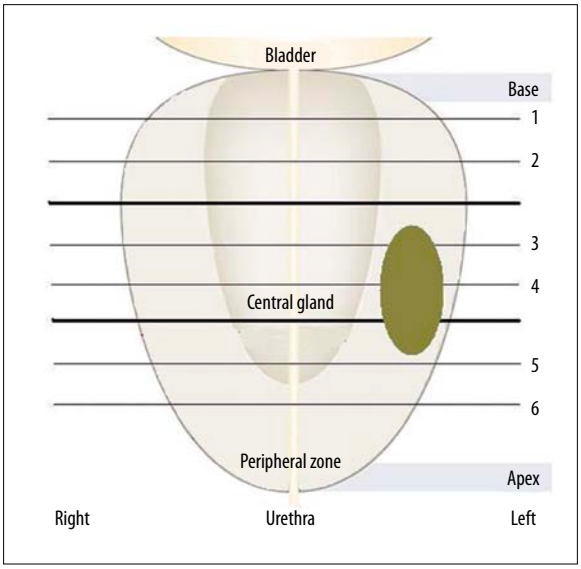

Figure 4. Ultrasound elastography data collection process using the sextant approach; RF data was acquired in axial planes (1–6) from the gland's base towards the apex. For illustration purposes, a lesion is outlined in the left mid section, peripheral zone of the specimen, similar with the case of specimen #3.

USE, the prostate specimens were placed in prone position on a surgical table. USE scans were performed in a systematic sextant approach, similar to that used for image guided biopsies. RF data was acquired in axial planes (from gland's base, through mid gland, to apex) on the left and right side of the gland (Figure 4). The sextant approach was necessary to ensure that the scans were in the same plane with the histopathology diagrams (axial) which constituted the gold standard for comparison. USE coronal scans from the left to the right of the gland were also performed; these scans were in alignment with the MR coronal scans.

Hardware and software specification

For the second study, USE acquisition was conducted using a Siemens Antares US scanner (Siemens Medical Solutions USA, Inc. Ultrasound Division, Issaquah, WA) with an

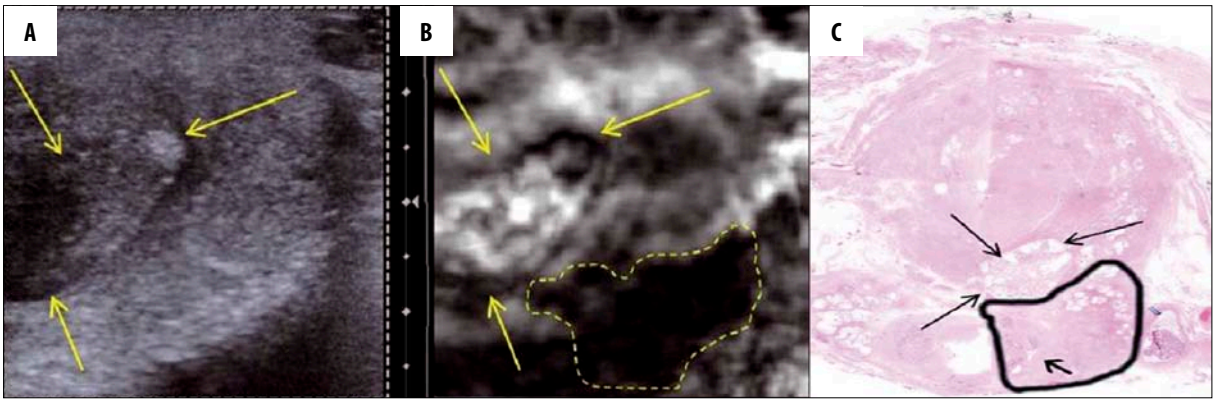

Figure 5. Axial section of prostate specimen #1 peripheral zone. Left lateral section of the prostate's base; classic ultrasound B-mode (**A**) and elastogram (**B**). Hard lesion is outlined, arrows point to adjacent nodule. (**C**) Hematoxylin & eosin stained histological section of prostate base. The tumor (Gleason score 3+5=8, outlined in black) extended beyond the prostatic capsule in this section and invaded the left seminal vesicle (arrow).

Table 1. Table summarizing the experimental results of the palpation study: sensitivity and specificity.

	Manual palpation	Ultrasound elastography
Sensitivity	66%	84%
Specificity	67%	71%
Detection rate <20 mm depth	80%	68%
Detection rate >20 mm depth	0%	66%
Detection rate	80%	84%

ultrasound research interface to access raw RF data. Data was acquired by manual handling using a Siemens VF 10-5 linear array for prostate specimens. After RF data collection, elastograms were obtained using the dynamic programming (DP) elastography algorithm developed in our lab [27,28].

Each prostate specimen underwent routine pathologic processing and analysis. Due to the high volume of prostatectomies performed at our institution, the routine pathological process does not result in a whole mount mapping. Instead, for histopathological evaluation the prostatectomy specimens were initially sliced at every 3–4 mm from apex to base, according to the Stanford protocol. Each slice (6 to 10 master slices) were then incorporated in a paraffin block and sliced at 5 µ meter thickness. The slices were stained with hematoxylin-eosin and were then analyzed under a microscope by a pathologist blinded to the surgeon's findings and also to the elastography results. The localization and size of each tumor focus were documented for all step master slices on axial diagrams, with Gleason score. Large macro photographs were reconstructed in several specimens (Figure 5C). All data collected were stored in the database.

N=10 target areas were analyzed from N=6 patients enrolled so far into the elastography analysis. Histological findings served as the *gold standard* in determining the presence, location and size of any prostatic nodules, malignant and benign. The objective of our study was then to compare axial elastograms findings with the histological findings recorded by the pathologist (mapping diagrams, measurements and nodule characteristics such as malignant *vs.* benign). Since histopathology diagrams often specified just the maximum diameter of a lesion, coronal elastograms were used to better establish the location and extent of the identified lesions. MRI images (both axial and coronal planes) were aligned to the elastograms and provided help with their anatomical co-registration using anatomical details such as urethra or boundaries of peripheral zone *vs.* central gland.

Results

Comparative study for tumor detection

Overall sensitivity and specificity results are summarized in Table 1. USE showed higher accuracy in tumor detection with a sensitivity of 84% and specificity of 71%, compared to a sensitivity of 66% and a specificity of 67% for manual palpation. At depths greater than 20 mm, no subject was able to identify a lesion by manual palpation. 66% of these lesions were correctly identified on elastograms.

Diameter estimation for synthetic phantoms using manual palpation was less accurate than USE (p=0.001) with a root mean squared error of estimation (RMSE) of 4.81 for manual palpation (95% CI between 3.83 and 5.78), versus mean RMSE=3.02 for USE (95% CI between 2.57 and 3.47). For *ex-vivo* phantoms, estimations were comparable in both manual palpation and USE, at a RMSE of about 11.0 mm. Depth estimation for synthetic phantoms was statistically higher using manual palpation than USE (p=0.0001) with a mean value of the RMSE of 8.81 for manual palpation (95% CI between 6.24 and 11.39) versus a mean value of the RMSE=3.02 for USE (95% CI between 2.42 and 3.63) – Figure 3. For *ex-vivo* phantoms, estimations were comparable again for both manual palpation and USE, at a RMSE of about 1.0 mm.

Ex-vivo human prostate study

Elastography identified N=10 lesions, 8 hard nodules in the peripheral zone, 1 hard and 1 soft nodule in the central gland (Table 2). Pathology reports showed 8 of these

Table 2. Prostate specimen data: A total of 10 (ten) elastography lesions were identified in 6 (six) patients' specimens (8 malignant and 2 benign).

#	Location	Gleason score	Size (cm)		
			Elastography	Pathology	MRI
1.1	PZ base	3+5	1.4×0.8	1.3×0.8	1.3×1.1
1.2	CG base	N/A-Solid	0.7×1.1	1.0×1.0	1.0×1.1
1.3	CG base	N/A-Soft	1.1×0.8	1.0×1.0	1.0×0.9
2.1	PZ base	5+3	3.0×1.3	2.4×1.0	2.0×1.5
3.1	PZ mid	4+5	2.4×0.8	1.9×1.0	1.5×1.2
4.1	PZ mid	3+3	1.0×0.5	0.5×0.4	0.6×0.7
4.2	PZ mid	3+4	1.5×0.9	1.1×0.5	1.1×0.8
5.1	PZ apex	3+3	0.5×0.6	0.5×0.5	0.6×0.6
5.2	PZ apex	4+3	0.6×1.0	0.8×0.9	0.9×0.9
6.1	PZ base	3+3	0.7×1.2	0.7×1.8	0.7×0.7

PZ – peripheral zone; CG – central gland.

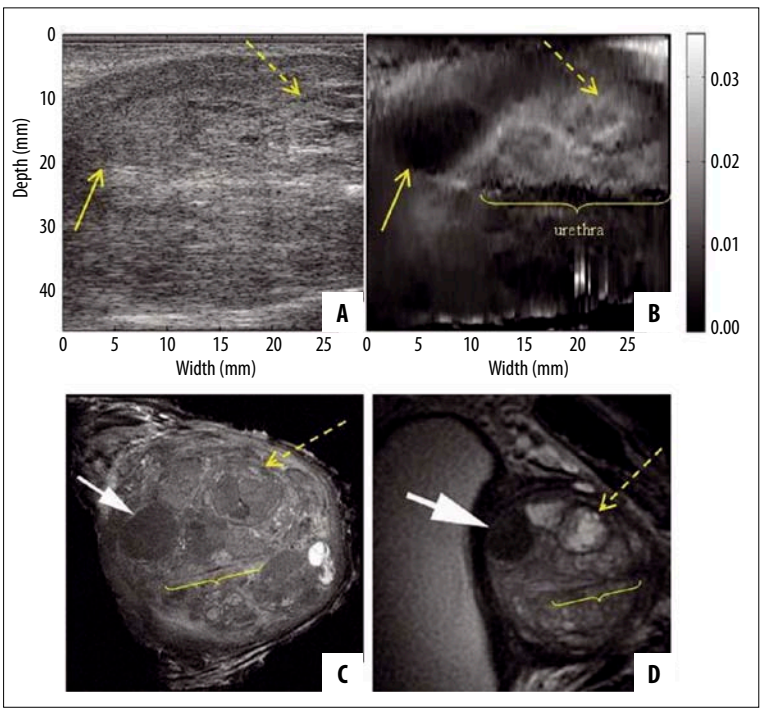

Figure 6. Coronal section of prostate specimen #1 at the level of the central gland. Classic ultrasound B-mode (**A**) and elastogram (**B**). 9.4 Tesla *ex-vivo* (**C**) and 3 Tesla *in-vivo* (**D**) MRI images are presented in coronal planes, in CCW (counter clock wise) orientation for better visualization of the correlation between USE and MRI of the specimen. Benign solid (arrow) and soft (dashed arrow) nodules and urethra are visible.

lesions as malignant and 2 as benign. Diameter measurements correlation proved difficult because of the inability to perfectly register the three investigative modalities. USE and MRI measurements were within on average 2.05 mm *vs.* 2.25 mm of the diameters measured by pathology (standard deviation of 1.9 mm for USE and 2.9 mm for MRI). Size measurements and Gleason score are reported in Table 2.

Specimen #1 presented multiple hard and soft lesions, located in the central gland of the prostate (Figure 6). The *ex-vivo* T2-weighted coronal image from specimen MRI obtained at 9.4 Tesla (Figure 6C) – here in counter clock wise orientation for better visualization of the correlation between USE and MRI of the specimen) shows detailed anatomy of the heterogeneous central gland with a solid benign prostatic hypertrophy nodule (BPH) confirmed by pathology. Elastography was able to detect this solid nodule despite the heterogeneity of the prostate (Figure 6B) – solid arrow, whereas the lesion was not clearly identified by gray scale ultrasound. *Ex-vivo* T2-weighted 9.4 Tesla coronal image from specimen MRI also shows an additional soft cystic BPH nodule (dashed arrow). Urethra is also visible on the elastogram, as well as MRI exam (labeled *urethra*).

Axial scans of the same specimens were compared with histopathology axial cross-sections. The prostate, submitted for

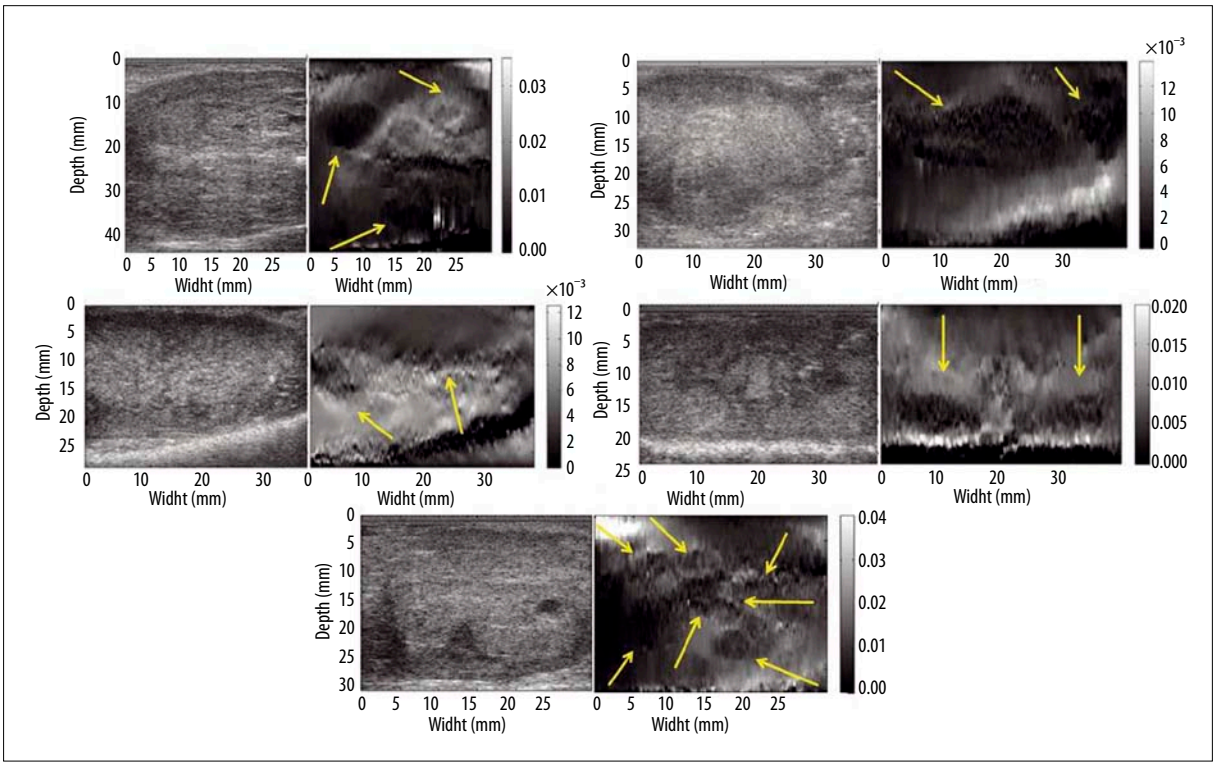

Figure 7. B-mode image (left) and elastogram (right) from specimens # 2–6. Dark regions at the very bottom of elastograms represent structures outside the prostate tissue (e.g. operating table). The border of the prostatic tissue can be easily noticed as a highly reflective band at the bottom of B-mode images.

histological processing in four quadrant sections per slice, was digitally realigned to reconstruct a full histological cross-section (Figure 5C). Specimen #1 was found with a tumor with Gleason score of 8 at the prostate base, left side (outlined). Figure 5A shows an ultrasound B-mode image and an elastogram obtained through an axial plane at the prostate's base on the left side. The same tumor was identified by elastography (Figure 5B – dashed contour) but is not visible on grey-scale ultrasound. For an anatomical correlation, a soft - cystic nodule anterior to cancer can be seen on B-mode image and USE (Figure 5A,B – arrows) and on histopathology (Figure 5C – arrows).

The remaining 5 (five) prostate specimens presented with superficial lesions in the peripheral zone of the gland. USE identified multiple hard malignant lesions in various locations, from the base to the apex of the prostate gland. One can notice the clear delimitations of these lesions on USE (Figure 7) as well as the close estimations of size versus pathology and MRI.

Discussion

In surgical procedures where manual palpation would be helpful but not possible to perform, e. g. laparoscopic robotic surgery, USE can offer added value if proven to be accurate in detecting pathologic lesions. Our comparative study showed USE to be superior to manual palpation in general sensitivity and specificity, and also in identifying deeper lesions. Despite of the inexperience of our subjects with USE and elastogram evaluation, USE demonstrated good performance in detection of hard lesions. This is particularly important as surgeons can be considered inexperienced elastogram readers as well. Our feasibility study showed that USE was able to identify both hard and soft lesions in the *ex-vivo* prostate specimens, located in the deep prostatic central gland and in the peripheral zone. Histopathologic findings validated USE, and results compared favorably with the *in-vivo* pre-surgical and *ex-vivo* post-surgical MRI scans. In the central gland of the prostate, elastography showed excellent detection of hard and soft areas, despite the complexity of the central gland. Elastography was able to identify both hard and soft BPH nodules and anatomical landmarks like the urethra (note excellent anatomical correlation to MR scan findings). In the peripheral zone USE identified multiple hard malignant lesions, from the base to the apex of the prostate gland. These preliminary results demonstrate the ability of USE to detect hard nodules in the prostate and are encouraging in the pursuit of this technology as a palpation equivalent imaging tool for prostatectomy.

USE maps tissue elasticity which makes it an ideal imaging modality to serve as a surrogate and possible equivalence to manual palpation in identifying hard cancerous tissue in the prostate gland, especially in the peripheral zone but also in the central gland. Real-time intra-operative imaging guidance is needed for identifying the presence of cancer within the prostate, especially near the capsule where tumor can invade and spread outside of the gland, and also for studying surrounding structures. If diseased hard lymph nodes could be detected, then lymphadenectomy may provide a more accurate cancer staging, help tailor future therapy, and potentially prevent recurrence. A better delineation of the bladder neck and apex during dissection, especially

when prostate cancer is located at the apex could perhaps improve patients' outcome. If deemed possible, imaging cavernous nerves (CNs) located along the immediate surface of the prostate gland may lead to their preservation, and thus improved preservation of potency and urinary continence [29]. Further more, the development of the elastography technology as an imaging guiding tool during prostatectomy could potentially be useful in the open procedures as well, where the manual palpation would not be enough to identify deeper lesions. It has been documented in the literature that prostate carcinoma originates in the central gland and transitional zone in up to 30% of cases [30,31].

Conclusions

Our initial experience showed USE was able to reliably identify hard nodules in the peripheral zone of the prostate that were prostate cancers. Additionally, USE showed its ability to define tissue hardness of BPH nodules despite the underlying tissue complexity in the central gland. Our comparative study demonstrated USE can approach the efficacy of manual palpation for superficial lesions and has the potential to surpass it for smaller, deeper lesions. We employed a laparoscopic ultrasound probe which was successfully used and tested in conjunction with elastography algorithms. Our initial experience with USE encourages us to pursue further the evaluation of this technique. Further testing of the laparoscopic probe is needed in a real laparoscopic environment. We can conclude that there is promise is integrating laparoscopic ultrasound elastography as a real-time, *in-vivo* imaging tool to guide surgeons during robotic-assisted prostatectomies.

Acknowledgements

We thank our colleagues, surgeon Mohammed Allaf and Naima Carter-Monroe, and also Intuitive Surgical for their help. Ioana Fleming is supported by the Department of Defense Prostate Cancer Predoctoral Fellowship.

References:

1. Jemal A, Siegel R, Xu J, Ward E: Cancer statistics, 2010. CA: A Cancer Journal for Clinicians. 2010; 60(5): 277–300
2. Bill-Axelson A, Holmberg L, Ruutu M et al: Radical prostatectomy versus watchful waiting in early prostate cancer. N Engl J Med, 2011; 364(18): 1708–17
3. Box GN, Ahlering TE: Robotic radical prostatectomy: long-term outcomes. Curr Opin Urol, 2008; 18(2): 173–79
4. Pruthi RS, Wallen EM: Current status of robotic prostatectomy: promises fulfilled. J Urol, 2009; 181(6): 2420–21
5. Nelson B, Kaufman M, Broughton G et al: Comparison of length of hospital stay between radical retropubic prostatectomy and robotic assisted laparoscopic prostatectomy. J Urol, 2007; 177(3): 929–31
6. Artibani W, Fracalanza S, Cavalleri S et al: Learning curve and preliminary experience with da Vinci-assisted laparoscopic radical prostatectomy. Urol Int, 2008; 80(3): 237–44
7. Colombo J, Jose R, Santos B et al: Robotic assisted radical prostatectomy: surgical techniques and outcomes. International Braz J Urol, 2007; 33(6): 803–9
8]. Badani KK, Kaul S, Menon M: Evolution of robotic radical prostatectomy: assessment after 2766 procedures. Cancer, 2007; 110(9): 1951–58
9. Ficarra V, Cavalleri S, Novara G et al: Evidence from robot-assisted laparoscopic radical prostatectomy: a systematic review. Eur Urol, 2007; 51(1): 45–55; discussion 56
10. Berryhill J Roy, Jhaveri J, Yadav R et al: Robotic prostatectomy: a review of outcomes compared with laparoscopic and open approaches. Urology, 2008; 72(1): 15–23
11. Hu JC, Wang Q, Pashos CL et al: Utilization and outcomes of minimally invasive radical prostatectomy. J Clin Oncol, 2008; 26(14): 2278–84
12. Walsh PC, Lepor H, Eggleston JC: Radical prostatectomy with preservation of sexual function: anatomical and pathological considerations. Prostate, 1983; 4(5): 473–85
13. Salomon G, Kllerman J, Thederan I et al: Evaluation of prostate cancer detection with ultrasound real-time elastography: a comparison with step section pathological analysis after radical prostatectomy. Eur Urol, 2008; 54(6): 1354–62
14. Ukimura O, Gill IS, Desai MM et al: Real-time transrectal ultrasonography during laparoscopic radical prostatectomy. J Urol, 2004; 172(1): 112–18
15. Ukimura O, Magi-Galluzzi C, Gill IS: Real-time transrectal ultrasound guidance during laparoscopic radical prostatectomy: impact on surgical margins. J Urol, 2006; 175(4): 1304–10
16. Coley CM, Barry MJ, Fleming C, Mulley AG: Early detection of prostate cancer. Part I: Prior probability and effectiveness of tests. Ann Intern Med, 1997; 126(5): 394–406
17. Daehnert WF, Hamper UM, Eggleston JC et al: Prostatic evaluation by transrectal sonography with histopathologic correlation: the echopenic appearance of early carcinoma. Radiology, 1986; 158(1): 97–102
18. Ophir J, Alam SK, Garra B et al: Elastography: ultrasonic estimation and imaging of the elastic properties of tissues. Proc Inst Mech Eng H, 1999; 213(3): 203–33
19. Cochlin DL, Ganatra RH, Griffiths DFR: Elastography in the detection of prostatic cancer. Clin Radiol, 2002; 57(11): 1014–20
20. Koenig K, Scheipers U, Pesavento A et al: Initial experiences with real-time elastography guided biopsies of the prostate. J Urol. 2005; 174(1): 115–17
21. Sumura M, Shigeno K, Hyuga T et al: Initial evaluation of prostate cancer with real-time elastography based on step-section pathologic analysis after radical prostatectomy: a preliminary study. Int J Urol, 2007; 14(9): 811–16
22. Leven J, Burschka D, Kumar R et al: DaVinci canvas: a telerobotic surgical system with integrated, robot-assisted, laparoscopic ultrasound capability. Med Image Comput Comput Assist Interv, 2005; 8(Pt 1): 811–18
23. Schneider CM, Dachs GW II, Hasser CJ et al: Robot-assisted laparoscopic ultrasound. In: Proceedings of the First international conference on Information processing in computer-assisted interventions. IPCAI'10. Berlin, Heidelberg: Springer-Verlag, 2010; 67–80
24. Schneider CM, Peng PD, Taylor RH et al: Robot-assisted laparoscopic ultrasonography for hepatic surgery. Surgery, 2012; 151(5): 756–62
25. Billings S, Deshmukh N, Kang HJ et al: System for robot-assisted real-time laparoscopic ultrasound elastography. In: Proceedings of the SPIE Medical Imaging, 2012; 67
26. Mansy HA, Grahe JR, Sandler RH: Elastic properties of synthetic materials for soft tissue modeling. Phys Med Biol, 2008; 53(8): 2115–30
27. Rivaz H, Boctor E, Foroughi P et al: Ultrasound elastography: a dynamic programming approach. IEEE Trans Med Imaging, 2008; 27(10): 1373–77
28. Rivaz H, Boctor EM, Choti MA, Hager GD: Real-time regularized ultrasound elastography. IEEE Trans Med Imaging, 2011; 30(4): 928–45
29. Su L, Link RE, Bhayani SB et al: Nerve-sparing laparoscopic radical prostatectomy: replicating the open surgical technique. Urology, 2004; 64(1): 123–27
30. McNeal JE, Redwine EA, Freiha FS, Stamey TA: Zonal distribution of prostatic adenocarcinoma. Correlation with histologic pattern and direction of spread. Am J Surg Pathol, 1988; 12(12): 897–906
31. Cohen RJ, Shannon BA, Phillips M et al: Central zone carcinoma of the prostate gland: a distinct tumor type with poor prognostic features. J Urol, 2008; 179(5): 1762–67; discussion 1767

Surgical Technique

Robot-assisted laparoscopic ultrasonography for hepatic surgery

Caitlin M. Schneider, BS,[a] Peter D. Peng, MD,[b] Russell H. Taylor, PhD,[a] Gregory W. Dachs II, MS,[c] Christopher J. Hasser, PhD,[c] Simon P. DiMaio, PhD,[c] *and* **Michael A. Choti, MD, MBA, FACS,[a]**
Baltimore, MD, and Sunnyvale, CA

Introduction. *This study describes and evaluates a novel, robot-assisted laparoscopic ultrasonographic device for hepatic surgery. Laparoscopic liver surgery is being performed with increasing frequency. One major drawback of this approach is the limited capability of intraoperative ultrasonography (IOUS) using standard laparoscopic devices. Robotic surgery systems offer the opportunity to develop new tools to improve techniques in minimally invasive surgery. This study evaluates a new integrated ultrasonography (US) device with the da Vinci Surgical System for laparoscopic visualization, comparing it with conventional handheld laparoscopic IOUS for performing key tasks in hepatic surgery.*
Methods. *A prototype laparoscopic IOUS instrument was developed for the da Vinci Surgical System and compared with a conventional laparoscopic US device in simulation tasks: (1) In vivo porcine hepatic visualization and probe manipulation, (2) lesion detection accuracy, and (3) biopsy precision. Usability was queried by poststudy questionnaire.*
Results. *The robotic US proved better than conventional laparoscopic US in liver surface exploration (85% success vs 73%;* P = *.030) and tool manipulation (79% vs 57%;* P = *.028), whereas no difference was detected in lesion identification (63 vs 58;* P = *.41) and needle biopsy tasks (57 vs 48;* P = *.11). Subjects found the robotic US to facilitate better probe positioning (80%), decrease fatigue (90%), and be more useful overall (90%) on the post-task questionnaire.*
Conclusion. *We found this robot-assisted IOUS system to be practical and useful in the performance of important tasks required for hepatic surgery, outperforming free-hand laparoscopic IOUS for certain tasks, and was more subjectively usable to the surgeon. Systems such as this may expand the use of robotic surgery for complex operative procedures requiring IOUS. (Surgery 2012;151:756-62.)*

From the Department of Surgery,[a] The Johns Hopkins Hospital; the Department of Computer Science,[b] The Johns Hopkins University, Baltimore, MD; and Intuitive Surgical, Inc.,[c] Sunnyvale, CA

Over the last 2 decades, advances in the operative management of liver malignancies have resulted in increased patient survival. Complete resection of hepatocellular carcinoma or colorectal liver metastasis can now achieve overall 5-year survival of >50%.[1-3] Laparoscopic liver resection is being utilized increasingly, with approximately 3000 published cases worldwide.[4] As observed with laparoscopic approaches in other fields of surgery, the advantages include less postoperative pain, smaller incision scars, and lesser durations of hospitalization.[5-9] Familiarity with both hepatobiliary surgery and advanced laparoscopy are necessary for successful laparoscopic liver surgery. Several recent reports of robotic liver surgery have introduced the potential advantages of the use of robotic assistance in minimally invasive liver surgery.[10,11]

The da Vinci Surgical System (Intuitive Surgical, Mountain View, CA) combines high dexterity telerobotic control of advanced laparoscopic instruments with high-fidelity, 3-dimensional (3D) visualization to give surgeons the ability to perform complex operations through a minimally invasive approach. Experiences in urology and cardiac surgery have already demonstrated outcomes equivalent or better than those of open surgery

Supported in part by NIH STTR Grant R42RR019159 and NSF cooperative agreement EEC9731748, respectively, as well as by internal funds from our institutions.

Accepted for publication July 8, 2011.

Reprint requests: Michael A. Choti, MD, MBA, FACS, Department of Surgery, The Johns Hopkins University School of Medicine, 600 North Wolfe Street, Blalock 665, Baltimore, MD 21287. E-mail: mchoti@jhmi.edu.

0039-6060/$ - see front matter

doi:10.1016/j.surg.2011.07.040

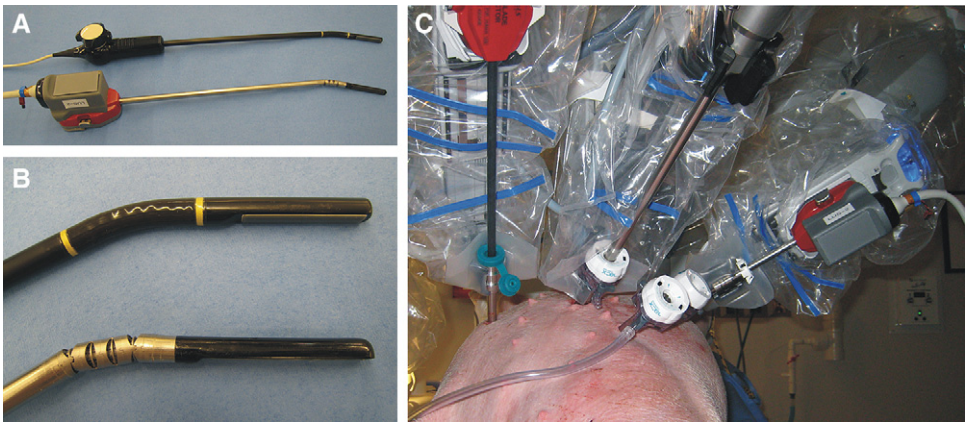

Fig 1. (*A*) An Aloka UST-5536-7.5 hand-held laparoscopic US probe (*top*) and the da Vinci US instrument prototype (*bottom*). (*B*) A close-up of the Aloka (*top*) and da Vinci (*bottom*) transducers and wrists. (*C*) The US instrument manipulated by a da Vinci robotic manipulator.

and similar to laparoscopic surgery.[12,13] Improved ergonomic dexterity and 3D magnified visualization offer advantages over traditional laparoscopy in terms of usability. Robotic assistance may expand the use of minimally invasive techniques in hepatobiliary surgery and the development of additional robotic resection, ablation, and new imaging tools will help to potentiate its adoption.

Both open and laparoscopic liver surgery depends greatly on intraoperative ultrasonography (IOUS) for the evaluation of vascular and biliary anatomy, identification of known and occult intrahepatic lesions, and operative planning.[14-16] Although laparoscopic handheld ultrasonography (US) can be used currently in robotic surgery, we have found it to be a cumbersome approach. The introduction of a practical integrated US instrument may facilitate the wider adoption of robotic liver surgery.

In this study, we describe the development of a high dexterity robotic laparoscopic US tool (RLUS) for the da Vinci surgical robot with integration into our previously described open-source research environment of imaging software.[17,18] Our central goal focuses on the need for an easily usable, integrated, surgical US tool in the robotic environment that expands the application of robotic surgery to hepatobiliary operations. We report the general specifications and capabilities of RLUS and detail comparative experiments comparing the RLUS system with hand-held laparoscopic US in tasks that are encountered in liver surgery.

METHODS

US instrument design. A prototype da Vinci laparoscopic US instrument was developed based on the 5-mm EndoWrist instrument architecture but scaled to a diameter of 10 mm to accommodate an off-the-shelf linear laparoscopic transducer (Gore Tetrad, Englewood, CO). The 5-mm wrist is based on a cable-driven, multilink, snake architecture that—when scaled to 10 mm—is able to accommodate the coaxial cable bundle that is routed through the center of the instrument shaft from the transducer to the system cable interface at the rear of the instrument (Fig 1).

The linear transducer contains 128 elements, has a total array length of 46 mm, and operates at a center frequency of 7.5 MHz. In terms of geometry and imaging performance, the RLUS instrument is similar to standard hand-held laparoscopic probes that are in use today, such as the Aloka UST-5536-7.5 (Aloka America, Wallingford, CT). The articulated wrist provides a 6-degree-of-freedom control of the probe, from the master tool manipulators of the surgical console.

Image visualization. An open-source software framework has been used to display US images, probe status, and guidance information in the stereo display of the robotic surgical console. B-Mode US images can be displayed in a variety of ways:

- A split screen display mode in which the surgeon sees the endoscopic and US views side by side (Fig 2, *A*). To standardize the experiment, this mode was preselected for all subsequent usability experiments.
- A picture-in-picture display mode that insets the US image into the endoscopic view. In this configuration, the surgeon is able to select the position and size of the inset image by manipulating the master tool manipulators within the console—this is a user interface feature that is provided by a 3D user interface module implemented within the software library.

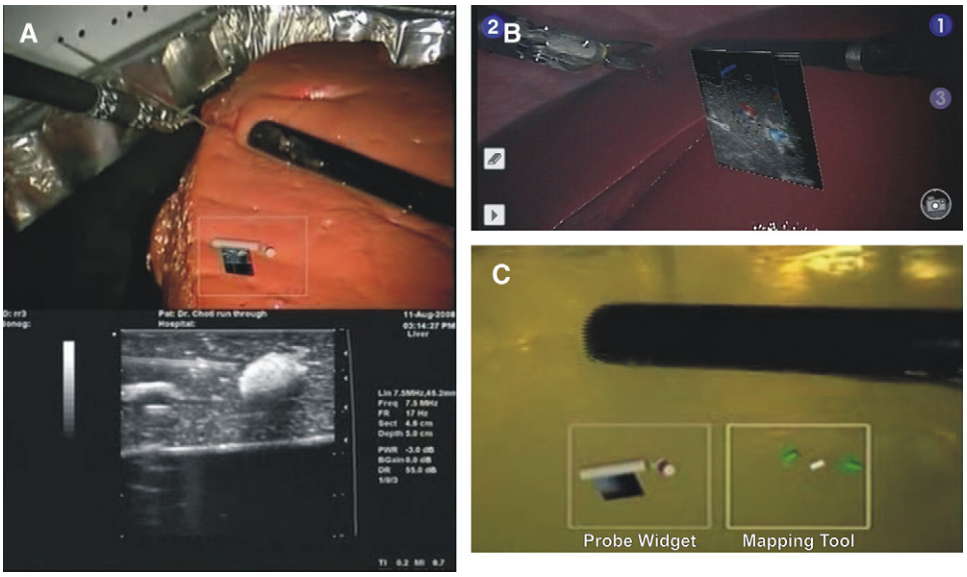

Fig 2. (*A*) A split-screen display that shows the endoscopic view (*top*) and the US image (*bottom*) adjacent to one another in the surgical console. (*B*) The US "flashlight" overlay. (*C*) The display overlays for visualizing probe orientation (probe widget tool) and for mapping probe waypoints (mapping tool).

- A "flashlight" display mode in which the US image is overlaid onto a 3D representation of the imaging plane in the stereo view of the console. The effect of this mode is to display the US image in the plane in which it is physically acquired by the transducer, such that the image is co-located with the view of the tissue that is being imaged in the surgical field. Issues of automatic calibration and image-probe registration were addressed in our prior work with a nonarticulated probe[17] (Fig 2, *B*).

In addition to the image overlay, the system displays a graphic representation of the probe, imaging plane, and wrist configuration at the lower margin of the endoscopic view. This graphic widget provides the user with cues for orienting the imaging plane of the probe, as well as for avoiding wrist range of motion limits, particularly when the US probe fills the field of view of the endoscope and the wrist is not visible (Fig 2, *C*).

Usability experiments. A usability study was conducted to evaluate the performance of the RLUS and compare it with a conventional handheld laparoscopic device. The study was approved through The Johns Hopkins University Institutional Review Board, and there were no protocol violations. Board-certified/eligible surgeons with experience in laparoscopy and IOUS met enrollment criteria. A total of 10 subjects participated in the study: 7 completing the full protocol and 3 completing only lesion-finding tasks.

Table I. Methods: task categories and score weighting

	%
Imaging and anatomic structure identification	
Liver surface exploration	27
Anatomy identification	55
Tool manipulation	9
Image quality	9
Lesion detection	
Number of lesions found	33
Accuracy of volumetric measurement	33
Self-assessed confidence in lesion finding	33
Needle biopsy guidance	
Number of positive biopsies	33
Number of access attempts	33
Total time needed	33

Hepatic surgery was the focusing application and specific tasks were based on surgical relevance and difficulty with traditional laparoscopic techniques. As categorized in Table I, the tasks included: (1) general quality of liver surface accessibility, volume imaging, and intrahepatic anatomic structure identification (n = 7); (2) lesion detection (n = 10); and (3) needle biopsy guidance (n = 8). The time to complete each task was recorded, in addition to other specific measures related to the successful completion. A short period of practice was allowed for each task. The task was explained in detail before beginning and all questions from the

subjects were answered at this time. Each task was completed with both the RLUS and the handheld laparoscopic US. The order of instrument usage was randomized. A questionnaire assessing instrument usability was administered immediately after completion of the tasks.

Task 1: Imaging and anatomic structure identification: Subjects were asked to manipulate the US probe over the entire exposed anterior surface of in vivo porcine liver while imaging as much of the liver volume as possible. They were then asked to identify and image-capture specific hepatic structures in 2 views: The portal vein confluence, hepatic vein confluence, inferior vena cava, and gallbladder. Still images and video recordings were captured and subsequently scored blinded by expert observers. Anatomic identification accounted for 24 out of 44 possible points in this task, with greater weight owing to complexity of subtask. Liver surface exploration was scored out of 12 points, and both tool manipulation and image quality were scored out of 4 points.

Task 2: Lesion detection: Ex vivo study with phantoms were constructed of PVC plastic as described previously.[19] Briefly, both hypoechoic and hyperechoic lesions were constructed with glass microspheres. Varying in echogenicity, depth, and size, 1–8 lesions were placed in each phantom. Subjects were provided a phantom without knowledge of the number of lesions contained. They were then asked to identify and measure all lesions as accurately and rapidly as possible. The score for this task was compiled from (1) the number of lesions found within each phantom, (2) the accuracy in lesion volumetric measurements, and (3) the self-assessed confidence in finding all lesions. Each category was scored out of 12 points for a total task score of 36 possible points.

Task 3: Needle biopsy guidance: This task simulated clinical US-guided needle-based tasks, such as tumor biopsy and ablation. Phantoms were developed from ex vivo bovine liver and target 1-cm lesions created using intraparenchymally injected dental alginate polymer.[20] The liver phantom was then placed in a visually shielded torso model. Subjects were asked to guide and perform a core biopsy of the target lesion using a spring-loaded biopsy gun, conducted either using robotic or free-hand laparoscopic assistance. This task was scored as successful on recovery and visual inspection of white alginate material within the biopsy core. Overall score was compiled from the sum of 3 categories: (1) number of positive biopsies, (2) number of access attempts, and (3) total time necessary to acquire biopsies. Each category was scored out of 12 for a total possible score of 36 for this task.

Statistical analysis. Each score was calculated, and the subtasks were compiled into task scores as described previously. The weighting for the subtasks reflected the importance and measurement accuracy in each grouping. The mean and standard deviations were calculated for each task. Paired *t* test comparison was performed for each subtask and task group.

Questionnaire. Study subjects were administered a survey immediately after completion of the US simulation tasks. This questionnaire was composed of 14 questions comparing robotic versus conventional handheld laparoscopic US devices for usability, ergonomics, and effectiveness. The survey aimed to address the subjective experience of the subject when using the 2 devices.

RESULTS

US task completion experiment. The findings from the task performance between RLUS and conventional handheld laparoscopic IOUS are summarized in Table II.

Task 1: For imaging and anatomic identification tasks, the RLUS scored greater in several subtask categories including liver surface exploration (85% vs 73%; $P = .030$) and tool manipulation (79% vs 57%; $P = .028$). The RLUS had similar ability anatomic identification (76% vs 62%; $P = .12$). There was no difference in time for surface exploration between the 2 groups.

Task 2: The RLUS demonstrated no difference in scoring for the remainder of the tasks. For lesion detection tasks, the RLUS and handheld laparoscopic US scored similarly (72% vs 71%NS). There was no difference in questionnaire assessed confidence in lesion identification (73% vs 70%). The time for completing lesion identification was greater when using the RLUS (mean, 10.7 vs 7.9 minutes; $P = .008$); however, there was no difference in the time for lesion volume assessment (6.1 vs 7.1 minutes; $P = .11$).

Task 3: For needle biopsy guidance tasks, the RLUS did not demonstrate significant performance differences. These tasks included confidence in positive biopsy (64% vs 60%), positive biopsy (50% vs 42%), and number of punctures needed for successful biopsy (2.7 vs 4.6; $P = .11$). There was no difference in time to completion for biopsy tasks between RLUS and handheld laparoscopic US.

As depicted in Fig 3, the RLUS was comparable to the handheld laparoscopic US in surface exploration, tool manipulation, and anatomic

Table II. Results: task scoring, averages, standard deviations and statistical comparison

Task	*da Vinci mean ± σ [%]*	*Handheld mean ± σ [%]*	P-*value*
Task 1: imaging and anatomic structure identification			
Liver surface exploration	85 ± 9	73 ± 13	.03
Anatomy identification	76 ± 14	62 ± 11	NS
Tool manipulation	79 ± 9	57 ± 19	.028
Image quality	93 ± 12	96 ± 10	NS
Combined imaging task score	80 ± 7	68 ± 8	.026
Task 2: lesion detection			
Lesions found	72 ± 16	71 ± 11	NS
Lesion volume error	28 ± 11	32 ± 14	NS
Confidence in lesion identification	73 ± 15	70 ± 21	NS
Overall lesion task score	63 ± 16	58 ± 18	NS
Task 3: needle biopsy guidance			
Confidence in positive biopsy	64 ± 21	59 ± 19	NS
Positive biopsy	50 ± 36	42 ± 30	NS
Average number of punctures	2.7 ± 2.1	4.6 ± 3.8	NS
Overall biopsy task score	57 ± 20	48 ± 20	NS

NS, Not significant.

identification, and required a similar number of requisite passes for successful biopsy.

Questionnaire. All 10 subjects completed the questionnaire after the US task experiments. All subjects had extensive laparoscopic experience (>30 cases) and 40% of subjects had moderate experience (>15 cases) with laparoscopic US. The RLUS was noted by the majority of subjects to be associated with better positioning (8/10), more comfortable (6/10), greater confidence in lesion finding (8/10), less fatigue inducing (9/10), and an overall more useful tool (9/10). The RLUS was associated with less fatigue, increased ergonomic comfort, and improved lesion identification among the subjects. Overall, 9 out of 10 subjects identified the robotic US as the more useful imaging tool in the study. A sample of comments from the questionnaire noted that subjects "loved the mapping and measurement tools" and thought the "design was excellent"; however, the RLUS was limited by "no tactile feedback" and "although scanning/screening was more rapid with the (handheld) laparoscopic US device, I had sense that I was/could be more thorough with the robot."

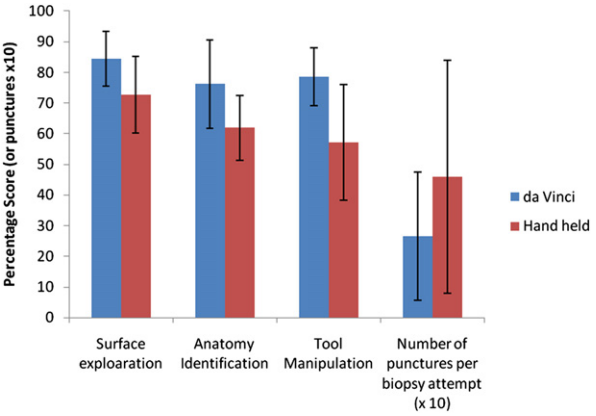

Fig 3. Comparison of the da Vinci and handheld laparoscopic US for liver surface exploration, intrahepatic vascular anatomy identification, tool manipulation, and number of punctures needed for successful biopsy (scaled, ×10, s.d.).

DISCUSSION

IOUS plays an important role in both open and laparoscopic liver surgery. Studies have demonstrated the importance of IOUS in the identification of occult metastases or undetected vascular invasion, which can change the operative plan or identify unresectable disease in up to 50% of patients.[21-23] The recent development of laparoscopic and robotic liver surgery has increased the importance of IOUS, as manual palpation and direct visualization are impaired. Although laparoscopic IOUS has been effective in assessing liver for operative planning, there are some constraints to its use.[24] The limitations include restricted angulation, torque required to maintain surface contact, fewer degrees of freedom for orientation, and difficulty in optimizing probe alignment for biopsy or ablation.

Although laparoscopic liver surgery is becoming an increasingly common operative approach for the management of various benign and malignant tumors, the limitations of laparoscopic US are

restricting. The advantages of laparoscopic liver surgery parallel those seen in other minimally invasive operative procedures, including decreased postoperative pain, lesser duration of hospitalization, and shorter incisions.[25] Success depends on advanced surgical expertise in hepatobiliary surgery and laparoscopic surgery; however, the inherent ergonomic restrictions of laparoscopy continue to limit its use and is very operator dependent.

Robot-assisted liver surgery allows for high-dexterity control and 3D visualization, and retains the advantages of minimally invasive access. Although robot-assisted liver surgery may potentially be more effective than the laparoscopic approach, it is similar to laparoscopic liver surgery in that is relies heavily on laparoscopic US for intraoperative assessment and planning. Certain constraints limit the use of a separate laparoscopic US in robotic operations, including lack of probe mobility, maneuverability, and image incorporation onto existing displays. With the absence of a dedicated robotic US, currently the limitations of laparoscopic US persist.

We have developed a dedicated robotic US and evaluated its utility in simulated liver surgery tasks. With the loss of tactile feedback in robotic surgery, the use of intraoperative US is essential for operative planning. The robotic US device was developed as an integrated instrument with those previous limitations in mind. Our experiments comparing the robotic US with conventional laparoscopic US found the robotic US to be more ergonomic, associated with less user fatigue, and associated with improved liver exploration and instrument manipulation. Additionally, we have developed additional features for the robotic US system, including image fusion with picture-in-picture, robust measurement tools, and dropped virtual markers, which leverage the advantages of increased integration and kinematic tracking. Although the robotic US required more time for completion of one of the tasks, further studies may define learning curve improvements and whether the increase in time is associated with improved liver US exploration. Future studies may also investigate its utility in urologic, gynecologic, endocrine, and pancreatic robotic procedures. This system can also facilitate the clinical transition of more advanced IOUS imaging tools such as US elastography for intraoperative ablation monitoring.[26]

The authors acknowledge Dr. Emad Boctor for his assistance during the development of this work.

REFERENCES

1. Pawlik TM, Schulick RD, Choti MA. Expanding criteria for resectability of colorectal liver metastases. Oncologist 2008; 13:51-64.
2. Choti MA, Sitzmann JV, Tiburi MF, et al. Trends in long-term survival following liver resection for hepatic colorectal metastases. Ann Surg 2002;235:759-66.
3. Palavecino M, Chun YS, Madoff DC, et al. Major hepatic resection for hepatocellular carcinoma with or without portal vein embolization: perioperative outcome and survival. Surgery 2009;145:399-405.
4. Nguyen KT, Gamblin TC, Geller DA. World review of laparoscopic liver resection-2,804 patients. Ann Surg 2009;250: 831-41.
5. Dagher I, Belli G, Fantini C, et al. Laparoscopic hepatectomy for hepatocellular carcinoma: a European experience. J Am Coll Surg 2010;211:16-23.
6. Aldrighetti L, Guzzetti E, Pulitano C, et al. Case-matched analysis of totally laparoscopic versus open liver resection for HCC: short and middle term results. J Surg Oncol 2010;102:82-6.
7. Aldrighetti L, Pulitano C, Catena M, et al. A prospective evaluation of laparoscopic versus open left lateral hepatic sectionectomy. J Gastrointest Surg 2008;12:457-62.
8. Nanashima A, Sumida Y, Oikawa M, et al. Usefulness and limitation of laparoscopic assisted hepatic resections: a preliminary report. Hepatogastroenterology 2009;56: 447-51.
9. Polignano FM, Quyn AJ, de Figueiredo RS, Henderson NA, Kulli C, Tait IS. Laparoscopic versus open liver segmentectomy: prospective, case-matched, intention-to-treat analysis of clinical outcomes and cost effectiveness. Surg Endosc 2008;22:2564-70.
10. Giulianotti PC, Coratti A, Sbrana F, et al. Robotic liver surgery: results for 70 resections. Surgery 2011;149:29-39.
11. Berber E, Akyildiz HY, Aucejo F, Gunasekaran G, Chalikonda S, Fung J. Robotic versus laparoscopic resection of liver tumours. HPB (Oxford) 2010;12:583-6.
12. Modi P, Rodriguez E, Hargrove WC III, Hassan A, Szeto WY, Chitwood WR Jr. Minimally invasive video-assisted mitral valve surgery: a 12-year, 2-center experience in 1178 patients. J Thorac Cardiovasc Surg 2009;137:1481-7.
13. Patel VR, Palmer KJ, Coughlin G, Samavedi S. Robot-assisted laparoscopic radical prostatectomy: perioperative outcomes of 1500 cases. J Endourol 2008;22: 2299-305.
14. Lai EC, Tang CN, Ha JP, Tsui DK, Li MK. The evolving influence of laparoscopy and laparoscopic ultrasonography on patients with hepatocellular carcinoma. Am J Surg 2008; 196:736-40.
15. Machi J, Sigel B, Zaren HA, Kurohiji T, Yamashita Y. Operative ultrasonography during hepatobiliary and pancreatic surgery. World J Surg 1993;17:640-5.
16. van Vledder MG, Pawlik TM, Munireddy S, Hamper U, de Jong MC, Choti MA. Factors determining the sensitivity of intraoperative ultrasonography in detecting colorectal liver metastases in the modern era. Ann Surg Oncol 2010;17: 2756-63.
17. Leven J, Burschka D, Kumar R, et al. DaVinci canvas: a telerobotic surgical system with integrated, robot-assisted, laparoscopic ultrasound capability. Med Image Comput Comput Assist Interv 2005;8:811-8.
18. Schneider CM, Dachs GW, Hasser CJ, et al. Robot-Assisted Laparoscopic Ultrasound, in Information Processing in

Computer-Assisted Interventions (IPCAI). Geneva; June 23, 2010. pp. 67-80.
19. Mansy HA, Grahe JR, Sandler RH. Elastic properties of synthetic materials for soft tissue modeling. Phys Med Biol 2008;53:2115-30.
20. Bush NL, Hill CR. Gelatine-alginate complex gel: a new acoustically tissue-equivalent material. Ultrasound Med Biol 1983;9:479-84.
21. Bismuth H, Castaing D, Garden OJ. The use of operative ultrasound in surgery of primary liver tumors. World J Surg 1987;11:610-4.
22. Parker GA, Lawrence W Jr, Horsley JS III, et al. Intraoperative ultrasound of the liver affects operative decision making. Ann Surg 1989;209:569-76.
23. Makuuchi M, Hasegawa H, Yamazaki S, Takayasu K, Moriyama N. The use of operative ultrasound as an aid to liver resection in patients with hepatocellular carcinoma. World J Surg 1987;11:615-21.
24. Jakimowicz JJ. Intraoperative ultrasonography in open and laparoscopic abdominal surgery: an overview. Surg Endosc 2006;20(Suppl 2):S425-35.
25. Nguyen KT, Marsh JW, Tsung A, Steel JJ, Gamblin TC, Geller DA. Comparative benefits of laparoscopic vs open hepatic resection: a critical appraisal. Arch Surg 2011;146:348-56.
26. Van Vledder MG, Boctor EM, Assumpcao LR, et al. Intraoperative ultrasound elasticity imaging for monitoring of hepatic tumour thermal ablation. HPB (Oxford) 2010;12:717-23.

Ultrasound Elastography Mosaicing

****

****

Abstract. Panoramic ultrasound imaging is emerging as a prevalent technique in clinical practice with a high clinical value. In the literature of ultrasound mosaicing, registering the underlying displacement field for elastography has not yet been addressed. The clinical advantages of ultrasound mosaics can be improved with the additional corresponding strain information. In this paper, we propose a technique for generating a reliable, wide field-of-view displacement field, robust to sources of decorrelation. Elastography mosaics are generated from two pairs of ultrasound images, and then from multiple image pairs. Tissue mimicking phantom data is used for the validation of the multi-image elastography mosaic. Finally, the method is extended to 3D ultrasound elastography mosaicing using multiple 3D volume pairs.

1 Introduction

Compared to other imaging modalities like CT and MR, ultrasound suffers from a limited field of view. Monitoring a structure can be particularly challenging when it is too large to be visualized in a single image or 3D sweep. Size and distance measurements are unreliable in large organs. Panoramic imaging is emerging as a prevalent technique used in widening the field of view (FOV) of medical ultrasound images. Also referred to as stitching or panorama, the ultrasound mosaic aims to achieve several clinical advantages which come along with extended FOV: 1) improving the understanding of spatial relationships among structures when the size of a single image/volume is not large enough to cover the entire area, 2) allowing for measurements of size and distance in large organs and lesions, 3) allowing multi-modal registration and fusion with pre-operative data for guidance in minimally-invasive interventions.

Ultrasound elastography is a technique first proposed two decades ago by [1] for the clinical imaging of tissue stiffness. Numerous clinical applications have been investigated, among them cancer imaging [1], ablation monitoring [2], and the detection and grading of deep vein thrombosis [3]. In this work we focus on extended FOV displacement estimation for quasi-static ultrasound elastography. The tissue is imaged while it is slowly deformed using an external mechanical force and the images are used for the estimation of tissue motion or displacement [1]. Elastography maps the mechanical properties of tissue which can add valuable features to the B-mode panorama. Many clinical applications deal with large cancerous lesions which expand beyond the span of one ultrasound image [4]. An ultrasound elastography mosaic can improve the understanding of the size of the

lesion and its layout among surrounding structures. In the ablation of hepatic cancerous tissue, the size of the HIFU-induced ablative lesions often exceeds 4 cm in diameter, which is the width of a typical ultrasound transducer. Thermal lesions are not visible in conventional B-mode ultrasound but a panoramic ultrasound elastogram can help visualize the entire extent of the ablation [2], monitoring and insuring all cancerous tissue is ablated. In the assessment of venous thrombi, a combination of ultrasound B-mode and Doppler imaging help detect the presence of the blood clot, but it is elastography which can provide its age and clinical grading [3]. An in-plane ultrasound elastography mosaic can provide mapping of the thrombi all along the femoral vein. It could take up to eight mosaiced volumes to depict an entire organ like the liver or kidney [5], but having the corresponding elastography mosaic would allow for registration with pre-operative imaging data (CT or MRI) which would help with intra-operative navigation. Although the basics of medical elastography have long been defined, new clinical applications are constantly emerging are we are seeing an increasing commercial and clinical interest.

Multiple approaches have been published in the literature on 2D and 3D wide FOV ultrasound mosaics [6, 5, 7, 8], but very little of it concerns registering the underlying strain field. As various sources of decorrelation are usually affecting the computation of strain images, this problem becomes even more important when attempting to generate a unified, wide displacement field. Further more, most elastography algorithms result in qualitative strain; 2 image pairs with even very slightly different degrees of compression will produce 2 strain images in which different structures could be visible. Another problem rises in the ambiguity of the interpretation of strain images: low strain can be indicative of high stiffness but this interpretation may not be the right one if the stress field is not uniform throughout the tissue [1, 9]. To address these issues and to improve the quality of strain images, several metrics of stability, consistency/persistency and reliability have been developed [10–12]. In these paper we propose using similar techniques to select a stable pair of RF lines which will become the *seed* for generating a reliable, wide FOV displacement field. Displacement on the *seed* line is calculated using dynamic programming and later propagated in both lateral directions of the mosaic using an analytic minimization approach [13]. Each new image pair adds to the unified displacement field. Here we present tissue mimicking phantom data for 2D validation. Finally, the method is extended to 3D ultrasound elastography mosaicing using multiple 3D volume pairs.

2 Methodology

Consider a sequence of radio frequency (RF) data (Im_{11}, Im_{12}) collected at position t_0, before and after the compression of tissue using a 2D ultrasound transducer (Fig. 1b). Each sequence contains n RF lines of length m. A second sequence (Im_{21}, Im_{22}) is collected (Fig. 1c) after the transducer has been moved in the lateral direction of the probe to position t_1, with the help of a moving stage (Fig. 1a). A vertical stage was used to achieve an almost identical compression

rate between the two sequences. The translation between the 2 image sequences is:

$$T_{lines} = T_{mm} * n/w \tag{1}$$

where w is the width of the ultrasound transducer in millimeters (mm), n is the number of RF lines, T_{mm} is the ground truth translation in mm as read on the stage and T_{lines} is the corresponding translation as number of RF lines. The overlap area consists of (n - T_{lines}) RF lines (Fig. 1d).

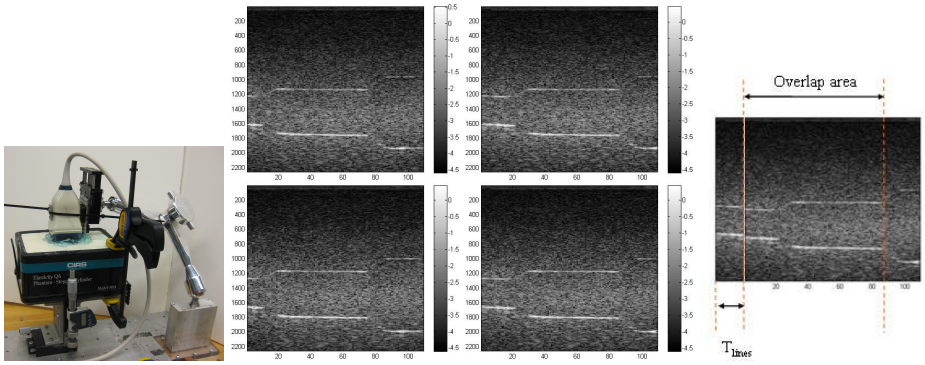

(a) (b) (c) (d)

Fig. 1. Experimental setup (a). Bmode ultrasound data before and after compression for (b) position t_0, and (c) position t_1. Translation T_{lines} and the length of the overlap area are shown in (d).

Pairwise Mosaicing In Analytic Minimization (AM) elastography [13], 2D integer displacements are first obtained using dynamic programming (DP) on a single pair of RF lines and are later propagated to produce 2D subsample displacements for the entire image. For pairwise mosaicing we aim to find a robust and stable *seed* RF line pair in the overlap area, which also gives consistent DP integer displacement results in the two sequences. The displacement estimate on the *seed* line will serve as initial guess in the AM propagation. The pairwise strain mosaicing is implemented as follows:

1. Robustness and stability measures are used to identify in the overlap area a suitable *seed* RF line for the mosaicing algorithm, similarly to [12]. The process filters those candidates which exhibit a high degree of decorrelation (Figure 2):
   - $k = 5$ $(i_1, i_2, ..., i_5)$ random corresponding positions (RF line pairs) are selected from the overlap area (Fig. 3-1).
   - Compute integer axial displacement for each RF line pair using the dynamic programming approach [13]: $(a_1^1, a_2^1, ..., a_5^1)$ and $(a_1^2, a_2^2, ..., a_5^2)$ (Fig.

3-2). Note: in this step, both axial and later integer displacements are computed, but from here on only axial displacement values will be used.
- In a continuous piece of tissue, the axial displacement profile resulting from a stress field induced by applied compression has a monotonous ramp [14]. A pair of decorrelated RF lines would affect the DP displacement estimation algorithm. Instead of a globally optimal solution, the estimate could exhibit regions of locally optimal solutions. For small deformations, these locally optimal solutions would correspond to perturbations in the monotonously decreasing slope of their displacement profile, which in turn could result in *artifacts* in the final strain image. If three or more positions along the displacement profile would exhibit a continuous change in the slope of displacement, this could point to a region of poorly correlated data.
- For the remaining positions which satisfy the monotonous slope criterion,

$$d_k = abs(a_k^1 - a_k^2); avg_k = mean(d_k); std_k = stdev(d_k) \tag{2}$$

We select the *seed* RF line s as the position with the minimum std_k and $avg_k < 1$.
- At the end of the subinteger displacement estimation process on the a pair of RF lines, $A_i = a_i + \Delta a_i, L_i = l_i + \Delta l_i$ are the axial and lateral displacements at each sample i. The magnitude of the normalized cross-correlation could be used to assess the degree of matching between the pre- and post-compression data.

$$C(I_1(s), I_2(s)) = \left| \frac{\sum_m^{i=1}(I_1(i,s)-\bar{I}_1)(I_2(i+A_i,s+L_i)-\bar{I}_2)}{\sqrt{\sum_m^{i=1}(I_1(i,s)-\bar{I}_1)^2 \sum_m^{i=1}(I_2(i+A_i,s+L_i)-\bar{I}_2)^2}} \right| \tag{3}$$

where $\bar{I}_1$ and $\bar{I}_2$ are the means of RF values along the *seed* line s. The value of C could be used as an additional check to verify if the displacement estimate for the selected *seed* line is a good fit. If C value would fall below a certain threshold (to be established by the user), the *seed* line would be deemed not suitable and the next stable *seed* line would be selected (Fig. 3-3).

2. Subinteger displacement values are calculated for *seed* line s (Fig. 3-4).
3. The subinteger displacement values are propagated using AM:
   - in one sequence towards the first RF line, and
   - in the second sequence towards the last RF line.

   The unified displacement field will have $n + T_{lines}$ RF lines and the stitch will be around RF line number $s + T_{lines}$ (Fig. 3-5).
4. Generate the ultrasound elastography mosaic from the unified displacement field (Fig. 3-6).

Multi-image Mosaicing Given an existing n_t wide displacement map, computed for image pairs 1 through t, we expand our displacement map to include information from image pair $t + 1$ as follows:

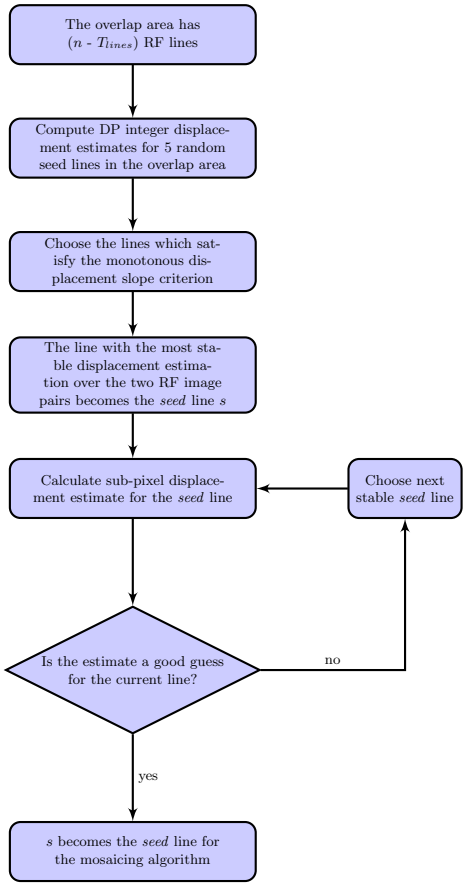

Fig. 2. Robust *seed* selection method.

1. Compute the translation T_{lines}^{t+1} between position t and position $t+1$ and the overlap area.
2. Select the *seed* RF line s_{t+1} in the new overlap area.
3. Use the subinteger values form the wide FOV displacement map at RF line number $s_{t+1} + T_{lines}$ as *seed* values to propagate using AM:
   − in the new sequence towards the first RF line.
   Stitch the newly computed $(s_{t+1} + T_{lines})$ lines at the beginning of the previous displacement map. The new mosaiced displacement field will have $n_t + T_{lines}^{t+1}$ RF-lines.
4. Generate the new ultrasound elastography mosaic from the updated displacement field.

Multi-volume Mosaicing In the three-dimenssional case, consider a pair of RF volumes (V_{11}, V_{12}) collected at position t_0, before and after the compression

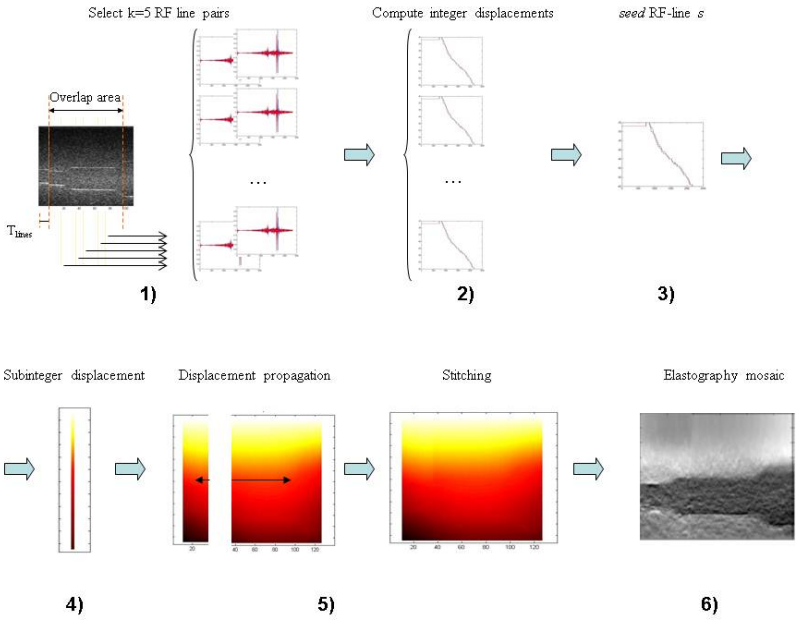

Fig. 3. Pairwise Mosaicing workflow: $k = 5$ random RF positions are selected (1), integer displacement is calculated for each position (2), the *seed* RF-line s is selected (3), subinteger displacement values are calculated for s (4), propagated in the 2 sequences and stitched (5). The ultrasound elastography mosaic is generated from the displacement field (6).

of tissue using a 3D ultrasound wobbler transducer. Each volume contains k frames and each frame has n RF-lines of length m. One or more subsequent pairs of volumes are collected after the wobbler transducer is moved in the lateral direction of the probe with the help of a moving stage. Once again, a vertical stage was used to achieve an almost identical compression rate between the two sequences. Using the lateral and axial stages ensures the first frame of the first volume pair is alligned with the first frame of each subsequent pair volume, and all the other frames are simillarly aligned, with no out-of-plane motion between each position. The same steps of multi-image mosaicing can be applied on a frame by frame basis, resulting in a unified displacement field for each elevational position of the wobbler motor.

Note: here we present a very controlled way of acquiring 3D ultrasound data for the purpose of building 3D strain mosaics. In a routine 3D ultrasound exam, using stages to control the imaging of a certain human tissue is absolutely not feasibile. This does not, however invalidate our framework. As electromagnetic trackers become integrated into ultrasound transducers, it is feasibile to select ultrasound volumes consisting only of aligned frames with no out-of-plane rotation. The work presented here makes a case for in-plane mosaicing where translation is the only component of the transformation. One can easily envision an ultrasound

system equipped with a tracked transducer like in the Foroughi set-up [15]. Here we used a controlled setup for proof of concept, but using the Foroughi method [15] one could achieve a 3D elastography mosaic as follows:

1. Perform freehand palpation with tracked 3D transducer,
2. Use the tracking information [15] to select suitable aligned frames separated only by in-plane translation,
3. Apply 2D multi-image mosaic method on a frame-by-frame basis to estimate a unified displacement field, and
4. Generate the 3D elastography mosaic from the unified displacement field.

3 Results and Validation

For experimental validation we palpated a CIRS (Norfolk, VA) elastography phantom *049a* (Fig. 1a) using a high-frequency ultrasound transducer (L14-5W/60) at center frequency of 10 MHz. Ultrasound RF data was acquired from an Ultrasonix system (Vancouver, BC) at 40MHz sampling rate. The *049a* phantom consists of a series of stepped cylinders of varying diameters. The transducer was placed on top of one of the cylinders, parallel with its direction. The phantom was placed on a stage which controlled the compression in the axial direction and the translation in the lateral direction (Fig. 1a). RF data sequences were acquired from four axial compression levels ($c_0 = 0$, $c_1 = 2.54$mm, $c_2 = 5.08$mm, c_3 = back to 0), for each of four lateral translation positions of the transducer ($t_0 = 0$, $t_1 = 5.08$mm, $t_2 = 10.16$mm, $t_3 = 20.32$mm), for a total of sixteen data sets. The width of the ultrasound transducer L14-5W is 59mm, and as a consequence any 2 sets separated by a lateral translation had some amount of overlap.

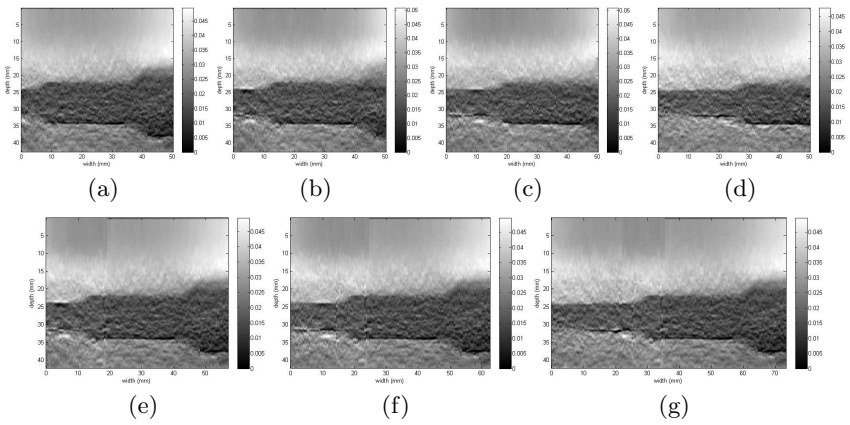

Fig. 4. Ultrasound elastography at position t_0 (a), t_1 (b), t_2 (c), t_3 (d) and elastography mosaic of positions t_0 and t_1 (e), t_0, t_1 and t_2 (f), and t_0, t_1, t_2 and t_3 (g).

Ultrasound elastography images were obtained for each translation position t_0 - t_3 ((Fig. 4a-d). A pairwise elastography mosaic was produced from positions t_0 and t_1 ((Fig. 4e), and then multi-image elastography mosaics from positions t_0, t_1 and t_2 ((Fig. 4f), and t_0, t_1, t_2 and t_3 ((Fig. 4g).

Mosaicing multiple images in a pairwise fashion can cause errors to accumulate with each new added image. To calculate this error we computed the wide FOV displacement map from positions t_0 and t_3, and compared it with the multi-image displacement map from positions t_0, t_1, t_2 and t_3 added consecutively. The random search algorithm was run 5 times and the results were averaged. For the resulting displacement maps, we computed an absolute difference per pixel, as well as mean and standard deviation absolute difference for the entire FOV.

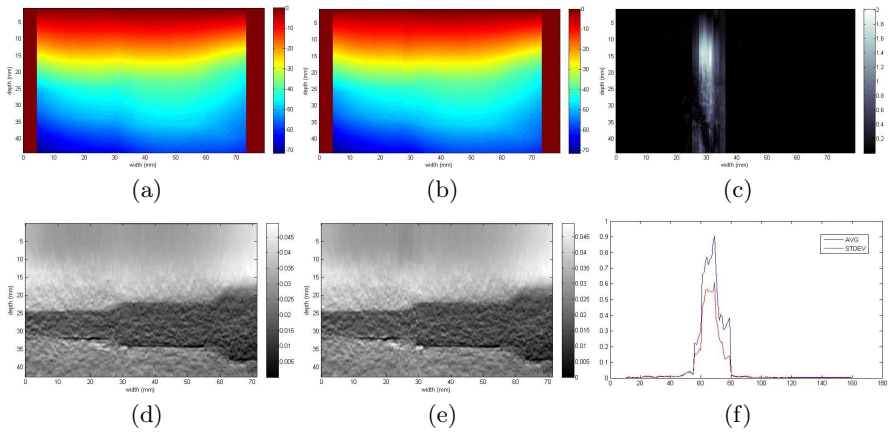

Fig. 5. Panoramic displacement map of positions t_0 and t_3 (a), and of positions t_0, t_1, t_2 and t_3 (b), the absolute difference between them (c), and the mean and standard deviation of this difference, per line (f). The unit of displacement is pixels. Corresponding ultrasound elastography mosaics of positions t_0 and t_3 (d), and t_0, t_1, t_2 and t_3 (e).

Figure 5 shows the results of the validation experiment. The two panoramic displacement maps agree almost exactly; the absolute difference for the entire image had a mean of 0.0755 and a standard deviation of 0.2386 pixels. The maximum difference was 2.0168 pixels and it did not exceed 1 pixel on a mean, per-line basis. For a metric correspondent, 2.0168 pixels, is the equivalent of 0.0406 mm in the axial direction. Once the displacement maps are converted in elastogram mosaics (Fig. 5 e,f), the difference becomes indistinguishable even on close inspection. With the clinical application in mind, we conclude that these small differences are acceptable.

4 3D mosaicing

For 3D validation, RF data was acquired using an Ultrasonix system (Vancouver, BC) at 20MHz sampling rate. The same CIRS (Norfolk, VA) elastography phantom *049a* (Fig. 1a) was palpated with a 38mm width linear 4D volumetric transducer (4DL14-5/38). As with the 2D experiment, the phantom was placed on a stage to controll the compression in the axial direction and the translation in the lateral direction (Fig. 1 a). RF data sequences were acquired from four axial compression levels ($c_0 = 0$, $c_1 = 2.54$mm, $c_2 = 5.08$mm, $c_3 =$ back to 0), for each of five lateral translation positions of the transducer ($t_0 = 0$, $t_1 = 5.08$mm, $t_2 = 10.16$mm, $t_3 = 20.32$mm, $t_4 = 22.86$mm), for a total of twenty data sets.

Figure 6 shows the results of the 3D ultrasound elastography mosaic. Strain in the middle frames of the axial-lateral plane (Figure 6a), lateral-elevational plane (Figure 6b), and 3 axial-elevational planes (Figure 6c-e) is shown. The diameters of the stiff cyclinder along the mosaicing direction were: 4.05 mm (Figure 6c), 2.53 mm (Figure 6d) and 1.58 mm (Figure 6e).

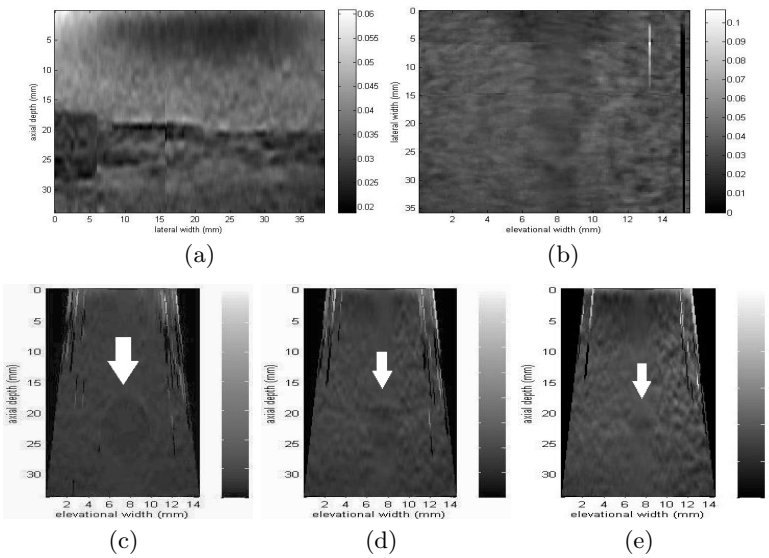

(a) (b) (c) (d) (e)

Fig. 6. 3D ultrasound elastography mosaic: axial-lateral plane (a), lateral-elevational plane (b), and 3 axial-elevational planes through 3 different diameters of the stepped cylinder (c,d,e)

5 Conclusion

We have presented an algorithm for generating reliable multi-image ultrasound elastography mosaics, robust to regions of decorrelation. Panoramic B-mode ultrasound has been reported with success in the literature and, with the addition of corresponding elastograms, an ultrasound system with these capabilities

has great potential in clinical diagnostic and monitoring. Elastography has the advantage that is requires no additional hardware to be implemented, and a majority of commercial ultrasound systems now present an elastography interface. Furthermore, the challenge of mosaicing while freehand scanning can be met as efforts are under way to incorporate electromagnetical (EM) tracking in ultrasound transducers.

References

1. Ophir, J., Alam, S.K., Garra, B., Kallel, F., Konofagou, E., Krouskop, T., Varghese, T.: Elastography: ultrasonic estimation and imaging of the elastic properties of tissues. Proceedings of the Institution of Mechanical Engineers. Part H, Journal of Engineering in Medicine **213**(3) (1999) 203–233
2. Varghese, T., Zagzebski, J., Lee Jr., F.: Elastographic imaging of thermal lesions in the liver in vivo following radiofrequency ablation: preliminary results. Ultrasound in Medicine & Biology **28**(1112) (December 2002) 1467–1473
3. Emelianov, S., Chen, X., ODonnell, M., Knipp, B., Myers, D., Wakefield, T., Rubin, J.: Triplex ultrasound: elasticity imaging to age deep venous thrombosis. Ultrasound in Medicine & Biology **28**(6) (June 2002) 757–767
4. Garra, B., Cespedes, E., Ophir, J., Spratt, S., Zuurbier, R., Magnant, C., Pennanen, M.: Elastography of breast lesions: initial clinical results. Radiology **202**(1) (1997) 79–86
5. Poon, T.C., Rohling, R.N.: Three-dimensional extended field-of-view ultrasound. Ultrasound in Medicine & Biology **32**(3) (March 2006) 357–369
6. Gee, A.H., Treece, G.M., Prager, R.W., Cash, C.J., Berman, L.: Rapid registration for wide field of view freehand three-dimensional ultrasound. IEEE Transactions on Medical Imaging **22**(11) (November 2003) 1344–1357
7. Wachinger, C., Wein, W., Navab, N.: Registration strategies and similarity measures for three-dimensional ultrasound mosaicing. Academic Radiology **15**(11) (November 2008) 1404–1415
8. Rajpoot, K., Noble, J.A., Grau, V., Szmigielski, C., Becher, H.: Multiview RT3D echocardiography image fusion. In Ayache, N., Delingette, H., Sermesant, M., eds.: Functional Imaging and Modeling of the Heart. Volume 5528. Springer Berlin Heidelberg, Berlin, Heidelberg (2009) 134–143
9. Lindop, J.E., Treece, G.M., Gee, A.H., Prager, R.W.: 3d elastography using freehand ultrasound. Ultrasound in Medicine & Biology **32**(4) (2006) 529 – 545
10. Jiang, J., Hall, T.J., Sommer, A.M.: A novel image formation method for ultrasonic strain imaging. Ultrasound in Medicine & Biology **33**(4) (2007) 643 – 652
11. Lindop, J., Treece, G., Gee, A., Prager, R.: An intelligent interface for freehand strain imaging. Ultrasound in Medicine & Biology **34**(7) (2008) 1117 – 1128
12. Fleming, I., Rivaz, H., Boctor, E., Hager, G.: Robust dynamic programming method for ultrasound elastography. SPIE **8320**(1) (2012) 83201–83206
13. Rivaz, H., Boctor, E., Choti, M., Hager, G.: Real-time regularized ultrasound elastography. IEEE Transactions on Medical Imaging **30**(4) (April 2011) 928–945
14. Mase, G., Smelser, R., Mase, G.: Continuum Mechanics for Engineers, Third Edition. Computational Mechanics and Applied Analysis Series. CRC Press (2009)
15. Foroughi, P., Kang, H.J., Carnegie, D.A., van Vledder, M.G., Choti, M.A., Hager, G.D., Boctor, E.M.: A freehand ultrasound elastography system with tracking for in-vivo applications. Ultrasound in Medicine & Biology (2012) In Press.

Robust Dynamic Programming Method for Ultrasound Elastography

Ioana Fleming[a], Hassan Rivaz[a], Emad Boctor[b] and Gregory Hager[a]

[a]Johns Hopkins University, [b]Johns Hopkins Medical Institutions, Baltimore, MD, USA

ABSTRACT

Ultrasound elastography is an imaging technology which can detect differences in tissue stiffness based on tissue deformation. For successful clinical use in cancer diagnosis and monitoring the method should be robust to sources of decorrelation between ultrasound images. A regularized Dynamic Programming (DP) approach was used for displacement estimation in compressed tissue. In the Analytic Minimization (AM) extension of DP, integer displacements are calculated just for one RF-line, and later propagated laterally throughout the entire image. This makes the seed RF-line very important; faulty seed lines could propagate erroneous displacement values throughout the image resulting in the appearance of false "lesions". In this paper we analyze the robustness of this method in free-hand palpation of laboratory tissue phantoms. We are proposing an update to the algorithm which includes a random search for the most robust seed RF-line. Axial integer displacements are obtained on each random seed line individually with DP optimization. For each random axial RF-line, multiple random values for decorrelation compensation are used in the displacement estimation. The displacement values are then compared and several metrics of stability and consistency are considered. A ranking is established and the line deemed most robust will become the seed line for displacement propagation, while also selecting the most stable value for decorrelation compensation. The random search can be achieved at no additional computational cost in a parallel implementation. The results indicate significant improvement in the robustness of the DP approach, while maintaining real-time computation of strain images.

1. BACKGROUND AND RATIONALE

Ultrasound Elastography is an imaging technology which can detect differences in tissue stiffness based on tissue deformation.[1] Our work in this paper focuses on real-time quasi-static elastography. The tissue is compressed and relaxed in a continuous free-hand motion and ultrasound images are simultaneously acquired. This method is easy to use and also cheap as it requires no extra hardware. This makes it particularly appealing for medical imaging applications; diagnosis or monitoring could be done at the patient's bed side. There are two hurdles which once resolved would ensure success for clinical use: real-time computation of strain images and dealing with the potential for global and local decorrelation between pre- and post-compression ultrasound signals. Various sources of decorrelation are affecting the computation of strain images in *in-vivo* data, such as incoherent fluid (blood) motion, out-of-plane motion of structures within one image due to transducer or respiratory motion, subsample speckle motion, and a high degree of compression.

Rivaz and Hall initially proposed optimizing a recursive regularized cost function using Dynamic Programming (DP).[2,3] The method resulted in integer values for axial displacement and subsample displacement could also be achieved but at a high computational cost. Rivaz et al. refined the method further using a 1D and 2D Analytic Minimization (AM) of the cost function.[4] It takes the integer displacement of a single axial radio frequency (RF)-line from DP and produces the subsample axial and lateral displacement fields for the entire image.

In this work we analyze the robustness of the AM2D method. Since this method is based on computing integer displacements using DP on only one RF-line, it is crucial that we choose a starting line with little or no decorrelation between the two images. Here we present a method for identifying robust, stable lines and reducing the potential to generate artifact lesions.

2. 2D AM SUBPIXEL DISPLACEMENT ESTIMATION

Here we briefly review the 2D AM method in which 2D integer displacements are first obtained using DP on a single RF-line and are then used to produce 2D subsample displacements for the entire image.

1. Calculate integer axial a_i and lateral l_i displacements of one *seed* RF-line using DP ([2]). Calculate an initial subsample estimate using linear interpolation of the integer displacements.

   Let I_1 and I_2 be two ultrasound images acquired before and after deformation. Let m be the number of RF-lines. Each signal is sampled at $i = 1,\ 2 \cdots m$. A regularized cost function is generated combining the prior of displacement continuity (regularization term) and an amplitude similarity term. The displacement continuity term for line j can be written as:

   $$R_j(a_i, l_i, a_{i-1}, l_{i-1}) = \alpha_a (a_i - a_{i-1})^2 + \alpha_l (l_i - l_{i-1})^2 \tag{1}$$

   where α_a and α_l are axial and lateral regularization weights respectively.

   The regularized cost function at the ith sample of the jth A-line becomes:

   $$C_j(a_i, l_i, i) = [I_1(i,j) - I_2(i + a_i, j + l_i)]^2 + \min_{d_a, d_l} \left\{ \frac{C_j(d_a, d_l, i-1) + C_{j-1}(d_a, d_l, i)}{2} + w R_j(a_i, l_i, d_a, d_l) \right\} \tag{2}$$

   where w is a regularization weight for smoothness; d_a and d_l are temporary axial and lateral displacements which are varied in order to minimize eqn. (2).

2. Calculate subsample axial and lateral displacements for the *seed* RF-line using 2D AM (below). They will be added to the initial integer estimates.

3. Propagate the solution of the *seed* RF-line to the left and right. using the displacement of the previous line as initial estimate.

   The aim is to calculate Δa_i and Δl_i such that the duple $(a_i + \Delta a_i, l_i + \Delta l_i)$ gives the axial and lateral displacements at the sample i. The regularized cost function becomes:

   $$\begin{aligned} &C_j(\Delta a_1, ..., \Delta a_m, \Delta l_1, ..., \Delta l_m) = \textstyle\sum_m^{i=1} \{ [I_1(i,j) - I_2(i + a_i + \Delta a_i, j + l_i + \Delta l_i)]^2 + \\ &+ \alpha \left(a_i + \Delta a_i - a_{i-1} - \Delta a_{i-1} \right)^2 + \beta_a \left(l_i + \Delta l_i - l_{i-1} - \Delta l_{i-1} \right)^2 + \beta_l^{'} \left(l_i + \Delta l_i - l_{i,j-1} \right)^2 \} \end{aligned} \tag{3}$$

   ,where the index j was dropped for the j^{th} RF-line and $l_{i,j-1}$ is the lateral displacement of the previous RF-line (except for the *seed* line where $l_{i,j-1} = l_i$. α, β_a and $\beta_l^{'}$ are regularization terms which ensure continuity in displacements with respect to the top (axial α), and the top and left/right (lateral β_a and $\beta_l^{'}$). If the displacement of the previous line is not accurate, it will affect the displacement of the next line through the last term in the right-hand side of (3).

3. EXPERIMENTAL DESIGN AND RESULTS

For experimental evaluation we palpated a breast elastography phantom with a 10mm ϕ lesion and three times stiffer than the background. RF data was acquired with a 7.27MHz linear array at a sampling rate of 40MHz. In order to evaluate the magnitude of the problem, we first set out to evaluate the percentage of *seed* RF-lines with faulty DP displacement estimations. When propagated laterally to the neighboring lines, these faulty displacement estimations would result in artifact lesions, clearly visible on the final elastogram (Fig. 1). Many of the artifacts created by the erroneous displacement estimation were very small (Fig. 1 b) and localized at the

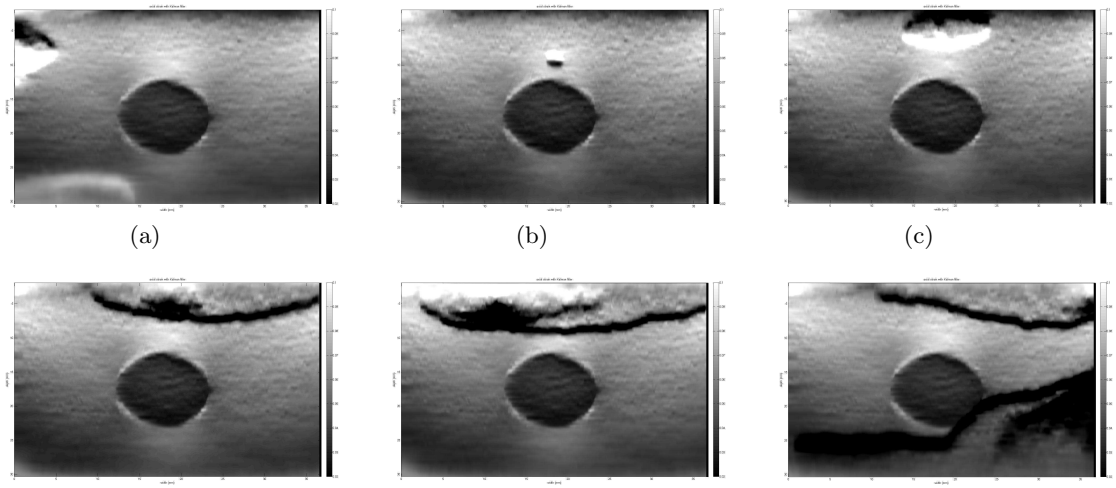

(a) (b) (c)

(d) (e) (f)

Figure 1. Examples of art1fact lesions in strain images using DP AM2D method. Data collected from breast phantom freehand palpation.

top of the image (Fig. 1 b, c). Some artifacts were however large, sometimes propagating through a big part of the image (Fig. 1 d, e) and, in very rare cases, obscuring the real lesion (Fig. 1 f).

DP displacement computation uses a smoothness regularization parameter w (2), which should prevent regions with high local decorrelation from introducing errors in displacement estimation, but if chosen too large would result in oversmoothing. Strain images were obtained with the AM2D method using each RF-line as a *seed*, each for 11 (eleven) values for w: 0.1, 0.15, 0.2, 0.25, 0.3, 0.35, 0.4, 0.45, 0.5, 0.55 and 0.6. Each resulting elastogram was visually inspected for the presence of artifacts, knowing the shape and size of the expected lesion. The percentages of faulty and good *seed* lines are summarized in Table 1. Some lines produced very faint, very small artifacts on the order of a couple of pixels which were not clearly visible at first inspection and they were categorized as *indeterminate*.

Table 1. Percentage distribution of AM2D behavior for *seed* RF-lines given multiple values for w (smoothness regularization parameter)

w	Good Lines (%)	Faulty Lines (%)	Indeterminate (%)
0.10	44.2	55.8	-
0.15	57.8	42.2	-
0.20	61.3	33.6	5.1
0.25	68.1	30.0	1.9
0.30	65.0	30.5	4.5
0.35	61.7	32.0	5.3
0.40	53.3	41.8	4.9
0.45	53.1	46.9	-
0.50	43.4	56.6	-
0.55	32.1	67.9	-
0.60	24.3	75.8	-

The results were very revealing both about the importance of the value of w, but also of the magnitude of the decorrelated areas. We noted that faulty lines did not appear to be predominant in certain locations, like for example towards the lateral margins of the imaged area, but they were actually widely dispersed throughout the image. In light of the results, for this specific data set we continued our investigation only for w in the range $(0.25, 0.35)$, to ensure a high probability of finding a good starting RF-line.

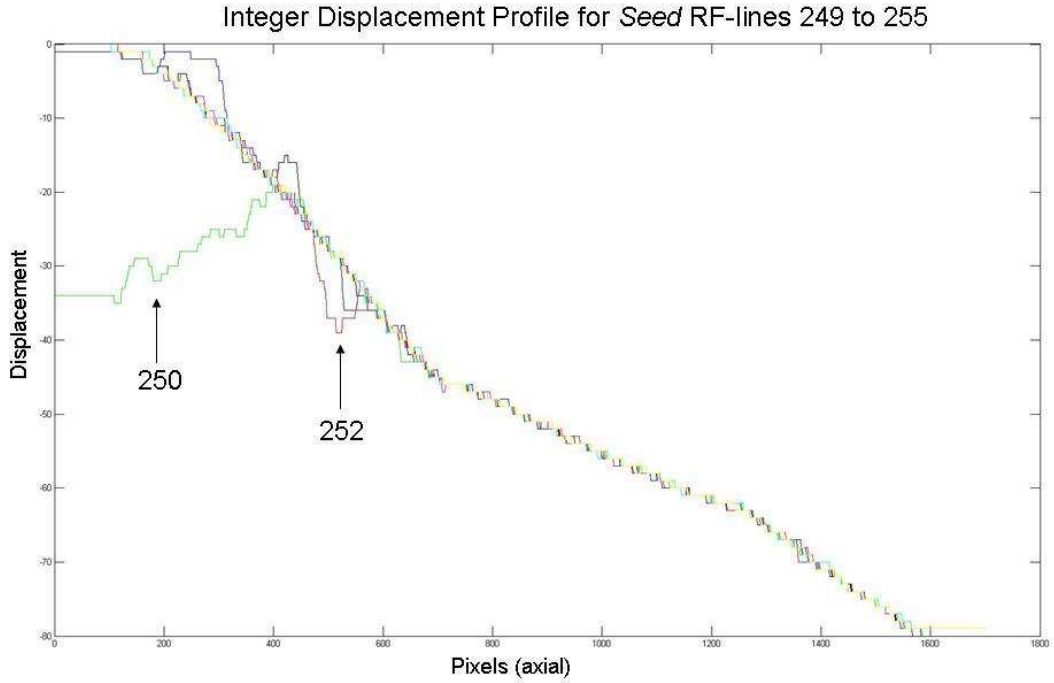

Figure 2. Integer DP displacement estimation for *seed* RF-lines 249 to 255. Note the areas (for lines 250 and 252 respectively) where the change in slope produces the artifact lesions

3.1 *Deformation Slope*

In a continuous piece of tissue, the deformation field resulting from a stress field induced by applied compression has a monotonous ramp profile.[5] Our hypothesis was that faulty lines would exhibit a perturbation in the monotonously decreasing slope of their displacement profile. For example, when plotting DP displacement values for *seed* RF-lines 249 to 255 (Fig. 2), faulty lines 250 and 252 respectively exhibited a change in slope towards the top portion of the imaging area, which in the end resulted in artifact lesions (Fig. 1 c - 250 and b - 252).

A *change-in-slope* parameter was computed for the DP displacement profile for each *seed* RF-line, for $w=$ $0.25, 0.30, 0.35$. 486 lines were evaluated for each of the three values for w, for a total of 1458 computations. The *change-in-slope* test was considered positive when the 3 (three) or more positions exhibited a continuous change in the slope of displacement. Note that the 3 (three) positions did not need to be consecutive, as long as the ramp stayed flat or continued the change direction(Fig. 3 a, b).

3.2 *Displacement Stability*

Another measure of robustness is stability. A robust *seed* RF-line needs to exhibit the same or similar DP displacement estimation across different w values. We computed the percentage of positions (pixels) for which displacement values differed more than 3 (three) pixels between different values of w. For all 486 lines, 3 (three) pairs of displacement values were compared: 1) $w = 0.25$ vs. $w = 0.30$, 2) $w = 0.30$ vs. $w = 0.35$, 3) $w = 0.25$ vs. $w = 0.35$. The score received by each line was averaged over the three comparisons for a final score, potentially ranging from 0 to 1 (100% of pixels exhibited more than 3 (three) pixels differences). We wanted to test the statistical significance of the difference between the faulty lines population and the robust lines population.

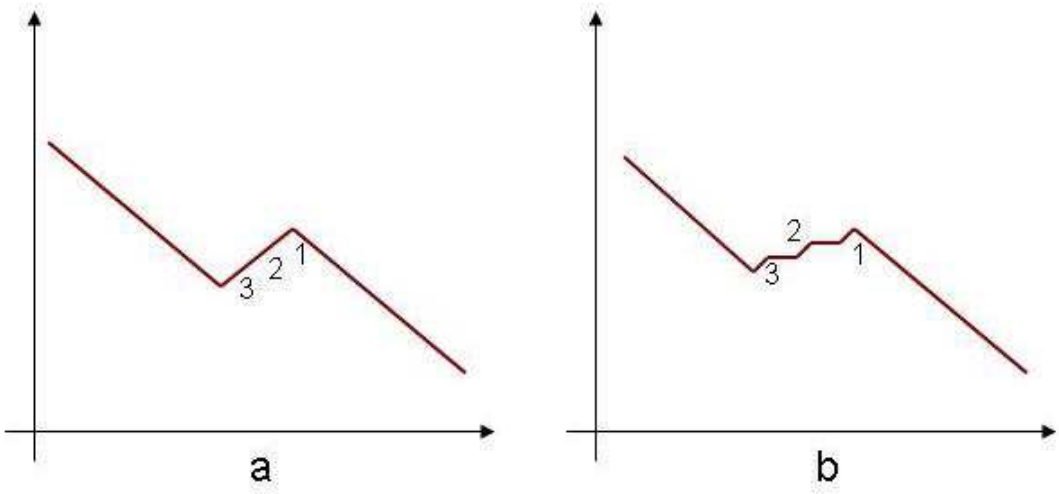

Figure 3. *Change-in-slope* detection algorithm. The 3 (three) positions where the change in slope is exhibited could be consecutive (a) or not (b)

4. RESULTS AND DISCUSSION

4.1 *Deformation Slope*

For a robust AM2D algorithm one single successful *seed* RF-line is sufficient. The *change-in-slope* parameter was designed to select good *seed* lines with monotonously increasing/decreasing displacement profile. Over all 1458 computations of the parameter (486 lines * 3 w values), the sensivity for selecting a good line was **91.7%**, while the specificity was **48.6%** (Table 2). The measure performed up to 93.1% sensitivity when tested across just one w value. We concluded the measure was promising but not sufficient on its own.

Table 2. *Change-in-Slope* (TP = true positive, FP = false positive, TN = true negative, FN = false negative)

		Prediction outcome		
		p	**n**	**total**
actual value	p′	TP = 835	FN = 238	P′
	n′	FP = 76	TN = 252	N′
	total	P	N	

4.2 *Displacement Stability*

486 scores were computed, one for each potential *seed* RF-line. The scores ranged from 0 to 0.2649. The average score for the good lines was 0.0058 (stdev = 0.0186) and the average score for the faulty lines was 0.0444 (stdev = 0.0586). A one-side Student t-test showed a **p-value** of $3.73909e-17$ (Table 3).

To increase the significance of the prediction value, we also computed a combined score for the two detection algorithms. The averaged *Change-in-Slope* score over the 3 (three) values for w was either 0, 0.33, 0.66, or 1, depending on how many of the three instances were deemed positive by the test. This score was added to the *Displacement Stability* score for a combined overall score. This overall score ranged from 0 to 1.1588. The average score for the good lines was 0.0795 (stdev = 0.2422) and the average score for the faulty lines was 0.4939 (stdev = 0.4444), for a **p-value** of $1.75837e-27$ (Table 3).

Table 3. Robustness score: Displacement Stability vs. Combined score for Displacement Stability + Change-in-Slope

	Displ. Stability		Displ. Stability + Change-in-Slope	
	Good Lines	Faulty Lines	Good Lines	Faulty Lines
Min	0	0	0	0
Max	0.1002	0.2649	1	1.1588
Avg	0.0058	0.0444	0.0795	0.4939
StDev	0.0186	0.0586	0.2422	0.4444
p-value	**3.73909E-17**		**1.75837E-27**	

Following the results of this analysis, a random search algorithm was implemented for the selection of a robust, stable *seed* RF-line as follows:

1. DP integer displacement is calculated for 5 random RF-lines, each at 5 random w values
2. A combined *Change-in-Slope* average plus *Displacement Stability* average score is computed
3. The most robust, stable line is chosen as the line with the smallest combined score, which also does not have any positive *Change-in-Slope* score
4. The chosen *seed* line's displacement values are propagated using the AM2D method

Given the current parallel computational resources, the addition of this selection test does not add a significant amount of time to the overall running time. DP takes the same time as before but it's now computed 25 times, and the computation of each score takes on the order of a couple of milliseconds. On 100 random runs of our testing algorithm, we only encountered 1 (one) situation where a faulty line was selected. The reason for the selection was that all 5 of the random line tested were faulty. This prompted us to introduce the additional condition that the chosen line should not have any positive *Change-in-Slope* score. Following this modification, no faulty situation has been encountered so far. We will continue to test our algorithm on the presented data set, as well as on new *ex-vivo* and *in-vivo* tissue data.

5. CONCLUSION

We proposed and successfully implemented an algorithm for the selection of a robust, stable RF-line to be used as *seed* for the DP displacement estimation and later propagated using the AM2D algorithm for elastography. The benefit of this algorithm is significant as it has the potential to improve the robustness of ultrasound elastography in *in-vivo* tissue which can be highly decorrelated. We are in the process of evaluating this hypothesis. The selection of robust *seed* RF-lines becomes even more important as we move towards real-time 3D ultrasound elastography.

REFERENCES

[1] J. Ophir, S. K. Alam, B. Garra, F. Kallel, E. Konofagou, T. Krouskop, T. Varghese, Elastography: ultrasonic estimation and imaging of the elastic properties of tissues, Proceedings of the Institution of Mechanical Engineers. Part H, Journal of Engineering in Medicine 213 (3) (1999) 203–233.

[2] H. Rivaz, E. Boctor, P. Foroughi, R. Zellars, G. Fichtinger, G. Hager, Ultrasound elastography: a dynamic programming approach, IEEE Transactions on Medical Imaging 27 (10) (2008) 1373–1377.

[3] J. Jiang, T. Hall, A regularized real-time motion tracking algorithm using dynamic programming for ultrasonic strain imaging, in: IEEE Ultrasonics Symp., Vancouver, Canada, 2006, pp. 606–609.

[4] H. Rivaz, E. M. Boctor, M. A. Choti, G. D. Hager, Real-time regularized ultrasound elastography, IEEE Transactions on Medical Imaging 30 (4) (2011) 928–945.

[5] G. Mase, Continuum Mechanics for Engineers, Third Edition (Computational Mechanics and Applied Analysis).

A Robust Dynamic Programming Method for Ultrasound Elastography

Ioana N. Fleming[1], Hassan Rivaz[1] , Emad M. Boctor[1,2] , and Gregory D. Hager[1]

[1] Johns Hopkins University, [2] Johns Hopkins Medical Institutions, Baltimore, MD, USA

ABSTRACT: *Ultrasound elastography is an imaging technology which can detect differences in tissue stiffness based on tissue deformation. For successful clinical use in cancer diagnosis and monitoring the method should be robust to sources of decorrelation between ultrasound images. A regularized Dynamic Programming (DP) approach was used for displacement estimation in compressed tissue. In the Analytic Minimization (AM) extension of DP, integer displacements are calculated just for one RF-line, and later propagated laterally throughout the entire image. This makes the seed RF-line very important; faulty seed lines could propagate erroneous displacement values throughout the image resulting in the appearance of false "lesions". In this paper we analyze the robustness of this method in free-hand palpation of laboratory tissue phantoms. An update to the algorithm includes a random search for the most robust seed RF-line. Axial integer displacements are obtained for 5 random lines individually with DP optimization. For each random axial RF-line, multiple random values for decorrelation compensation are used in the displacement estimation. The displacement values are then compared and several metrics of stability and consistency are considered. A ranking is established and the line deemed most robust will become the seed line for displacement propagation, while also selecting the most stable value for decorrelation compensation. The random search can be achieved at no additional computational cost in a parallel implementation. The results indicate significant improvement in the robustness of the DP approach, while maintaining real-time computation of strain images.*

INTRODUCTION:

- Take one image before compression,
- Compress tissue and take second image,
- Compare images and calculate displacement (tissue motion) field,
- Calculate strain image from the motion field

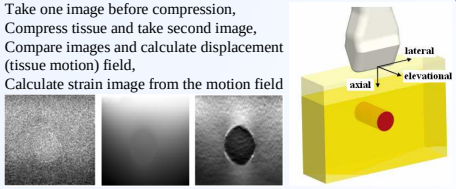

DYNAMIC PROGRAMMING (*DP*) + ANALYTIC MINIMIZATION (*AM*):

1. For images I_1 and I_2, calculate integer axial a_i and lateral l_i displacements of one seed RF-line using DP.
   - Displacement continuity term for line *j*:

$$R_j(a_i, l_i, a_{i-1}, l_{i-1}) = \alpha_a (a_i - a_{i-1})^2 + \alpha_l (l_i - l_{i-1})^2$$

   - Regularized cost function at the *i*th sample of the *j*th A-line:

$$C_j(a_i, l_i, i) = [I_1(i,j) - I_2(i + a_i, j + l_i)]^2 + \min_{d_a, d_l} \left\{ \frac{C_j(d_a, d_l, i-1) + C_{j-1}(d_a, d_l, i)}{2} + wR_j(a_i, l_i, d_a, d_l) \right\}$$

2. Calculate sub-sample axial and lateral displacements for the seed RF-line using 2D Analytic Minimization.
3. Propagate the solution of the seed RF-line to the left and right, using the displacement of the previous line as initial estimate.
   - Calculate a_i and l_i such as $(a_i + \Delta a_i, l_i + \Delta l_i)$ gives the axial and lateral displacements at the sample *i*. The regularized cost function becomes:

$$C_j(\Delta a_1, ..., \Delta a_m, \Delta l_1, ..., \Delta l_m) = \sum_m^{i=1} \{[I_1(i,j) - I_2(i + a_i + \Delta a_i, j + l_i + \Delta l_i)]^2 + \alpha (a_i + \Delta a_i - a_{i-1} - \Delta a_{i-1})^2 + \beta_a (l_i + \Delta l_i - l_{i-1} - \Delta l_{i-1})^2 + \beta_l' (l_i + \Delta l_i - l_{i,j-1})^2$$

, where α_a and α_l are axial and lateral regularization weights; *w* is a regularization weight for smoothness; α, β_a and β_l' are regularization terms which ensure continuity in displacements with respect to the top (axial a), and top - left/right (lateral β_a and β_l')

PROBLEM – Faulty *seed* RF-lines:

The displacement of the previous line will affect the displacement of the next line:
- bad initial estimate
- the last term → enforces lateral smoothness

For experimental evaluation we palpated a breast elastography phantom with a 10mm lesion and three times stiffer than the background. RF data was acquired with a 7.27MHz linear array at a sampling rate of 40MHz.
- Strain images using the AM-2D method, with each RF-line as a seed, each for 11 (eleven) values for *w* (smoothness regularization

w	Good Lines (%)	Faulty Lines (%)	Indeterminate (%)
0.10	44.2	55.8	-
0.15	57.8	42.2	-
0.20	61.3	33.6	5.1
0.25	68.1	30.0	1.9
0.30	65.0	30.5	4.5
0.35	61.7	32.0	5.3
0.40	53.3	41.8	4.9
0.45	53.1	46.9	-
0.50	43.4	56.6	-
0.55	32.1	67.9	-
0.60	24.3	75.8	-

Table 1: Percentage distribution of AM2D behavior for seed RF-lines given multiple values for *w* (smoothness regularization parameter)

***w* = (0.25, 0.35)** → high probability of finding a good *seed* RF-line

METHODS:

1. DEFORMATION SLOPE

Hypothesis: faulty lines would exhibit a perturbation in the monotonously decreasing slope of their displacement profile.

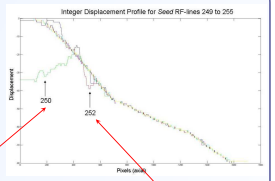

Figure 1: Integer DP displacement estimation for seed RF-lines 249 to 255. Note the areas (for lines 250 and 252 respectively) where the change in slope produces the artifact lesions

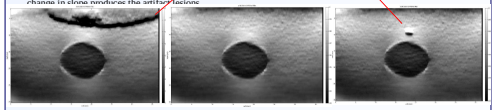

Figure 2. Examples of artifact lesions in strain images using DP AM2D method. Data collected from breast phantom freehand palpation.

A *change-in-slope* parameter was computed for the DP displacement profile for each seed RF-line, for w= 0:25; 0:30; 0:35.
486 lines were evaluated for each of the three values for w, for a total of **1458 computations**. Positive *change-in-slope* test: 3 or more positions exhibited a continuous change in the slope of displacement (Figure 3).

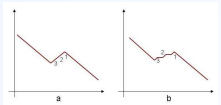

Figure 3: *Change-in-slope* detection algorithm. The 3 (three) positions where the change in slope is exhibited could be consecutive (a) or not (b)

		Prediction outcome		
		p	n	total
actual value	p'	TP = 835	FN = 238	P'
	n'	FP = 76	TN = 252	N'
	total	P	N	

Table 2: *Change-in-slope* predictor (TP = true positive, FP = false positive, TN = true negative, FN = false negative)

Sensitivity = 91.7%
Specificity = 48.6%

2. DISPLACEMENT STABILITY

Hypothesis: A robust seed RF-line will exhibit the same or similar DP displacement estimation across different *w* values.

Displacement Stability test: percentage of positions (pixels) where displacement values differ by more than 3 pixels for different values of *w*. For all 486 lines, 3 (three) pairs of displacement values were compared: 1) w = 0:25 vs. w = 0:30, 2) w = 0:30 vs. w = 0:35, 3) w = 0:25 vs. w = 0:35. Average the score for each line; final score between 0 and 1.

Combined score: the avg. *Change-in-Slope* score over the 3 values for *w* (0, 0.33, 0.66, or 1) was added to the

Table 3. Robustness score: Displacement Stability vs. Combined score for Displacement Stability + Change-in-Slope)

	Displ. Stability		Displ. Stability + Change-in-Slope	
	Good Lines	Faulty Lines	Good Lines	Faulty Lines
Min	0	0	0	0
Max	0.1002	0.2649	1	1.1588
Avg	0.0058	0.0444	0.6795	0.4939
StDev	0.0186	0.0586	0.2422	0.4444
p-value	3.73909E-17		1.75837E-27	

RESULTS:

MODIFIED DP + AM2D ALGORITHM

Select a robust, stable *seed* RF-line using random search:
1. DP integer displacement is calculated for 5 random RF-lines, each at 5 random *w* values;
2. A combined *Change-in-Slope* average plus *Displacement Stability* average score is computed;
3. The most robust, stable line is chosen as the line with the smallest combined score, which also does not have any positive *Change-in-Slope* score;
4. The chosen seed line's displacement values are propagated with AM2D.

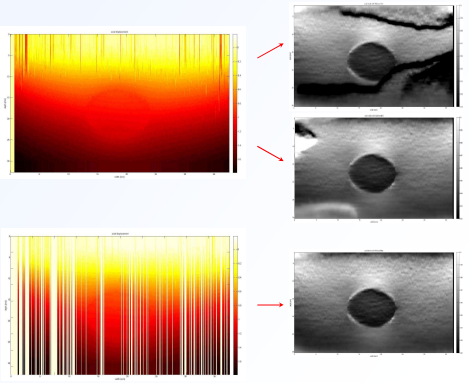

CONCLUSIONS:

We proposed and successfully implemented an algorithm for the selection of a robust, stable RF-line to be used as *seed* for the DP displacement estimation and later propagated using the AM2D algorithm for elastography. The benefit of this algorithm is significant as it has the potential to improve the robustness of ultrasound elastography in in-vivo tissue which can be highly decorrelated. The selection of robust seed RF-lines becomes even more important as we move towards real-time 3D ultrasound elastography.

REFERENCES:

[1] J. Ophir, et al, "Elastography: ultrasonic estimation and imaging of the elastic properties of tissues", Proceedings of the Institution of Mechanical Engineers. Part H, Journal of Engineering in Medicine 213 (3) (1999) 203-233.
[2] H. Rivaz, et al, "Ultrasound elastography: a dynamic programming approach", IEEE Trans Med Img 27 (10) (2008) 1373-1377.
[3] J. Jiang, T. Hall, "A regularized real-time motion tracking algorithm using dynamic programming for ultrasonic strain imaging", in: IEEE Ultrasonics Symp., Vancouver, Canada, 2006, pp. 606-609.
[4] H. Rivaz, et al, "Real-time regularized ultrasound elastography", IEEE Trans. on Medical Imaging 30 (4) (2011) 928-945.

Acknowledgements: Ioana Fleming is supported by the DOD Predoctoral Prostate Cancer Fellowship

System for Robot-Assisted Real-Time Laparoscopic Ultrasound Elastography

Seth Billings*[a], Nishikant Deshmukh[a], Hyun Jae Kang[a], Russell Taylor[a], Emad Boctor[ab]

[a]Dept. of Computer Science, Johns Hopkins University, 3400 N. Charles St., Baltimore, MD, USA 21218;

[b]Div. of Medical Imaging Physics, Johns Hopkins Medicine, 600 N. Wolfe St., Baltimore, MD, USA 21287

ABSTRACT

Surgical robots provide many advantages for surgery, including minimal invasiveness, precise motion, high dexterity, and crisp stereovision. One limitation of current robotic procedures, compared to open surgery, is the loss of haptic information for such purposes as palpation, which can be very important in minimally invasive tumor resection. Numerous studies have reported the use of real-time ultrasound elastography, in conjunction with conventional B-mode ultrasound, to differentiate malignant from benign lesions. Several groups (including our own) have reported integration of ultrasound with the daVinci robot, and ultrasound elastography is a very promising image guidance method for robot-assisted procedures that will further enable the role of robots in interventions where precise knowledge of sub-surface anatomical features is crucial. In this paper, we present a novel robot-assisted real-time ultrasound elastography system for minimally invasive robot-assisted interventions. Our system combines a daVinci surgical robot with an experimental software interface, a robotically articulated laparoscopic ultrasound probe, and our GPU-based elastography system. Elastography and B-mode ultrasound images are displayed as picture-in-picture overlays in the daVinci console. Our system minimizes dependence on human performance factors by incorporating computer-assisted motion control that automatically generates the tissue palpation required for elastography imaging, while leaving high-level control in the hands of the user. In addition to ensuring consistent strain imaging, the elastography assistance mode avoids the cognitive burden of tedious manual palpation. Preliminary tests of the system with an elasticity phantom demonstrate the ability to differentiate simulated lesions of varied stiffness and clearly delineate lesion boundaries.

DESCRIPTION OF PurPOSE / NEW WORK PRESENTED

Surgical robots provide many advantages for surgery, including minimal invasiveness, precise motion, high dexterity, and crisp stereovision. One limitation of current robotic procedures, compared to open surgery, is the loss of haptic information for such purposes as palpation, which can be very important in minimally invasive tumor resection. Numerous studies have reported the use of real-time ultrasound elastography, in conjunction with conventional B-mode ultrasound, to differentiate malignant from benign lesions in prostate, breast, pancreas, lymph nodes, and thyroid.[1,2,3,4,5] Ultrasound elastography is thus a very promising image guidance method for robot-assisted procedures that will further enable the role of robots in interventions where precise knowledge of hidden anatomical features is crucial. Several groups (including our own) have reported integration of ultrasound with the daVinci robot.[6,7,8] In this paper, we present a novel robot-assisted real-time ultrasound elastography system for minimally invasive robot-assisted interventions.

METHODS

In general, cancerous tissue has higher cell density than surrounding healthy tissue, which leads to elevated tumor stiffness that can be visualized using elastography techniques. As first described by Ophir et al.,[9] the principle of ultrasound elastography is to estimate tissue stiffness from measurement of tissue strain induced by an applied force. This is accomplished by measuring relative tissue displacements between ultrasound image pairs under different states of induced compression. Because ultrasound elastography algorithms assume an axial compression, strain image quality may degrade when non-axial motion or probe rotation occurs during compression. Axial compression is typically on the order of only a millimeter or two, and even small amounts of unwanted motion may affect image quality. Due to the variability in manual compression, image quality for free-hand elastography is highly dependent on practitioner skill and experience.

The quality of elastography imaging as a function of human performance is minimized by our robot-assisted elastography system through computer-integrated motion control for tissue compression, whereby tissue is autonomously compressed along the direction axial to the ultrasound probe. The system computer provides assistive

control of robot motion by generating a sinusoidal palpation motion that is overlaid onto motion commands from the master manipulators (**Error! Reference source not found.**). By this method, the surgeon retains overall control of the ultrasound probe position and orientation, while the computer controls the finer points of tissue compression. Because the computer has accurate knowledge of the ultrasound probe position and is not subject to motion errors like a human operator, consistent tissue compression in the precise axial direction is ensured.

The elastography assistance mode improves the precision and consistency of tissue compression beyond what can be achieved by manually controlled teleoperation while also reducing the cognitive burden for the user. Continual palpation of tissue under manual control is a tedious task imposing a large cognitive burden and demand of focus. By relieving this burden through computer assistance, the user is able to focus on more important tasks such interpreting real-time imaging information and conducting surgery.

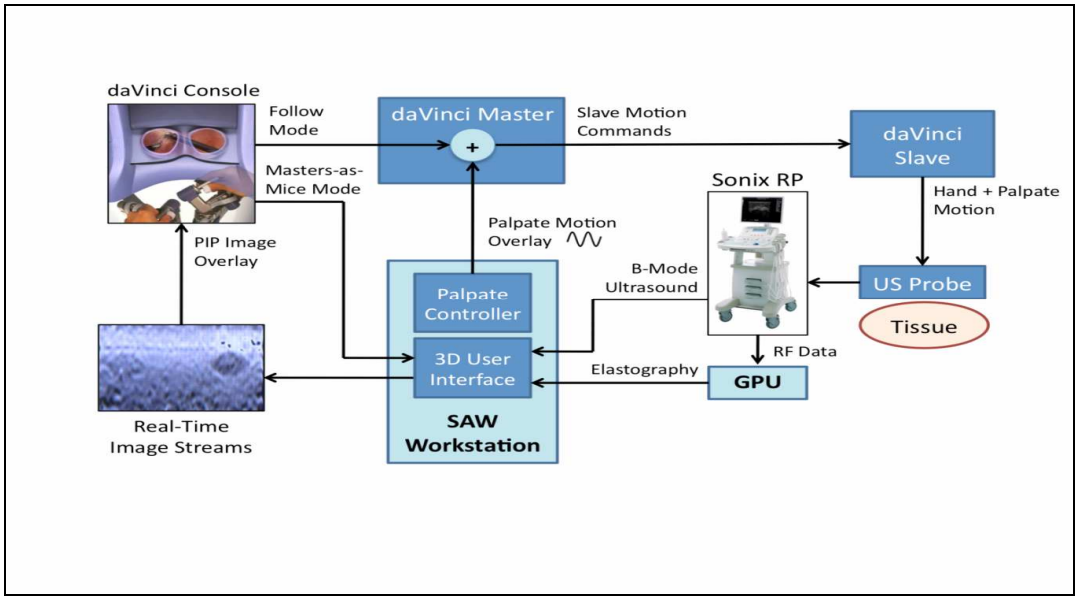

Figure 1. Block diagram of our robot-assisted system for real-time ultrasound elastography.

Error! Reference source not found. shows a block diagram of our complete system for robot-assisted ultrasound elastography. At the heart of the system is the daVinci S surgical robot (Intuitive Surgical Inc., Sunnyvale, CA). Computer integrated control of robot motion is facilitated by an experimental "Read/Write" Research Application Programming Interface (API) provided by Intuitive Surgical Inc., which enables robot motion to be controlled from computer in addition to control inputs from the master console, as discussed below. The daVinci robot manipulates a prototype version of a robotically articulated laparoscopic ultrasound probe (Figure 2a), also developed by Intuitive Surgical Inc., which was built into the form factor of a standard daVinci tool. The ultrasound probe has a linear array transducer (Gore, Newark DE) with 128 elements that measures 50mm in length with a probe diameter of approximately 9mm. The ultrasound probe is driven by a Sonix RP ultrasound system (Ultrasonix Medical Corp., Richmond BC Canada), which provides an Ultrasound Research Interface granting access to pre-beam formed RF data from the ultrasound probe. Access to this RF data is critical to reaching optimal performance from elastography algorithms. The RF data is processed by a high-performance external NVIDIA Tesla series GPU, which connects locally to the Sonix RP system. The GPU provides sufficient parallel computing power to generate strain images from RF data in real time using an elastography algorithm based on normalized cross-correlation.[10] The elastography images from the GPU are streamed from the Sonix RP system to a network port on the system's central workstation. The workstation also receives a parallel stream of conventional B-mode ultrasound images from the Sonix RP machine directly. The workstation sends both image streams to picture-in-picture overlays shown in the stereo display of the daVinci console. The picture overlays enable the surgeon to observe the ultrasound and elastography image feeds in real-time without releasing control of the robot arms or diverting attention away from the task at hand.

In collaboration with Intuitive Surgical, the Engineering Research Center for Computer-Integrated Surgical Systems and Technology (CISST ERC) at Johns Hopkins University has developed an open-source software framework for

medical robotics and computer assisted surgical systems research, which we call Surgical Assistant Workstation (SAW).[11,12,13,14] This open-source framework is an extension of the CISST software libraries developed at Johns Hopkins to enable rapid application development by providing capabilities including basic mathematics and numerical routines, thread execution management, inter-process communication, construction and control of video pipelines, and many other things.[15,16,17,18] Although the software components providing its basic capabilities are all open-source, SAW is designed to be compatible with proprietary modules through module wrappers using well-defined interface protocols. In particular, we have developed SAW wrappers that provide the ability to interface with the read-only and read-write research interfaces of the daVinci robot. The capabilities of the Read-Only daVinci Research Interface include the ability to query the state of the master and slave robot arms and of user console events.[14] The Read/Write daVinci Research Interface extends these features with the capability to use software to command motions of the master and slave robot arms and to trigger user events. One such feature allows us to superimpose an externally computed motion onto motion inputs from the master manipulators. We use this capability in our system to create computer generated motion overlays for tissue palpation. Another function of SAW allows us to use a master arm controller effectively as a 3D mouse. We call this masters-as-mice mode. We use this mode in our system to build an interactive environment for the daVinci operator to control and interact with video overlays.

The SAW software package is implemented on the central workstation of our system, which centralizes processing for user interaction with image overlays, acquisition of real-time image streams, and implementation of the control loop generating assistive motion for tissue palpation. A command terminal on the central workstation allows the user to set the amplitude and frequency of tissue palpation. These settings may be updated in real-time. The terminal also allows palpation to be activated/deactivated at will. The user interacts with the image overlays from the daVinci console using the SAW masters-as-mice mode, which, for the daVinci system, is activated by engaging the clutch foot pedal followed by a double-pinch of both master manipulators in unison. The masters-as-mice mode activates an interactive menu environment in which the daVinci master controllers manipulate virtual cursors in the daVinci console's stereo display (Figure 2a). Menu selections are made by moving a cursor to a menu icon and pinching the corresponding master controller. The elastography and B-mode ultrasound image overlays are activated by selecting the appropriate menu icon with a virtual cursor (pinching master controller selects). The image overlays are resized and repositioned in the daVinci display by dragging them with a cursor. Releasing the clutch pedal returns the master manipulators to control of the slave arms and maintains the image overlays in the user's field of view.

Results

Preliminary tests of the system have been conducted with a CIRS Model 049 Elasticity QA Phantom, which has simulated lesions of different calibrated stiffness. Figure 2b presents a snap-shot of the daVinci display taken during phantom testing with image overlays displaying the real-time imaging results. The elastography image in this figure shows clear difference in contrast between a soft and hard lesion, with the hard lesion appearing darker in the image. This distinction cannot be made from the B-mode ultrasound image in this figure. The elastography image also establishes clear delineation of lesion boundaries, which would not be discernible from B-mode ultrasound in the case of isoechoic lesions. These images were recorded with tissue palpation set to 1mm amplitude and 1Hz frequency.

CONCLUSION

We have successfully implemented a robot-assisted system for minimally invasive, real-time ultrasound elastography. Our system provides an improvement over manual elastography techniques by unifying motion commands from a user with the precision and accuracy of computer-assisted motion control to ensure consistent and precise tissue strain. Our approach effectively reduces the cognitive load of the human operator while maintaining a user's control of the procedure. Preliminary tests using an elasticity phantom demonstrate the system's capability to generate strain images in real-time that can be used to delineate simulated lesion boundaries and differentiate lesions of varying stiffness.

Acknowledgements

Funding for this work was provided by Intuitive Surgical Research Grant, National Institutes of Health Individual Graduate Partnership Program (Clinical Center, Radiology & Imaging Sciences), and Johns Hopkins Internal Funds.

Significant background technology for this project was funded in part by NSF cooperative agreement EEC9731478 and by NIH Grants R41RR019159 and R42RR019159.

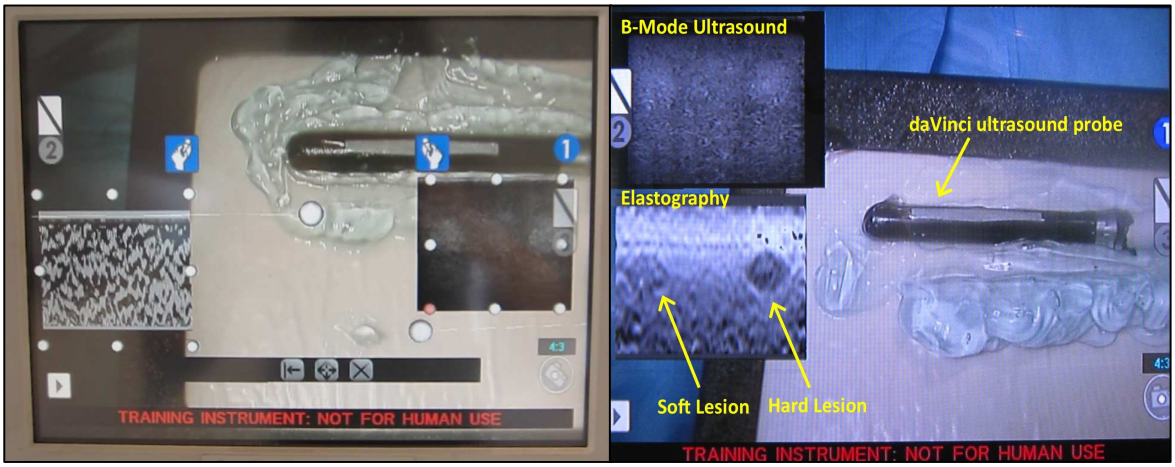

(a) (b)

Figure 2. a) Interactive menu environment for displaying image overlays in the daVinci console display, showing an active menu with two virtual mice corresponding to the left and right master manipulators and two picture-in-picture image overlays (picture taken of a patient side monitor). b) View of the daVinci console display during a test with an elasticity phantom; the elastography image overlay differentiates lesions of different stiffness.

THIS WORK HAS NOT BEEN SUBMITTED FOR PUBLICATION OR PRESENTATION ELSEWHERE.

REFERENCES

[1] Kamoi, K., Okihara, K., Ochiai, A., Ukimura, O., Mizutani, Y., Kawauchi, A., Miki, T., "The utility of transrectal real-time elastography in the diagnosis of prostate cancer," Ultrasound in Medicine & Biology 34(7), 1025-1032 (2008).

[2] Tan, S., Teh, H., Kent Mancer, J., and Poh, W., "Improving B mode ultrasound evaluation of breast lesions with real-time ultrasound elastography–A clinical approach," The Breast 17(3), 252-257 (2008).

[3] Hong, Y., Liu, X., Li, Z., Zhang, X., Chen, M., and Luo, Z., "Real-time ultrasound elastography in the differential diagnosis of benign and malignant thyroid nodules," J. Ultrasound Med. 28(7), 861-867 (2009).

[4] Saftoiu, A., Vilmann, P., Hassan, H., Gorunescu, F., "Analysis of endoscopic ultrasound elastography used for characterisation and differentiation of benign and malignant lymph nodes," Ultraschall in Med 27(6), 535-542 (2006).

[5] Saftoiu, A., Vilmann, P., Gorunescu, F., Gheonea, D., Gorunescu, M., Ciurea, T., Popescu, G., Iordache, A., Hassan, H., and Iordache, S., "Neural network analysis of dynamic sequences of EUS elastography used for the differential diagnosis of chronic pancreatitis and pancreatic cancer," Gastrointestinal Endoscopy 68(6), 1086-1094 (2008).

[6] Leven, J., Burschka, D., Kumar, R., Zhang, G., Blumenkranz, S., Dai, X., Awad, M., Hager, G., Marohn, M., Choti, M., Hasser, C., and Taylor, R., "DaVinci canvas: A telerobotic surgical system with integrated, robot-assisted, laparoscopic ultrasound capability", MICCAI 2005, LNCS Vol. 3749, 811-818 (2005).

[7] Schneider, C., Dachs, G., Hasser, C., Choti, M., DiMaio, S., and Taylor, R., "Robot-Assisted Laparoscopic Ultrasound," IPCAI 2010, LNCS Vol. 6135, 67-80 (2010).

[8] Schneider, C., Guerrero, J., Nguan, C., Rohling, R., and Salcudean, S., "Intra-operative "pick-up" ultrasound for robot assisted surgery with vessel extraction and registration: A feasibility study", IPCAI 2011, LNCS Vol. 6689, 122-132 (2011).

[9] Ophir, J., Cespedes, I., Ponnekanti, H., Yazdi, Y., and Li, X., "Elastography: A quantitative method for imaging the elasticity of biological tissues", Ultrasonic Imaging 13(2), 111-134 (1991).

[10] Deshmukh, N., Rivaz, H., and Boctor, E., "GPU-based elasticity imaging algorithms", Proc. Int. Conf. Med. Imag. Comp. & Comp. Assist. Interven., (2009).

[11] Jung, M., Deguet, A., and Kazanzides, P., "A component-based architecture for flexible integration of robotic systems", IROS 2010, 6107-6112 (2010).

[12] Jung, M., Xia, T., Deguet, A., Kumar, R., Taylor, R., and Kazanzides, P., "A Surgical Assistant Workstation (SAW) application for teleoperated surgical robot system", Sys. & Arch. for Comp. Assist. Interven., Midas Journal, (2009).

[13] Balazs, V., Simon, D., Anton, D., Peter, K., Rajesh, K., Christopher, H., and Russell, T., "The Surgical Assistant Workstation", MICCAI 2008 Workshop, Midas Journal, (2008).

[14] DiMaio, S. and Hasser, C., "The da Vinci research interface", MICCAI 2008 Workshop, Midas Journal, (2008).

[15] Kazanzides, P., Deguet, A., Kapoor, A., "An architecture for safe and efficient multi-threaded robot software", TePRA 2008, 89-93 (2008).

[16] Deguet, A., Kumar, R., Taylor, R., and Kazanzides, P., "The cisst libraries for computer assisted intervention systems", MICCAI 2008 Workshop, Midas Journal, (2008).

[17] Kapoor, A., Deguet, A., Kazanzides, P., "Software components and frameworks for medical robot control," ICRA 2006, 3813-3818 (2006).

[18] Kazanzides, P., Deguet, A., Kapoor, A., Sadowsky, O., LaMora, A., and Taylor, R., “Development of open source software for computer-assisted intervention systems”, 2005 MICCAI Open-Source Workshop, Insight Journal, (2005).